

# OPTIMIZATION OF NIOBIUM-BASED IN-SITU COMPOSITES FOR HIGH-TEMPERATURE APPLICATIONS

Final Report  
SwRI® Project No. 18.04368

by  
Kwai S. Chan

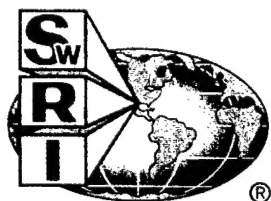
## AFOSR FINAL REPORT

This research was sponsored by the Air Force Office of Scientific Research  
Air Force Research Laboratory  
Under Contract F49620-01-C-0016  
Approved for Release; Distribution Unlimited

*The views and conclusions contained in this document are those of the authors and should not be interpreted as necessarily representing the official policies or endorsements, either expressed or implied, of the Air Force Office of Scientific Research or the U.S. Government*

March 2003

20040915 132



**SOUTHWEST RESEARCH INSTITUTE®**  
SAN ANTONIO  
DETROIT  
HOUSTON  
WASHINGTON, DC

# OPTIMIZATION OF NIOBIUM-BASED IN-SITU COMPOSITES FOR HIGH-TEMPERATURE APPLICATIONS

Final Report  
SwRI® Project No. 18.04368

by  
Kwai S. Chan

## AFOSR FINAL REPORT

This research was sponsored by the Air Force Office of Scientific Research  
Air Force Research Laboratory  
Under Contract F49620-01-C-0016  
Approved for Release; Distribution Unlimited

*The views and conclusions contained in this document are those of the authors and should not be interpreted as necessarily representing the official policies or endorsements, either expressed or implied, of the Air Force Office of Scientific Research or the U.S. Government*

March 2003

Approved:



---

Dr. Robert L. Bass, Vice President  
Mechanical and Materials Engineering Division

**REPORT DOCUMENTATION PAGE***Form Approved*  
*OMB No. 074-0188*

Public reporting burden for this collection of information is estimated to average 1 hour per response, including the time for reviewing instructions, searching existing data sources, gathering and maintaining the data needed, and completing and reviewing this collection of information. Send comments regarding this burden estimate or any other aspect of this collection of information, including suggestions for reducing this burden to Washington Headquarters Services, Directorate for Information Operations and Reports, 1215 Jefferson Davis Highway, Suite 1204, Arlington, VA 22202-4302, and to the Office of Management and Budget, Paperwork Reduction Project (0704-0188), Washington, DC 20503

<b>1. AGENCY USE ONLY (Leave blank)</b>		<b>2. REPORT DATE</b> March 2003	<b>3. REPORT TYPE AND DATES COVERED</b> Final Report, 01/01/2000 through 12/31/2002	
<b>4. TITLE AND SUBTITLE</b> Optimization of Niobium-Based In-Situ Composites for High-Temperature Applications			<b>5. FUNDING NUMBERS</b>	
<b>6. AUTHOR(S)</b> Kwai S. Chan				
<b>7. PERFORMING ORGANIZATION NAME(S) AND ADDRESS(ES)</b> Southwest Research Institute® 6220 Culebra Road San Antonio, TX 78238			<b>8. PERFORMING ORGANIZATION REPORT NUMBER</b>  18.04368	
<b>9. SPONSORING / MONITORING AGENCY NAME(S) AND ADDRESS(ES)</b> AFOSR 4015 Wilson Boulevard, Room 713 Arlington, VA 22203-1954			<b>10. SPONSORING / MONITORING AGENCY REPORT NUMBER</b>  F49620-01-C-0016	
<b>11. SUPPLEMENTARY NOTES</b>				
<b>12a. DISTRIBUTION / AVAILABILITY STATEMENT</b>			<b>12b. DISTRIBUTION CODE</b>	
<b>13. ABSTRACT (Maximum 200 Words)</b>  A computational material science approach, involving the application of several material models, was utilized to optimize the oxidation, fracture, and creep resistance of Nb-based in-situ composites. Using this computational approach, several candidate Nb-based, in-situ composites were designed and fabricated. The microstructure, oxidation, and fracture properties of the candidate alloys were characterized and evaluated. Both experimental data and theoretical modeling indicated that the fracture resistance of Nb-based in-situ composites is enhanced by a Ti addition, but is reduced by a high Cr addition, while a high Cr content enhances the oxidation resistance. A high volume fraction of intermetallics in the Nb-based in-situ composites enhances the oxidation resistance but reduces the fracture resistance. The fracture and oxidation resistance of Nb-based in-situ composites could not be optimized simultaneously because of opposite effects of Ti and Cr additions as well as the Nb solid solution and intermetallics (Laves and silicides) on the fracture and oxidation resistance of the in-situ composites. The theoretical results suggest that a microstructure of fine shearable sub-micron-sized precipitates embedded in a Nb solid solution containing high Ti and Cr contents might be required to improve both the oxidation and fracture resistance of Nb-based in-situ composites.				
<b>14. SUBJECT TERMS</b>			<b>15. NUMBER OF PAGES</b>	
			<b>16. PRICE CODE</b>	
<b>17. SECURITY CLASSIFICATION OF REPORT</b> Unclassified		<b>18. SECURITY CLASSIFICATION OF THIS PAGE</b> Unclassified	<b>19. SECURITY CLASSIFICATION OF ABSTRACT</b> Unclassified	<b>20. LIMITATION OF ABSTRACT</b>

NSN 7540-01-280-5500

Standard Form 298 (Rev. 2-89)  
Prescribed by ANSI Std. Z39-18  
298-102

## **PREFACE**

### **Disclaimer**

This work was sponsored by the Air Force Office of Scientific Research, USAF, under Contract Number F49620-01-C-0016, Dr. Craig S. Hartley, Program Manager. The views and conclusions contained herein are those of the authors and should not be interpreted as necessarily representing the official policies or endorsements, either expressed or implied, of the Air Force Office of Scientific Research or the U.S. Government.

### **Acknowledgments**

The authors are thankful to Drs. Melvin Jackson, Bernard Bewlay, and J. C. Zhao at General Electric CR&D (Schenectady, NY) for supplying alloy compositions, technical reports and previously unpublished phase diagrams, and to Dr. Young-Wom Kim at UES (Dayton, OH) for supplying the UES-AX and CNG-1B materials. Technical assistance of F. Campbell, J. Spencer, B. Chapa, and Dr. David L. Davidson (consultant), and the clerical assistance of Ms. L. Salas, all of Southwest Research Institute<sup>®</sup>, is appreciated.



## EXECUTIVE SUMMARY

The Air Force has established a milestone to increase the surface temperature of the high-pressure turbine blade in future aeroengine designs in order to enhance efficiency and performance. The target temperatures are about 1350°C at the metal surface and 1150°C in the bulk of a hollow blade with internal cooling passages. Niobium-based, in-situ composites containing silicides and Laves phases in a matrix of Nb solid solution show promising, though still inadequate, oxidation resistance at 1200°C or above. Increasing the alloying elements to increase the oxidation resistance has led to reduction in creep and fracture resistance. Thus, there is a practical need for means to improve the oxidation, creep, and fracture resistance in the silicide-containing, in-situ composites.

The main objectives of this research were: (1) to develop Nb-based, in-situ composites with enhanced oxidation, creep, and fracture resistance for very high temperature service in the range of 1200 to 1400°C, and (2) to develop a fundamental understanding of the relationships between alloy composition, microstructure, creep, oxidation, and fracture resistance.

A computational material science approach was extended and utilized to optimize the oxidation, fracture, and creep resistance of Nb-based in-situ composites. The extension included the development of several material models for computing the creep and oxidation resistance of Nb-based in-situ composites, as well as a method for computing the fracture resistance on intermetallics. Using this computational approach, several candidate Nb-based, in-situ composites were designed and fabricated. The microstructure, oxidation, and fracture properties of the candidate alloys were characterized and evaluated against model predictions.

Both experimental data and theoretical modeling indicated that the fracture resistance of Nb-based in-situ composites was enhanced by a Ti addition, but was reduced by a high Cr addition, while a high Cr content in the Nb solid solution phase enhanced the oxidation resistance. A high volume fraction of intermetallics in the Nb-based in-situ composites enhanced the oxidation resistance but reduced the fracture resistance. The fracture and oxidation resistance of Nb-based in-situ composites could not be optimized because of the opposite effects of Ti and Cr additions as well as the volume fractions of Nb solid solution and intermetallics (Laves and silicides) on fracture and oxidation resistance.

To overcome these opposite effects, the Ti and Cr contents in Nb-based in-situ composites must be increased and the Nb content must be decreased in order to improve oxidation and fracture resistance. In particular, the formation of Nb<sub>2</sub>O<sub>5</sub> must be suppressed and replaced by the formation of a protective Cr<sub>2</sub>O<sub>3</sub> or CrNbO<sub>4</sub> oxide layer. The microstructure of Nb-based in-situ composites must be refined to contain fine shearable intermetallic precipitates in the sub-micron size range in order to mitigate the high plastic constraints in the Nb solid solution and to facilitate the formation of a continuous Cr<sub>2</sub>O<sub>3</sub> or CrNbO<sub>4</sub> layer. Such a microstructure is predicted to exhibit a high creep resistance if the creep exponent (n) of the intermetallic is low (n ≈ 1-2).

## TABLE OF CONTENTS

	<i>Page</i>
REPORT DOCUMENTATION PAGE.....	i
PREFACE.....	ii
Disclaimer .....	ii
Acknowledgments.....	ii
EXECUTIVE SUMMARY .....	iii
1.0 INTRODUCTION .....	1
2.0 APPROACH .....	1
3.0 SUMMARY OF KEY RESULTS .....	1
3.1 Microstructure.....	3
3.2 Fracture Toughness and Modeling.....	6
3.3 Oxidation Resistance and Modeling .....	15
3.4 Creep Resistance and Modeling.....	23
4.0 CONCLUSIONS.....	24
5.0 RECOMMENDATIONS .....	26
6.0 PERSONNEL SUPPORTED.....	27
7.0 PUBLICATIONS.....	27
8.0 AWARDS RECEIVED.....	28
9.0 TRANSITIONS .....	28
10.0 REFERENCES.....	28
APPENDIX 1    “Improving the Fracture Toughness of Constituent Phases and Nb-Based In-Situ Composites by a Computational Alloy Design Approach” .....	A-1
APPENDIX 2    “Relationships of Fracture Toughness and Dislocation Mobility in Intermetallics” .....	A-2
APPENDIX 3    “Computer-Assisted Design of Nb-Based In-Situ Composites and Superalloys” .....	A-3

## TABLE OF CONTENTS (Continued)

	<i>Page</i>
APPENDIX 4 "Brittle-To-Ductile Fracture Transition in Nb-Based Alloys and Intermetallics" .....	A-4
APPENDIX 5 "Cyclic Oxidation Response of Niobium-Silicide Based In-Situ Composites" .....	A-5
APPENDIX 6 "Cyclic Oxidation Resistance of Niobium-Based In-Situ Composites: Modeling and Experimentation" .....	A-6
APPENDIX 7 "Modeling Creep Behavior of Niobium Silicide In-Situ Composites" ...	A-7

## LIST OF TABLES

<i>Table</i>	<i>Page</i>
1 The Actual Chemical Composition and Interstitial Contents of Various Nb-Based In-Situ Composites. ....	2
2 The Chemical Compositions and Crystal Structures of Constituent Phases in Various Nb-Based In-Situ Composites in the As-Cast and Heat-Treated Conditions.....	5
3 A Summary of the Volume Percents of Intermetallics and Fracture Toughness Results for Nb-Based In-Situ Composites Determined by Three-Point Bend and Compact Tension Techniques .....	7
4 Average Values of Fracture Toughness of Nb-Based, In-Situ Composites and Individual Phases in the Composites .....	10

## LIST OF FIGURES

<i>Figure</i>	<i>Page</i>
1 Overview of the computational model utilized in this program. Dotted lines show models that are still under development.....	2
2 Microstructures of Nb-based in-situ composites heat-treated at 1350°C for 100 hrs.: (a) M2, (b) AX, (c) M1, (d) Nbx, (e) UES-AX, and (f) CNG-1B. ...	4
3 Fracture toughness ( $K_C$ ) decreases with increasing volume percent of intermetallics (Ge-rich phase, silicides, and Laves phases). ....	8
4 Frequency distribution of the indentation fracture toughness ( $K_{VC}$ ) of constituent silicide phases in Nb-based in-situ composites.....	8
5 Frequency distribution of the indentation fracture toughness ( $K_{VC}$ ) of the Nb solid solution phase in in-situ composites: (a) high Ti and low Cr contents, and (b) low Ti and high Cr contents. ....	9
6 Dependence of fracture toughness on the number of d+s electrons per atom in Nb-based and Ti-based silicides. ....	10

## LIST OF FIGURES (Continued)

<i>Figure</i>		<i>Page</i>
7	Fracture toughness of alloyed silicides: (a) indentation toughness, $K_{VC}$ , (left side) and bond order (right side) of alloyed silicides as a function of Ti content. Trend lines are shown, and (b) computed $K_C$ compared against experimental data and the complex stacking fault energy, $\gamma_{CSF}$ , required to fit the fracture model to the experimental data of alloyed $Nb_5Si_3$ and $Ti_5Si_3$ . .....	11
8	Crack path follows mostly the silicide phase in the CNG-1B alloy: (a) crack re-initiation in a silicide when the main crack is trapped by an $Nb_{ss}$ grain at $K = 6 \text{ MPa}\sqrt{m}$ , (b) crack deflection around an $Nb_{ss}$ grain and into silicide phase at $K = 8 \text{ MPa}\sqrt{m}$ , and (c) microscopic view of the crack path at $K = 9 \text{ MPa}\sqrt{m}$ . Notch on the left. Crack growth from left to right. Light phase is $Nb_{ss}$ , gray phase is silicide, and dark phase is Laves phase.....	13
9	A comparison of the fracture toughness values of Nb-based in-situ composites against model calculations based on crack-tip trapping/bridging with and without plastic constraint, and the rule of mixtures (ROM).....	14
10	A comparison of the fracture toughness data of intermetallic [8-14] and metallic alloys [15] under plane-strain and non-plane strain fracture conditions against model calculations. ....	14
11	Experimental weight change curves of various Nb-based, in-situ composites for $1100^\circ\text{C}$ . ....	16
12	Experimental weight change curves of as-cast M2 for thermal cycling (22 hr/cycle) at various peak temperatures. ....	16
13	Characteristic XRD peaks of oxide spalls of alloy M2 for various peak cyclic oxidation temperatures: (a) $1100^\circ\text{C}$ and (b) $1400^\circ\text{C}$ . ....	17
14	XRD intensity ratio, $I_{CrNbO_4} / I_{Nb_{2.05}TiO_2}$ , plotted as a function of volume percents of Nb solid solution in Nb-based in-situ composites for various peak oxidation temperatures.....	18
15	Metal recession and relative intensity ratio plotted as a function of Nb solid solution in Nb-based in-situ composites for cyclic oxidation at $1100^\circ\text{C}$ peak temperature. ....	19

## LIST OF FIGURES (Continued)

<i>Figure</i>		<i>Page</i>
16	Experimental weight change data compared against calculated weight change curves for Nb-based in-situ composites. Model calculations were performed via Eq. (4) and the assumption of independent oxidation of individual phases. The area fractions of surfaces covered by $\text{Nb}_2\text{O}_5 \cdot \text{TiO}_2$ and $\text{CrNbO}_4$ were taken to correspond to the volume fractions of Nb solid solution ( $f_\alpha$ ) and intermetallic (silicide + Laves) phases, respectively. ....	20
17	Comparison of measured and computed weight change curves for Nb-based in-situ composites. The model was fitted to the experimental weight change data to deduce the area fractions ( $f_\alpha$ ) of Nb solid solution phases covered by $\text{Nb}_2\text{O}_5 \cdot \text{TiO}_2$ for M1, UES-AX and AX. The deduced values $f_\alpha$ for these alloys are significantly lower than the volume fraction of the Nb solid solution phase, which suggests that there is a tendency to form $\text{CrNbO}_4$ in the expense of $\text{Nb}_2\text{O}_5 \cdot \text{TiO}_2$ . ....	21
18	Comparison of computed and measured volume fractions and particle sizes for the formation of a continuous $\text{CrNbO}_4$ scale. The D value required to fit the experimental data is $2.2 \times 10^{-5} \mu\text{m}^2/\text{hr}$ , compared to $D = 8.3 \times 10^{-6} \mu\text{m}^2/\text{hr}$ for Cr in Nb. With $D = 2.2 \times 10^{-5} \mu\text{m}^2/\text{hr}$ , the model predicts the occurrences of a continuous $\text{CrNbO}_4$ on M2, a nearly continuous $\text{Cr}_2\text{NbO}_4$ on AX and UES-AX, and a mixture of $\text{Nb}_2\text{O}_5 \cdot \text{TiO}_2$ and $\text{CrNbO}_4$ oxides on M1. ....	22
19	Model calculations of the critical volume fraction of particles as a function of particle size (diameter) for forming a protective oxide layer for silicide, Cr Laves phase, and aluminide particles. ....	23
20	Comparison of experimental and calculated steady-state creep rates for Nb, $\text{Nb}_5\text{Si}_3$ , and three Nb-Ti-Hf-Si in-situ composites. Experimental data are from the literature [25, 26].....	24

## **1.0 INTRODUCTION**

The Air Force has established a milestone to increase the surface temperature of the high-pressure turbine blade in future aeroengine designs in order to enhance efficiency and performance. The target temperatures are about 1350°C at the metal surface and 1150°C in the bulk of a hollow blade with internal cooling passages. Niobium-based, in-situ composites containing silicides in a matrix of Nb solid solution show promising, though still inadequate, oxidation resistance at 1200°C or above. Increasing the alloying elements to increase the oxidation resistance has led to reduction in creep and fracture resistance. Thus, there is a practical need for means to improve the oxidation, creep, and fracture resistance in the silicide-containing, in-situ composites.

The main objectives of this research program were: (1) to develop Nb-based, in-situ composites with enhanced oxidation, creep, and fracture resistance for very high temperature service in the range of 1200 to 1400°C, and (2) to develop a fundamental understanding of the relationships between alloy composition, microstructure, creep, oxidation, and fracture resistance.

## **2.0 APPROACH**

A materials science-based approach was used to develop a computer code for predicting yield strength, fracture toughness, creep strength, and oxidation resistance as a function of composition and microstructure. The computational code was used to optimize creep, fracture, and oxidation resistance of Nb-based, in-situ composites. Based on the computational results, several candidate alloys were designed and fabricated. The microstructure, fracture, and oxidation resistance of the candidate alloys were characterized and evaluated against model predictions to assess the validity of the computational approach.

## **3.0 SUMMARY OF KEY RESULTS**

A computational approach was extended and utilized to optimize the oxidation, fracture, and creep resistance of Nb-based in-situ composites. The extension included the development of several material models for computing the creep and oxidation resistance of Nb-based in-situ composites, as well as a method for computing the fracture resistance of intermetallics. A schematic of the computational approach is shown in Figure 1.

Using this computational approach, several candidate Nb-based, in-situ composites were designed and fabricated. Chemical compositions of these candidate materials (Nbx, M1, M2, and AX) are summarized in Table 1 together with two materials (UES-AX, and CNG-1B) supplied by UES. The microstructure, phase constituents, oxidation, and fracture properties of the candidate materials were characterized in this program. In addition, appropriate microstructure-based oxidation, fracture, and creep models were further developed. These models were used to analyze the experimental data, to develop scientific understanding of the

performance/microstructure relationships, and to guide further material development. Key results of these efforts are highlighted as follows.

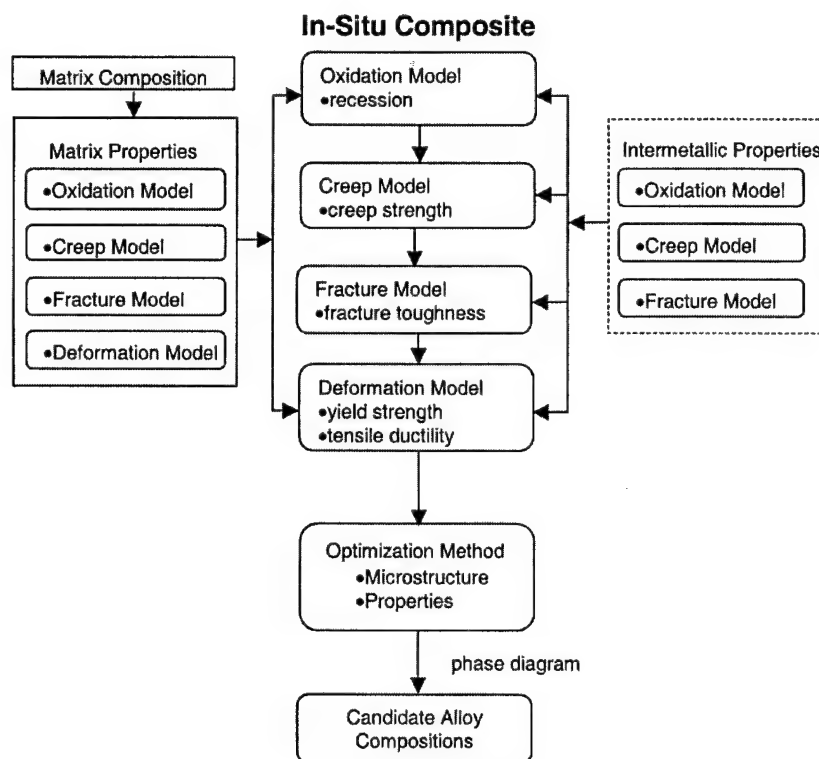


Figure 1. Overview of the computational model utilized in this program. Dotted lines show models that are still under development.

Table 1. The Actual Chemical Composition and Interstitial Contents of Various Nb-Based In-situ Composites

Alloy	Compositions (at.%)						Interstitial Contents (wt. ppm)		
	Nb	Ti	Hf	Cr	Si	Ge	C	N	O
Nbx	62.7	26.6	4.2	2.50	1.0	3.0	< 100	62	210
M1	46.3	22.2	4.4	12.3	9.7	5.1	< 100	34	320
M2	35.8	22.5	4.0	15.6	17.3	4.8	100	26	220
AX	41.3	22.4	3.9	12.5	14.8	5.1	100	60	220
UES-AX	41.2	23.0	4.7	11.2	15.2	4.7	100	36	280
CNG-1B*	48.7	21.5	2.0	6.7	9.0	4.7	200	44	320

\* Also contained 3.5% Fe, 2.6% Al, and 1.3% Sn.



### 3.1 Microstructure

The microstructures of Nb-based, in-situ composites were varied by heat-treatment at 1350°C for 24 hours and 100 hours in a flowing Argon atmosphere, followed by furnace cool. These heat treatments were designed to investigate the microstructural stability of the candidate materials. The microstructures of the as-cast and heat-treated materials were characterized by scanning electron microscopy, energy dispersive spectroscopy, X-ray diffraction, and quantitative metallographic techniques. Results of the microstructure, chemical compositions, and volume fractions of constituent phases in these composites are highlighted in the section below, while more detailed results are reported in Appendix 1 [1].

The typical microstructure of the Nb-based, in-situ composites is usually comprised of three phases: (1) an Nb solid solution, (2) one or maybe two silicide phases, and (3) a Laves phase. These phases can be distinguished individually by back-scattered electron (BSE) microscopy. In the BSE images, the Nb solid solution, Nb<sub>ss</sub>, appears as the lightest gray phase, while the silicide appears as gray and the Laves phase is dark gray. The microstructure of the heat-treated alloys at 1350°C/100 hrs is illustrated in Figure 2.

The chemical compositions of individual phases present in the candidate materials were determined by selected area energy-dispersive spectroscopy. A summary of the chemical compositions of constituent phases in the heat-treated alloys is presented in Table 2. The accuracy of the EDS result is  $\pm 2$  atomic percent. X-ray diffraction results indicated that the silicides are a mixture of predominantly alloyed Nb<sub>5</sub>Si<sub>3</sub> (D8<sub>1</sub> structure) with small amounts of alloyed Ti<sub>5</sub>Si<sub>3</sub> (D8<sub>2</sub> structure) and Nb<sub>3</sub>Si (TiP<sub>3</sub> structure). The Laves phase is consistent with an alloyed NbCr<sub>2</sub> (C14 structure), while the Nb solid solution has the bcc (A2) crystal structure. The resulting Nb solid solution usually contains a relatively high Cr (9-14 percent) content.

Quantitative image analysis was performed to determine the volume fraction of individual phases in the as-cast and heat-treated microstructures. Table 3 shows a summary of the volume percents of Nb solid solution, silicide phase, and Laves phase for the heat-treated materials. Heat treatment at 1350°C reduced the volume percents of Laves and silicide phases, and increased the volume fraction of the Nb solid solution phase.

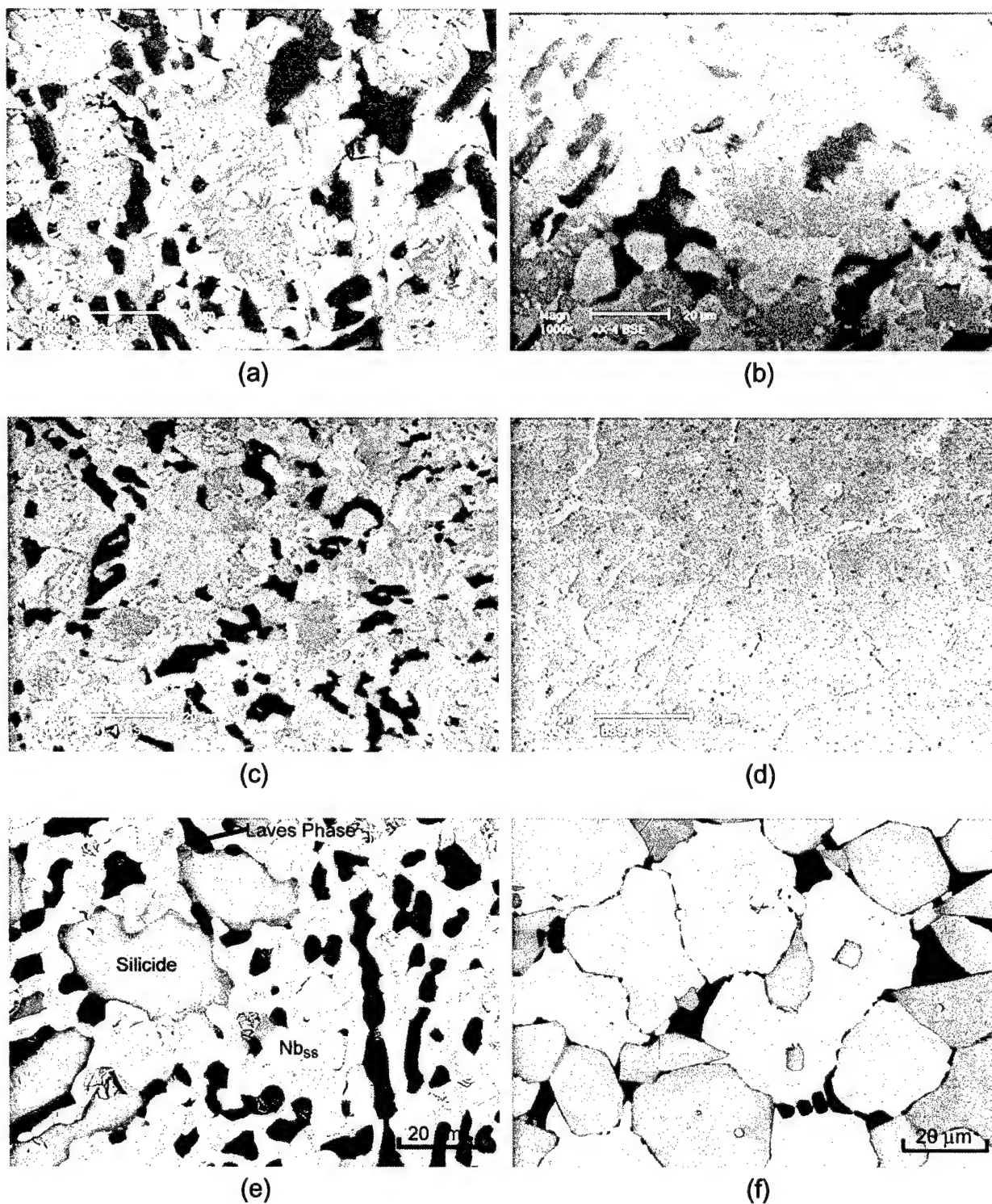


Figure 2. Microstructures of Nb-based in-situ composites heat-treated at 1350°C for 100 hrs.: (a) M2, (b) AX, (c) M1, (d) Nbx, (e) UES-AX, and (f) CNG-1B.

Table 2. The Chemical Compositions and Crystal Structures of Constituent Phases in Various Nb-Based In-Situ Composites in the As-Cast and Heat-Treated Conditions

Alloy	Heat-Treatment	Nb <sub>ss</sub> Phase (bcc)	Silicide Phase* (D8 <sub>1</sub> )	Laves Phase (C14)	Ge-rich Phase (Unknown)
M2-1	As-Cast	—	Nb-23Ti-3Hf-4Cr-6Ge-28Si	Nb-12Ti-4Hf-52Cr-2Ge-9Si	—
M1-1	As-Cast	Nb-20Ti-3Hf-12Cr-4Ge-4Si	Nb-20Ti-4Hf-3Cr-10Ge-25Si	Nb-10Ti-4Hf-49Cr-2Ge-9Si	—
AX-1	As-Cast	Nb-24Ti-3Hf-14Cr-Ge-1Si	Nb-21Ti-3Hf-3Cr-8Ge-27Si	Nb-15Ti-6Hf-49Cr-2Ge-8Si	—
Nbx-1	As-Cast	Nb-29Ti-4Hf-3Cr-3Ge-3Si	—	—	Nb-39Ti-6Hf-3Cr-9Ge-6Si
UES-AX	1350°C/100 hr.	Nb-26Ti-3Hf-14Cr-3Ge-1Si	Nb-24Ti-4Hf-1Cr-6Ge-29Si	Nb-12Ti-3Hf-54Cr-1Ge-8Si	—
M2-3	1350°C/100 hr.	Nb-23Ti-1Hf-10Cr-3Ge-3Si	Nb-19Ti-5Hf-2Cr-7Ge-28Si	Nb-12Ti-4Hf-50Cr-2Ge-8Si	—
M1-3	1350°C/100 hr.	Nb-18Ti-1Hf-10Cr-2Ge-3Si	Nb-17Ti-5Hf-3Cr-12Ge-23Si	Nb-10Ti-4Hf-49Cr-2Ge-9Si	—
AX-3	1350°C/100 hr.	Nb-20Ti-1Hf-10Cr-3Ge-3Si	Nb-18Ti-5Hf-1Cr-8Ge-28Si	Nb-11Ti-4Hf-48Cr-2Ge-9Si	Not determined
Nbx-3	1350°C/100 hr.	Nb-24Ti-3Hf-3Cr-4Ge-3Si	—	—	Nb-28Ti-19Hf-0.3Cr-27Ge-10Si
CNG-1B <sup>+</sup>	1350°C/100 hr.	Nb-21Ti-1Hf-8Cr-0.8Ge-0.8Si-2.6Fe-2Sn-2Al	Nb-19Ti-2.3Hf-1.7Cr-9.5Ge-20Si-2Al-1.8Fe-1Sn	Nb-15Ti-2.8Hf-31Cr-1Ge-8Si-2Al-15Fe-0.1 Sn	—

+ HIP'ped at 1420°C under 207 MPa pressure for 6 hrs.

\* Also contained small amounts of (Ti, Nb)<sub>5</sub>Si<sub>3</sub> (D8 structure) and possibly Nb<sub>3</sub>Si (Ti<sub>3</sub>P structure).

### 3.2 Fracture Toughness and Modeling

The fracture toughness of Nb-based, in-situ composites was characterized by three-point bending of notched specimens and in-situ fracture testing of compact-tension (CT) specimens in a SEM equipped with a loading stage. These results are presented in Table 3. Figure 3 plots the fracture toughness as a function of volume percents of intermetallics (silicide plus Laves phases) for the as-cast and heat-treated materials. At above 50 percent intermetallics, the fracture toughness is relatively constant at about 8 to 9 MPa $\sqrt{m}$ .

To understand the observed fracture behavior, an indentation technique with an appropriate calibration procedure was developed to measure the fracture toughness of individual phases in the in-situ composites. The technique involved making Vickers hardness indentation on individual phases under a small load such that the entire indent and the microcracks all resided within the phase of interest. The indentation toughness of the Laves phase ranged from 2 to 5 MPa $\sqrt{m}$ . In contrast, the indentation toughness of the silicide phases ranged from 3 to 12 MPa $\sqrt{m}$ . The frequency distribution of the indentation toughness,  $K_{VC}$ , for the silicides was measured and the result is presented in Figure 4. Only some Nb<sub>ss</sub> grains in AX and UES-AX cracked by indentation, most of the Nb<sub>ss</sub> grains in M1 did not crack, and none in the Nb<sub>x</sub> cracked by indentation. Since the Nb solid solution Nb<sub>x</sub> did not crack under indentation, only the minimum values of the indentation toughness could be estimated. The fracture toughness of Nb<sub>ss</sub> ranged from 22 to 32 MPa $\sqrt{m}$ , Figure 5, and it is sensitive to the Ti and Cr contents. Table 4 presents the average indentation toughness of the composites and those of individual phases. The fracture toughness of the alloyed silicide and Laves phase is 8 MPa $\sqrt{m}$  and 3 MPa $\sqrt{m}$ , respectively, which is a factor of 2 to 3 higher than the unalloyed compounds. The fracture toughness of Nb<sub>ss</sub> ranged from 11 to 27 MPa $\sqrt{m}$  because of variation in Ti and Cr contents and the plastic constraints caused by the intermetallics.

The effects of alloying addition on the fracture toughness of the silicides and Nb<sub>ss</sub> were investigated by theoretical computation of the bond order [2] and the Peierls-Nabarro barrier energy [3, 4], which are described in Appendix 1. Bond order is a quantum mechanics parameter that, defined in terms of the overlap electron population, measures the strength of the covalent bond between atoms [2]. A higher bond order means a stronger covalent bond existing between atoms. Correlation of fracture toughness and the number of d+s electrons per atom in the silicide, shown in Figure 6, indicates increasing  $K_C$  with decreasing number of d+s electrons. Theoretical computation of the bond order, Bo, for Nb<sub>5</sub>Si<sub>3</sub> indicates that Ti addition reduces the bond order in the alloyed silicide, Figure 7. Thus, the reduction in the bond order is accompanied by an increase in the fracture toughness, Figure 7. This finding suggests that the fracture toughness of the silicide may be improved further by Ti addition to reduce the bond order in the silicide phase. In addition, the P-N barrier energy calculation indicates that the low fracture toughness of the Nb solid solution phase is the consequence of a higher Cr content relative to the Ti and Hf contents. To improve the fracture toughness of the Nb solid solution phase, it is necessary to increase the Ti and Hf contents or reduce the Cr content.

Table 3. A Summary of the Volume Percents of Intermetallics and Fracture Toughness Results for Nb-Based In-Situ Composites Determined by Three-Point Bend and Compact Tension Techniques

Alloy	HT	Vol.% Nb <sub>ss</sub>	Vol.% Silicides	Vol.% Laves Phase	Vol.% Ge-rich Phase	K <sub>C</sub> , MPa√m (3-pt. Bend)	K <sub>C</sub> , MPa√m (CT Tests)
M2-1	As-Cast	0	73	27	0	8.4 ± 1.2*	8.8
M1-1	As-Cast	64	28	8	0	12.2 ± 0.7*	—
AX-1	As-Cast	20	66	14	—	10.3 ± 0.3*	9.9
Nbx-1	As-Cast	91	—	—	9	22.1 ± 2.2*	—
UES-AX	1350°C/100 hr.	54	32	14	—	10.9 ± 1.4*	11.4
M2-3	1350°C/100 hr.	22	53	25	—	7.4	—
M1-3	1350°C/100 hr.	54	35	11	—	13.1	—
Nbx-3	1350°C/100 hr.	94	—	—	6	24.7	—
AX-3	1350°C/100 hr.	39	40	15	6	11.8	—
CNG-1B <sup>+</sup>	1350°C/100 hr.	43.6	50.7	5.7	—	6.3 ± 2*	11.0
M2-4	1350°C/24 hr.	24.0	48.7	26.5	—	8.7	—
M1-4	1350°C/24 hr.	60.2	27.9	10	—	11.5	—
AX-4	1350°C/24 hr.	50.6	33.7	14	—	10.1	—
Nbx-4	1350°C/24 hr.	83.7	—	—	16.3	27.2	—

<sup>+</sup> HIP'ped at 1420°C under 207 MPa pressure for 6 hours.

\* Average of three tests.

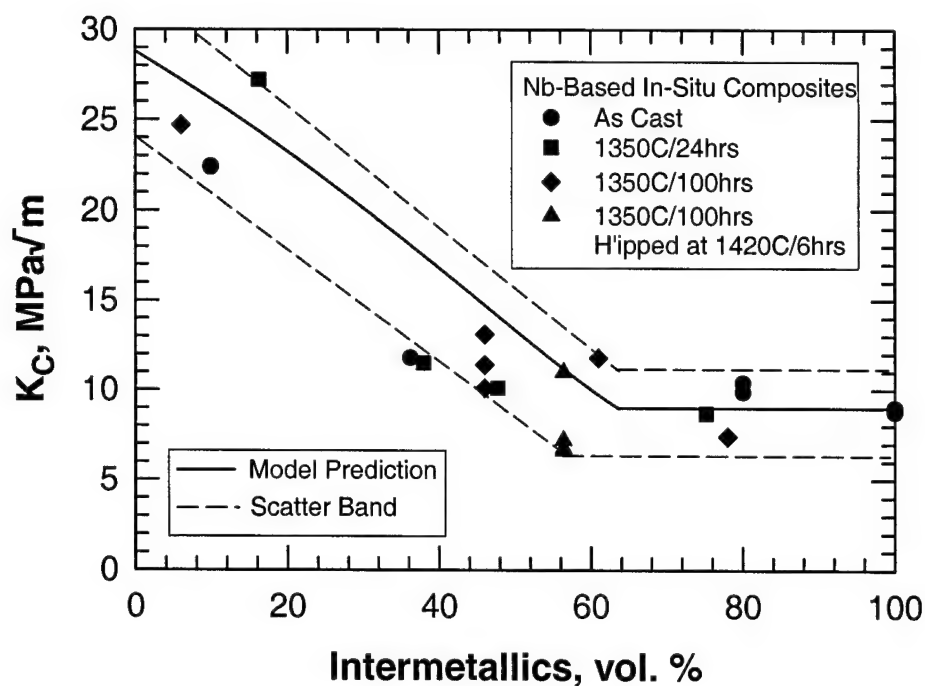


Figure 3. Fracture toughness ( $K_C$ ) decreases with increasing volume percent of intermetallics (Ge-rich phase, silicides, and Laves phases).

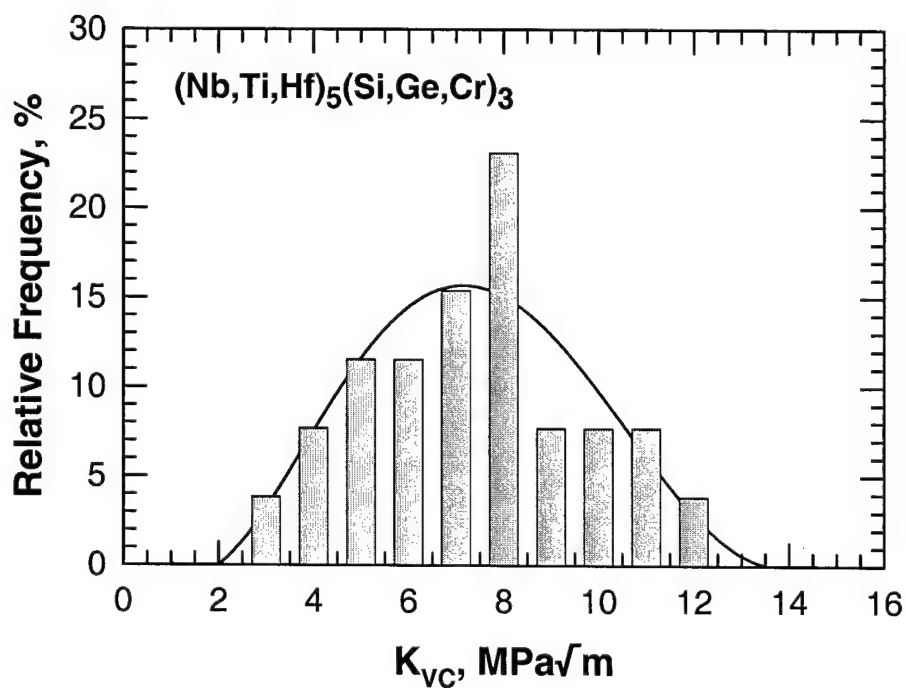


Figure 4. Frequency distribution of the indentation fracture toughness ( $K_{VC}$ ) of constituent silicide phases in Nb-based in-situ composites.

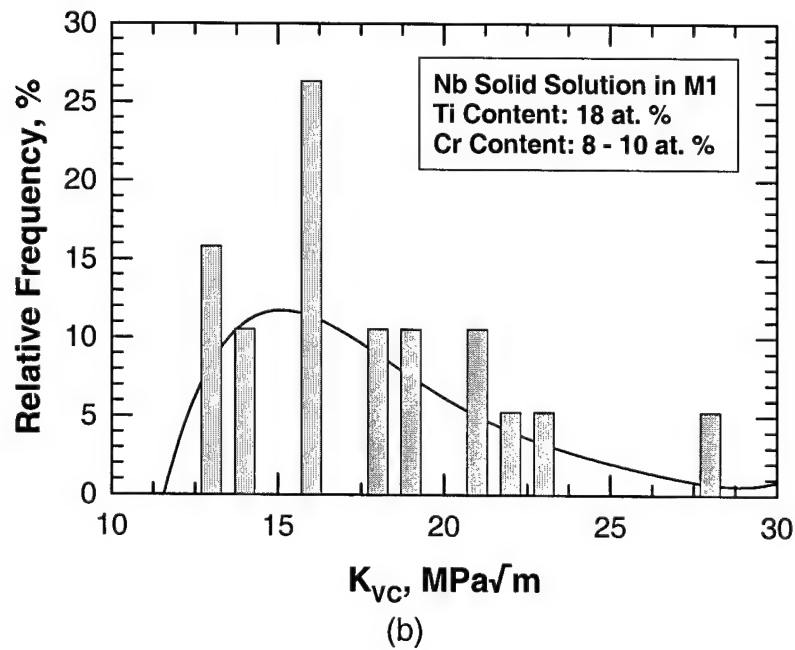
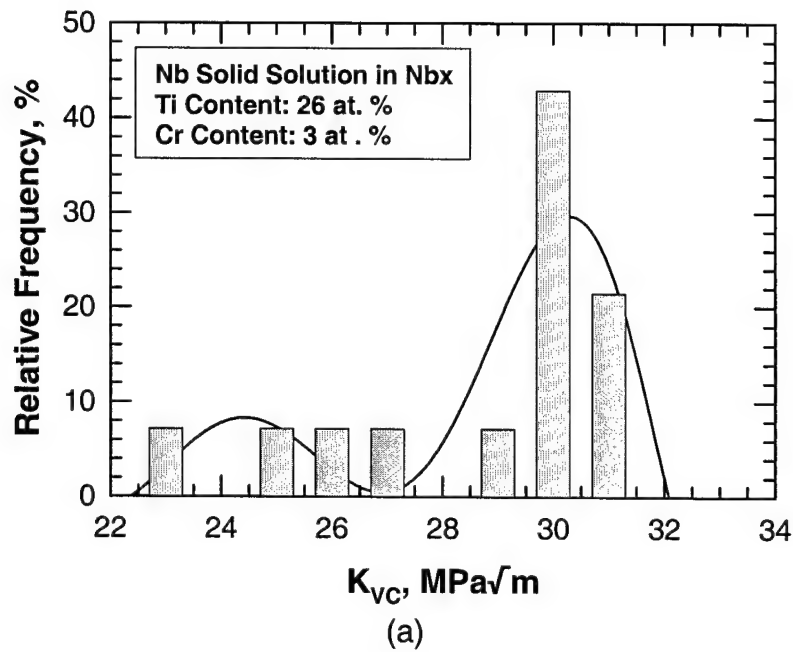


Figure 5. Frequency distribution of the indentation fracture toughness ( $K_{VC}$ ) of the Nb solid solution phase in in-situ composites: (a) high Ti and low Cr contents, and (b) low Ti and high Cr contents.

Table 4. Average Values of Fracture Toughness of Nb-Based, In-Situ Composites and Individual Phases in the Composites

Alloy	Composite Fracture	Indentation Toughness, MPa√m		
		Nb Solid Solution	Silicide	Laves Phase
Nbx	24.7	26.2	—	—
M1	13.1	18.9	—	—
AX	11.8	16.6	7.2	—
UES-AX	10.1	15.3	8.8	—
M2	7.4	11.0	8.1	3.0-5.0

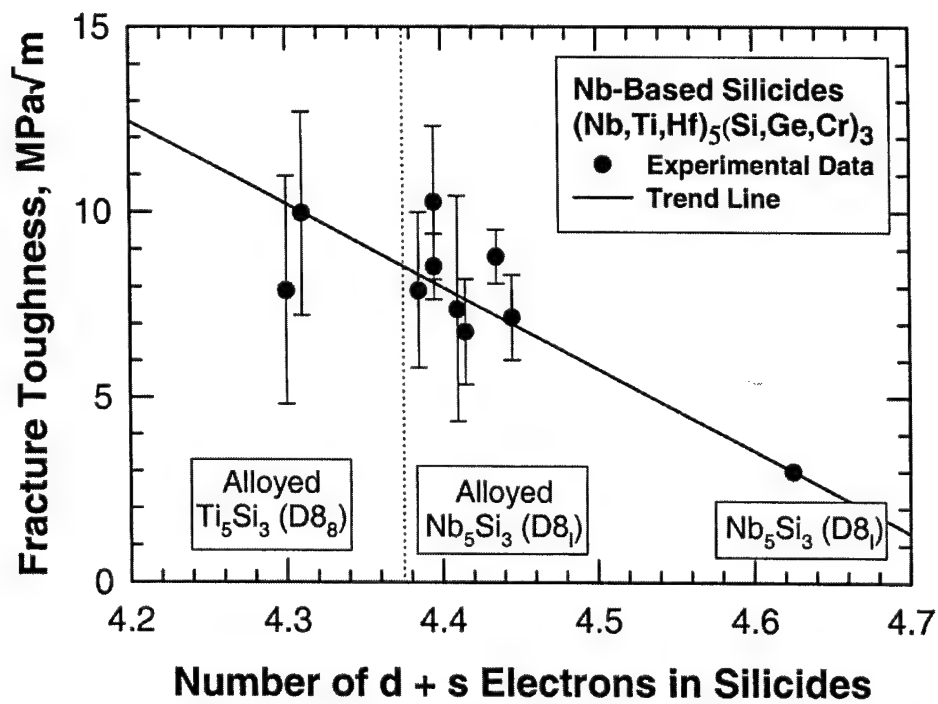
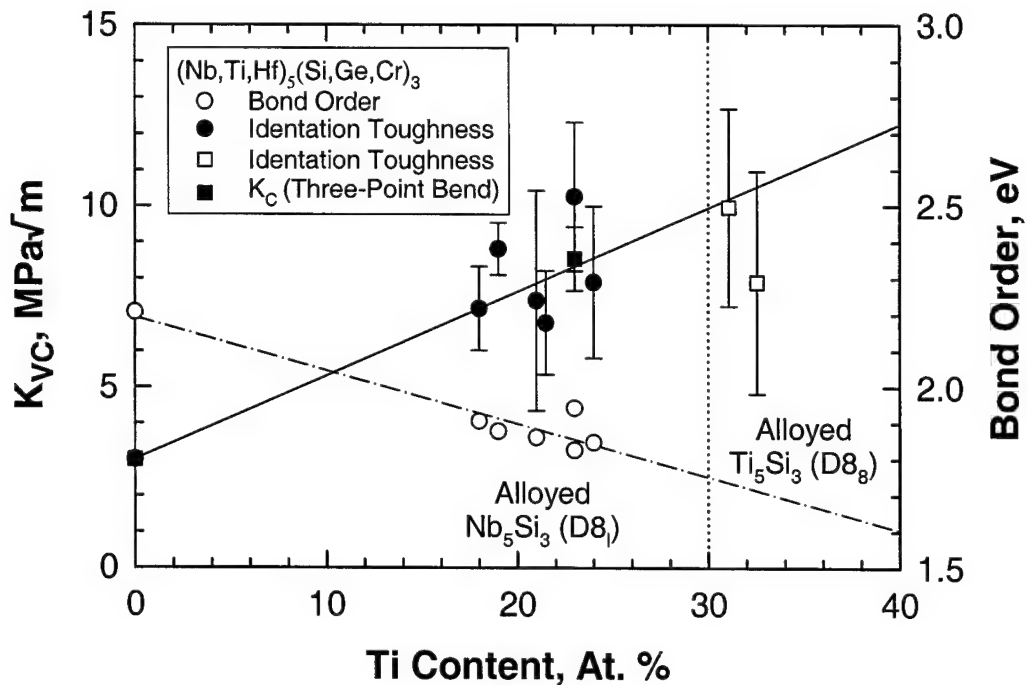
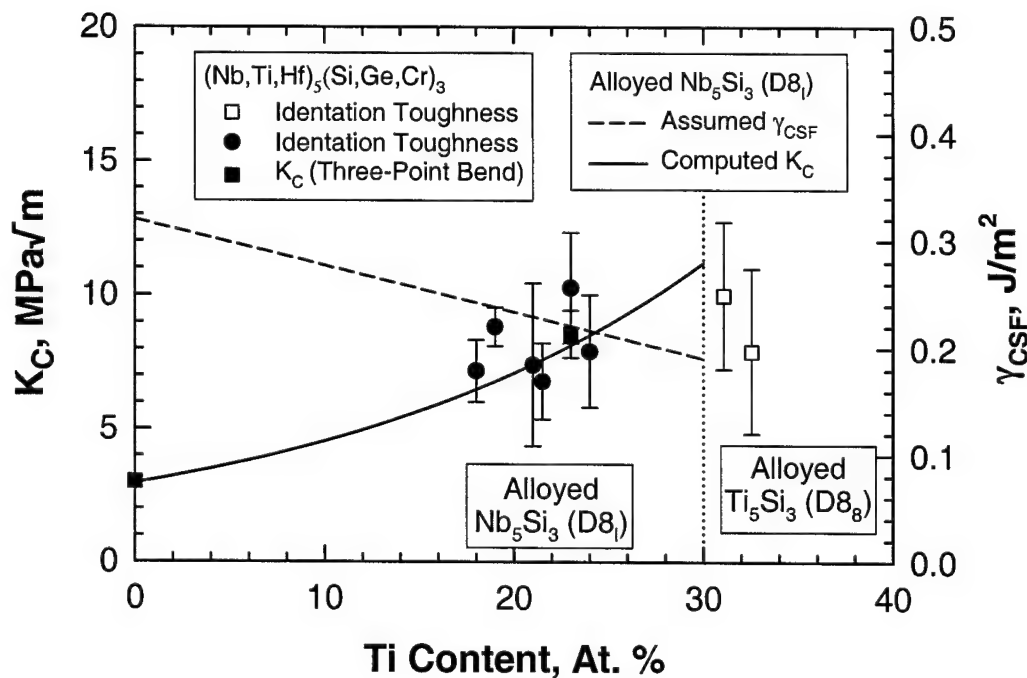


Figure 6. Dependence of fracture toughness on the number of d+s electrons per atom in Nb-based and Ti-based silicides.





(a)



(b)

Figure 7. Fracture toughness of alloyed silicides: (a) indentation toughness,  $K_{VC}$ , (left side) and bond order (right side) of alloyed silicides as a function of Ti content. Trend lines are shown, and (b) computed  $K_C$  compared against experimental data and the complex stacking fault energy,  $\gamma_{CSF}$ , required to fit the fracture model to the experimental data of alloyed  $Nb_5Si_3$  and  $Ti_5Si_3$ .

The fracture mechanism in the in-situ composite involves the formation of microcracks ahead of the main crack. Most of these microcracks are initiated in the Laves phase, which has the lowest fracture toughness among the constituent phases in the microstructure. Once initiated in the Laves phase, the microcracks propagated into the silicide phase. The linkage of the main crack and microcracks, which dictates the observed fracture toughness, often occurs without plastic stretching of the Nb<sub>ss</sub> particles. The absence of ductile-phase toughening in the Nb-based in-situ composites appears to originate from the phase morphology in the composite microstructure. In-situ fracture toughness testing results shown in Figure 8 for CNG-1B, revealed that this crack path tended to follow the silicide and Laves phases in this material. At lower K levels, the crack was seen to arrest at or within an Nb<sub>ss</sub> grain. The main crack, however, was able to get around the more ductile Nb<sub>ss</sub> grains by crack reinitiation or deflection. Figure 8(a) illustrates the reinitiation of a microcrack in a silicide grain, located ahead of the trapped initial crack at  $K = 6 \text{ MPa}\sqrt{\text{m}}$ . In contrast, Figure 8(b) shows that the main crack changed its path to follow the silicide phase by deflecting to propagate around the Nb<sub>ss</sub> obstacles at  $K = 8 \text{ MPa}\sqrt{\text{m}}$ . Consequently, the crack path follows mostly the silicide phase at  $K = 9 \text{ MPa}\sqrt{\text{m}}$ , Figure 8(c). Because of this fracture path, the ductile Nb solid solution was not able to enhance the fracture toughness of the in-situ composites. Comparison of the experimental data against theoretical calculation of a fracture toughness model [5], which was developed in a previous AFOSR program at SwRI®, suggested that the lack of ductile-phase toughening by the Nb solid solution phase was caused by the high plastic constraint induced on the continuous matrix by the silicide and Laves phases. In particular, Figure 9 shows the computed  $K_c$  curves for crack-tip trapping/bridging [6] by ductile phase in the in-situ composites with (solid curve) and without (dashed curve) plastic constraint acting on the Nb<sub>ss</sub> phase, as well as that computed based on the rule-of-mixtures (ROM). The  $K_c$ -curve without plastic constraint and that for the ROM were computed using Eqs. (4) and (12) of Chan and Davidson [5], respectively; while the  $K_c$ -curve with the plastic constraint (solid curve) was computed using Eqs. (10) and (11) of Chan and Davidson [5]. For these calculations, the constraint parameter,  $q$ , was taken to be unity ( $q=1$ ) and  $K_d = 28 \text{ MPa}\sqrt{\text{m}}$  as the average value of the fracture toughness of Nb<sub>ss</sub>. For spherical particles, the intermetallics begin to make contact when their volume percents exceed the theoretical value of  $\approx 72\%$  and the crack can propagate exclusively in the intermetallic phase. For irregular-shaped particles the intermetallic phase can occur with high contiguity at lower volume fraction. This appears to be case in the Nb-based in-situ composites. The fracture toughness of the in-situ composites was essentially identical to those of the silicides when the volume fraction of intermetallics was greater than approximately 60%, Figure 9.

To address the issues of a high plastic constraint in a composite microstructure, a computation method was developed in this program for estimating the Peierls-Nabarro barrier energy for slip in ordered intermetallics [7]. In addition, a fracture toughness model on the basis of thermally activated slip was formulated and applied to various intermetallic alloys. Figure 10 shows a plot of the fracture toughness,  $K_C$ , versus  $\gamma_s/(U_{P-N} + \gamma_{APB})$ , where  $\gamma_s$  is the surface energy,  $U_{P-N}$  is the Peierls-Nabarro barrier energy, and  $\gamma_{APB}$  is the antiphase boundary energy. This figure compares the fracture toughness data of intermetallic [8-14] and metallic alloys [15] under plane-strain and non-plane strain fracture conditions against model calculations for two values of the plastic zone size,  $h$ .

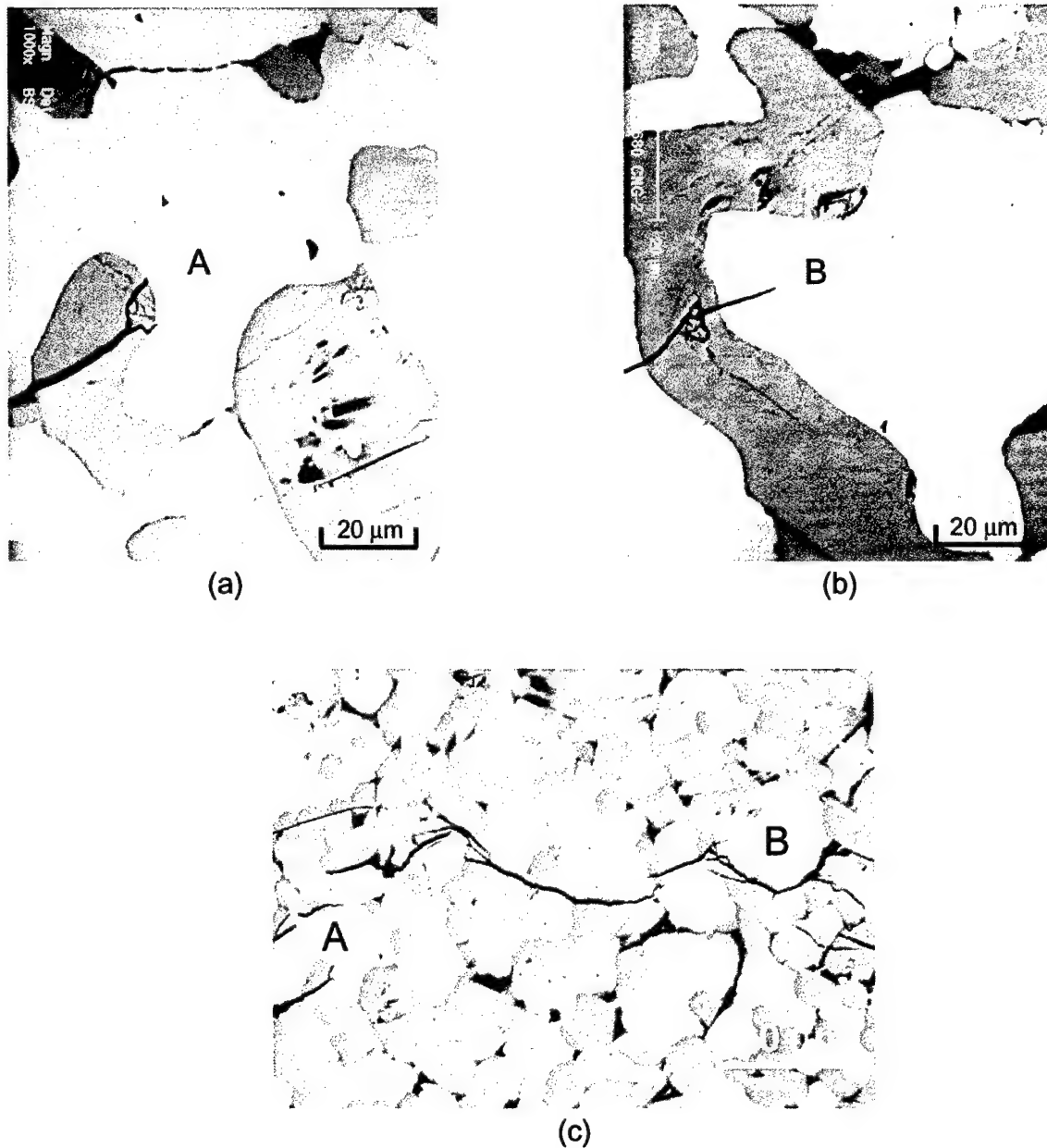


Figure 8. Crack path follows mostly the silicide phase in the CNG-1B alloy: (a) crack re-initiation in a silicide when the main crack is trapped by an Nb<sub>ss</sub> grain at  $K = 6 \text{ MPa}\sqrt{\text{m}}$ , (b) crack deflection around an Nb<sub>ss</sub> grain and into silicide phase at  $K = 8 \text{ MPa}\sqrt{\text{m}}$ , and (c) microscopic view of the crack path at  $K = 9 \text{ MPa}\sqrt{\text{m}}$ . Notch on the left. Crack growth from left to right. Light phase is Nb<sub>ss</sub>, gray phase is silicide, and dark phase is Laves phase.

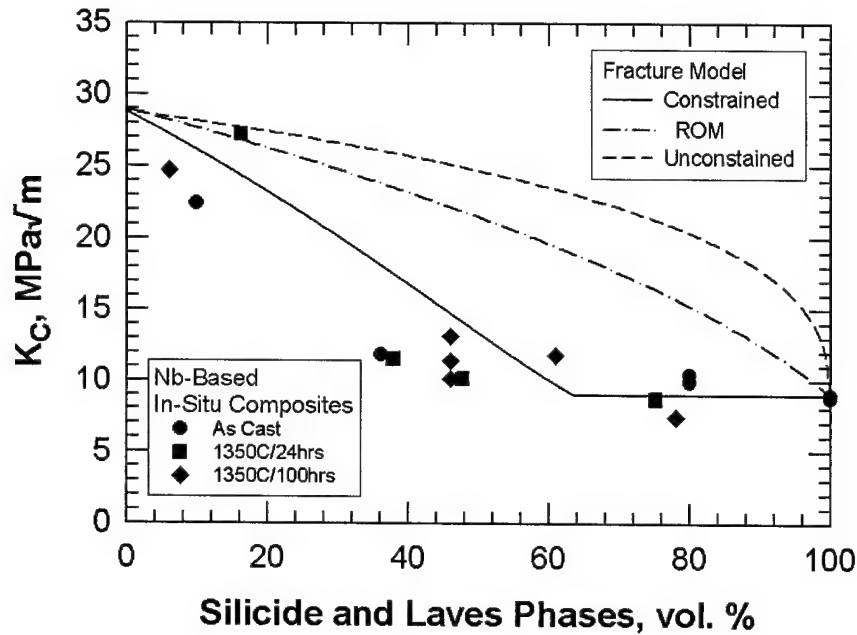


Figure 9. A comparison of the fracture toughness values of Nb-based in-situ composites against model calculations based on crack-tip trapping/bridging with and without plastic constraint, and the rule of mixtures (ROM).

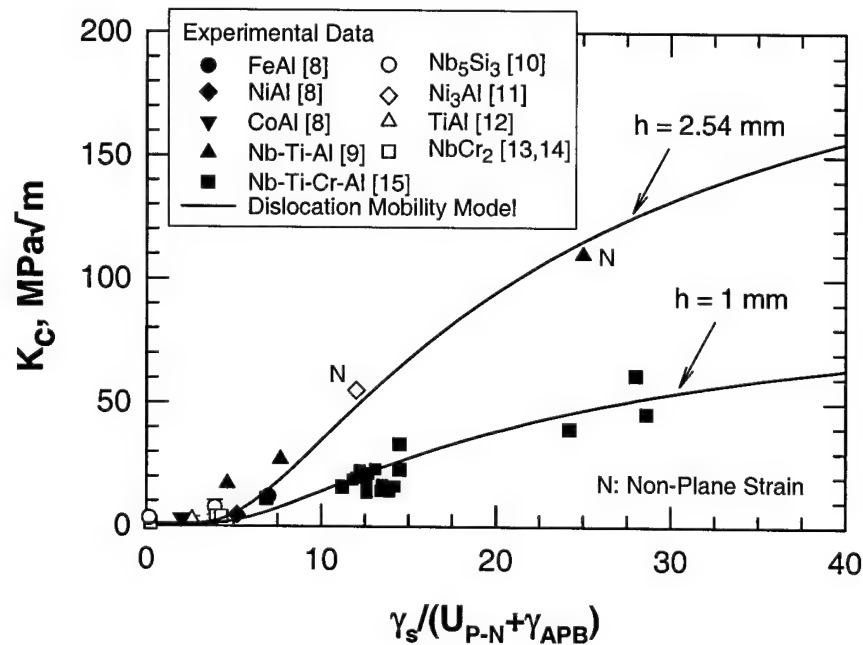


Figure 10. A comparison of the fracture toughness data of intermetallic [8-14] and metallic alloys [15] under plane-strain and non-plane strain fracture conditions against model calculations.

The development of this fracture model for intermetallics is described in Appendix 2 [7]. A summary of the computational approach for designing fracture-resistant Nb-based in-situ composites and alloys is presented in Appendix 3 [16]. The computational approach developed in this program is particularly well-suited for designing multi-component metallic alloys. Design of multi-component fracture-resistant Nb-based solid solution alloys was investigated and the results are presented in Appendix 4 [17]. The aims of these efforts were mostly focused on developing the computational methodology (Figure 1) for computing the fracture properties of the intermetallic phases in an in-situ composite (dotted box in Figure 1).

### 3.3 Oxidation Resistance and Modeling

The cyclic oxidation resistance of the Nb-based, in-situ composites was characterized by thermal cycling that involved exposing the specimens to an elevated temperature (900, 1100, 1200, 1315, or 1400°C) for 22 hours, followed by furnace cool to ambient temperature in 2 hours. The thermal cycles were applied up to 500 total hours, depending on the peak temperature. Weight change data were measured as a function of thermal cycle. The spalled oxides were collected and identified by X-ray diffraction. Selected specimens were sectioned to determine the recession rate. These results were compared against theoretical models developed in this program to assess the source of oxidation resistance and to guide further alloy development. Detailed descriptions of the experimental results are presented in Appendix 5 [18].

Figure 11 shows a comparison of the weight change data of various Nb-based, in-situ composites for thermal cycling at a peak temperature of 1100°C. The weight change data of M2 tested at various peak temperatures are compared in Figure 12. Good oxidation resistance was observed in M2 at 1100 and 1200°C. Spallation of the oxide scale increased when the peak temperature was lowered to 900°C or increased above 1315°C. Breakaway oxidation occurred in M2 after only 20 hours at 1400°C. Among the five alloys studied, M2 exhibited the best oxidation resistance.

X-ray diffraction data revealed that a mixture of  $\text{CrNbO}_4$  and  $\text{Ti}_x\text{Nb}_y\text{O}_z$  existed in the scales in Nbx, M1, AX, UES-AX, and M2.  $\text{Ti}_x\text{Nb}_y\text{O}_z$  includes  $3\text{Nb}_2\text{O}_5 \cdot \text{TiO}_2$ ,  $\text{Ti}_2\text{Nb}_{10}\text{O}_{29}$ ,  $\text{Nb}_2\text{O}_5$ , and  $\text{TiNbO}_7$ . The oxidation products in M2 were mostly  $\text{CrNbO}_4$  with small amounts of  $\text{Nb}_2\text{O}_5$  and  $\text{Nb}_2\text{O}_5 \cdot \text{TiO}_2$ , Figure 13(a). At other temperatures as well as in other alloys, the oxidation resistance decreased with increasing amounts of  $\text{Nb}_2\text{O}_5$  and  $\text{Nb}_2\text{O}_5 \cdot \text{TiO}_2$  in the oxide mixtures. For these alloys, the worst oxidation resistance occurred at 1400°C and the oxide product mixture contained mostly  $\text{Nb}_2\text{O}_5$  and  $\text{Nb}_2\text{O}_5 \cdot \text{TiO}_2$  with little  $\text{CrNbO}_4$ , Figure 13(b). The intensity of the XRD pattern for  $\text{CrNbO}_4$  occurs at  $2\theta = 27.3^\circ$ , while those for  $\text{Nb}_2\text{O}_5$  and  $\text{Nb}_2\text{O}_5 \cdot \text{TiO}_2$  occur at  $2\theta = 23.9^\circ$ . The ratio of the intensity,  $I_{\text{CrNbO}_4}$ , of the  $\text{CrNbO}_4$  peak at  $2\theta = 27.3^\circ$  to the intensity,  $I_{\text{Nb}_2\text{O}_5 \cdot \text{TiO}_2}$ , at  $2\theta = 23.9^\circ$  can be used as a measure of the relative amounts of  $\text{CrNbO}_4$ ,  $\text{Nb}_2\text{O}_5$  and  $\text{Nb}_2\text{O}_5 \cdot \text{TiO}_2$  in the oxidation product. The values of this relative intensity ratio were obtained for all six alloys tested at various temperatures. The results are plotted as a function of volume percents of Nb solid solution phase in the alloy in Figure 14.

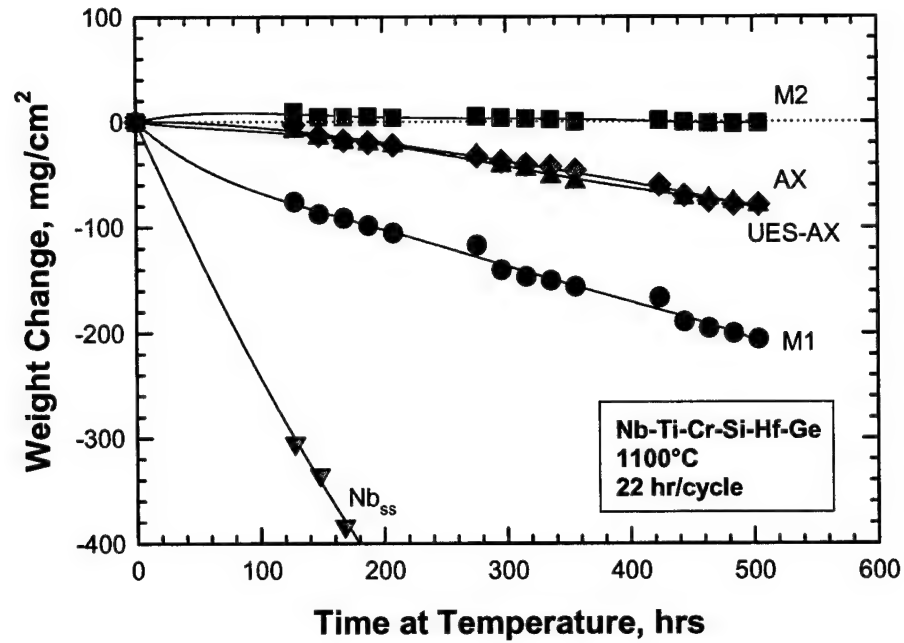


Figure 11. Experimental weight change curves of various Nb-based, in-situ composites for 1100°C.

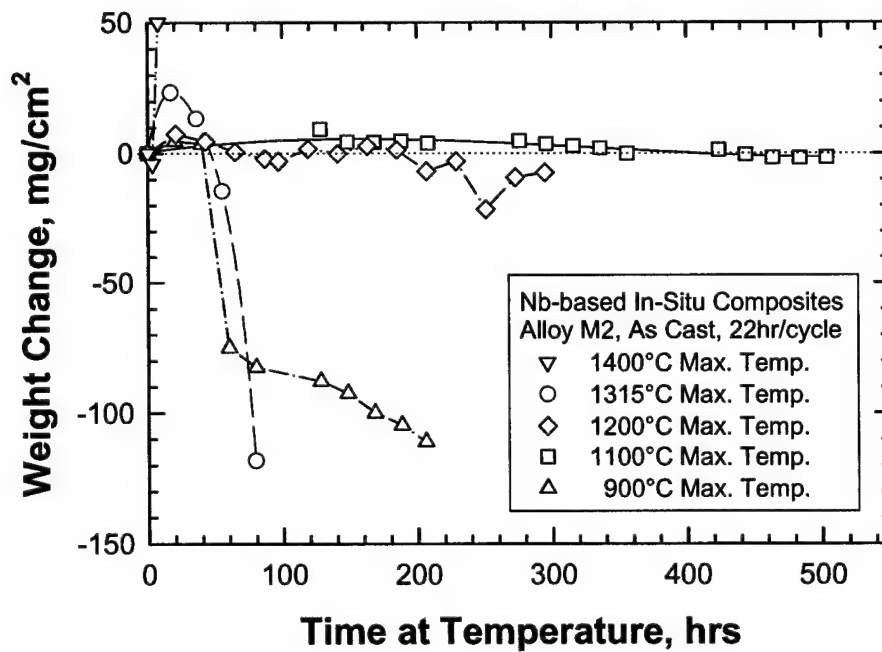
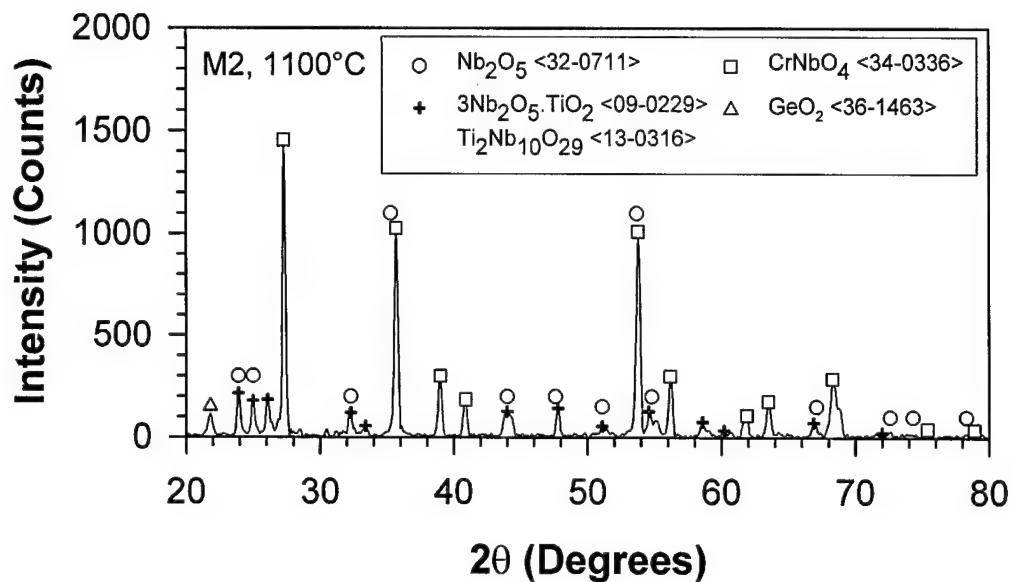
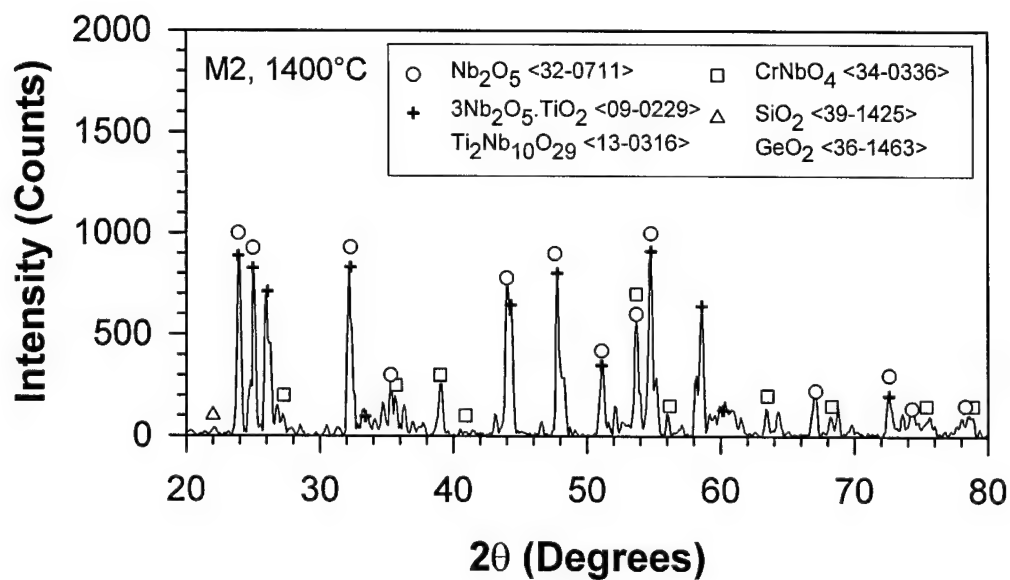


Figure 12. Experimental weight change curves of as-cast M2 for thermal cycling (22 hr/cycle) at various peak temperatures.



(a)



(b)

Figure 13. Characteristic XRD peaks of oxide spalls of alloy M2 for various peak cyclic oxidation temperatures: (a) 1100°C and (b) 1400°C.

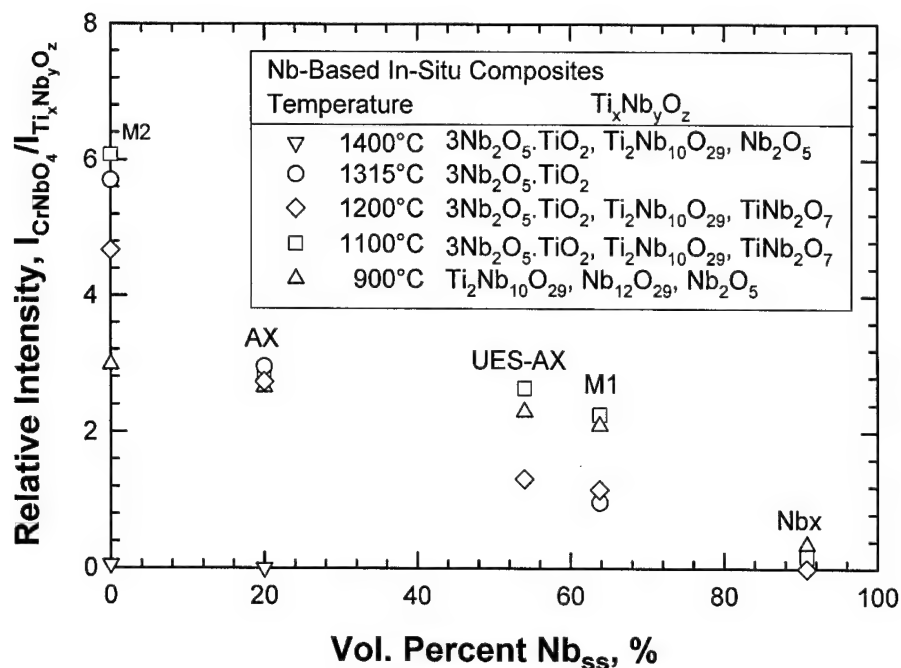


Figure 14. XRD intensity ratio,  $I_{CrNbO_4} / I_{Nb_2O_5 \cdot TiO_2}$ , plotted as a function of volume percents of Nb solid solution in Nb-based in-situ composites for various peak oxidation temperatures.

A clear picture of the relationship between the microstructure and oxidation resistance emerged when the relative intensity ratio and metal recession were plotted as a function of volume percent Nb solid phase. Figure 15 shows the results of the relative intensity ratio and material recession of the various alloys after 500 hours of cyclic oxidation at a peak temperature of 1100°C. Three general trends can be deduced from Figure 15: (1) high material recession is associated with the formation and spallation of  $Nb_2O_5$  and  $Nb_2O_5 \cdot TiO_2$ , (2) low material recession is associated with the formation and spallation of  $CrNbO_4$ , and (3) the formation and spallation of  $Nb_2O_5$  and  $Nb_2O_5 \cdot TiO_2$  is favored in alloys containing high volume percents of Nb solid solution phase, while  $CrNbO_4$  formation and spallation is favored in alloys with high volume percents of silicide and Laves phase. The lowest oxidation resistance was observed in Nb<sub>x</sub>, which contained the lowest Cr content, while M2, which contained the highest Cr content, exhibited the highest oxidation resistance. Unfortunately,  $CrNbO_4$  does not offer long-term protection and the oxidation resistance of M2, which varies widely with temperatures, is limited to 500 hours at 1100°C and is less at other temperatures. The good oxidation resistance in M2 was the result of the formation of a nearly continuous layer of  $CrNbO_4$ . A nearly continuous layer of  $CrNbO_4$  appeared to form in M2 at 1100 and 1200°C, which led to a higher intensity ratio and the oxidation resistance. In general, the propensity to spallation increases with (1) increasing amount of  $Ti_xNb_yO_z$  in the oxide scale, and (2) increasing amount of Nb<sub>ss</sub> in the in-situ composites. A high Cr content appears to improve the oxidation resistance by promoting the formation of  $CrNbO_4$ .



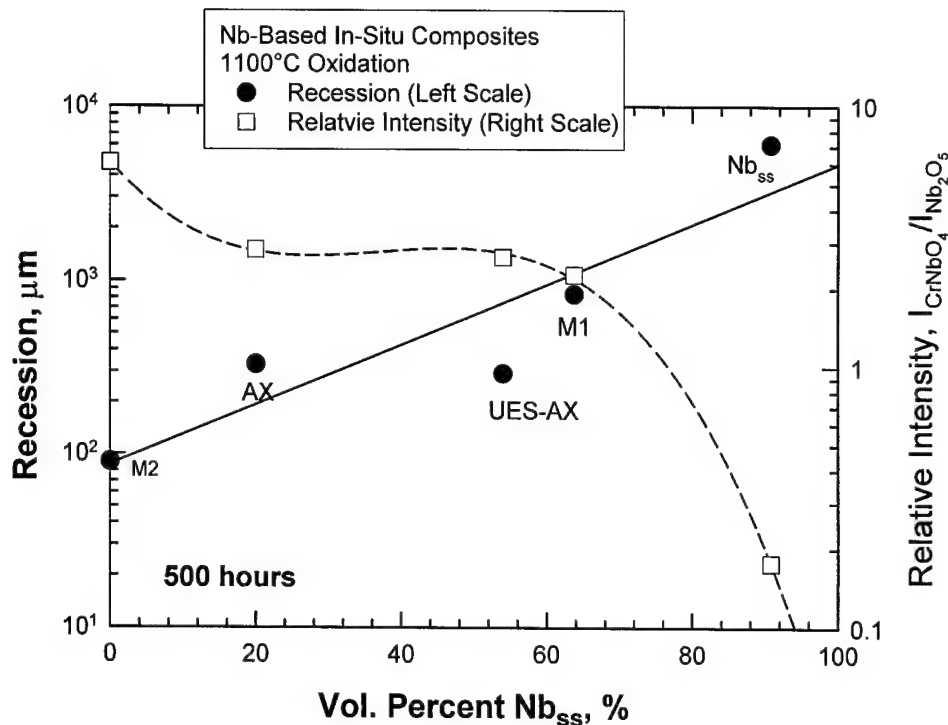


Figure 15. Metal recession and relative intensity ratio plotted as a function of Nb solid solution in Nb-based in-situ composites for cyclic oxidation at 1100°C peak temperature.

An oxidation model was developed in this model for treating independent cyclic oxidation of individual phases in a microstructure. Development of this oxidation model is described in detail in Appendix 6 [19].

The experimental weight change results of the Nb-based in-situ composites were compared against the theoretical model for independent cyclic oxidation. In applying the model for independent cyclic oxidation, the in-situ composites were treated as a two-phase microstructure containing an Nb solid solution phase and intermetallic phases that included both the silicide and Laves phases.  $\text{Nb}_x$  weight change data was used to obtain the parabolic rate and the spallation constants for the formation of  $\text{Nb}_2\text{O}_5 \cdot \text{TiO}_2$  on the Nb solid solution phase. Similarly, the weight change data for M2 were used to determine the parabolic rate and spallation constants for the formation of  $\text{CrNbO}_4$  on the silicide and Laves phases. The calculated curves are in perfect agreement with experimental data for  $\text{Nb}_x$  and M2, as shown in Figure 16, because the model was fitted to these experimental data. The calculated curves for AX, UES-AX, and M1 are model predictions. As indicated in Figure 16, the model over-predicted the weight changes for M1, AX, and UES-AX, when the actual values of the volume fraction of Nb solid solution phase in the alloys were used. The discrepancy indicated that the area fractions covered by  $\text{Nb}_2\text{O}_5 \cdot \text{TiO}_2$  in these alloys were smaller than the area fractions of Nb solid solution phase in the microstructure. Conversely, the area fractions covered by  $\text{CrNbO}_4$  were larger than the area fractions of silicide and Laves phase. The implication is that oxidation of the constituent phases in the microstructure was not totally

independent. More importantly, it suggested that there might be a tendency for  $\text{CrNbO}_4$  to displace  $\text{Nb}_2\text{O}_5$  or  $\text{Nb}_2\text{O}_5 \cdot \text{TiO}_2$ , which might ultimately result in a continuous layer of  $\text{CrNbO}_4$ . The area fractions that were covered by  $\text{Nb}_2\text{O}_5 \cdot \text{TiO}_2$  were deduced by fitting the model to the weight change data. As shown in Figure 17, the area fractions covered by  $\text{CrNbO}_4$  were 0.06, 0.06, and 0.2 for AX, UES-AX, and M1, respectively. In comparison, the volume fractions of Nb solid solution phase in these alloys were 0.2, 0.54 and 0.64 for AX, UES-AX, and M1, respectively. Thus, the oxide layer on AX and UES-AX was close to being continuous and was comprised of mostly  $\text{CrNbO}_4$ . Nonetheless, the small amounts of  $\text{Nb}_2\text{O}_5 \cdot \text{TiO}_2$  that formed on AX and UES-AX exerted significant influence on the spallation behavior.

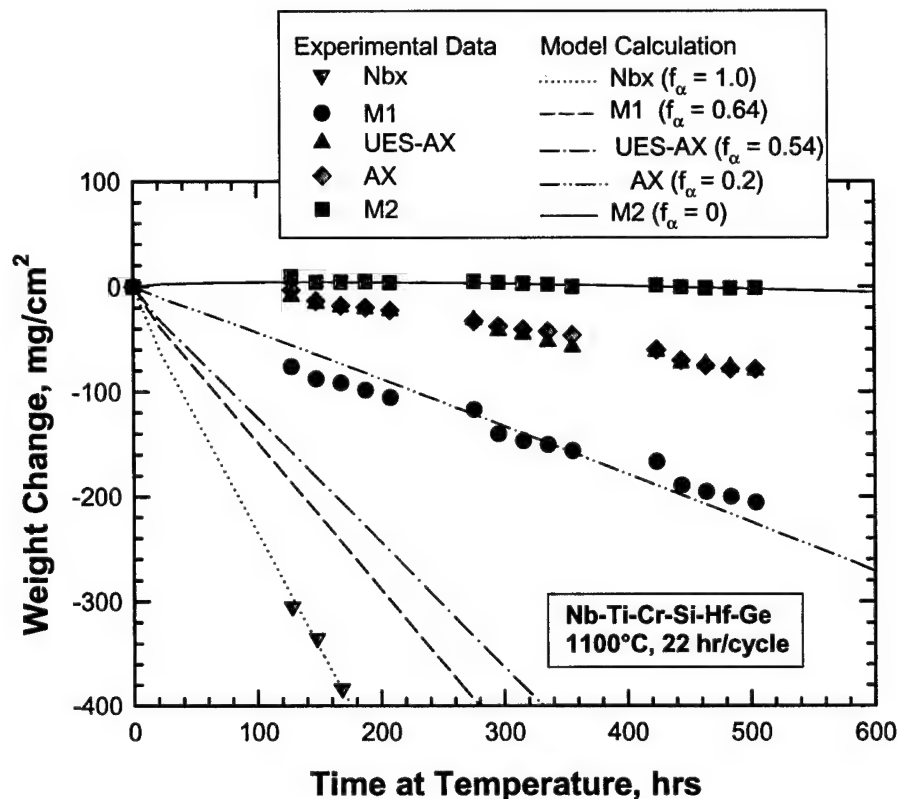


Figure 16. Experimental weight change data compared against calculated weight change curves for Nb-based in-situ composites. Model calculations were performed via Eq. (4) in Appendix 6 and the assumption of independent oxidation of individual phases. The area fractions of surfaces covered by  $\text{Nb}_2\text{O}_5 \cdot \text{TiO}_2$  and  $\text{CrNbO}_4$  were taken to correspond to the volume fractions of Nb solid solution ( $f_\alpha$ ) and intermetallic (silicide + Laves) phases, respectively.

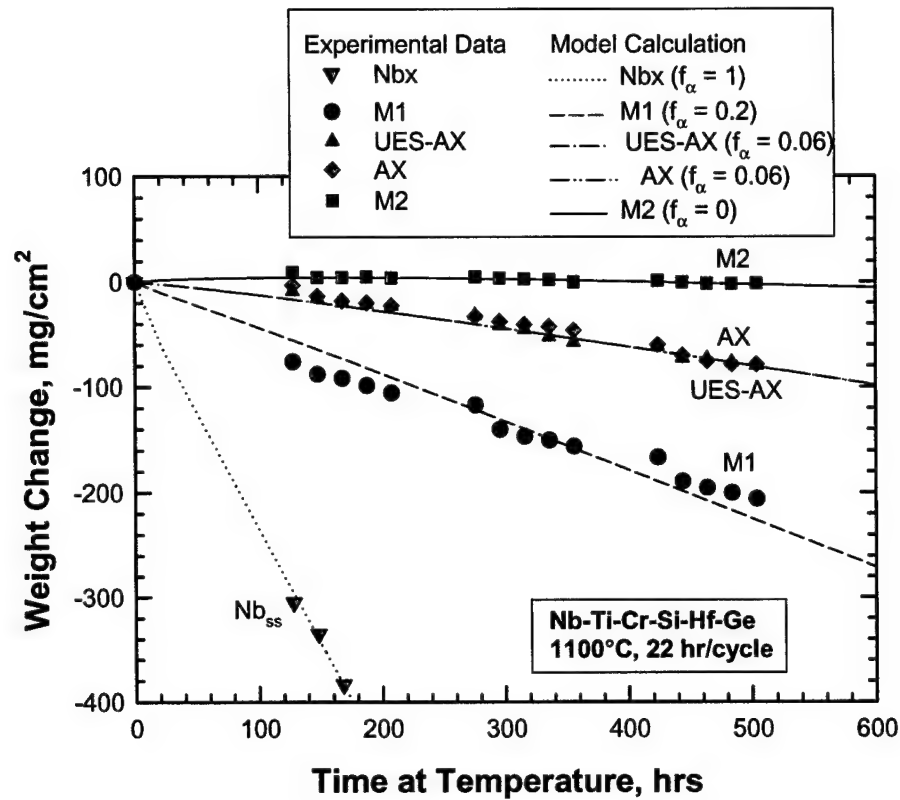


Figure 17. Comparison of measured and computed weight change curves for Nb-based in-situ composites. The model was fitted to the experimental weight change data to deduce the area fractions ( $f_\alpha$ ) of Nb solid solution phases covered by  $\text{Nb}_2\text{O}_5 \cdot \text{TiO}_2$  for M1, UES-AX and AX. The deduced values  $f_\alpha$  for these alloys are significantly lower than the volume fraction of the Nb solid solution phase, which suggests that there is a tendency to form  $\text{CrNbO}_4$  in the expense of  $\text{Nb}_2\text{O}_5 \cdot \text{TiO}_2$ .

The critical condition for the exclusive formation of  $\text{CrNbO}_4$  was computed by fitting an existing model (Eq. (18) Appendix 6) proposed by Wang et al. [20], to the oxidation data of M2 to determine that the interdiffusion coefficient ( $D = 2.2 \times 10^{-5} \mu\text{m}^2/\text{hr}$ ) for Cr diffusion in silicide and Laves phase was  $2.2 \times 10^{-5} \mu\text{m}^2/\text{hr}$ . Using this  $D$  value, the predicted critical particle sizes for continuous oxide layer formation are in good agreement with the experimental data. As shown in Figure 18, the model predicted the exclusive formation of  $\text{CrNbO}_4$  in M2 and the occurrence of nearly continuous layers of  $\text{CrNbO}_4$  in AX and UES-AX, as well as the absence of a continuous  $\text{CrNbO}_4$  in M1. Furthermore, the identical cyclic oxidation behaviors observed in AX and UES-AX can be explained on the basis of the smaller particle size in UES-AX.

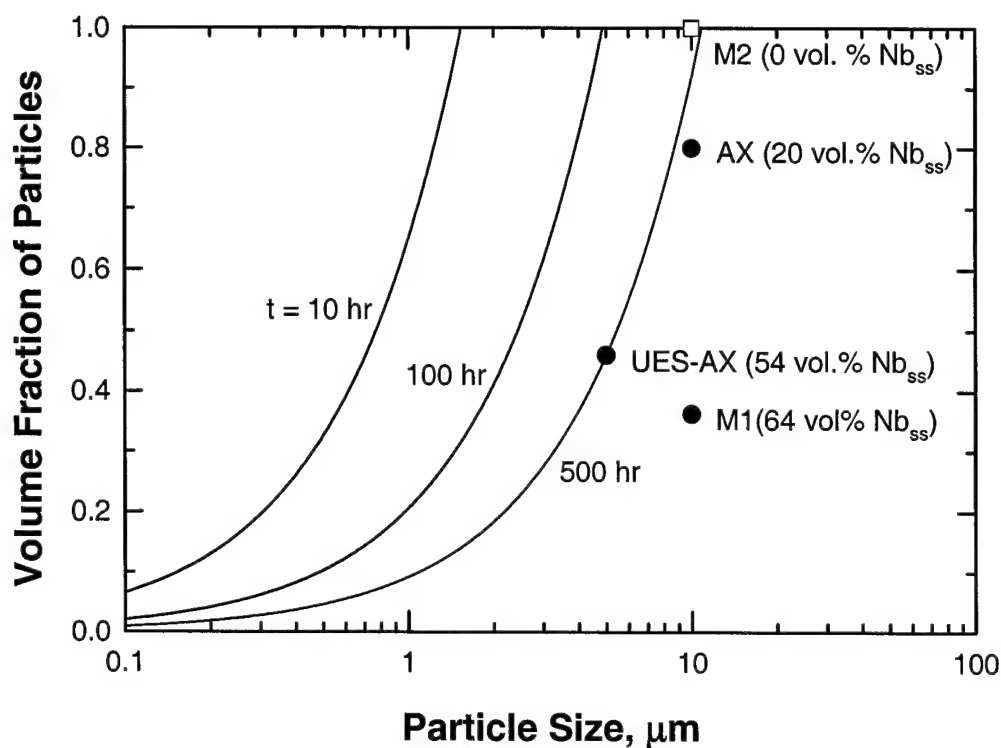


Figure 18. Comparison of computed and measured volume fractions and particle sizes for the formation of a continuous  $\text{CrNbO}_4$  scale. The  $D$  value required to fit the experimental data is  $2.2 \times 10^{-5} \mu\text{m}^2/\text{hr}$ , compared to  $D = 8.3 \times 10^{-6} \mu\text{m}^2/\text{hr}$  for Cr in Nb. With  $D = 2.2 \times 10^{-5} \mu\text{m}^2/\text{hr}$ , the model predicts the occurrences of a continuous  $\text{CrNbO}_4$  on M2, a nearly continuous  $\text{Cr}_2\text{NbO}_4$  on AX and UES-AX, and a mixture of  $\text{Nb}_2\text{O}_5 \cdot \text{TiO}_2$  and  $\text{CrNbO}_4$  oxides on M1.

The possibility of controlling the particle size as a means for improving the oxidation resistance of Nb-based in-situ composites was examined using the criterion, Eq. (18) in Appendix 6, proposed by Wang et al. [20]. Figure 19 shows the critical volume fraction of particles as a function of particle size (diameter) required for onset of the formation of a continuous oxide layer for silicides, Laves, or aluminide particles. The size requirements are most severe for silicides, followed by Laves particles and aluminide particles. This ranking is the consequence of a low Si solubility ( $\approx .015$ ) in Nb [21] and a high Al diffusivity in Nb [22]. The stringent conditions required for the exclusive formation of a  $\text{SiO}_2$  or  $\text{Cr}_2\text{O}_3$  oxide layer dictates that mixed oxides form on Nb-based in-situ composites as observed experimentally.

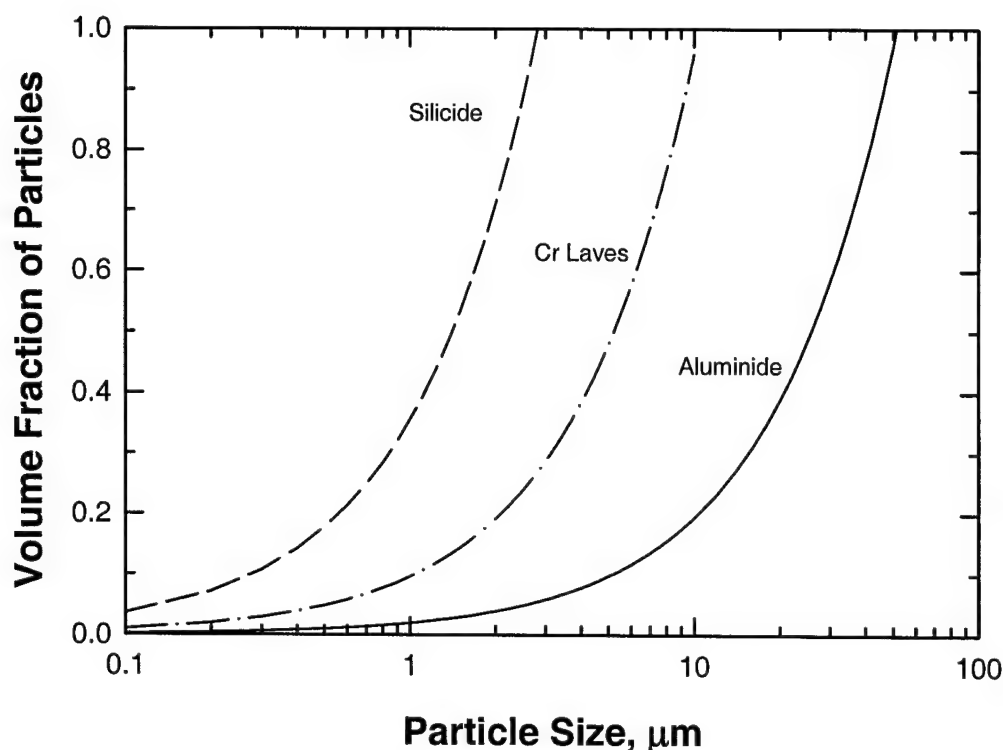


Figure 19. Model calculations of the critical volume fraction of particles as a function of particle size (diameter) for forming a protective oxide layer for silicide, Cr Laves phase, and aluminide particles.

### 3.4 Creep Resistance and Modeling

Detail of this work has been published and is presented in Appendix 7 [23]. The creep model of Kelly and Street [24] was extended to treat creep in Nb-based in-situ composites containing silicides in a creeping matrix. Model calculations revealed that the creep exponent of the in-situ composites is significantly influenced by the creep behavior of the stronger reinforcement (silicide or Laves) phase. Figure 20 shows a comparison of the calculated creep curves against those of Nb-Ti-Hf-Si in-situ composites using experimental data [25] of Nb and Nb<sub>5</sub>Si<sub>3</sub>, which were used as input. As can be seen in Figure 19, Nb<sub>5</sub>Si<sub>3</sub> exhibits a higher creep resistance than Nb. For Nb-33Ti-7.5Hf-16Si and Nb-21Ti-12.5Hf-16Si [26], the slopes of the creep curves resemble that for the composite with rigid silicides even though the model over-predicted the creep rate at a given stress level. The creep curve for Nb-7.5Hf-16Si agrees with that calculated for creeping silicides with matrix interaction. The wide range of creep exponent (1 to 11) observed in Nb-Ti-Hf-Si in-situ composites can be explained on the basis of the rigid or creeping behavior of the silicide (or Laves) phase during creep in the in-situ composites. Creeping silicides are beneficial for creep resistance as long as the creep exponent of the creep silicides is low (e.g.,  $n = 1$ ) [24]. Rigid particles or creeping particles with a high creep exponent ( $n > 3$ ) are undesirable. For optimum creep resistance, the desirable characteristics are reinforcement phases that are rigid at low stresses but creep with a low stress exponent ( $n = 1$ ) at higher stresses.

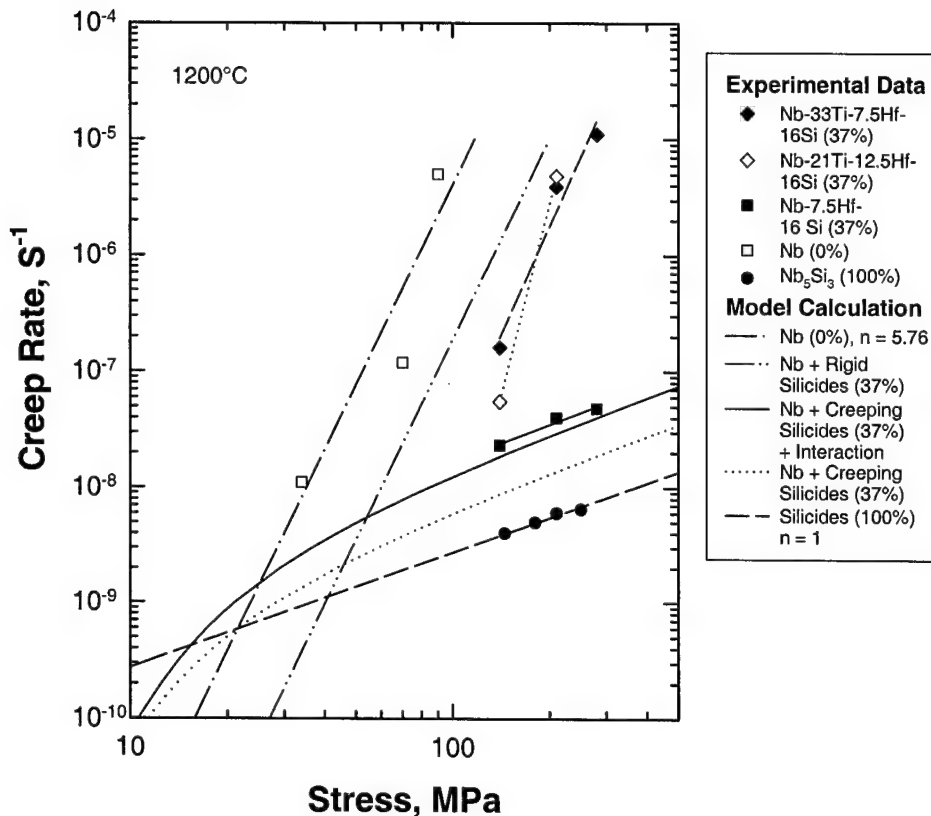


Figure 20. Comparison of experimental and calculated steady-state creep rates for Nb, Nb<sub>5</sub>Si<sub>3</sub>, and three Nb-Ti-Hf-Si in-situ composites. Experimental data are from the literature [25, 26].

#### 4.0 CONCLUSIONS

The results of this study have led to important conclusions with regard to the fracture, oxidation, and creep resistance of Nb-based in-situ composites. These conclusions are listed as follows:

- (a) On optimized properties of Nb-based in-situ composites:
  1. The fracture resistance of Nb-based in-situ composites is enhanced by a Ti addition, but is reduced by a high Cr addition, while a high Cr content in the Nb solid solution phase enhances the oxidation resistance.
  2. A high volume fraction of intermetallics in the Nb-based in-situ composites enhances the oxidation resistance but reduces the fracture resistance.
  3. The fracture and oxidation resistance of Nb-based in-situ composites could not be optimized because of (i) the opposite effects of Ti and Cr additions on fracture and creep resistance, and (ii) the conflicting influence of volume fractions of Nb solid solution and intermetallics (Laves and silicides) on fracture and oxidation resistance.

- (b) On fracture resistance of Nb-based in-situ composites (Appendices 1 and 3):
1. An addition of Si and Ge in NbCr<sub>2</sub> stabilized the C14 and increased the fracture toughness from 1 MPa√m to 2-5 MPa√m. The toughness enhancement may be attributed to a reduction of unstable stacking and P-N barrier energies for slip by synchroshear in the C14 structure.
  2. Ti and Hf additions appeared to enhance the fracture toughness of Nb-rich and Ti-rich M<sub>5</sub>Si<sub>3</sub> from 2-3 MPa√m to 8-10 MPa√m. The toughness enhancement may be attributed to slip by [001] partial dislocations and correlates with increasing fracture toughness with decreasing bond order by increasing Ti and Hf additions.
  3. The fracture toughness of the Nb<sub>ss</sub> in the in-situ composites are limited to 25-30 MPa√m because the Ti + Hf content is limited to 29% and the Cr content can reach as high as 14%.
  4. The Cr content (10-14 at.%) in the Nb solid solution phase in the Nb-Ti-Hf-Cr-Si-Ge in-situ composites is higher than that (≈ 3 at.%) expected based on the ternary Nb-Si-Cr phase diagram. A high Cr content (10-14at.%) and a high plastic constraint in the Nb solid solution phase is responsible for the relatively low fracture resistance exhibited by the Nb-based in-situ composites.
  5. The fracture mechanism in Nb-based in-situ composites containing large volume fraction of intermetallics involves the nucleation of microcracks in the Laves phase, propagation of microcracks in the silicide phases, and linkage of the main crack with microcracks without substantial plastic stretching occurring in the Nb<sub>ss</sub> particles.
  6. The fracture toughness of the in-situ composites decreases with increasing volume fractions of intermetallics phases. Ductile-phase toughening is ineffective in composites containing more than 40-50% intermetallics because the crack tends to propagate in the intermetallic phases and bypass the Nb<sub>ss</sub> phase. The fracture toughness of the Nb-based in-situ composites is approximately the fracture toughness of the silicide phase when the volume percent of intermetallics exceeds 60%.
- (c) On fracture resistance and dislocation mobility in intermetallics (Appendices 2 and 4):
1. The fracture toughness of intermetallics can be related to dislocation mobility and described in terms of a thermally activated slip formulation.
  2. Fracture toughness of intermetallics increases with decreasing values of the Peierls-Nabarro barrier energy and the generalized stacking fault (stacking, anti-phase boundary, and complex stacking fault) energies.
  3. The effects of alloying addition on the fracture toughness of intermetallics can be predicted on the basis of its effects on the P-N barrier energy, stacking fault energy or anti-phase boundary energy.

- (d) On oxidation resistance of Nb-based in-situ composites (Appendices 5 and 6):
1. The oxidation products associated with thermal cycling of Nb-based in-situ composites at a peak temperature of 900 to 1400°C are a mixture of  $\text{CrNbO}_4$ ,  $\text{Nb}_2\text{O}_5$ ,  $\text{Ti}_2\text{Nb}_{10}\text{O}_{29}$ , and  $\text{Nb}_2\text{O}_5 \bullet \text{TiO}_2$ , with possibly small amounts of  $\text{SiO}_2$  or  $\text{GeO}_2$ .
  2. The oxidation resistance of Nb-based in-situ composites is enhanced by the formation of  $\text{CrNbO}_4$  instead of  $\text{Nb}_2\text{O}_5$ ,  $\text{Ti}_2\text{Nb}_{10}\text{O}_{29}$ , and  $\text{Nb}_2\text{O}_5 \bullet \text{TiO}_2$ .
  3. The oxidation resistance of Nb-based in-situ composites increased with increasing Cr content in the Nb solid solution and decreasing volume fractions of the Nb solution phase in the microstructure.
  4. Among the materials investigated, the best oxidation resistance was observed in as-cast M2 whose microstructure contained Nb-based silicides and Laves phase, with little or no Nb solid solution phase. The oxidation resistance in M2 is provided by the interaction of  $\text{Nb}_2\text{O}_5$  and  $\text{Cr}_2\text{O}_3$  to form a continuous layer of  $\text{CrNbO}_4$ .
  5. For Nb-based in-situ composites, a high volume fraction of small (5 to 10  $\mu\text{m}$ ) Laves and silicide phases is required for the formation of a continuous  $\text{CrNbO}_4$  oxide layer.
- (e) On creep resistance:
1. The wide ranges of the creep exponent observed in Nb in-situ composites, can be explained on the basis of the presence of rigid or creeping silicides in the composites.
  2. The presence of both rigid and creeping phases in a creeping matrix can result in an apparent threshold in the creep curve.
  3. Composites with rigid silicides exhibit a creep exponent that is identical to that of the creeping matrix, while composites with creeping matrix and creeping silicides exhibit the creep exponent of the silicides.
  4. The creep resistance of in-situ composites can be tailored by controlling the relative volume fractions of rigid and creeping intermetallics in the microstructure.
  5. A creep resistant microstructure requires the stronger reinforcement phase to exhibit low creep rates with a small stress exponent (e.g.,  $n = 1$ ).

## 5.0 RECOMMENDATIONS

Recommendations reached as the result of this investigation are as follows:

1. The Ti and Cr contents in Nb-based in-situ composites must be increased and the Nb content must be decreased in order to improve oxidation and fracture



- resistance. The formation of  $\text{Nb}_2\text{O}_5$  must be suppressed and replaced by a protective  $\text{Cr}_2\text{O}_3$  or  $\text{CrNbO}_4$  oxide layer.
2. The microstructure of Nb-based in-situ composites must be refined to contain fine shearable sub-micron-sized precipitates in order to mitigate the high plastic constraints in the Nb solid solution and to facilitate the formation of a continuous  $\text{Cr}_2\text{O}_3$  or  $\text{CrNbO}_4$  layer.
  3. Thermal and environment barrier coatings are required to improve the long-term oxidation resistance of Nb-based in-situ composites.

## 6.0 PERSONNEL SUPPORTED

Kwai. S. Chan	Institute Scientist, Southwest Research Institute®
David L. Davidson	Consultant, Southwest Research Institute
John B. Campbell	Institute Technician, Southwest Research Institute
Byron K. Chapa	Senior Technician, Southwest Research Institute
James F. Spencer	Senior Technician, Southwest Research Institute

## 7.0 PUBLICATIONS

1. "Improving the Fracture Toughness of Constituent Phases and Nb-Based In-Situ Composites by a Computational Alloy Design Approach," Kwai S. Chan and David L. Davidson, *Metallurgical and Materials Transactions A*, Vol. 34A, 2003, pp. 1833-1849.
2. "Relationships of Fracture Toughness and Dislocation Mobility in Intermetallics," Kwai S. Chan, *Metallurgical and Materials Transactions A*, Vol. 34A, 2003, pp. 2315-2328.
3. "Computer-Assisted Design of Nb-Based In-Situ Composites and Superalloys," Kwai S. Chan, THERMEC' 2003 Conference Proceedings, Materials Science Forum, Trans. Tech. Publications, Vols. 426-432, 2003, pp. 2059-2064.
4. "Cyclic Oxidation Response of Multiphase Niobium-Based Alloys," Kwai S. Chan, *Metallurgical and Materials Transactions A*, Vol. 35A, 2004, pp. 589-597.
5. "Cyclic Oxidation Resistance of Niobium-Based In-Situ Composites: Modeling and Experiment," Kwai S. Chan, *Oxidation of Metals*, Vol. 61, Nos. 3/4, 2004, pp. 165-194.
6. "Brittle-To-Ductile Fracture Transition in Nb-Based Alloys and Intermetallics," K. S. Chan, Mechanisms and Mechanics of Fracture: The John Knott Symposium, edited by W. O. Soboyejo, J. J. Lewandowski, and R. O. Ritchie, TMS, Warrendale, PA, 2002, pp. 143-148.

7. "Modeling Creep Behavior of Niobium Silicide In-Situ Composites," Kwai S. Chan, *Materials Science and Engineering A*, Vol. A329-331, 2002, pp. 513-522.

## 8. AWARDS RECEIVED

TMS Champion H. Mathewson Medal for 2001. The winning series of closely related papers are "Evidence of Void Nucleation and Growth on Planar Slip Bands in a Nb-Cr-Ti Alloy," "Effects of Ti Addition on Cleavage Fracture in Nb-Cr-Ti Solid-Solution Alloys," and "The Fatigue and Fracture Resistance of a Nb-Cr-Ti-Al Alloy," which appeared in the March, April, and August 1999 issues of *Metallurgical and Materials Transactions A*, respectively.

Best Paper Award for Structural Intermetallics 2001 (ISSI-3). The paper is entitled "Fracture Behavior of Binary Lamellar Ti-46Al" and coauthored by K. S. Kumar, P. Wang, K. Chan, J. Arata, N. Bhate, J. Onstott, W. Curtin, and A. Needleman.

ASM Henry Marion Howe Medal for 2002. The paper selected for the best paper award is entitled, "A Computational Approach to Designing Ductile Nb-Ti-Cr-Al Solid-Solution Alloys." Authored by K. S. Chan, the paper appeared in the October issue of *Metallurgical and Materials Transactions A*.

## 9. TRANSITIONS

Papers on creep modeling and oxidation resistance of Nb-based, in-situ composites were sent to GE, UES, Rolls-Royce Allison, and AFRL.

## 10.0 REFERENCES

1. K. S. Chan and D. L. Davidson: "Improving the Fracture Toughness of Constituent Phases and Nb-Based In-Situ Composites by a Computational Alloy Design Approach," *Metallurgical and Materials Transactions A*, Vol. 34A, 2003, pp. 1833-1849.
2. Y. Harada, M. Morinaga, J. I. Saito, and Y. Takagi: *J. Phys: Condens. Matter.*, Vol. 9, 1997, pp. 8011-8030.
3. R. E. Peierls: *Proc. Phys. Soc.*, Vol. 52, 1940, pp. 34-37.
4. F. R. N. Nabarro: *Proc. Phys. Soc.*, Vol. 59, 1947, pp. 236-394.
5. K. S. Chan and D. L. Davidson: *Metall. Mat. Trans. A*, Vol. 32A, 2001, pp. 2717-2727.
6. A. F. Bower and M. Ortiz: *J. Mech. Phys. Solids*, Vol. 39, 1991, pp. 815-858.

7. K. S. Chan: "Relationships of Fracture Toughness and Dislocation Mobility in Intermetallics," *Metallurgical and Materials Transactions A*, Vol. 34A, 2003, pp. 2315-2328.
8. K. Chang, R. Darolia, and H. Lipsitt: *Acta Metall. Mater.*, Vol. 1, 1992, pp. 2727-2737.
9. F. Ye, C. Mercer, and W. O. Soboyejo: *Metall. Mater. Trans. A*, Vol. 29A, 1998, pp. 2361-2374.
10. R. M. Nekkanti, and D. M. Dimiduk: *Mat. Res. Soc Symp. Proceedings*, Vol. 194, Pittsburgh, PA, 1990, pp. 175-182.
11. G. P. Zhang, Z. G. Wang, and G. Y. Li: *Acta Mater.*, Vol. 45, 1997, pp. 1705-1714.
12. K. S. Chan, J. Onstott, and K. S. Kumar: *Metall. Mater. Trans. A*, Vol. 31A, 2000, pp. 71-80.
13. D. L. Davidson, K. S. Chan, and D. L. Anton: *Metall. Mater. Trans. A*, Vol. 27A, 1996, pp. 3007-3018.
14. D. J. Thomas, K. A. Nibur, K. C. Chen, J. C. Cooley, L. B. Dauelsberg, W. L. Hults, and P. G. Kotula: *Mat. Sci. Eng.*, Vol. A329-331, 2002, pp. 408-415.
15. K. S. Chan: *Metall. Mater. Trans. A*, Vol. 32A, 2001, pp. 2475-2487.
16. K. S. Chan: "Computer-Assisted Design of Nb-Based In-Situ Composites and Superalloys," THERMEC' 2003 Conference Proceedings, Materials Science Forum, Trans. Tech. Publications, Vols. 426-432, 2003, pp. 2059-2064.
17. K. S. Chan: "Brittle-To-Ductile Fracture Transition in Nb-Based Alloys and Intermetallics," Mechanisms and Mechanics of Fracture: The John Knott Symposium, edited by W. O. Soboyejo, J. J. Lewandowski, and R. O. Ritchie, TMS, Warrendale, PA, 2002, pp. 143-148.
18. K. S. Chan: "Cyclic Oxidation Response of Multiphase Niobium-Based Alloys," *Metallurgical and Materials Transactions A*, Vol. 35A, 2004, pp. 589-597.
19. K. S. Chan: "Cyclic Oxidation Resistance of Niobium-Based In-Situ Composites: Modeling and Experiment," *Oxidation of Metals*, Vol. 61, Nos. 3/4, 2004, pp. 165-194.
20. G. Wang, B. Gleeson, and D. L. Douglass: *Oxid. Met.*, Vol. 35, 1991, pp. 333-348.
21. P. R. Subramanian, M. G. Mendiratta, D. M. Dimiduk, and M. A. Stucke: *Mat. Sci. Eng.*, Vol. A239-340, 1997, pp. 1-13.

22. J. G. L. Ruiz-Aparicio and F. Ebrahimi, *J-Alloy Compound*, Vol. 202, Issue 12, 1993, pp. 117-123.
23. K. S. Chan: "Modeling Creep Behavior of Niobium Silicide In-Situ Composites," *Materials Science and Engineering A*, Vol. A329-331, 2002, pp. 513-522.
24. A. Kelly and K. N. Street: *Proceedings of Royal Society of London A*, Vol. 328, 1972, pp. 283-293.
25. G. A. Henshall, P. R. Subramanian, M. J. Strum, and M. G. Mendiratta: *Acta Materialia*, Vol. 45, 1997, pp. 3135-3142.
26. B. P. Bewlay, P. W. Whiting, A. W. Davis, and C. L. Briant: *Material Research Society Symposium Proceedings*, Vol. 552, 1999, pp. KK6.11.1-KK6.11.5.

## **APPENDIX 1**

**"Improving the Fracture Toughness of Constituent Phases and Nb-Based In-Situ Composites by a Computational Alloy Design Approach"**

**Kwai S. Chan and D. L. Davidson**

**Metallurgical and Materials Transactions A  
Volume 34A, (2003) pp. 1833-1849**

**September 2003**

Reprinted with permission from  
*Metallurgical and Materials Transactions A*, Pittsburgh, PA

# Improving the Fracture Toughness of Constituent Phases and Nb-Based *In-Situ* Composites by a Computational Alloy Design Approach

KWAI S. CHAN and DAVID L. DAVIDSON

A computational alloy design approach has been used to identify a ductile matrix for Nb-based *in-situ* composites containing Ti, Hf, Cr, Si, and Ge additions. Candidate alloys in the form of cast buttons were fabricated by arc melting. Coupon specimens were prepared and heated treated to vary the microstructure. Backscattered electron (BSE) microscopy, quantitative metallography, energy-dispersive spectroscopy (EDS), and X-ray diffraction (XRD) were utilized to characterize the morphology, volume fraction, composition, and crystallography of individual phases in the microstructure. The fracture toughness of the composites was characterized by three-point bending and compact-tension techniques, while the fracture toughness of individual phases in the *in-situ* composites was determined by an indentation technique. The composition, crystallography, and volume fraction of individual phases were correlated with the fracture-toughness results to assess (1) the role of constituent properties in the overall fracture resistance of the composites and (2) the effectiveness of the computational design approach. The results indicated that the effects of alloy addition and plastic constraint on fracture toughness were reasonably predicted, but the conditions for relaxing plastic constraint to attain higher fracture toughness were not achieved.

## I. INTRODUCTION

NB-BASED *in-situ* composites are multiphase alloys that contain an Nb (bcc) solid-solution phase and brittle intermetallic phases such as silicide and Laves phases.<sup>[1-12]</sup> Depending on the alloy composition, as many as four silicide (Nb<sub>5</sub>Si<sub>3</sub>, Nb<sub>3</sub>Si, Ti<sub>5</sub>Si<sub>3</sub>, and Ti<sub>3</sub>Si) and two Laves phases (C14 and C15 NbCr<sub>2</sub>) in alloyed forms can exist in the microstructure.<sup>[4-6,9-12]</sup> NbCr<sub>2</sub> is normally C15 at ambient temperature, but transforms to C14 when alloyed with  $\approx 2$  at pct Si or greater.<sup>[12]</sup> The silicide and Laves phases are intended for providing high-temperature creep and oxidation resistance, while the Nb solid solution (Nb<sub>ss</sub>) is intended to improve the ambient-temperature fracture resistance. Extensive research has demonstrated that alloy additions can impart fracture resistance in the Nb solid-solution, silicide, and Laves phases.<sup>[4-11,13-20]</sup> The large number of potential alloying elements, however, makes the discovery of beneficial alloy additions a daunting task if undertaken *via* empirical means.

There is considerable interest in developing computational tools for designing materials with a desired composition, microstructure, and performance. For designing against brittle fracture, some investigators<sup>[21,22,23]</sup> have focused on alloy effects on the unstable stacking energy<sup>[24]</sup> and the crack-tip dislocation-emission process, while others<sup>[17,25-29]</sup> have emphasized the influence of alloying additions on the Peierls-Nabarro (P-N) barrier energy<sup>[30,31]</sup> and the mobility of dislocations moving away from the crack tip. A computational design approach had been developed to identify toughening or embrittling elements on the

basis of the P-N barrier energy.<sup>[19,25,26]</sup> For enhancing fracture toughness and ductility, beneficial alloy additions include Ti, Hf, and Zr, while detrimental alloying elements include Cr, Al, Mo, W, and Re.<sup>[26]</sup> In this investigation, a computer-assisted alloying approach was used to design Nb-based *in-situ* composites, with the aim of achieving a balance in properties of creep, oxidation, and fracture resistance. In particular, computational models<sup>[25,26,32-34]</sup> were used to predict alloy compositions based on three considerations: (1) the desired Nb solid-solution alloy, (2) the volume fraction of intermetallics, and (3) the properties of candidate Nb-based *in-situ* composites. The candidate alloys selected by the computational approach were fabricated by arc melting into cast buttons. The microstructure, fracture, and oxidation properties were then characterized. The experimental results were used to assess the predictive capability of the computational design approach and to identify potential areas for model improvement. In this article, the design of the alloy composition, the fabrication, and the characterization of fracture properties of individual constituent phases and the Nb-based *in-situ* composites are reported. The experimental results on the oxidation resistance and oxidation modeling are to be published in a companion article elsewhere,<sup>[34]</sup> while modeling of the creep resistance of the Nb-based *in-situ* composites was published earlier.<sup>[33]</sup>

## II. DESIGN OF CANDIDATE NB-BASED *IN-SITU* COMPOSITES

The design of candidate materials started with a review of the oxidation data of Nb-based *in-situ* composites in the literature. Additional oxidation data of General Electric (GE) alloys were obtained from the GE Global Research Laboratories (Schenectady, NY).<sup>[35]</sup> The composition of the

KWAI S. CHAN, Institute Scientist, is with the Southwest Research Institute® (SwRI®), San Antonio, TX 78238. Contact e-mail: kchan@swri.edu DAVID L. DAVIDSON, Consultant, SwRI, is retired.

Manuscript submitted January 16, 2003.

**Table I. Compositions of Nb-Based Alloys (in Atomic Percent) and Volume Percent of Silicide, Laves, and Nb<sub>ss</sub> Constituent Phases Targeted**

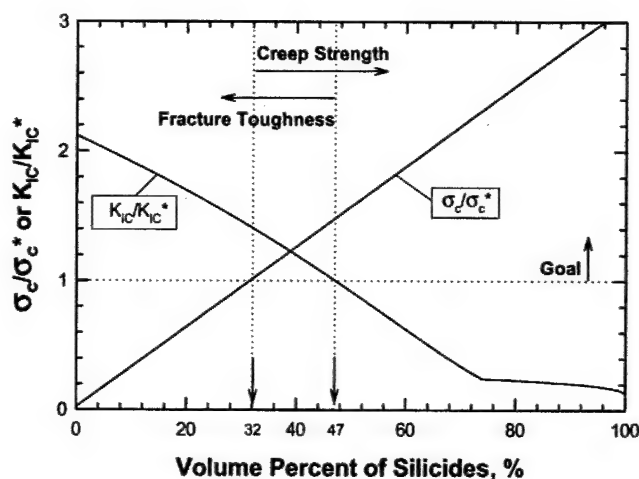
Alloy	Targeted Compositions (At. Pct)						Constituent Phase (Vol. Pct)		
	Nb	Ti	Hf	Cr	Si	Ge	Silicide	Laves Phase	Nb <sub>ss</sub>
Nbx	61	28	4	3	1	3	0	0	100
M1	45.5	22.5	4	13	10	5	20	20	60
M2	34.5	22.5	4	16	18	5	30	30	40
AX	40.5	22.5	4	13	15	5	30	20	50
Clp	20.3	10	4	45	20	0.7	0	100	0

Nb matrix in the most-oxidation-resistant *in-situ* composites in the data set were identified. This information was used as input to a composite-design computer code, which is still under development at Southwest Research Institute, to compute the P-N barrier energy,<sup>[30,31,36,37]</sup> tensile ductility, and fracture toughness for ambient temperature. Based on these results, the compositions of candidate *in-situ* composites in atomic percent were selected and are shown as Nb<sub>ss</sub> in Table I.

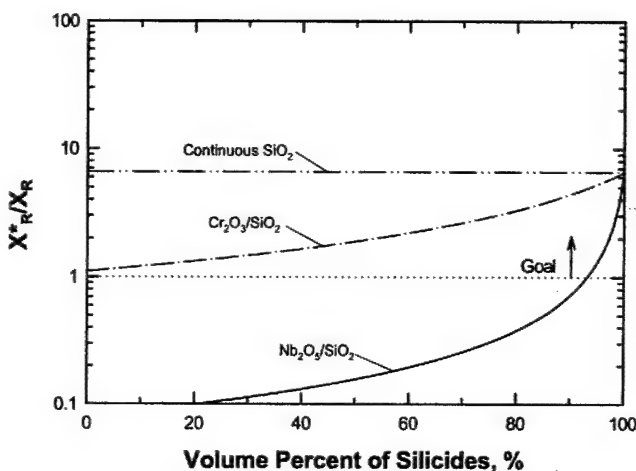
The fracture toughness and the creep strength (at 1200 °C) of *in-situ* composites containing the candidate Nb solid solution were then computed as a function of volume percents of silicides using the methods developed earlier.<sup>[32,33]</sup> These results were normalized by the target properties ( $K_{IC}^* = 25 \text{ MPa}\sqrt{\text{m}}$  at ambient temperature and  $\sigma_c^* = 150 \text{ MPa}$  at 1200 °C). Figure 1 indicates that the fracture toughness and creep properties can be achieved when the volume percent of silicides is 32 to 47 pct.

Computation of metal recession using the oxidation model<sup>[34]</sup> indicated that the oxidation-resistance goal ( $X_R^* \leq 25 \mu\text{m}$  after 100 hours at 1200 °C, where  $X_R^*$  is the maximum recession) could not be achieved if Nb<sub>2</sub>O<sub>5</sub> and SiO<sub>2</sub> form on the matrix and silicides, respectively. The oxidation goal could be attained with the formation of a continuous SiO<sub>2</sub> layer, but it would be difficult to achieve because of the low solubility of Si (<2 pct) in the Nb solid solution. Because of this, the strategy used to achieve the oxidation goal was to select alloy compositions that would induce the formation Cr<sub>2</sub>O<sub>3</sub> on the Nb solid solution and SiO<sub>2</sub> on the silicides. This approach was selected since the oxidation model of Wang *et al.*<sup>[38]</sup> suggested that it might be possible to induce the formation of a continuous SiO<sub>2</sub> layer beneath the Cr<sub>2</sub>O<sub>3</sub> layer formed on the Nb solid solution, if the silicide and Laves phases are in the form of small disks or spheres.

Based on the previous considerations, we selected the composites AX, M1, and M2 for further studies, whose compositions are shown in Table I along with the compositions of the solid-solution alloy (Nbx) and the Laves alloy (Clp). The Nbx alloy was intended to be the Nb solid-solution phase; unfortunately, small amounts ( $\approx 6$  to 9 vol pct) of a low-temperature Ge-rich intermetallic phase formed along the grain boundary. In contrast, the composition of the Clp alloy was chosen to give a microstructure of 100 pct C14 Laves phase. In the other alloys, the target for the volume percent of silicide ranged from 20 to 30 pct, and the same ranges were expected



(a)



(b)

Fig. 1—(a) Optimization of creep and fracture resistance and (b) oxidation resistance of Nb-based *in-situ* composites by controlling the volume fraction of silicides.

for the C14 Laves phase based on incomplete ternary-phase diagrams available at the time. The total volume percent of silicide and Laves phases was expected to range from 40 to 60 pct, which exceeds the fracture-toughness range shown in Figure 1. Thus, some alloys are shown not to meet the  $K_C$  requirement (e.g., AX and M2), but these alloys should manifest higher creep and oxidation resistance compared to other alloys (e.g., M1 and Nbx). These microstructures should provide a sufficiently wide range of properties for a systematic evaluation of the computational design models.

### III. EXPERIMENTAL PROCEDURE

#### A. Material Fabrication

One 76-mm-diameter cast button, each, was fabricated for alloys AX, M1, M2, Nbx, and the C14 Laves-phase alloy (Clp). The cast buttons were made by arc melting in a high-purity argon atmosphere at Pittsburgh Materials Technology (PMT). Each of the buttons was remelted 6 times to ensure chemical



**Table II. The Actual Chemical Composition and Interstitial Contents of Various Nb-Base *In-Situ* Composites**

Alloy	Compositions (At. Pct)						Interstitial Contents (Wt. Ppm)		
	Nb	Ti	Hf	Cr	Si	Ge	C	N	O
Nbx	62.7	26.6	4.2	2.5	1.0	3.0	<100	62	210
M1	46.3	22.2	4.4	12.3	9.7	5.1	<100	34	320
M2	35.8	22.5	4.0	15.6	17.3	4.8	100	26	220
AX	41.3	22.4	3.9	12.5	14.8	5.1	100	60	220
UES-AX	41.2	23.0	4.7	11.2	15.2	4.7	100	36	280
CNG-1B*	48.7	21.5	2.0	6.7	9.0	4.7	200	44	320

\*Also contained 3.5 Pct Fe, 2.6 Pct Al, and 1.3 Pct Sn.

homogeneity. All buttons were cast successfully, except Clp; the C14 Laves-phase alloy exhibited an inhomogeneous microstructure and significant cracking upon cooling.

Besides the PMT-cast buttons, cast bars of alloy AX and an alloy (CNG-1B) that contained Al, Fe, Sn, and B in addition to Ti, Hf, Cr, Si, and Ge, were supplied by the United States Air Force Research Laboratory (AFRL Wright-Patterson Air Force Base, Dayton, OH) through UES (Dayton, OH).<sup>[39]</sup> The actual chemical compositions of the various alloys are summarized in Table II, which indicates that the actual compositions of the alloys are close to the target, and the interstitial contents are low in all alloys.

Coupon specimens were cut from the cast materials and then heat treated. One set of specimens was heat treated at 1350 °C for 100 hours in a flowing argon environment and then furnace cooled (FC), while another set was heat treated at 1350 °C for 24 hours and FC under a similar environment. The UES-AX material was hot-isostatically pressed (hipped) at 1350 °C under a pressure of 207 MPa for 6 hours before it was heat treated (1350 °C/100 hours/FC). The CNG-1B alloy received the same heat treatment (1350 °C/100 hours/FC), but it was subsequently hipped at 1420 °C under 207 MPa pressure for 6 hours and FC.

### B. Characterization of Microstructures

Backscattered electron (BSE) microscopy was used to characterize the microstructures of various Nb-based *in-situ* composites. Figure 2 shows the microstructure of the various materials heat treated at 1350 °C/100 hours. Because of atomic-number contrast, Nb-based solid solution appeared as the light phase, Nb-rich silicides (Nb<sub>5</sub>Si<sub>3</sub> and Nb<sub>3</sub>Si) appeared as the medium-dark or gray phase, and the Laves phase (C14) appeared as the dark phase in the BSE images. Ti-rich silicides (Ti<sub>5</sub>Si<sub>3</sub> and Ti<sub>3</sub>Si) and Hf particles were occasionally detected, and they appeared as one of the light phases in the BSE micrographs.

Using BSE micrographs, quantitative metallography was used to determine the volume fractions of silicides (Nb<sub>5</sub>Si<sub>3</sub>, Nb<sub>3</sub>Si, Ti<sub>5</sub>Si<sub>3</sub> and Ti<sub>3</sub>Si), Laves phases, and Nb-based solid solution. Since Ti-rich silicides and Hf particles sometimes appeared as a light phase in the BSE images, the volume fraction of Nb solid solution might be overestimated due to the presence of Ti-rich Ti<sub>5</sub>Si<sub>3</sub> and Hf particles, but the error was expected to be small because both Ti<sub>5</sub>Si<sub>3</sub> and Hf particles were detected only occasionally. Summaries of the chem-

ical compositions and volume fractions of constituent phases (silicides, Laves phase, and Nb solid solution) in the various materials are presented in Tables III and IV, respectively.

The compositions of individual phases in individual Nb-based *in-situ* composites were determined by energy-dispersive spectroscopy (EDS) performed on selected grains. Some of these grains had been indented to measure the fracture toughness using the Vickers indentation technique. Furthermore, the crystal structure of individual phases in the composites was identified by X-ray diffraction (XRD) and by comparing the diffraction peaks against published standards. After fracture testing, the fracture surfaces were characterized by a scanning electron microscope (SEM) operated in the secondary-electron mode.

### C. Fracture-Toughness Testing

The fracture toughness of individual composites was determined by three-point bending of notched specimens. The specimen dimensions were 40 mm in length, 6 mm in width, and 3 mm in thickness, with a 3-mm notch fabricated by electrodischarge machining (EDM). Fracture-toughness testing was performed at 25 °C using a loading rate of 60 N/s, and the applied load was measured as a function of displacement. The peak load was used to compute the fracture toughness using the analysis described in the ASTM standard.<sup>[40]</sup> Triplicate specimens were tested for the as-cast alloys, which showed relatively small scatter; consequently, a single test was performed on most of the heat-treated specimens.

Compact-tension specimens with a fatigue precrack were also used to determine the fracture toughness of individual alloys. The specimen dimensions were 20 mm in width, 19 mm in height, and 4.8 mm in thickness. The specimens were fabricated by EDM and contained a notch of 7.14 mm in length. Fatigue cracks were introduced at 25 °C by cyclic loading at an *R* ratio of 0.1, where *R* is the ratio of the minimum to maximum load. After precracking, fracture-toughness testing was performed at 25 °C in an SEM equipped with a loading stage.<sup>[41]</sup> The near-tip region was first photographed at a stress-intensity factor (*K*) of about 5 MPa√m. Subsequently, the *K* level increased by 1 MPa√m, and the near-tip region was photographed again in order to identify the fracture process and follow the crack path. This process was repeated until final fracture of the specimen occurred. Crack extension at each *K* increment was measured from the near-tip photographs, and the *K*-resistance curve was obtained by plotting *K* as a function of crack extension.

In addition, the fracture toughness of the constituent phases in individual alloys was determined at 25 °C by the Vickers indentation technique.<sup>[42]</sup> A Vickers-hardness indent was made in the phase of interest using a small indentation load. The load was selected such that it was large enough to produce indentation cracks but was sufficiently low that the resulting Vickers indent and cracks resided entirely within the phase of interest. For silicide and Laves phases, fracture toughness was determined using an indentation load of 20 or 50 g. At these load levels, indentation cracks were induced in the Nb solid solution only occasionally, and most of the indents produced no cracks at loads as high as 200 g. After indentation, individual indents were photographed in the SEM using the BSE



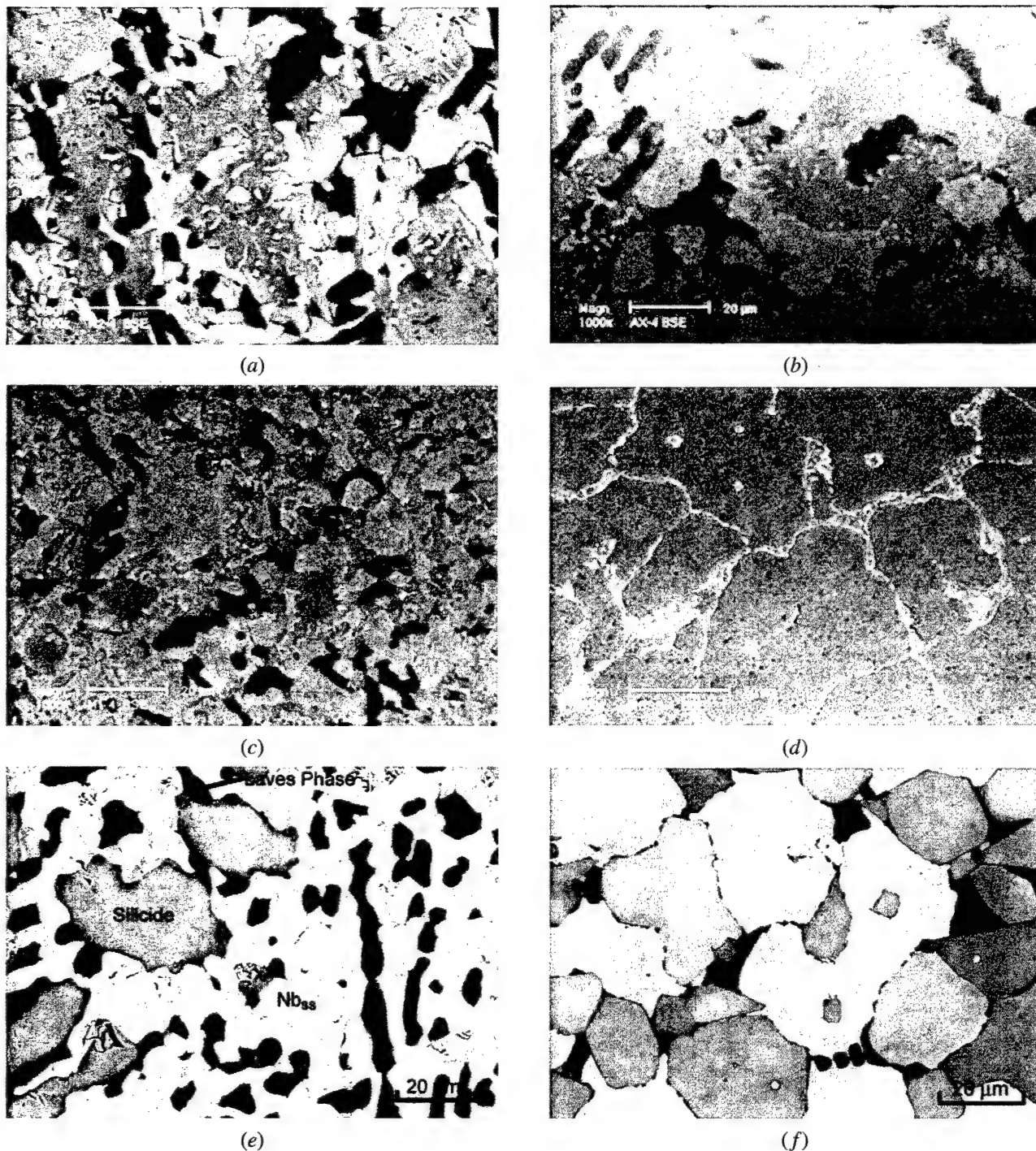


Fig. 2—Microstructures of Nb-based *in-situ* composites heat treated at 1350 °C for 100 h: (a) M2, (b) AX, (c) M1, (d) Nbx, (e) UES-AX, and (f) CNG-1B.

mode. The chemical composition of the indented grain with microcracks was determined by energy-dispersive spectroscopy. The size of the indents and the corresponding crack lengths were then determined from the BSE photographs. These results were then used to obtain the indentation fracture toughness.

According to Anstis *et al.*,<sup>[42]</sup> the indentation toughness ( $K_{VC}$ ) can be computed using the expression given by<sup>[42]</sup>

$$K_{VC} = \phi_V (E/H)^{1/2} P/c^{3/2} \quad [1]$$

where  $E$  is the Young's modulus,  $H$  is the hardness in units of MPa,  $P$  is the indentation load,  $c$  is the crack length measured from the apex of the Vickers indent, and  $\phi_V$  is a load/boundary correction factor. The origin of the load/boundary correction factor was investigated by several investigators.<sup>[42,43,44]</sup> These investigations indicated that the tensile stress that caused crack initiation and growth in an indentation-toughness test was induced under the indenter during unloading.<sup>[42,43,44]</sup> The manner by which these tensile stresses were induced was analogous to that at a notch root subjected to

**Table III. The Chemical Compositions and Crystal Structures of Constituent Phases in Various Nb-Based *In-Situ* Composites in the As-Cast and Heat-Treated Conditions**

Alloy	Heat Treatment	Nb <sub>ss</sub> Phase (bcc)	Silicide Phase* (D8 <sub>1</sub> )	Laves Phase (C14)	Ge-Rich Phase (Unknown)
M2-1	as-cast	—	Nb-23Ti-3Hf-4Cr-6Ge-28Si	Nb-12Ti-4Hf-52Cr-2Ge-9Si	—
M1-1	as-cast	Nb-20Ti-3Hf-12Cr-4Ge-4Si	Nb-20Ti-4Hf-3Cr-10Ge-25Si	Nb-10Ti-4Hf-49Cr-2Ge-9Si	—
AX-1	as-cast	Nb-24Ti-3Hf-14Cr-2Ge-1Si	Nb-21Ti-3Hf-3Cr-8Ge-27Si	Nb-15Ti-6Hf-49Cr-2Ge-8Si	—
Nbx-1	as-cast	Nb-29Ti-4Hf-3Cr-3Ge-3Si	—	—	Nb-39Ti-6Hf-3Cr-9Ge-6Si
UES-AX	1350 °C/100 h	Nb-26Ti-3Hf-14Cr-3Ge-1Si	Nb-24Ti-4Hf-1Cr-6Ge-29Si	Nb-12Ti-3Hf-54Cr-1Ge-8Si	—
M2-3	1350 °C/100 h	Nb-23Ti-1Hf-10Cr-3Ge-3Si	Nb-19Ti-5Hf-2Cr-7Ge-28Si	Nb-12Ti-4Hf-50Cr-2Ge-8Si	—
M1-3	1350 °C/100 h	Nb-18Ti-1Hf-10Cr-2Ge-3Si	Nb-17Ti-5Hf-3Cr-12Ge-23Si	Nb-10Ti-4Hf-49Cr-2Ge-9Si	—
AX-3	1350 °C/100 h	Nb-20Ti-1Hf-10Cr-3Ge-3Si	Nb-18Ti-5Hf-1Cr-8Ge-28Si	Nb-11Ti-4Hf-48Cr-2Ge-9Si	not determined
Nbx-3	1350 °C/100 h	Nb-24Ti-3Hf-3Cr-4Ge-3Si	—	—	Nb-28Ti-19Hf-0.3Cr-27Ge-10Si
CNG-1B**	1350 °C/100 h	Nb-21Ti-1Hf-8Cr-0.8Ge-0.8Si-2.6Fe-2Sn-2Al	Nb-19Ti-2.3Hf-1.7Cr-9.5Ge-20Si-2Al-1.8Fe-1Sn	Nb-15Ti-2.8Hf-31Cr-1Ge-8Si-2Al-15Fe-0.1 Sn	—

\*\*Hipped at 1420 °C under 207 MPa pressure for 6 h.

\*Also contained small amounts of (Ti, Nb)<sub>5</sub>Si<sub>3</sub> (D8<sub>8</sub> structure) and possibly Nb<sub>3</sub>Si (Ti<sub>3</sub>P structure).

**Table IV. A Summary of the Volume Percents of Intermetallics and Fracture Toughness Results for Nb-Based *In-Situ* Composites Determined by Three-Point Bend and Compact Tension (CT) Techniques**

Alloy	Heat Treatment	Vol Pct Nb <sub>ss</sub>	Vol Pct Silicides	Vol Pct Laves Phase	Vol Pct Ge-Rich Phase	K <sub>IC</sub> , MPa√m (3-Point Bend)	K <sub>IC</sub> , MPa√m (CT Tests)
M2-1	as-cast	0	73	27	0	8.4 ± 1.2*	8.8
M1-1	as-cast	64	28	8	0	12.2 ± 0.7*	—
AX-1	as-cast	20	66	14	—	10.3 ± 0.3*	9.9
Nbx-1	as-cast	91	—	—	9	22.1 ± 2.2*	—
UES-AX	1350 °C/100 h	54	32	14	—	10.9 ± 1.4*	11.4
M2-3	1350 °C/100 h	22	53	25	—	7.4	—
M1-3	1350 °C/100 h	54	35	11	—	13.1	—
Nbx-3	1350 °C/100 h	94	—	—	6	24.7	—
AX-3	1350 °C/100 h	39	40	15	6	11.8	—
CNG-1B**	1350 °C/100 h	43.6	50.7	5.7	—	6.3 ± 0.2*	11.0
M2-4	1350 °C/24 h	24.0	48.7	26.5	—	8.7	—
M1-4	1350 °C/24 h	60.2	27.9	10	—	11.5	—
AX-4	1350 °C/24 h	50.6	33.7	14	—	10.1	—
Nbx-4	1350 °C/24 h	83.7	—	—	16.3	27.2	—

\*\*Hipped at 1420 °C under 207 MPa pressure for 6 h.

\*Average of three tests.

compression/compression fatigue.<sup>[45,46,47]</sup> In particular, the tensile stresses induced during unloading depend on the amount of inelastic deformation that occurred at the notch root. Inelastic deformation corresponds to plastic flow for ductile materials,<sup>[45]</sup> but originates from microcracking for brittle materials.<sup>[46,47]</sup> In general, Eq. [1] is applied to brittle materials, and the value of  $\phi_V$  was evaluated by fitting Eq. [1] to a set of fracture-toughness data for ceramics.<sup>[42]</sup> Since the tensile stresses induced during indentation depend on inelastic deformation under the indenter, it was uncertain whether Eq. [1] was applicable to Nb-based *in-situ* composites. Consequently, the fracture-toughness data of three-point bend tests were used to calibrate Eq. [1] to obtain the appropriate value for the load/boundary correction factor ( $\phi_V$ ). The  $\phi_V$  value was found to be 0.1168 for Nb-based composites, compared to  $\phi_V = 0.016$  for brittle ceramics.<sup>[42]</sup> Once  $\phi_V$  was determined, Eq. [1] was used to compute the  $K_{VC}$  values for individual phases (silicides, Laves phase, and Nb<sub>ss</sub>) in the *in-situ* composites.

## IV. RESULTS

### A. Microstructure

Typical XRD results of the as-cast materials are presented in Figures 3(a) and (b). Individual phases were identified by matching the characteristic XRD peaks against the JCPDF standards.<sup>[48]</sup> In as-cast M2, the microstructure was comprised of alloyed Nb<sub>5</sub>Si<sub>3</sub>, Nb<sub>3</sub>Si, Ti<sub>5</sub>Si<sub>3</sub>, and NbCr<sub>2</sub>; there was little or no Nb solid solution, since the observed XRD peaks did not match those of Nb (Figure 3(a)). In alloys M1 and AX, the microstructure contained Nb solid solution, alloyed silicides (Nb<sub>5</sub>Si<sub>3</sub>, Nb<sub>3</sub>Si, and Ti<sub>5</sub>Si<sub>3</sub>), and alloyed NbCr<sub>2</sub>; the results for M1 are shown in Figure 3(b). For alloy Nbx, XRD results showed only the Nb solution phase, but BSE microscopy indicated the presence of a Ge-rich grain-boundary phase that was identified as a low-melting-point metastable intermetallic.<sup>[49]</sup> The microstructures of the heat-treated

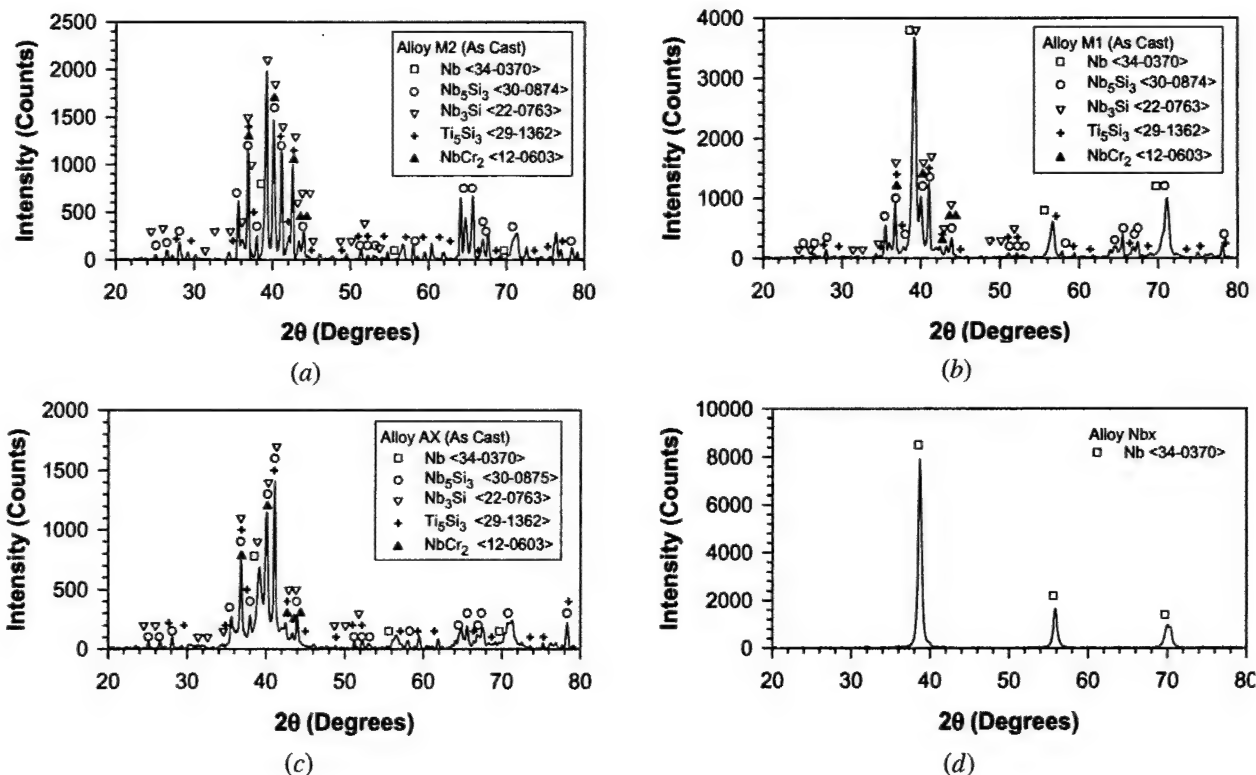


Fig. 3—Typical XRD results of as-cast Nb-based *in-situ* composites: (a) M2, (b) M1, (c) AX, and (d) NbX. The <> shows the JCPDF card number.

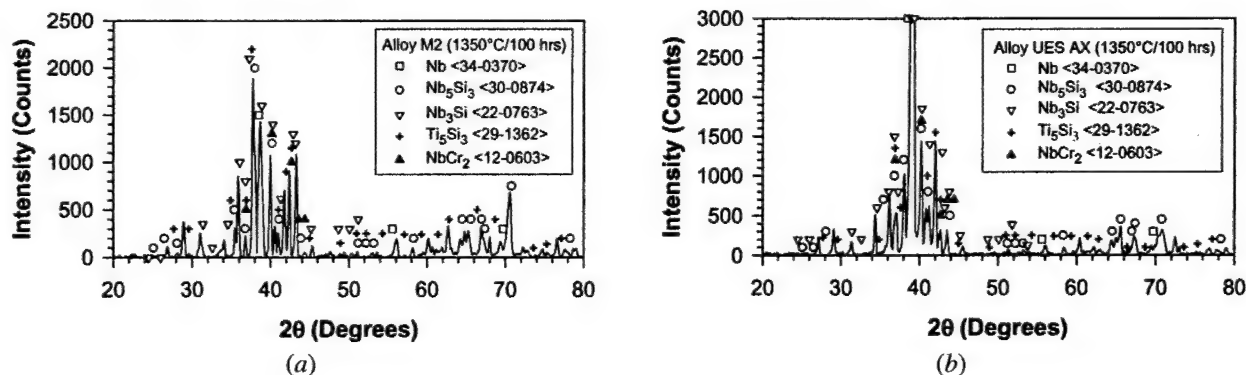


Fig. 4—Typical XRD results of Nb-based *in-situ* composites heat treated at 1350 °C for 100 h: (a) M2 and (b) UES-AX. The <> shows the JCPDF card number.

materials (1350 °C/100 hours and 1350 °C/24 hours) were comprised of Nb solid solution, alloyed silicides ( $\text{Nb}_5\text{Si}_3$ ,  $\text{Nb}_3\text{Si}$ , and  $\text{Ti}_5\text{Si}_3$ ), and alloyed  $\text{NbCr}_2$ . Typical results for M2 and UES-AX, which were heat treated at 1350 °C/100 hours, are presented in Figures 4(a) and (b), respectively.

Compositions of alloyed silicide, Laves phase, and  $\text{Nb}_{ss}$  in Nb-based *in-situ* composites are presented in Figure 5. The crystal structures of alloyed  $\text{Nb}_5\text{Si}_3$ ,  $\text{Nb}_3\text{Si}$ ,  $\text{Ti}_5\text{Si}_3$ , and  $\text{NbCr}_2$ , which were identified by matching the observed diffraction peaks against the JCPDF and then consulting the corresponding data cards,<sup>[48]</sup> are D8<sub>1</sub>, T<sub>13</sub>P, D8<sub>8</sub>, and C14, respectively, as summarized in Table III.

The phase diagrams for Nb-based *in-situ* composites containing three or more alloying elements are generally not available. Fortunately, Bewlay and Jackson<sup>[11]</sup> and Zhao *et al.*<sup>[12]</sup>

recently published several ternary-phase diagrams for the Nb-Ti-Si, Nb-Cr-Si, and Nb-Ti-Cr systems for selected temperatures in the range of 1000 °C to 1350 °C. Although the temperature was sometimes different, these phase diagrams were used to compare with the experimental data obtained in this study by treating selected elements as equivalent. For examples, Ti and Hf were treated as equivalent and, similarly, Si and Ge were considered equivalent. Figures 6(a) through (c), respectively, show the as-cast alloys in three pseudoternary phase diagrams for 1350 °C: Nb-Ti(+Hf)-Si(+Ge + Cr), Cr-Nb (+Ti + Hf)-Si(+Ge), and Nb-Ti(+Hf)-Cr(+Si + Ge). The phase boundaries shown in Figure 6(a) are for 1350 °C and are taken from Bewlay *et al.*<sup>[11]</sup> In Figures 6(b) and (c), the phase boundaries are for 1200 °C and both are from Zhao *et al.*<sup>[12]</sup> The results indicate that the alloys are located

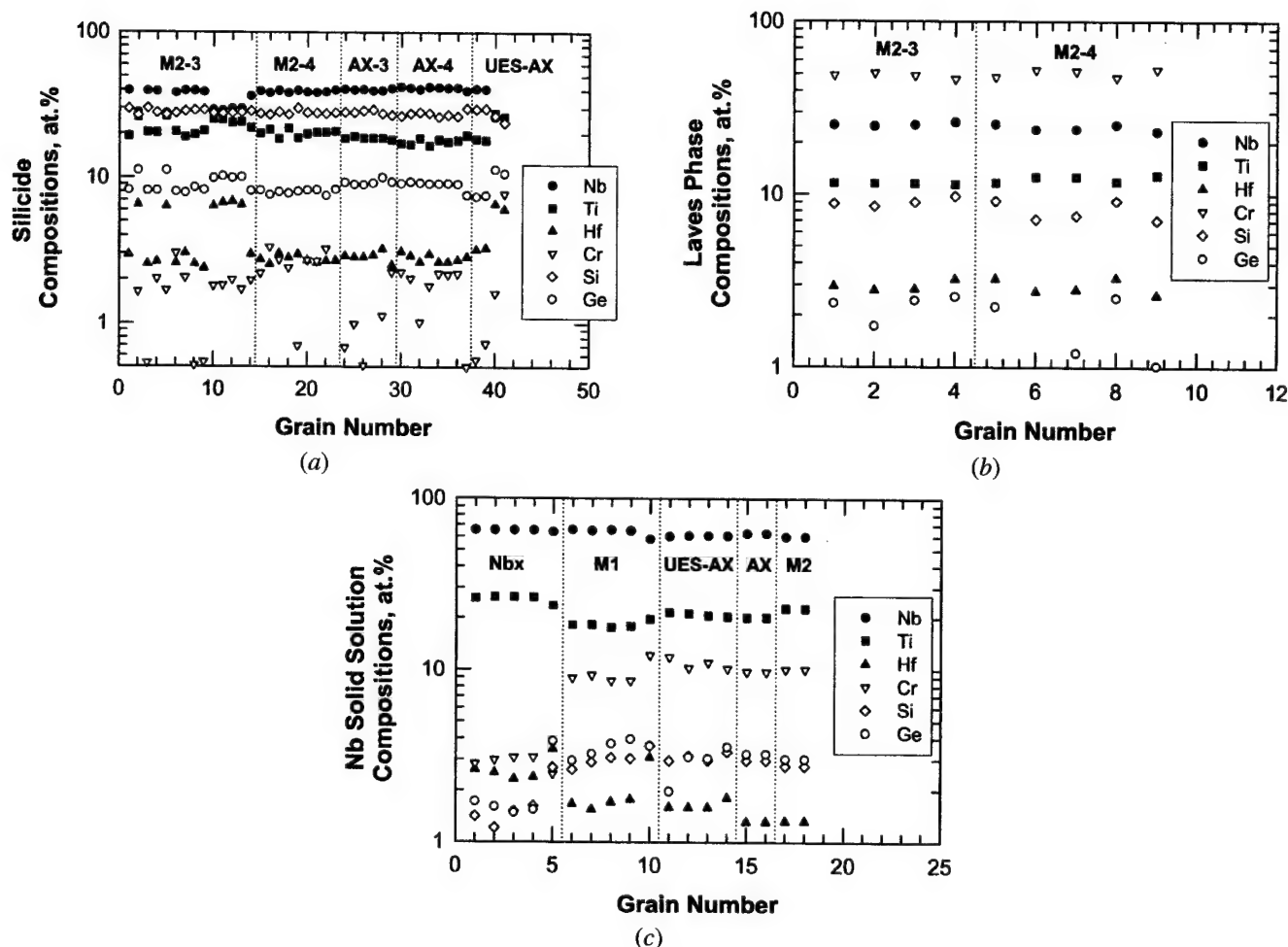


Fig. 5—Typical compositions of constituent phases in Nb-based *in-situ* composites: (a) silicide, (b) Laves phase, and (c) Nb<sub>ss</sub>. The heat treatment was 1350 °C/100 h for all specimens except M2-4 and AX-4, which were heat treated at 1350 °C/24 h. The grain number was assigned arbitrarily for plotting purposes only.

in a three-phase field containing silicides, Laves phase, and Nb solid solution, with the exception of as-cast M2, which contained silicides and Laves phase only. Another important observation from Figure 6 is that the compositions of the constituent phases are similar in the various *in-situ* composites, the only exception being Nb<sub>x</sub>, whose Nb solid solution exhibits a lower Cr content ( $\approx 3$  at. pct Cr) than those in other materials (9 to 14 at. pct Cr). Thus, the main difference among the various composites is in their volume fractions of the constituent phases. The discrepancies observed in the current data and the phase boundaries in Figures 6(b) and (c) are probably due to variants in the temperature of the phase diagram. Unfortunately, ternary-phase diagrams for Cr-Nb-Si and Nb-Ti-Cr at 1350 °C do not appear to be available in the literature.

### B. Fracture Toughness

The fracture-toughness values of Nb-based *in-situ* composites, determined by three-point bend and compact-tension specimens, are summarized in Table IV. The results are also plotted against the volume percent of intermetallics in Figure 7. In general,  $K_{IC}$  decreases with increasing volume percent of silicide and Laves phases in the composite.

Heat treatments varied the volume percents of the silicides, but the volume percent of Laves phase remained essentially unchanged before and after heat treatment. Despite these changes, the fracture toughness was not significantly altered by heat treatment, as shown in Figure 7. The fracture toughness of the *in-situ* composites appears to remain constant at approximately 10 MPa $\sqrt{m}$  when the volume percent of silicides and Laves phase exceeded about 50 pct.

Typical indentation cracks in Laves phase, silicide, and Nb solid solution are shown in Figure 8. The indentation toughness of the Laves phase ranged from 2 to 5 MPa $\sqrt{m}$ . In contrast, the indentation toughness of the silicide phases ranged from 3 to 12 MPa $\sqrt{m}$ . The frequency distribution of  $K_{IC}$  for the silicides was measured, and the result is presented in Figure 9. Only some Nb<sub>ss</sub> grains in AX and UES-AX cracked by indentation, most of the Nb<sub>ss</sub> grains in M1 did not crack, and none in the Nb<sub>x</sub> cracked by indentation. Since the Nb solid-solution Nb<sub>x</sub> did not crack under indentation, only the minimum values of the indentation toughness could be estimated, and they ranged from 22 to 32 MPa $\sqrt{m}$  (Figure 10). The actual toughness of the Nb solid solution in Nb<sub>x</sub> exceeded these minimum values.

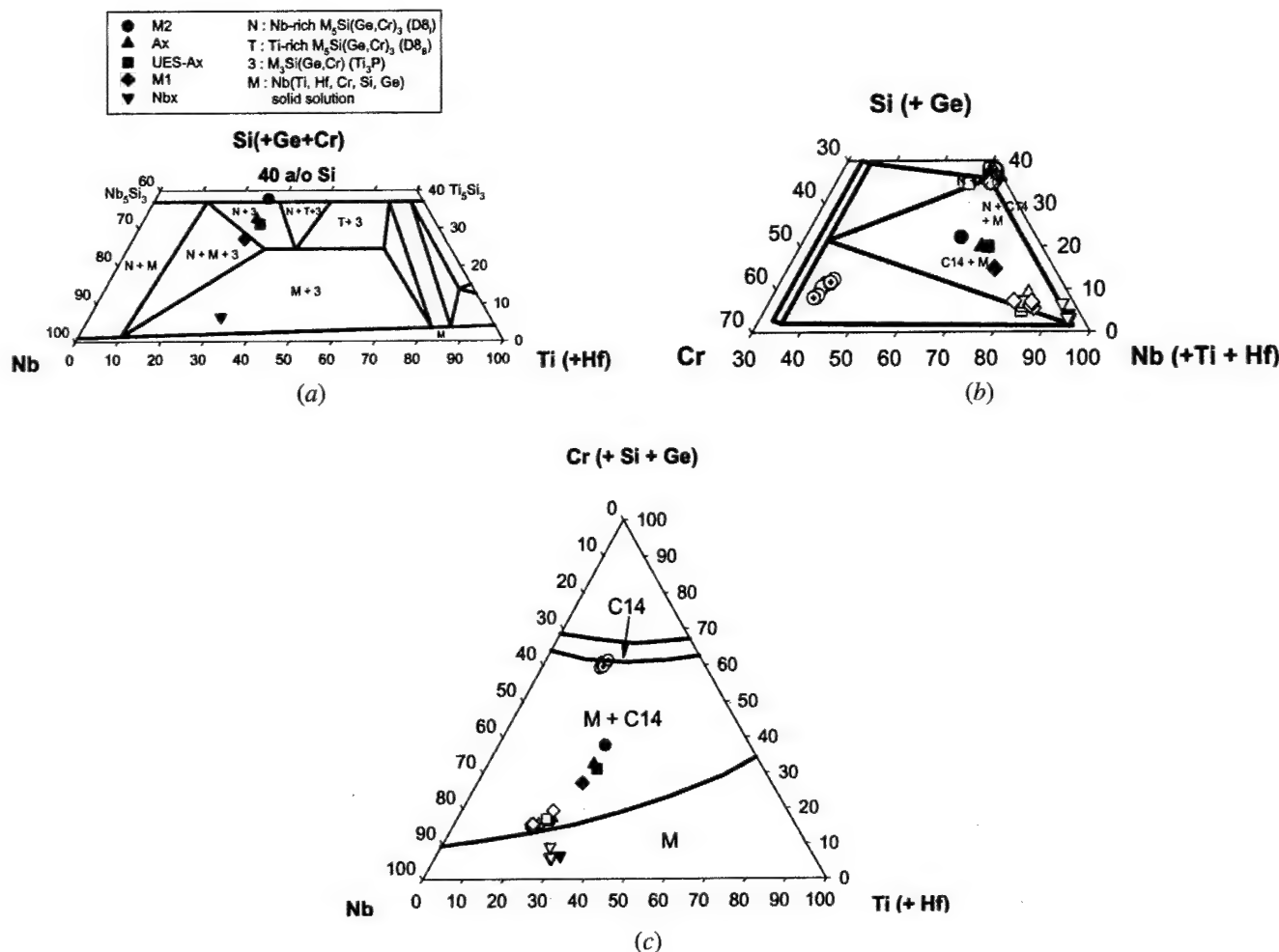


Fig. 6—Pseudoternary phase diagrams illustrate the phase relations in Nb-based *in-situ* composites at 1350 °C: (a) Nb-Ti(+Hf)-Si(+Ge+Cr), (b) Cr-Nb(+Ti+Hf)-Si(+Ge), and (c) Nb-Ti(+Hf)-Cr(+Si+Ge). A pseudoternary Nb-Ti-Si phase diagram is shown in (a), where (+Hf) designates that Hf is added to the Ti value and (+Ge+Cr) indicates that Ge and Cr are added to the Si value. Similar conventions are used (b) for Cr-Nb-Si and (c) for Nb-Ti-Cr. Solid lines are phase boundaries from the literature.<sup>[11,12]</sup> Open symbols are compositions determined on individual phases in the *in-situ* composites. Closed symbols are nominal compositions of the composites.

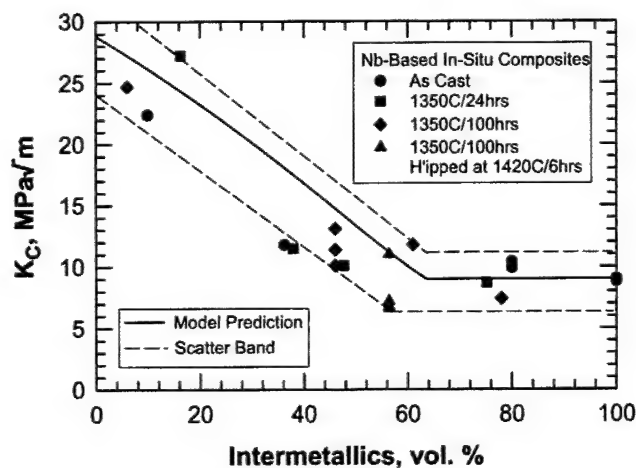
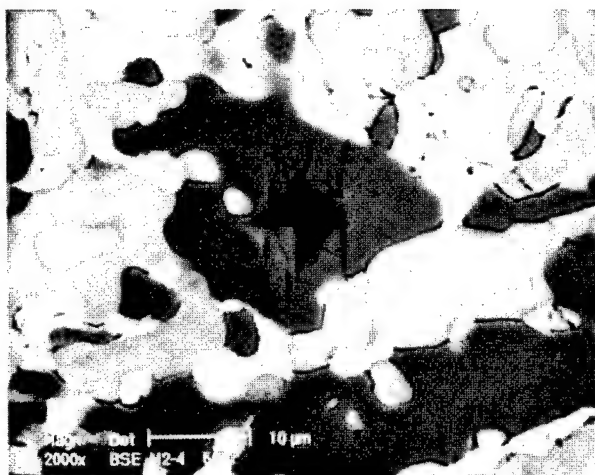


Fig. 7—Fracture toughness ( $K_{IC}$ ) decreases with increasing volume percent of intermetallics (Ge-rich phase, silicides, and Laves phases).

Fracture testing using compact-tension specimens indicated that the M2, AX, UES-AX, and CNG-1B alloys exhibited small amounts of stable crack growth and very flat  $K_R$  curves. The fracture process in as-cast M2 is summarized in the BSE images of the crack-tip region in Figures 11(a) through (d). At  $K = 5$  MPa $\sqrt{m}$ , microcracks formed ahead of the main crack due to cracking of the Laves phase (dark) and Ti-rich silicides (light gray), as shown in Figure 11(a). The microcracks opened up at  $K = 6$  MPa $\sqrt{m}$ , but did not extend. At  $K = 7$  MPa $\sqrt{m}$ , some of the microcracks linked up, and a new microcrack nucleated in a Nb-rich silicide grain (gray phase) located ahead of the crack tip (Figure 11(b)). At  $K = 8$  MPa $\sqrt{m}$ , the main crack linked up with a few microcracks, but a larger microcrack extended unstably over a distance of  $\approx 290$   $\mu m$  (Figure 11(c)). The new crack tip at  $K = 8$  MPa $\sqrt{m}$  is shown in Figure 11(d). Loading to  $K = 8.5$  MPa $\sqrt{m}$  caused the main crack to extend through a few Nb-rich silicide grains. Furthermore, additional microcracks were nucleated ahead of the main crack. Most of the microcracks initiated in the Laves grains (dark), which





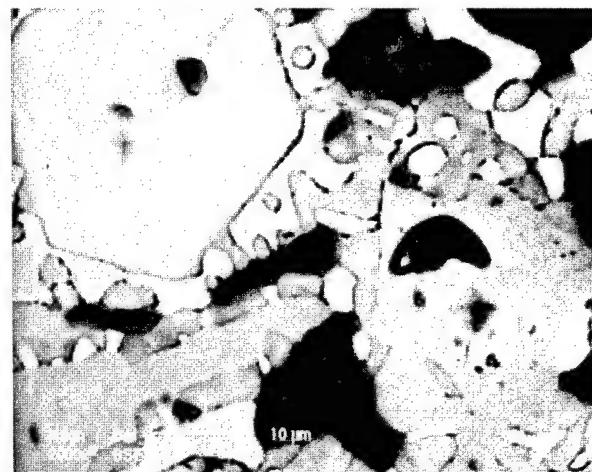
(a)



(b)



(c)



(d)

Fig. 8—Indentation cracks in constituent phases in Nb-based *in-situ* composites: (a) Laves phase in M2-3 (50-g load,  $K = 5 \text{ MPa}\sqrt{\text{m}}$ ), (b) silicide in CNG-1B (50-g load,  $K = 7 \text{ MPa}\sqrt{\text{m}}$ ), (c) silicide solid solution in M2-3 (25-g load,  $K = 7$  and  $13 \text{ MPa}\sqrt{\text{m}}$ ), and (d) Nb solid solution in NbX-3 (25-g load, no crack,  $K \geq 28 \text{ MPa}\sqrt{\text{m}}$ ).

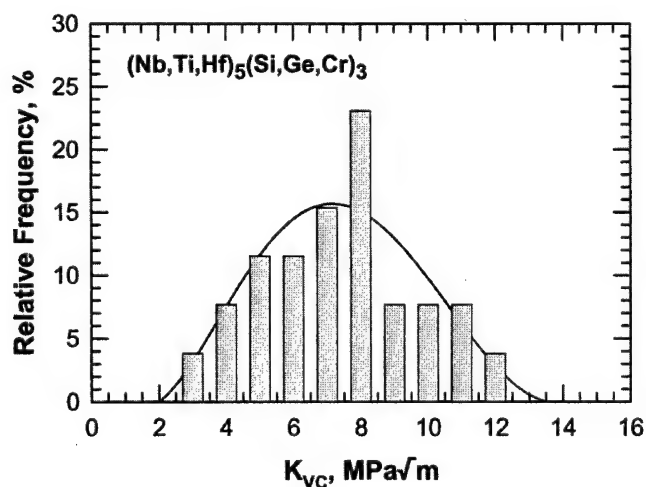


Fig. 9—Frequency distribution of the indentation fracture toughness ( $K_{VC}$ ) of constituent silicide phases in Nb-based *in-situ* composites.

subsequently propagated into and arrested in Nb-rich silicides. A further increase in load led to unstable crack propagation at  $K = 8.8 \text{ MPa}\sqrt{\text{m}}$ .

The fracture processes in alloys containing  $\text{Nb}_{ss}$  exhibited only small amounts of ductile-phase toughening. In as-cast AX, the main crack and microcracks were often blocked or trapped by  $\text{Nb}_{ss}$  particles, as shown in Figure 12(a) for  $K = 8 \text{ MPa}\sqrt{\text{m}}$ . The main crack, however, penetrated into the  $\text{Nb}_{ss}$  particle at  $K = 8 \text{ MPa}\sqrt{\text{m}}$  (Figure 12(b)) and, subsequently, linked up with the microcrack, causing unstable fracture at  $K = 9.9 \text{ MPa}\sqrt{\text{m}}$ . Crack bridging by  $\text{Nb}_{ss}$  particles was also observed in heat-treated UES-AX (1350 °C/100 hours). Figure 13(a) shows the bridged crack at  $K = 7 \text{ MPa}\sqrt{\text{m}}$ . Increasing the  $K$  levels incrementally to 8 and 9  $\text{MPa}\sqrt{\text{m}}$  caused the crack to open up without lengthening. At  $K = 10 \text{ MPa}\sqrt{\text{m}}$  the main crack propagated into a Laves grain (dark) and a Nb-rich silicide grain (gray), as shown in Figure 13(b). At  $K = 11 \text{ MPa}\sqrt{\text{m}}$ , the main crack propagated across several silicide and Laves grains,

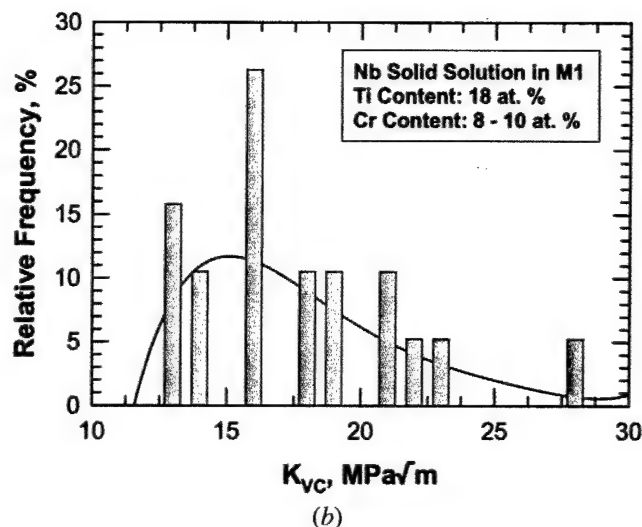
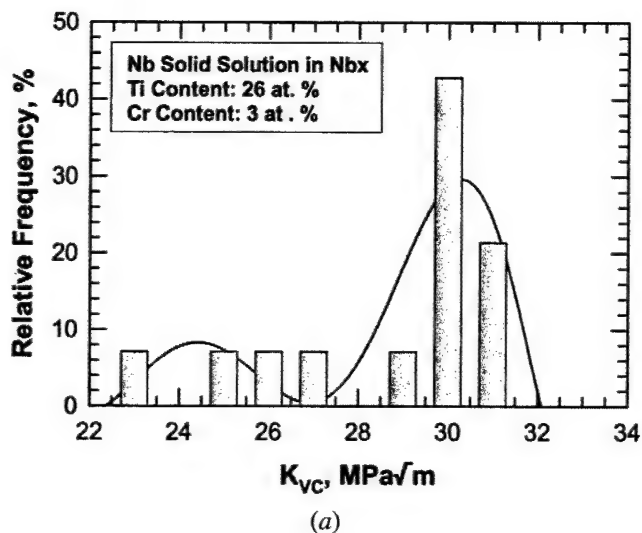


Fig. 10—Frequency distribution of the indentation fracture toughness ( $K_{VC}$ ) of the Nb solid solution phase in *in-situ* composites: (a) high Ti and low Cr contents and (b) low Ti and high Cr contents.

sometimes along grain boundaries. A subsequent increase in the applied load led to unstable fracture at  $K = 11.4 \text{ MPa}\sqrt{\text{m}}$ .

In CNG-1B, the crack tended to follow the silicide phase. At lower  $K$  levels, the crack was seen to arrest at or within an  $\text{Nb}_{ss}$  grain. The main crack, however, was able to get around the more ductile  $\text{Nb}_{ss}$  grains by crack reinitiation or deflection. Figure 14(a) illustrates the reinitiation of a microcrack in a silicide grain, located ahead of the trapped initial crack at  $K = 6 \text{ MPa}\sqrt{\text{m}}$ . In contrast, Figure 14(b) shows that the main crack changed its path to follow the silicide phase by deflecting to propagate around the  $\text{Nb}_{ss}$  obstacles at  $K = 8 \text{ MPa}\sqrt{\text{m}}$ . Consequently, the crack path follows mostly the silicide phase at  $K = 9 \text{ MPa}\sqrt{\text{m}}$ . (Figure 14(c)), resulting in the absence of ductile-phase toughening and a flat  $K_R$  curve.

## V. DISCUSSION

### A. Microstructure

The characteristic diffraction peaks of Nb are close to those of the silicides ( $\text{Nb}_5\text{Si}_3$ ,  $\text{Nb}_3\text{Si}$ , and  $\text{Ti}_5\text{Si}_3$ ). Consequently, considerable amounts of effort were spent on the EDS of individual light phases in the BSE mode, to confirm the XRD result that the  $\text{Nb}_{ss}$  did not exist in the as-cast M2 alloy. More than 40 light and gray grains were examined, and they were all silicides. The  $\text{Nb}_{ss}$  can be easily identified by its low Si content (1 to 3 pct), while the silicides are typically rich in Si (27 to 30 pct). The Laves phases contain typically about 8 to 9 pct Si and are high in Cr (47 to 53 pct). In CNG-1B, Cr in the Laves phase is partially replaced by Fe. Thus, Cr and Fe may be considered similar, if not equivalent. Based on the XRD and EDS results, the authors are confident that the as-cast M2 contained little or no  $\text{Nb}_{ss}$  in the microstructure.  $\text{Nb}_{ss}$ , however, existed in the heat-treated materials. The volume fractions of the Laves phase are approximately the same in all alloys before and after heat treatments; thus, the  $\text{Nb}_{ss}$  formed at

the expense of mostly the silicides during heat treatment at  $1350^\circ\text{C}$ . Since  $\text{Nb}_{ss}$  contains 10 to 14 pct Cr and 1 to 3 pct Si, while the silicides contain 1 to 3 pct Cr and 25 to 29 pct Si, repartitioning of Cr and Si in the  $\text{Nb}_{ss}$ , silicide, and Laves phase must have occurred. The repartitioning process of these elements is not understood, but it could have involved dissolution of the Laves phase and minor changes in the volume fraction of the Laves phase. The various silicides and Laves phases and their compositions observed in the present *in-situ* composites are generally consistent with those identified by researchers at the AFRL<sup>[4,9,10]</sup> and GE Global Research Laboratories.<sup>[5,6,11,12]</sup> The C14 Laves phase is mainly the result of the stabilization of this phase by Si.<sup>[11,12]</sup> It should also be noted that Ti partitions in the  $\text{Nb}_{ss}$ , Laves phase, and silicides. The solubility of Ti in the  $\text{Nb}_{ss}$  in the *in-situ* composites appears to have a range of 18 to 26 pct, while it is about 18 to 22 pct in Nb-rich silicides but is 26 to 28 pct in Ti-rich silicides. The Cr content in the  $\text{Nb}_{ss}$  was expected to be about 3 at. pct.<sup>[11,12]</sup> This level of Cr content was observed in the Nb-x Ti alloy only. For other alloys, the Cr content in the  $\text{Nb}_{ss}$  phase was in the 9 to 14 at. pct range. Si and Ge additions appeared to increase the Cr solubility in the  $\text{Nb}_{ss}$  phase. Unfortunately, this high level of Cr significantly reduced the fracture toughness of the  $\text{Nb}_{ss}$  phase.<sup>[17,25]</sup>

### B. Alloying Effects

The fracture toughness of Nb solid-solution alloys is known to depend on the Ti content.<sup>[17,25]</sup> A correlation between  $K_C$  and Ti content has been established in an earlier study.<sup>[25]</sup> The fracture toughness and Ti content of the  $\text{Nb}_{ss}$  phase in individual composites are compared against the experimental data and the established relation of Nb solid-solution alloys in Figure 15. The comparison indicates that there is reasonable agreement between the fracture toughness of individual  $\text{Nb}_{ss}$  particles in the *in-situ* composites and those obtained for bulk materials with equivalent Ti contents. The exception is Nb-x, whose fracture tough-

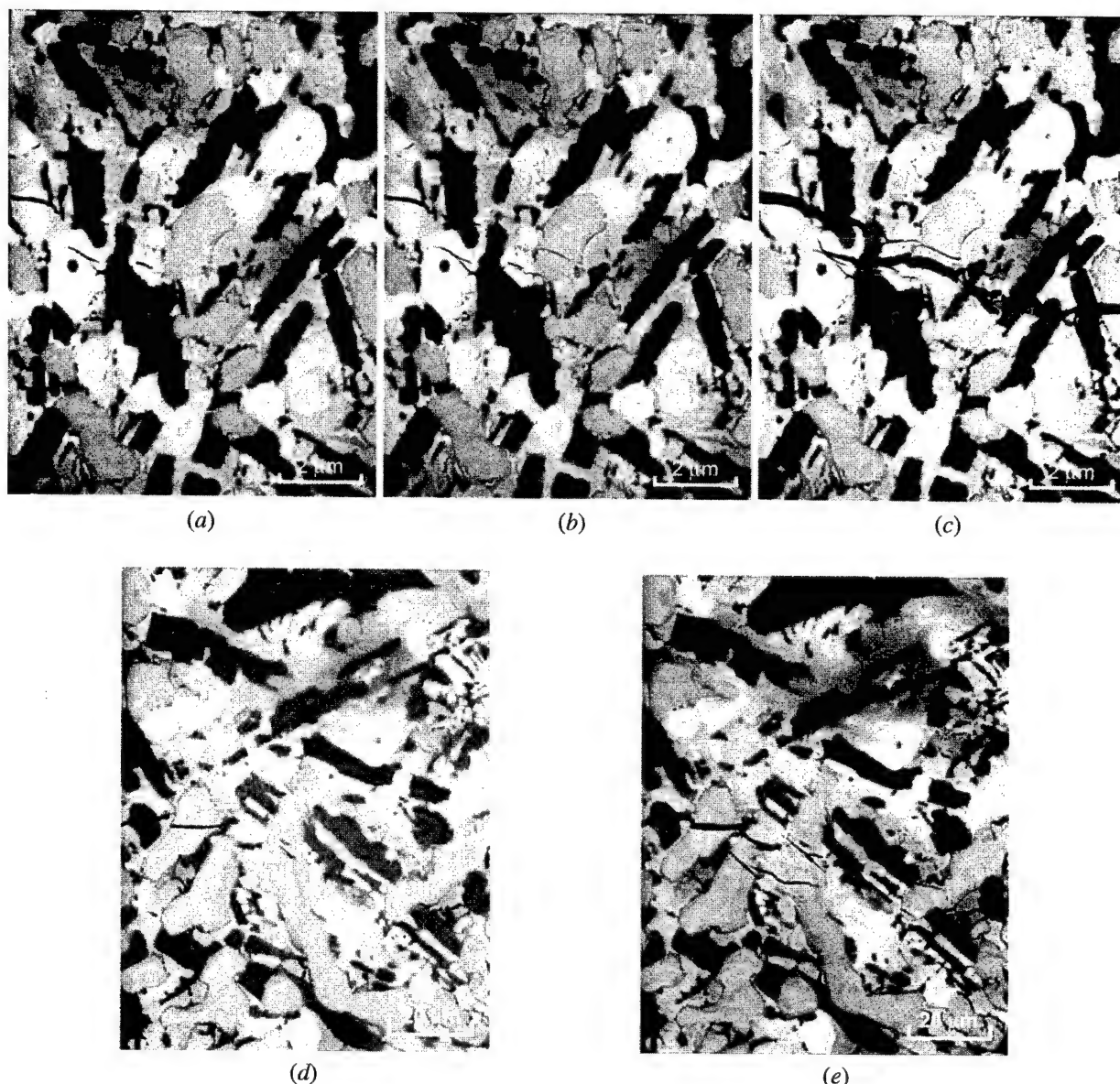


Fig. 11—Near-tip fracture processes observed in as-cast M2: (a) 5 MPa√m, (b) 7 MPa√m, (c) 8 MPa√m, (d) 8 MPa√m, new crack tip, and (e) 8.5 MPa√m. The light phase is (Ti, Nb)<sub>5</sub>Si<sub>3</sub> (D8<sub>g</sub>); the gray phase is (Nb, Ti)<sub>5</sub>Si<sub>3</sub> (D8<sub>1</sub>); and the dark phase is C14 Laves phase. Notch on the left; and crack growth from left to right.

ness of the Nb<sub>ss</sub> phase could not be determined accurately by the indentation technique, because indentation cracks could not be induced. Because of the lack of indent cracks, the deduced fracture-toughness values for the Nb<sub>ss</sub> phase Nb<sub>x</sub> are minimum values, and they are not shown in Figure 15. The experimental data are compared against the empirical fit (dashed line) developed earlier,<sup>[25]</sup> as well as against computed values based on a thermally activated slip model. For elastic-plastic fracture,

$$J_c = J_s + J_p \quad [2]$$

where  $J_s$  and  $J_p$ , the  $J$  integrals contributed by elastic and plastic processes during fracture, respectively, are given by<sup>[17]</sup>

$$J_s = 2\gamma_s \quad [3]$$

and

$$J_p = J_0 \exp\left(-\frac{U_{P-N}b^2}{kT}\right) \quad [4]$$

where  $J_0$  is a constant at a constant  $T$  and  $J_0 = 5 \times 10^4$  J/m<sup>2</sup> for 298 K;  $b$  is the magnitude of the Burgers vector;  $U_{P-N}$  is the Peierls-Nabarro barrier energy;  $k$  is Boltzmann's constant; and  $T$  is the absolute temperature. Equations [3] and [4] can be summed to give Eq. [2], leading to

$$K_c = \sqrt{\frac{E(J_s + J_p)}{(1 - \nu^2)}} \quad [5]$$



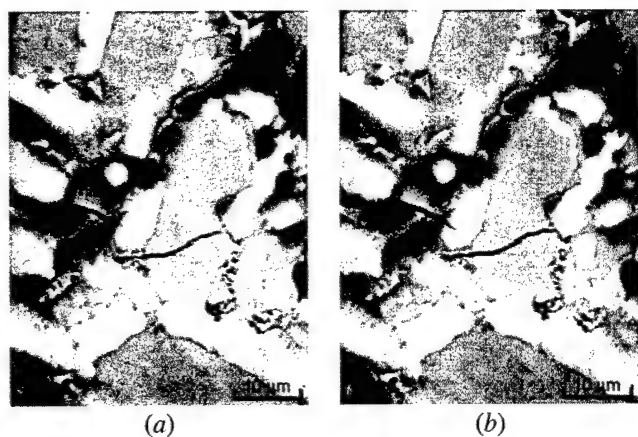


Fig. 12—Crack-tip interactions with  $Nb_{ss}$  particles in as-cast AX: (a) crack-tip trapping by  $Nb_{ss}$  at  $K = 8 \text{ MPa}\sqrt{\text{m}}$ , and (b) crack-tip penetration into an  $Nb_{ss}$  particle at  $K = 9 \text{ MPa}\sqrt{\text{m}}$ . The light phase is  $Nb_{ss}$ ; the gray phase is  $(Nb, Ti)_5Si_3$  (D8<sub>I</sub>); and the dark phase is C14 Laves phase.

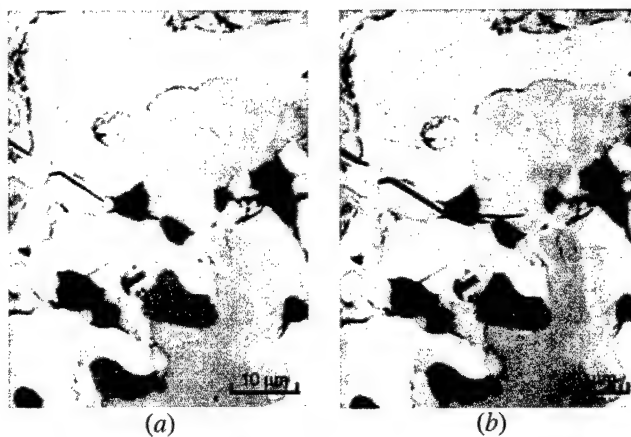


Fig. 13—Crack bridging by  $Nb_{ss}$  particles in heat-treated UES-AX (1350 °C/100 h): (a) bridged crack at  $K = 7 \text{ MPa}\sqrt{\text{m}}$ , and (b) crack extension into Laves and  $Nb_{ss}$  grains as  $K$  increased to  $10 \text{ MPa}\sqrt{\text{m}}$ . The light phase is  $Nb_{ss}$ ; the gray phase is silicide; and the dark phase is C14 Laves phase.

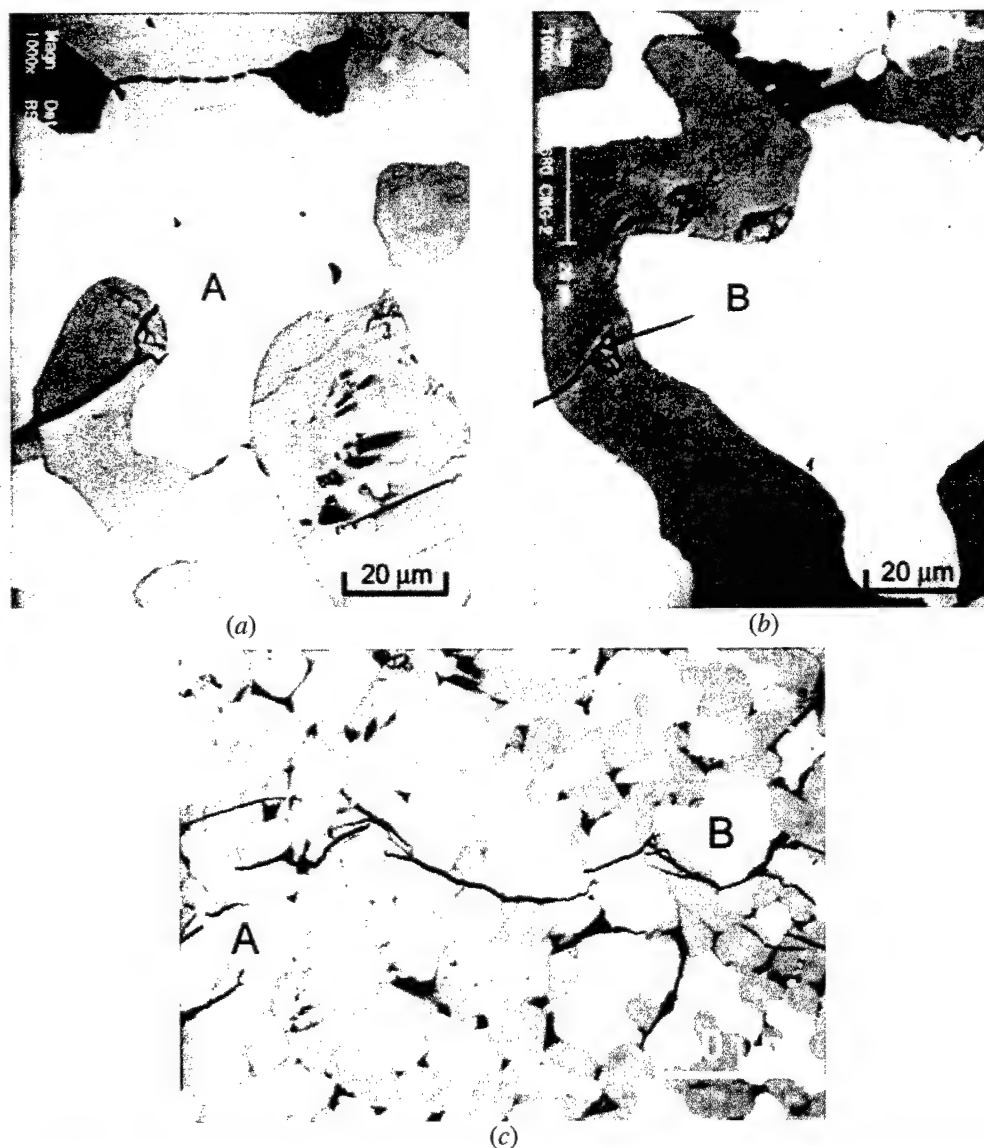


Fig. 14—The crack path follows mostly the silicide phase in the CNG-1B alloy: (a) crack reinitiation in a silicide when the main crack is trapped by an  $Nb_{ss}$  grain at  $K = 6 \text{ MPa}\sqrt{\text{m}}$ , (b) crack deflection around an  $Nb_{ss}$  grain and into silicide phase at  $K = 8 \text{ MPa}\sqrt{\text{m}}$ , and (c) microscopic view of the crack path at  $K = 9 \text{ MPa}\sqrt{\text{m}}$ . Notch on the left. Crack growth from left to right. The light phase is  $Nb_{ss}$ , the gray phase is silicide, and the dark phase is Laves phase.

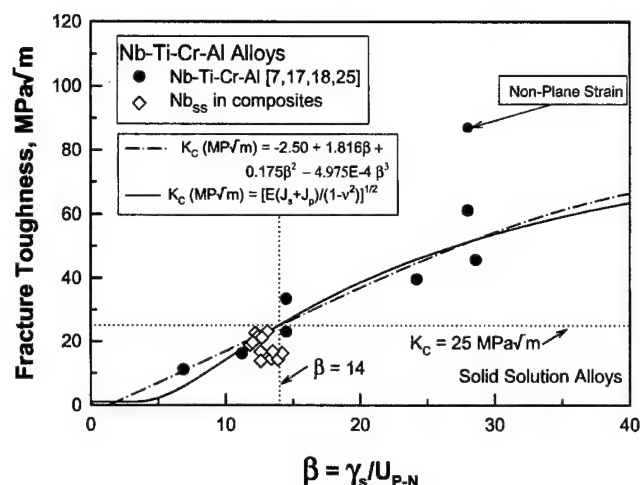


Fig. 15—Fracture toughness ( $K_C$ ) of Nb solid solution alloys as a phase in composites and as a function of the ratio of surface energy,  $\gamma_s$ , to the P-N barrier energy,  $U_{P-N}$ . Empirical fit was from Chan.<sup>[25]</sup>

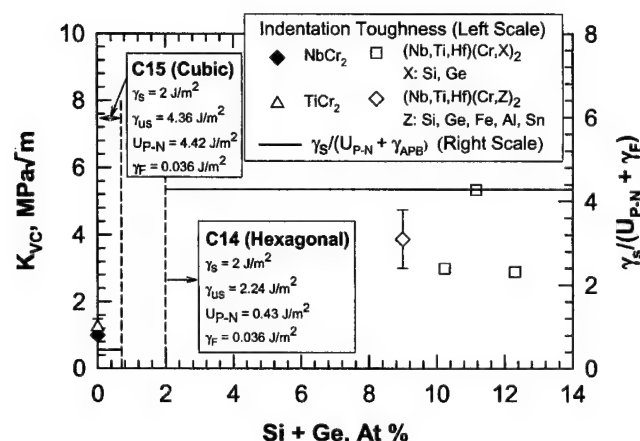


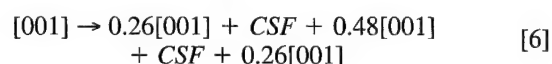
Fig. 16—Fracture toughness, unstable stacking energy ( $\gamma_{us}$ ), P-N barrier energy ( $U_{P-N}$ ), and crystal structure of Laves phase as a function of Si and Ge addition.

for plane-strain fracture in isotropic materials with a Young's modulus, ( $E$ ) and Poisson's ratio, ( $\nu$ ). The solid line in Figure 15 shows the computed  $K_C$  as a function of  $\gamma_s/U_{P-N}$  for Nb<sub>ss</sub> using Eq. [3] through [5] and  $\gamma_s = 2 \text{ J/m}^2$ ,  $J_0 = 5 \times 10^4 \text{ J/m}^2$  and  $b^2/kT = 20$ . Since  $\gamma_s \cong \text{constant}$ ,  $K_C$  varies with  $U_{P-N}$ ; thus, the dependence of  $K_C$  can be rationalized and treated as a manifestation of thermally activated slip.

NbCr<sub>2</sub> has a C15 (cubic) crystal structure and a fracture toughness of about  $1 \text{ MPa}\sqrt{\text{m}}$  at ambient temperature.<sup>[7,8,20]</sup> As shown in Figure 16, a small ( $>2$  at. pct) addition of Si+Ge changes C15 NbCr<sub>2</sub> to C14 (hexagonal), which is normally stable only at elevated temperatures. In addition, the Si and Ge addition improves the fracture toughness of NbCr<sub>2</sub> from  $1 \text{ MPa}\sqrt{\text{m}}$ <sup>[7,8,20]</sup> to about  $2$  to  $5 \text{ MPa}\sqrt{\text{m}}$ . Computations of unstable stacking energy and P-N barrier energy were performed for deformation of C15 by synchroshear<sup>[50]</sup> of a pair of  $1/6 \langle 211 \rangle$  partial dislocations on a  $\{111\}$  plane in C15 and C14.<sup>[51]</sup> These results indicated that  $\gamma_{us} = 4.36 \text{ J/m}^2$  and  $U_{P-N} = 4.42$  for synchroshear in C15.<sup>[51]</sup> In con-

trast,  $\gamma_{us} = 2.24 \text{ J/m}^2$  and  $U_{P-N} = 0.43 \text{ J/m}^2$  for  $\{0001\}1/3 \langle 10\bar{1}0 \rangle$  synchroshear in C14, because of a more favorable ratio of the slip-plane separation to the Burgers vector ( $d/b$ ). The lower values of  $\gamma_{us}$  and  $U_{P-N}$  suggest that dislocation glide or twinning by synchroshear may be easier in the C14 than in the C15 Laves phase. Consequently, a Si or Ge addition to NbCr<sub>2</sub> should improve the fracture resistance when C14 phase is stabilized, as observed experimentally.

Nb<sub>5</sub>Si<sub>3</sub> can exist in either the D8<sub>m</sub> or D8<sub>1</sub> crystal structures; both are bct phases whose deformation mechanisms are still unknown. On the other hand, Ito *et al.*<sup>[52]</sup> identified  $\langle 100 \rangle \{012\}$ ,  $\langle 100 \rangle \{001\}$ ,  $1/2 \langle 111 \rangle \{110\}$ , and  $\langle 110 \rangle \{001\}$  as possible slip systems in Mo<sub>5</sub>SiB<sub>2</sub> (T2 phase, D8<sub>1</sub> structure). Experimental evidence, however, indicates that  $[001](010)$  is the operative slip system in the T2 phase at  $1500^\circ\text{C}$ .<sup>[52]</sup> Because of the complex D8<sub>1</sub> structure, slip in T2 appears to occur through the actions of three fractional  $[001]$  partial dislocations separated by two complex stacking faults (CSFs), according to the dissociation reaction given by<sup>[52]</sup>



which was suggested by Ito *et al.*,<sup>[52]</sup> through a consideration of the overlapping volume encountered by atoms on the slip plane. Taking Eq. [6] as the operative slip mechanism, theoretical calculation indicates that the dislocation dissociation reaction is energetically favorable, and it leads to a significant reduction in both the unstable stacking and P-N barrier energies in Nb<sub>5</sub>Si<sub>3</sub> with the D8<sub>1</sub> crystal structure. Recent computations indicated that the  $\gamma_{us}$  and  $U_{P-N}$  values for  $[001](010)$  slip in Nb<sub>5</sub>Si<sub>3</sub> are  $8.88$  and  $9.81 \text{ J/m}^2$ , respectively.<sup>[51]</sup> In contrast, the  $\gamma_{us}$  and  $U_{P-N}$  values are reduced to  $3.25$  and  $0.01 \text{ J/m}^2$ , respectively, if slip on  $(010)$  is accomplished by three fractional  $[001]$  partial dislocations. An alloying addition that promotes slip by the fractional  $[001]$  partial dislocations should improve the fracture resistance of Nb<sub>5</sub>Si<sub>3</sub>.

The fracture toughness of Nb<sub>5</sub>Si<sub>3</sub> has been found to improve with the additions of Ti. In particular, the fracture toughness of alloyed (Nb,Ti,Hf)<sub>5</sub>(Si,Cr,Ge)<sub>3</sub> silicide appears to increase with increasing Ti additions but decrease with the bond order, as shown in Figure 17(a). Bond order is a measure of the strength of the covalent bond between atoms and is computed on the basis of the overlapping electron population.<sup>[53]</sup> This enhancement of fracture resistance by a Ti addition and its relation to bond order is not well understood. One possible explanation is that the Ti addition promotes the slip by the partial dislocation mechanism, as described in Eq. [6]. Previously, Ito *et al.*<sup>[52]</sup> suggested that the driving force for dislocation dissociation is the need to minimize the overlapping volume of atoms on the slip plane. Ito *et al.*<sup>[52]</sup> demonstrated this point in terms of contours of overlapping volume derived on the basis of a hard-ball model that was used to represent the atomic interference on the slip plane. Since the Ti addition reduces the bond order of Nb<sub>5</sub>Si<sub>3</sub>, the overlapping electron population and, possibly, the overlapping volume are reduced by Ti additions. Such a reduction of the overlapping volume, if proven to occur, could promote the

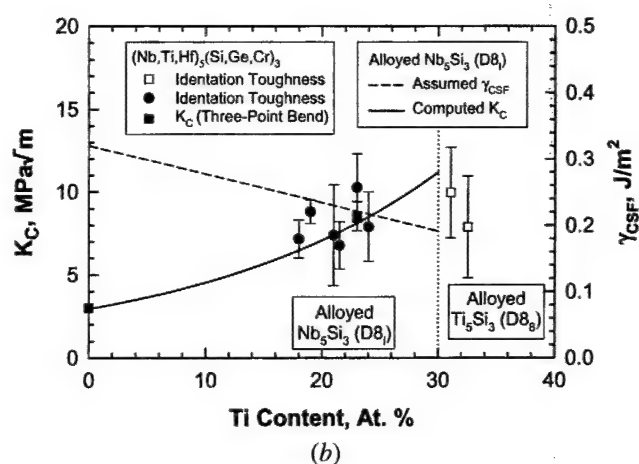
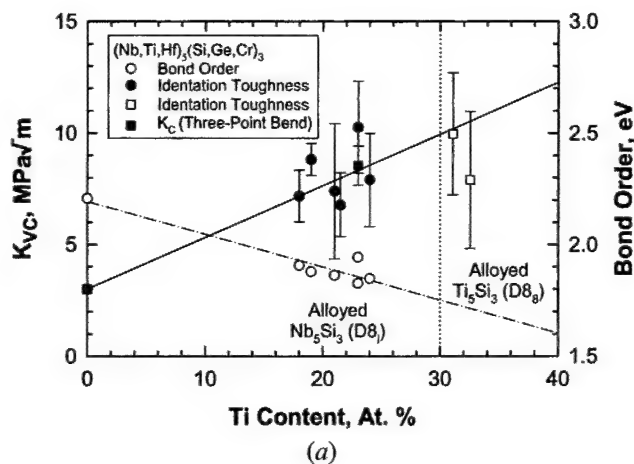


Fig. 17—(a) Fracture toughness (left side) and bond order (right side) of alloyed silicides as a function of Ti content. Trend lines are shown, and (b) computed  $K_{IC}$  compared against experimental data and the complex stacking fault energy,  $\gamma_{CSF}$ , required to fit the fracture model to the experimental data of alloyed  $Nb_5Si_3$ .

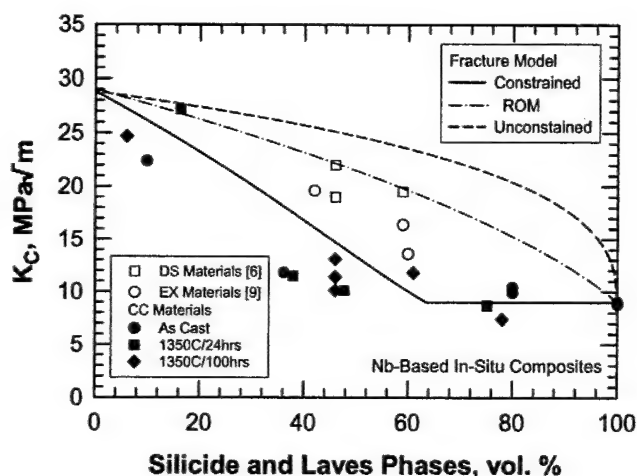


Fig. 18—A comparison of the fracture toughness values of conventionally cast (CC), directionally cast (DS), and extruded (EX) Nb-based *in-situ* composites against model calculations based on crack-tip trapping/bridging with and without plastic constraint, and the rule of mixtures (ROM).

partial-slip process by reducing the unstable stacking energy, the CSF energy, or the P-N barrier energy.

The beneficial effect of a reduced CSF energy on the fracture toughness of the  $(Nb,Ti)_5Si_3$  silicides ( $D8_1$ ) was evaluated by fitting Eq. [4] to the fracture-toughness data by adjusting the CSF energy. The computed  $K_{IC}$  and the deduced CSF energy are shown in Figure 17(b). The computation indicated that the CSF energy required to give the observed fracture toughness is in the range of 0.2 to 0.3 J/m<sup>2</sup>, which is substantially lower than the 0.89 J/m<sup>2</sup> value for the CSFs observed in  $Mo_5SiB_2$ . This reduction of the CSF energy, if proven to occur, would explain the increase of fracture resistance exhibited by  $Nb_5Si_3$  alloyed with Ti additions. Obviously, high-resolution transmission electron microscope studies of the dislocation structure and a determination of the CSF energy in alloyed  $Nb_5Si_3$  are required to verify this hypothesis. The effects of a Ti addition on the lattice parameter, the  $d$  spacing of the possible (or most likely) slip planes, and  $b$  may be determined by XRD, but the necessary analyses of the XRD data have not been performed.

The preceding sections illustrate the importance of compositional design on the fracture resistance of individual phases in the *in-situ* composites. Alloy composition alone, however, is not sufficient to ensure high fracture toughness. The size, shape, and morphology of individual phases are also important factors influencing the fracture resistance of Nb-based *in-situ* composites. Figure 18 shows a comparison of the  $K_{IC}$  values of conventionally cast (CC), directionally cast (DS),<sup>[6]</sup> and extruded (EX) Nb-based *in-situ* composites.<sup>[3,9]</sup> The DS and EX materials exhibit a higher fracture toughness than the CC materials.

The fracture mechanism in the *in-situ* composites involves the formation of microcracks ahead of the main crack. Most of these microcracks are initiated in the Laves phase, which has the lowest fracture toughness among the constituent phases in the microstructure. Once initiated in the Laves phase, the microcracks propagate into the silicide phase. The linkage of the main crack and microcracks, which dictates the observed fracture toughness, often occurs without plastic stretching of the  $Nb_{ss}$  particles. The absence of ductile-phase toughening in the Nb-based *in-situ* composites appears to originate from the phase morphology in the composite microstructure. *In-situ* fracture-toughness testing results, shown in Figure 11 through 14, revealed that the lower fracture toughness exhibited by the CC materials was the consequence of a relatively continuous silicide phase in the microstructure, such that the crack path resided in the silicide and Laves phases. Because of this fracture path, the ductile Nb solid solution was not able to enhance the fracture toughness of the *in-situ* composites. Comparison of the experimental data against the theoretical calculation of a fracture-toughness model<sup>[32]</sup> suggested that the lack of ductile-phase toughening by the Nb solid-solution phase was caused by the high plastic constraint induced by the continuous matrix of silicide and Laves phases. In particular, Figure 18 shows the computed  $K_{IC}$  curves for crack-tip trapping/bridging<sup>[54]</sup> by ductile phase in the *in-situ* composites with (solid curve) and without (dashed curve) plastic constraint acting on the  $Nb_{ss}$  phase, as well as that computed based on the rule of mixtures (ROM). The  $K_{IC}$  curve without plastic constraint and that for the ROM were computed using Eqs. [4] and [12] of Chan and Davidson,<sup>[32]</sup> respectively, while the  $K_{IC}$  curve with

the plastic constraint (solid curve) was computed using Eqs. [10] and [11] of Chan and Davidson.<sup>[32]</sup> For these calculations,  $q = 1$  and  $K_d = 28 \text{ MPa}\sqrt{\text{m}}$  as the average value of the fracture toughness of  $\text{Nb}_{ss}$ . For spherical particles, the intermetallics begin to make contact when their volume percents exceed the theoretical value of  $\approx 72$  pct and the crack can propagate exclusively in the intermetallic phase. For irregular-shaped particles, the intermetallic phase can occur with high contiguity at a lower volume fraction. This appears to be case in the Nb-based *in-situ* composites. The fracture toughness of the *in-situ* composites was essentially identical to that of the silicides when the volume fraction of intermetallics was greater than approximately 60 pct (Figures 7 and 18). At the present time, it is unclear why the DS and EX materials exhibited a higher fracture toughness than the CC materials, but it appears to originate from the lack of contiguity of the intermetallic and the changes in plastic constraint associated with the shape of the  $\text{Nb}_{ss}$  in the DS and EX microstructures.

### C. Computational Design

The observed fracture-toughness values of the *in-situ* composites are not as high as those predicted by the computational design model. The discrepancy can be attributed to several sources. First, the sum of Ti and Hf contents in the  $\text{Nb}_{ss}$  phase apparently has an upper limit, as none was able to exceed 29 pct in the presence of Nb-rich and Ti-rich silicides. In contrast, the Cr content increased to 10 to 14 pct. Previous work has shown that the fracture resistance of  $\text{Nb}_{ss}$  increases with increasing Ti additions,<sup>[17,25]</sup> but decreases with increasing Cr additions;<sup>[17,25]</sup> both have combined in the present composites to limit the fracture toughness of the  $\text{Nb}_{ss}$  phase. Second, the volume fraction of intermetallics is somewhat higher than that expected and assumed in the model. Since the design calculations were based on alloys without Ge, the addition of Ge to the composites appears to have altered the phase boundaries and the phase relations. Third, the silicide phase exhibits a high degree of contiguity, and a continuous path exists in the silicide phase for the crack to follow. As a result, the crack bypassed the more ductile  $\text{Nb}_{ss}$  and resulted in a composite toughness that corresponds to the fracture toughness of the silicide phase ( $8$  to  $10 \text{ MPa}\sqrt{\text{m}}$ ). Fourth, the Laves phase appears to serve as an initiation site where microcracks nucleate (by virtue of its lower fracture toughness) and then propagate into the silicide phase. Finally, a high plastic constraint exists in the  $\text{Nb}_{ss}$  that has prevented ductile-phase toughening from fully developing in the *in-situ* composites with a high intermetallic content. The high plastic constraints were not relaxed by the heat treatments used in this study. It is thought that all of these factors contribute to limit the fracture resistance of the *in-situ* composites and have caused the discrepancy between the experimental results and the model prediction for the unconstrained case.

To improve the fracture resistance of the *in-situ* composites, the volume fraction of the Laves phase should be reduced because of its low fracture toughness, providing that the oxidation resistance is not reduced. Similarly, the Ge addition should be reduced, since it tends to induce the formation of second phases along grain boundaries. More importantly, the microstructural constraint on the  $\text{Nb}_{ss}$  needs

to be reduced either by modifying the size and morphology of the constituent phases or their interface properties. The required microstructural modifications include (1) relatively large and elongated  $\text{Nb}_{ss}$  grains and (2) submicron or nanosized shearable silicide particles that are coherent with  $\text{Nb}_{ss}$ . *In-situ* composites with elongated  $\text{Nb}_{ss}$  particles have been achieved by extrusion<sup>[9]</sup> or directional solidification,<sup>[6]</sup> and improvements in fracture toughness have been made. Previous attempts were successful in reducing the size of Laves phase to the  $1$  to  $2 \mu\text{m}$  range by rapid solidification<sup>[55]</sup> and mechanical alloying<sup>[56]</sup> techniques. To refine the silicides to the nanoscale range may be a difficult task. Alternately, the alloying addition may be used to reduce the interface energy between the  $\text{Nb}_{ss}$  and silicides, in order to facilitate emission of dislocations from the interface or crack penetration into the  $\text{Nb}_{ss}$  particles.

The computational design method was successful in the sense that its predictions were realized in most cases. In particular, the computational model predicted correctly the effects of alloy additions (Ti, Cr, Hf, Al, etc.) and the volume fractions of intermetallics on the fracture resistance of the  $\text{Nb}_{ss}$  phase and the *in-situ* composites, respectively. As discussed in more detail in a separate article,<sup>[34]</sup> the computational model predicted correctly that the oxidation resistance of the  $\text{Nb}_{ss}$  and the *in-situ* composites would not come from the formation of  $\text{SiO}_2$ , but would depend on the Cr content, since Cr-based oxides are likely to form instead of  $\text{SiO}_2$  (Figure 1(b)). However, the computational model was not successful in improving or optimizing the fracture and oxidation resistance at the same time, because of the opposite effects of Ti and Cr additions on constituent properties and the different roles of constituent phases in the composite properties. For example, Ti improves the fracture resistance but reduces the oxidation resistance, while a Cr addition produces the opposite effects. Similarly, a large volume fraction of  $\text{Nb}_{ss}$  improves the fracture resistance but reduces the oxidation resistance, and *vice versa* for a large volume fraction of intermetallics. Because of this, the fracture and oxidation resistance of the *in-situ* composites could not be optimized to meet the property goals for the same microstructure. To overcome these difficulties, a microstructure with fine shearable particles is needed, so that the constraint on  $\text{Nb}_{ss}$  could be relaxed even at high intermetallic contents and  $\text{SiO}_2$  could be induced to form beneath the Cr oxide layers.

## VI. CONCLUSIONS

A computational method was used to design the composition and microstructure of several *in-situ* composites based on the Nb-Ti-Hf-Cr-Si-Ge system, with the objective of achieving balanced properties of creep, oxidation, and fracture resistance. The candidate materials were fabricated and evaluated. This article described the evaluation of the fracture toughness of the constituent phases and the composites of the candidate alloys. The conclusions reached in this study are as follows.

1. An addition of Si and Ge in  $\text{NbCr}_2$  stabilized the C14 and increased the fracture toughness from 1 to 2 to  $5 \text{ MPa}\sqrt{\text{m}}$ . The toughness enhancement may be attributed to a reduction of unstable stacking and P-N barrier energies for slip by synchroshear in the C14 structure.



2. Ti and Hf additions appeared to enhance the fracture toughness of Nb-rich and Ti-rich  $M_5Si_3$  from 2 to 3 to 8 to 10  $MPa\sqrt{m}$ . The toughness enhancement may be attributed to slip by [001] partial dislocations and correlates with increasing fracture toughness with decreasing bond order by increasing Ti and Hf additions.
3. The fracture toughness of the Nb<sub>ss</sub> in the *in-situ* composites is limited to 25 to 30  $MPa\sqrt{m}$ , because the Ti + Hf content is limited to 29 pct and the Cr content can reach as high as 14 pct.
4. The Cr content (10 to 14 at. pct) in the Nb solid-solution phase in the Nb-Ti-Hf-Cr-Si-Ge *in-situ* composites is higher than that ( $\approx 3$  at. pct) expected based on the ternary Nb-Si-Cr phase diagram.
5. A high Cr content (10 to 14 at. pct) and a high plastic constraint in the Nb solid-solution phase is responsible for the relatively low fracture resistance exhibited by the Nb-based *in-situ* composites.
6. The fracture mechanism in Nb-based *in-situ* composites containing a large volume fraction of intermetallics involves the nucleation of microcracks in the Laves phase, propagation of microcracks in the silicide phases, and linkage of the main crack with microcracks without substantial plastic stretching occurring in the Nb<sub>ss</sub> particles.
7. The fracture toughness of the *in-situ* composites decreases with increasing volume fractions of intermetallics phases. Ductile-phase toughening is ineffective in composites containing more than 40 to 50 pct intermetallics, because the crack tends to propagate in the intermetallic phases and bypass the Nb<sub>ss</sub> phase.
8. The fracture toughness of the Nb-based *in-situ* composites is approximately the fracture toughness of the silicide phase when the volume percent of intermetallics exceeds 60 pct.
9. The Vickers indentation technique appears to be a viable tool for characterizing the fracture toughness of the Laves and silicide phases in the Nb-based *in-situ* composites. However, a calibration curve must be developed since the induced tensile stresses acting on the indentation cracks depend on the amounts of inelastic deformation under the indenter.
10. The computational modeling effort was successful in that the predictions of the model with regard to the overall fracture and oxidation properties were essentially realized.

## ACKNOWLEDGMENTS

This work was supported by the Air Force Office of Scientific Research through Contract No. F4962001-C-0016, Dr. Craig S. Hartley, Program Manager. The authors are thankful to Drs. Melvin Jackson and J.C. Zhao, General Electric Global Research Laboratories (Schenectady, NY), for supplying alloy compositions and previously unpublished phase diagrams, and to Dr. Young-Wom Kim, UES (Dayton, OH), for supplying the UES-AX and CNG-1B materials. The technical assistance of F. Campbell, J. Spencer, and B. Chapa, and the clerical assistance of Ms. L. Salas and Ms. P. Soriano, all of Southwest Research Institute, is appreciated.

## REFERENCES

1. D.L. Anton and D.M. Shah: *MRS Symp. Proc.*, 1990, vol. 194, pp. 175-82.
2. R.M. Nekkanti and D.M. Dimiduk: *MRS Symp. Proc.*, 1990, vol. 194, pp. 175-82.
3. M.G. Mendiratta and D.M. Dimiduk: *Metall. Trans. A*, 1993, vol. 24A, pp. 501-04.
4. P.R. Subramanian, M.G. Mendiratta, and D.M. Dimiduk: *JOM*, 1996, vol. 48, pp. 33-38.
5. M.R. Jackson, B.P. Bewlay, R.G. Rowe, D.W. Skelly, and H.A. Lipsitt: *JOM*, 1996, vol. 48, pp. 39-44.
6. B.P. Bewlay, M.R. Jackson, and H.A. Lipsitt: *Metall. Mater. Trans. A*, 1996, vol. 27A, pp. 3801-08.
7. D.L. Davidson, K.S. Chan, and D.L. Anton: *Metall. Mater. Trans. A*, 1996, vol. 27A, pp. 3007-18.
8. K.S. Chan and D.L. Davidson: *JOM*, 1996, vol. 48(9), pp. 62-68.
9. P.R. Subramanian, M.G. Mendiratta, D.M. Dimiduk, and M.A. Stucke: *Mater. Sci. Eng.*, 1997, vols. A239-A240, pp. 1-13.
10. H.A. Lipsitt, M. Blackburn, and D.M. Dimiduk: in *Intermetallic Compounds—Principles and Practice—Vol. 3*, J. H. Westbrook and R.L. Fleischer, eds., John Wiley, New York, NY, 2002, pp. 471-99.
11. B.P. Bewlay and M.R. Jackson: in *Comprehensive Composite Materials*, A. Kelly and C. Zweben, eds. vol. 3, *Metal Matrix Composites*, T.W. Clyne, ed., Elsevier, New York, NY, 2000, vol. 3, pp. 579-613.
12. J.-C. Zhao, B.P. Bewlay, M.R. Jackson, and L.A. Peluso: in *Structural Intermetallics 2001*, K.J. Hemker, D.M. Dimiduk, H. Clemens, R. Darolia, H. Inui, J.M. Larsen, V.K. Sikka, M. Thomas, and J.D. Whittenberger, eds. TMS, Warrendale, PA, 2001, pp. 483-91; also J.-C. Zhao: GE CR&D, Schenectady, NY, private communication, 2001.
13. P.R. Subramanian, M.G. Mendiratta, and D.M. Dimiduk: *MRS Symp. Proc.*, 1994, vol. 322, pp. 491-502.
14. B.P. Bewlay, M.R. Jackson, W.J. Reeder, and H.A. Lipsitt: *MRS Symp. Proc.*, 1995, vol. 364, pp. 943-48.
15. J.D. Rigney, P.M. Singh, and J.J. Lewandowski: *JOM*, 1992, vol. 44(8), pp. 36-41.
16. J. Kajuch, J. Short, and J.J. Lewandowski: *Acta Metall. Mater.*, 1995, vol. 43, pp. 1955-67.
17. K.S. Chan and D.L. Davidson: *Metall. Mater. Trans. A*, 1999, vol. 30A, pp. 925-39.
18. D.L. Davidson and K.S. Chan: *Metall. Mater. Trans. A*, 1999, vol. 30A, pp. 2007-18.
19. K.S. Chan: *Mater. Sci. Eng.*, 2002, vols. A329-A331, pp. 513-22.
20. D.J. Thomas, K.A. Nibur, K.C. Chen, J.C. Cooley, L.B. Dauelsberg, W.L. Hults, and P.G. Kotula: *Mater. Sci. Eng.*, 2002, vols. A329-A331, pp. 408-15.
21. D. Farkas, S.J. Zhou, C. Vacilhe, B. Mutasa, and J. Panova: *J. Mater. Res.*, 1977, vol. 12, pp. 93-99.
22. D. Farkas: *Mater. Sci. Eng.*, 1998, vol. A249, pp. 249-58.
23. U.V. Waghmare, E. Kaxiras, V.V. Bulatov, and M.S. Duesberry: *Modelling Simul. Mater. Sci. Eng.*, 1998, vol. 6, pp. 493-506.
24. J.R. Rice: *J. Mech. Phys. Solids*, 1992, vol. 40, pp. 239-71.
25. K.S. Chan: *Metall. Mater. Trans. A*, 2001, vol. 32A, pp. 2475-87.
26. K.S. Chan: *Mechanisms and Mechanics of Fracture: The John F. Knott Symp.* W.O. Soboyejo, J.J. Lewandowski, and R.O. Ritchie, eds., TMS, Warrendale, PA, 2002, pp. 143-48.
27. P.B. Hirsch and S.G. Roberts: *Phil. Mag. A*, 1991, vol. 64, pp. 55-80.
28. S.G. Roberts and A.S. Booth: *Acta Mater.*, 1997, vol. 45, pp. 1045-53.
29. P.B. Hirsch and S.G. Roberts: in *Cleavage Fracture, Proc. George R. Irwin Symp.*, Kwai S. Chan, ed., TMS, Warrendale, PA, 1997, pp. 137-45.
30. R.E. Peierls: *Proc. Phys. Soc.*, 1940, vol. 52, pp. 34-37.
31. F.R.N. Nabarro: *Proc. Phys. Soc.*, 1947, vol. 59, pp. 236-394.
32. K.S. Chan and D.L. Davidson: *Metall. Mater. Trans. A*, 2001, vol. 32A, pp. 2717-27.
33. K.S. Chan: *Mater. Sci. Eng.*, 2002, vol. A337, pp. 59-66.
34. K.S. Chan: Southwest Research Institute, San Antonio, TX, unpublished research, 2003.
35. M.R. Jackson: General Electric Global Research Laboratories, Schenectady, NY, unpublished research and private communications, 1999.
36. J.N. Wang: *Mater. Sci. Eng. A*, 1996, vol. A206, pp. 259-69.
37. J.N. Wang: *Acta Mater.*, 1996, vol. 44, pp. 1541-46.

38. G. Wang, B. Gleeson, and D.L. Douglass: *Oxid. Met.*, 1991, vol. 35, pp. 333-48.
39. Y.-W. Kim: UES, Inc., Dayton, OH, unpublished research and private communications, 2000.
40. *Annual Book of ASTM Standards*, Vol. 03.01, ASTM E39-90, ASTM, Philadelphia, PA, 1995, pp. 412-42.
41. D.L. Davidson and A. Nagy: *J. Phys. E*, 1978, vol. 11, pp. 207-10.
42. G.R. Anstis, P. Chantikul, B.R. Lawn, and D.B. Marshall: *J. Am. Ceram. Soc.*, 1981, vol. 64, pp. 533-38.
43. P. Chantikul, G.R. Anstis, B.R. Lawn, and D.B. Marshall: *J. Am. Ceram. Soc.*, 1981, vol. 64, pp. 539-43.
44. B.R. Lawn, A.G. Evans, and D.B. Marshall: *J. Am. Ceram. Soc.*, 1980, vol. 63, pp. 574-81.
45. S. Suresh: *Fatigue of Materials*, Cambridge University Press, Cambridge, U. K. 1991, pp. 283-87.
46. J.R. Brockenbrough and S. Suresh: *J. Mech. Phys. Solids*, 1987, vol. 35, pp. 721-42.
47. S. Suresh: in *Modeling of Plastic Deformation and Its Engineering Applications*, 13th Risø Int. Symp. on Materials Science, S.I. Andersen, J.B. Bilde-Sørensen, N. Hansen, D. Juul Jensen, T. Leffers, H. Lilholt, T. Lorentzen, O.B. Pedersen, and B. Ralph, eds., Risø National Laboratory, Roskilde, Denmark, 1992, pp. 111-24.
48. Joint Committee on Powder Diffraction Files, International Center for Diffraction Data, Swarthmore, PA, 1992.
49. M.G. Mendiratta: UES, Dayton, OH, private communication, 2001.
50. P.M. Hazzledine, K.S. Kumar, D.B. Miracle, and A.G. Jackson: *MRS Symp. Proc.*, 1993, vol. 288, pp. 591-96.
51. K.S. Chan: *Proc. Thermec 2003, Mater. Science Forum*, 2003, in press; also Southwest Research Institute, San Antonio, TX, unpublished results, 2003.
52. K. Ito, K. Ihara, K. Tanaka, M. Fujikura, and M. Yamaguchi: *Intermetallics*, 2001, vol. 9, pp. 591-602.
53. Y. Harada, M. Morinaga, J.I. Saito, and Y. Takagi: *J. Phys: Condens. Matter.*, 1997, vol. 9, pp. 8011-30.
54. A.F. Bower and M. Ortiz: *J. Mech. Phys. Solids*, 1991, vol. 39, pp. 815-58.
55. K.S. Chan, D.L. Davidson, and D.L. Anton: *Metall. Mater. Trans. A*, 1997, vol. 28A, pp. 1797-808.
56. D.L. Davidson and K.S. Chan: *Metall. Mater. Trans. A*, 2002, vol. 33A, pp. 401-16.

## **APPENDIX 2**

### **“Relationships of Fracture Toughness and Dislocation Mobility in Intermetallics”**

**Kwai S. Chan**

**Metallurgical and Materials Transactions A  
Volume 34A, (2003) pp. 2315-2328**

**October 2003**

Reprinted with permission from  
*Metallurgical and Materials Transactions A*, Pittsburgh, PA

# Relationships of Fracture Toughness and Dislocation Mobility in Intermetallics

KWAI S. CHAN

An analytical method has been developed and used to compute the Peierls–Nabarro (P–N) barrier energy,  $U_{P-N}$ , for relevant slip systems in several intermetallics, including NiAl, FeAl, Nb–Ti–Al (B2), Ni<sub>3</sub>Al (L1<sub>2</sub>), TiAl (L1<sub>0</sub>), TiCr<sub>2</sub>, NbCr<sub>2</sub> (C14, C15), Nb<sub>5</sub>Si<sub>3</sub> (D8<sub>l</sub>), Mo<sub>5</sub>SiB<sub>2</sub> (D8<sub>l</sub>), and Mo<sub>5</sub>Si<sub>3</sub> (D8<sub>m</sub>). The P–N barrier energy and a generalized fault energy,  $\gamma_F$ , are combined and used as a measure of dislocation mobility. Furthermore, a fracture model has been developed to describe the process of thermally activated dislocations moving away from the crack tip and to predict the corresponding fracture resistance. A ductility index defined in terms of the ratio of  $\gamma_s/(U_{P-N} + \gamma_F)$ , where  $\gamma_s$  is the surface energy, is used to correlate with the fracture toughness,  $K_{IC}$ , of individual intermetallics. The correlation indicates that fracture toughness increases with increasing values of  $\gamma_s/(U_{P-N} + \gamma_F)$ , in accordance with the fracture model formulated based on thermally activated slip. The use of the fracture model for predicting the effects of slip behavior, temperature, and alloy additions on fracture resistance is demonstrated for selected intermetallics including NiAl, TiAl, Laves phase, and Nb<sub>5</sub>Si<sub>3</sub>.

## I. INTRODUCTION

THERE has been considerable interest in developing new structural intermetallics for high-temperature applications.<sup>[1–11]</sup> Substantial efforts have been made to develop a fundamental understanding of the effects of alloy additions on the deformation and fracture mechanisms. Despite many new alloy developments, inadequate fracture resistance at ambient temperature remains one of the major obstacles for widespread applications of intermetallic alloys or *in-situ* composites in fracture critical components. Many intermetallics remain brittle because the relationships between deformation mechanisms and fracture resistance are poorly understood. Alloy additions to toughen brittle intermetallics have largely been explored by trial and error, mostly through empirical means that are labor-intensive and time-consuming. As a result, there has been an increasing trend to use computer-assisted approaches or computation-based methods to accelerate alloy development.<sup>[12–17]</sup>

Brittle-to-ductile fracture transition is generally considered the result of a competition between cleavage fracture and emission of dislocation from the crack tip. The propensity to cleavage fracture is often measured in terms of the surface energy,  $\gamma_s$ . In contrast, dislocation emission from the crack tip can be controlled by the nucleation of dislocations from the crack tip<sup>[18]</sup> (Figures 1(a) and (b)) or the mobility of dislocations<sup>[12,13,19,20]</sup> moving away from the dislocation nucleation sites either at the crack tip or other nontip sources (Figures 1(b) and (c)). The propensity of crack-tip dislocation nucleation can be described in terms of the unstable stacking energy ( $\gamma_{us}$ )<sup>[18]</sup> (Figure 1(b)). On the other hand, dislocation mobility is represented in terms of the Peierls–Nabarro (P–N) barrier energy,<sup>[21,22]</sup>  $U_{P-N}$ , and the stacking fault energy,  $\gamma_F$  (Figure 1(d)). More importantly,  $\gamma_{us}$  and  $U_{P-N}$  are related through the lattice phase angle

( $\psi$ ),<sup>[12,13]</sup> which is a measure of the distortion in the periodic lattice due to the presence of the dislocation and is defined in terms of the elastic constants, Burgers vector, and slip plane spacing.

Two useful auxiliary parameters have emerged from  $\gamma_{us}$  and  $U_{P-N}$ : (1)  $U_{P-N}/\gamma_{us}$  and (2)  $\gamma_s/U_{P-N}$ , where  $\gamma_s$  is the surface energy. The ratio of  $U_{P-N}/\gamma_{us}$  is a measure of dislocation mobility relative to dislocation nucleation, while the  $\gamma_s/U_{P-N}$  ratio is a measure of the material's propensity to cleavage fracture relative to dislocation mobility moving away from the crack tip. Both  $U_{P-N}/\gamma_{us}$  and  $\gamma_s/U_{P-N}$  are functions of the lattice phase angle only and depend solely on elastic constants, crystallography, and the active slip system.<sup>[23]</sup> Theoretical calculations indicated that the  $U_{P-N}/\gamma_{us}$  ratio is large for brittle materials but is small for ductile materials, while  $\gamma_s/U_{P-N}$  is small for brittle materials but is large for ductile materials. Thus, a high dislocation mobility manifested as a low P–N barrier energy is essential in promoting a brittle-to-ductile fracture transition.

For metallic alloys, the  $\gamma_s/U_{P-N}$  ratio can be correlated to fracture toughness and tensile ductility.<sup>[12,13]</sup> In particular, the fracture toughness and tensile ductility of metallic alloys increase with increasing  $\gamma_s/U_{P-N}$  ratio; thus, the  $\gamma_s/U_{P-N}$  ratio can be considered as a ductility index. In addition, the tensile ductility and fracture toughness of a metallic alloy can be improved by alloy additions that increase the lattice phase angle. In contrast, the tensile ductility and fracture toughness are both reduced when an alloy addition decreases the lattice phase angle. Alloy addition causes small changes on the elastic constants, the Burgers vector, the lattice spacing, the lattice phase angle, and the unstable stacking energy, but it has significant effects on the P–N barrier energy because  $U_{P-N}$  depends inversely on  $\sinh 2\psi$ .<sup>[12]</sup> This new discovery provides an avenue for designing alloy addition to improve the fracture resistance of brittle materials by increasing the lattice phase angle, which in turn reduces the P–N barrier energy and promotes dislocation movement away from the crack tip.<sup>[23]</sup> This approach has been demonstrated for toughening Nb solid solution alloys through Ti addition.<sup>[12]</sup> This computational approach, however,

KWAI S. CHAN, Institute Scientist, is with the Southwest Research Institute®, San Antonio, TX 78238-5166. Contact e-mail: kchan@swri.edu  
Manuscript submitted January 27, 2003.



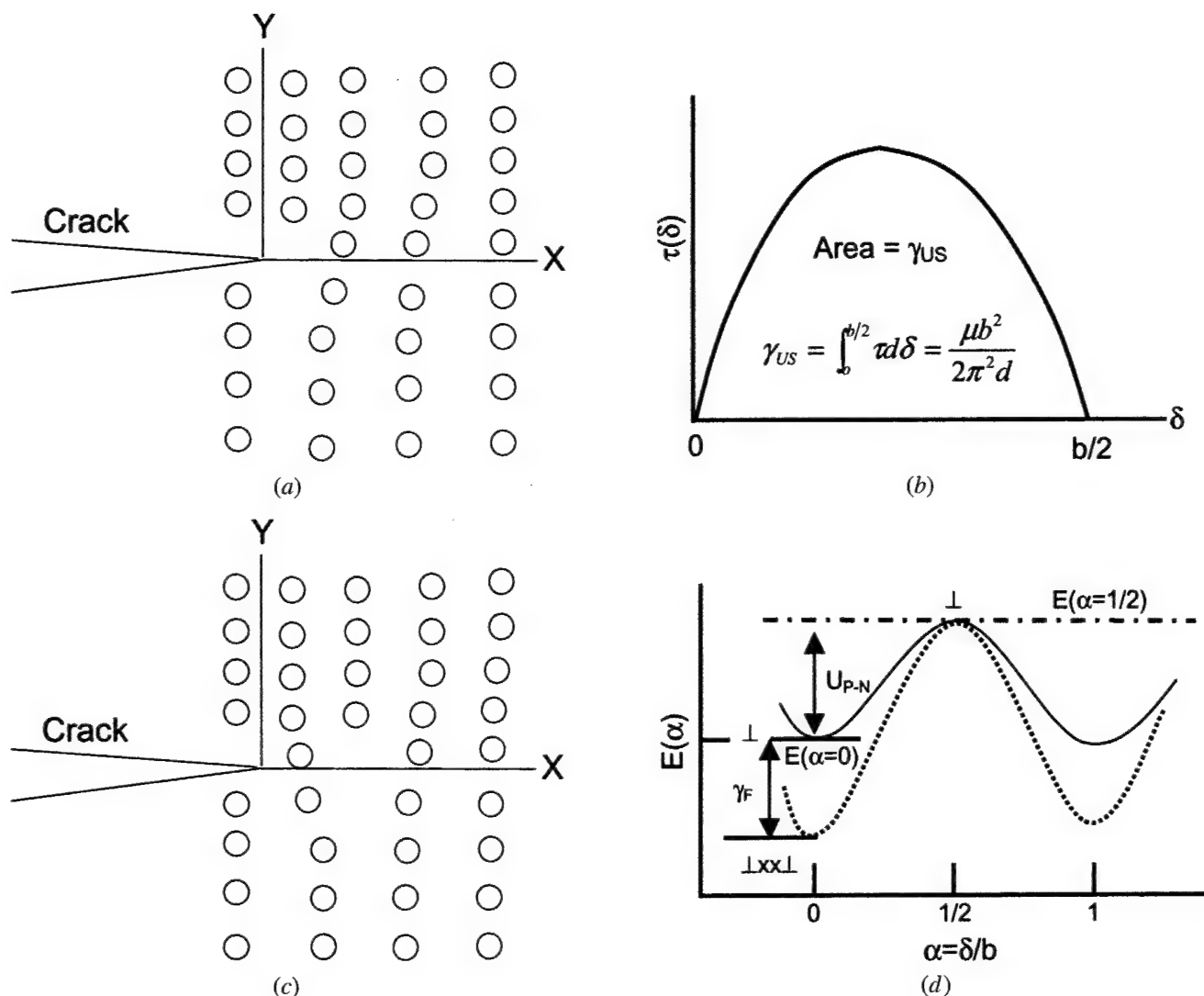


Fig. 1—Schematics of the dislocation emission process at a crack tip: (a) nucleation of a dislocation from the crack tip; (b) dislocation moving away from a crack tip; (c) the unstable stacking energy,  $\gamma_{us}$ , required to nucleate a dislocation at the crack tip; and (d) the P-N barrier energy,  $U_{P-N}$ , and the generalized stacking fault energy,  $\gamma_F$ , that a dislocation with an unspecified fault must overcome before it can move away from the crack tip.

is currently limited to bcc materials because of the lack of a method for computing the P-N barrier energy. Consequently, there is a lack of a means for identifying suitable alloying additions that toughen intermetallics.

In this article, we present the formulation of a fracture model that relates fracture toughness to dislocation mobility in intermetallics. First, we report an analytical method for computing the P-N barrier energy for intermetallics. The pertinent parameter for describing dislocation mobility in ordered intermetallics is shown to be  $U_{P-N} + \gamma_F$ , where  $\gamma_F$  is the energy of a generalized fault<sup>[24]</sup> that can be a stacking fault, a superlattice stacking fault, or an antiphase boundary. Second, a relationship between fracture toughness and  $\gamma_s/(U_{P-N} + \gamma_F)$  is then developed on the basis of thermal activation of slip at the crack tip. A correlation between experimental data of fracture toughness and the ratio of  $\gamma_s/(U_{P-N} + \gamma_F)$  is established for various intermetallics and compared against model calculations. Finally, the possible use of the fracture model and a ductility index, defined as  $\gamma_s/(U_{P-N} + \gamma_F)$ , for selecting alloy

additions to improve the fracture resistance of intermetallics alloys is illustrated and evaluated against experimental data from the literature.

## II. COMPUTATION OF THE P-N BARRIER ENERGY

### A. Perfect Dislocations

The energy required to move a perfect dislocation in the periodic lattice by a Burgers vector is the P-N barrier energy,  $U_{P-N}$ , and it can be computed as<sup>[12,23-26]</sup>

$$U_{P-N} = E(\alpha = 1/2) - E(\alpha = 0) \quad [1]$$

where  $E(\alpha)$  is the misfit energy of the dislocation and  $\alpha$  is displacement,  $\delta$ , normalized by the magnitude of the Burgers vector,  $b$ . For isotropic materials, the unstable stacking energy,  $\gamma_{us}$ , can be expressed in terms of the shear modulus,

$\mu_{\text{slip}}$ , in the slip direction, Burgers vector, and the slipband spacing ( $d$ ), as given by<sup>[18]</sup>

$$\gamma_{us} = \frac{\mu_{\text{slip}} b^2}{2\pi^2 d} \quad [2]$$

and the P-N barrier energy is related to the unstable stacking energy according to<sup>[12]</sup>

$$U_{\text{P-N}} = \frac{8\pi^2 \gamma_{us}}{\sinh 2\psi} \quad [3]$$

with

$$\psi = \frac{\pi \kappa d}{cb} \quad [4]$$

where  $\psi$  is the lattice phase angle that represents the amount of distortion in the periodic lattice due to the presence of the dislocation,  $\kappa$  is the dislocation line energy factor,<sup>[27]</sup> and

$$c = \frac{1}{3} (C_{11} - C_{12} + C_{44}) \quad [5]$$

where  $C_{ij}$  are elastic constants. For edge and screw dislocations in an isotropic material,  $\kappa/c = 1/(1 - \nu)$  and  $\kappa/c = 1$ , respectively, where  $\nu$  is Poisson's ratio. Equations [3] and [4] are applicable for slip in various crystal structures as long as the appropriate ratio of the slip plane spacing ( $d$ ) and the magnitude of the Burgers vector ( $b$ ) is used.<sup>[26]</sup>

### B. Partial Dislocations

A pair of partial dislocations separated by a generalized fault is considered here. The generalized fault can be a stacking fault, antiphase boundary, superlattice, or complex stacking fault. For this pair of partial dislocations, the misfit energy,  $E'(\alpha)$ , at  $\alpha = 0$  is reduced by the fault energy  $\gamma_F$ ,<sup>[24]</sup> leading to

$$E'(0) = E(\alpha = 0) - \gamma_F \quad [6]$$

and

$$E'(\alpha = 1/2) = E(\alpha = 1/2) \quad [7]$$

when the two partial dislocations recombine into a perfect dislocation. The difference between  $E'(\alpha = 1/2)$  and  $E'(\alpha = 0)$  gives the P-N barrier energy,  $U'_{\text{P-N}}$ , for the pair of partial dislocations; i.e.,

$$U'_{\text{P-N}} = E'(\alpha = 1/2) - E'(\alpha = 0) \quad [8]$$

which can be combined with Eq. [6] to give

$$U'_{\text{P-N}} = U_{\text{P-N}} + \gamma_F \quad [9]$$

and

$$U'_{\text{P-N}} = \frac{8\pi^2 \gamma_{us}}{\sinh 2\psi} + \gamma_F \quad [10]$$

after Eq. [3] is combined with Eq. [9]. For a pair of partial dislocations ( $i = 1$  and  $2$ ),

$$\gamma_{us} = \frac{\mu_{\text{slip}}}{2\pi^2 d} \sum_{i=1}^2 b_i^2 \quad [11]$$

and

$$\psi = \psi_i = \frac{\pi \kappa d}{cb_i} \quad [12]$$

where  $b_i$  is the magnitude of the Burgers vector of the partial dislocations.

## III. FRACTURE RESISTANCE AND DISLOCATION MOBILITY

For a crack tip under small-scale yielding, the  $J$  integral at fracture,  $J_c$ , can be considered to be comprised of an elastic term,  $J_s$ , and a plastic term,  $J_D$ , as given by<sup>[28]</sup>

$$J_c = J_s + J_D \quad [13]$$

where  $J_s = 2\gamma_s$  is the surface energy and  $J_D$  is the plastic work expanded per unit area of crack extension. By considering a counterclockwise contour around the crack-tip surface, it has been shown by Rice that<sup>[29]</sup>

$$J_D = \sigma \varepsilon h \quad [14]$$

where  $\sigma$  is the stress in the process zone,  $\varepsilon$  is the crack-tip strain, and  $h$  is the size of the process zone, which is the region of intense deformation surrounding the crack tip.

From the theory of thermally activated dislocation motion, the plastic strain rate for material being deformed at the crack tip is<sup>[30]</sup>

$$\dot{\gamma} = \dot{\gamma}_0 e^{-\Delta G/kT} \quad [15]$$

$$\Delta G = \Delta F - \nu^* \tau \quad [16]$$

where  $\Delta F$  is the energy of the intrinsic barrier to dislocation motion, which for most metals is taken to be the P-N barrier energy;  $\tau$  is the applied shear stress;  $\nu^*$  is the activation volume;  $k$  is Boltzmann's constant; and  $T$  is absolute temperature. The pre-exponential factor is<sup>[30]</sup>

$$\dot{\gamma}_0 = NA^* b \nu' \quad [17]$$

where  $N$  = number of points per unit volume where activation is occurring,  $A^*$  = area swept out by the activated dislocation,  $b$  = Burgers vector, and  $\nu'$  = the attempt frequency for dislocation activation, which is proportional to the Debye frequency. The activation volume is given by  $\nu^* = b\ell x^*$ , where  $\ell$  is the length of the dislocation line, and  $x^*$  is the activation distance. If  $\tau = \tau(t)$  or  $x = x(t)$ , then Eq. [15] can be integrated, giving<sup>[31]</sup>

$$\gamma = (\dot{\gamma}_0 kTt/\tau b x^*) e^{-\frac{\Delta F - \nu^* \tau}{kT}} \quad [18]$$

Combining Eqs. [14] and [18] with  $\sigma = \sqrt{3}\tau$  and  $\varepsilon = \gamma/\sqrt{3}$  gives for the fracture toughness

$$J_D = J_0 e^{-\frac{\Delta F - \nu^* \tau}{kT}} \quad [19]$$

with

$$J_0 = \frac{\dot{\gamma}_0 kTth}{b\ell x^*} \quad [20]$$

From Eq. [19], it is obvious that  $J_D$  is strongly influenced by the energy,  $\Delta F$ , of the intrinsic barrier. An intrinsic barrier

that controls dislocation nucleation and mobility is considered here. Therefore, we take

$$\Delta F = \gamma_{us} + U_{P-N} + \gamma_F \quad [21]$$

for a pair of partial dislocations separated by a generalized fault  $\gamma_F$ ; the plastic dissipation resulting from their slip can be expressed as

$$J_D = J_0 \exp \left[ -\frac{A^*[(U_{P-N} + \gamma_F) + (\gamma_{us} - \tau x^*)]}{kT} \right] \quad [22]$$

after Eq. [21] is combined with Eq. [19]. Equation [22] can be further simplified by recognizing that  $\tau x^* = \gamma_{us}$  at the onset of dislocation nucleation. Assuming that the external stress assists in dislocation nucleation only and the motion of the dislocation away from the crack tip is thermally assisted, Eq. [22] can be simplified to

$$J_D = J_0 \exp \left[ -\frac{A^*(U_{P-N} + \gamma_F)}{kT} \right] \quad [23]$$

by invoking  $\gamma_{us} = \tau x^*$  at the onset of dislocation nucleation. If the external stress field is insufficient of nucleating a dislocation (at either the crack tip or at other nontip sites elsewhere in the process zone) and thermal activation is required, Eq. [23] still applies but the apparent fault energy, defined as  $\gamma'_F = \gamma_F + \gamma_{us} - \tau x^*$ , would be higher than the actual stacking fault since  $\gamma_{us} - \tau x^* > 0$ .

The density of all possible activated sites,  $n_a$ , is given by

$$n_a = \frac{\dot{\gamma}_0 t}{A'} \left( \frac{h}{\ell} \right) \quad [24]$$

which leads to a dislocation density,  $\rho$ , given by

$$\rho = \frac{n_a}{\pi h^2} \quad [25]$$

when all possible sites are activated. For the P-N barrier, the activation distance, area, and volume are  $b$ ,  $b^2$ , and  $b^3$  (to be demonstrated in Section IV). Thus,  $x^* = b$ ,  $A^* = b^2$ , and  $v^* = b^3$ . Substituting these values into Eqs. [23] through [25] and combining the various terms leads one to

$$J_D = J_0 \exp \left[ -\frac{b^2}{kT} (U_{P-N} + \gamma_F) \right] \quad [26]$$

with

$$J_0 = \left( \frac{kT}{b^2} \right) \rho \pi h^2 \quad [27]$$

which can be interpreted as the maximum plastic dissipation attained per unit area when all activated sites are activated and the P-N barriers are overcome.

Equation [26] can be related to the stress-intensity factor,  $K_C$ , at fracture, leading to<sup>[28]</sup>

$$K_C = \sqrt{\frac{E(J_s + J_D)}{(1 - \nu^2)}} \quad [28]$$

for plane-strain fracture of isotropic materials with Young's modulus,  $E$ , and Poisson's ratio,  $\nu$ .

## IV. MODEL APPLICATIONS

The computational models were applied to compute the unstable stacking energy, P-N barrier energy, and, in some cases, the surface energy for a number of intermetallics, including B2 Nb-Ti-Al alloys, aluminides, silicides, and Laves phases. Computation of the P-N barrier energy, unstable stacking energy, and surface energy required knowledge of the elastic constants ( $C_{ij}$ ), the magnitude of the Burgers vector, and the slip plane spacing of the active slip system, as well as the character (edge, screw, or mixed) of the dislocation. With the exception of the B2 Nb-Ti-Al alloys, isotropic elasticity was assumed for all intermetallics. In all cases, edge dislocations were assumed in the P-N barrier energy calculation. Experimental values of the antiphase boundary or stacking fault energy were used to compute the ratio of  $\gamma_s/(U_{P-N} + \gamma_{APB})$ . These results were correlated with fracture toughness data from the literature and the observed correlation compared against predictions of the fracture model. Details of the model computation and the results are presented below for individual types of intermetallics.

### A. B2 Nb-Ti-Al Alloys

The computational model reported earlier was applied to compute the surface energy, unstable stacking energy, and P-N barrier energy for a number of B2 alloys of the Nb-Ti-Al system.<sup>[32]</sup> The input to these calculations was the alloy composition. Based on the number of  $d + s$  electrons/atom for the specified alloy composition, the analytical model computed the elastic moduli, the P-N barrier energy, the surface energy, and then the energy ratio. For these alloys, P-N calculations were performed for (110)[111] slip by edge dislocations. Experimental values of the antiphase boundary energy ( $\gamma_{APB}$ ), which are in the range of 0.015 to 0.18 J/m<sup>2</sup>,<sup>[33]</sup> were used in the calculations for B2 Nb-Ti-Al alloys. Results of the computed  $\gamma_{us}$ ,  $\gamma_s$ , and ratio of  $\gamma_s/(U_{P-N} + \gamma_{APB})$  are summarized in Table I.

### B. Aluminides

The P-N barrier energies for several aluminides, silicides, and Laves phases were estimated using Eqs. [3] through [5]. Isotropic materials were assumed so that  $\kappa/c = 1/(1 - \nu)$  for edge dislocations, where  $\nu$  is the Poisson's ratio and the elastic constant  $c$  was computed based on Young's and shear moduli. In previous studies, Farkas and co-workers computed the unstable stacking fault energies for FeAl, NiAl, CoAl, Ni<sub>3</sub>Al, and TiAl using an embedded atom method.<sup>[14,34]</sup> These  $\gamma_{us}$  values were used in conjunction with Eq. [3] to obtain the P-N barrier energy. In addition, the ratio of  $\gamma_s/(U_{P-N} + \gamma_{APB})$  was also computed using the  $\gamma_s$  and  $\gamma_{APB}$  values reported by Farkas *et al.*<sup>[34]</sup> The results of these calculations are presented in Table I.

### C. Silicides and Laves Phases

For silicides and Laves phases,  $\gamma_{us}$  and  $\gamma_s$  by first principal calculations were not available. For these materials,  $\gamma_{us}$  values were estimated based on the Rice Equation [18] (Eq. [2]), while  $\gamma_s$  was assumed to be 2 J/m<sup>2</sup>. Results of the  $\gamma_{us}$ ,  $c$ ,  $b$ ,  $d$ ,  $\psi$ ,  $U_{P-N}$ ,  $\gamma_s$ , and  $\gamma_s/U_{P-N}$  for the Laves phases and silicides are summarized in Tables II and III, respectively.

Table I. Summaries of Lattice Parameter ( $a_0$ ), Burgers Vector ( $b$ ), Slip Plane Spacing ( $d$ ), Elastic Constant ( $c$ ), Lattice Phase Angle ( $\psi$ ), Unstable Stacking Energy ( $\gamma_{us}$ ), Surface Energy ( $\gamma_s$ ), Antiphase Boundary Energy ( $\gamma_{APB}$ ), the P-N Barrier Energy ( $U_{P-N}$ ), the  $\gamma_s/(U_{P-N} + \gamma_{APB})$  Ratio, and Ambient-Temperature Fracture Toughness ( $K_C$ ) for Selected Intermetallics; Values of  $\gamma_{us}$ ,  $\gamma_s$ , and  $\gamma_{APB}$  for FeAl, NiAl, CoAl, Ni<sub>3</sub>Al, and TiAl are from Farkas *et al.*<sup>[34]</sup>

Material	Crystal Structure	Slip System	$a_0$ (nm)	$b$ (nm)	$d$ (nm)	$d/b$	$c$ (GPa)	$\ell$ (nm)	$\psi$ , Deg	$\gamma_{us}$ , J/m <sup>2</sup>	$\gamma_s$ , J/m <sup>2</sup>	$\gamma_{APB}$ , J/m <sup>2</sup>	$U_{P-N}$ , J/m <sup>2</sup>	$\gamma_s / (U_{P-N} + \gamma_{APB})$	$K_C$ , MPa√m
Nb-10Ti-15Al	B2	{110}<111>	0.327	$\sqrt{3}a_0/2$	$a_0/\sqrt{2}$	0.8165	49.1	0.291	210	0.861	2.251	0.18*	0.441	3.6	17 <sup>[32]</sup>
Nb-25Ti-15Al	B2	{110}<111>	0.327	$\sqrt{3}a_0/2$	$a_0/\sqrt{2}$	0.8165	47.1	0.291	210	0.827	2.166	0.098*	0.185	7.7	18 <sup>[32]</sup>
Nb-40Ti-15Al	B2	{110}<111>	0.327	$\sqrt{3}a_0/2$	$a_0/\sqrt{2}$	0.8165	41.2	0.291	210	0.725	2.138	0.07*	0.132	10.6	110 <sup>[32]</sup>
FeAl	B2	{110}<111>	0.291	$\sqrt{3}a_0/2$	$a_0/\sqrt{2}$	0.8165	62.93	0.326	219	0.377**	1.282**	0.115**	0.0281	7.0	12 <sup>[37]</sup>
NiAl	B2	{110}<111>	0.288	$\sqrt{3}a_0/2$	$a_0/\sqrt{2}$	0.8165	61.87	0.330	219	0.564**	1.699**	0.286**	0.0421	5.2	4.5 <sup>[37]</sup>
CoAl	B2	{110}<111>	0.286	$\sqrt{3}a_0/2$	$a_0/\sqrt{2}$	0.8165	65.07	0.332	219	0.888**	1.546**	0.715**	0.0663	2.0	3 <sup>[37]</sup>
FeAl	B2	{110}<001>	0.291	$a_0$	$a_0/\sqrt{2}$	0.7071	62.93	0.321	190	0.835**	1.281**	0.115**	0.1739	3.9	—
NiAl	B2	{110}<001>	0.288	$a_0$	$a_0/\sqrt{2}$	0.7071	61.87	0.286	190	0.971**	1.699**	0.286**	0.2022	3.5	—
CoAl	B2	{110}<001>	0.286	$a_0$	$a_0/\sqrt{2}$	0.7071	65.07	0.283	190	1.197**	1.546**	0.715**	0.2493	1.6	—
FeAl	B2	{211}<111>	0.291	$\sqrt{3}a_0/2$	$a_0/\sqrt{6}$	0.4714	62.93	0.326	127	0.528**	1.281**	0.211**	1.003	1.06	—
NiAl	B2	{211}<111>	0.288	$\sqrt{3}a_0/2$	$a_0/\sqrt{6}$	0.4714	61.87	0.330	127	0.718**	1.999**	0.348**	1.364	1.17	—
CoAl	B2	{211}<111>	0.286	$\sqrt{3}a_0/2$	$a_0/\sqrt{6}$	0.4714	65.07	0.332	127	1.904**	1.546**	0.793**	3.616	0.35	—
Ni <sub>3</sub> Al	L <sub>12</sub>	{111}1/6<112>	0.357	$a_0/\sqrt{6}$	$a_0/\sqrt{3}$	1.414	70.33	0.564	380	0.259**	1.684**	0.140**	$7 \times 10^{-5}$	12.0	55 <sup>†[38]</sup>
TiAl	L <sub>10</sub>	{111}1/6<112>	0.402	$a_0/\sqrt{6}$	$a_0/\sqrt{3}$	1.414	78.72	0.500	380	0.182**	1.146**	0.329**	$6 \times 10^{-5}$	3.5	2 to 4 <sup>[39]</sup>
—	—	{111}1/2<110>	0.402	$a_0/\sqrt{2}$	$a_0/\sqrt{3}$	0.817	78.72	0.289	220	1.390**	1.146**	0.329**	$1.30 \times 10^{-3}$	3.5	—

\*From Hou *et al.*<sup>[33]</sup>\*\*From Farkas *et al.*<sup>[34]</sup>†Estimated from the end point of  $d/dN$  curves $\ddagger c_0 \approx a_0$

**Table II. Summaries of Crystal Structure, Slip Systems, the Lattice Parameters ( $a_o$ ,  $c_o$ ), Burgers Vector (b), Slip Plane Spacing (d), Elastic Constant (c), Lattice Phase Angle ( $\psi$ ), Unstable Stacking Energy ( $\gamma_{us}$ ), Surface Energy ( $\gamma_{APB}$ ), Antiphase Boundary Energy ( $\gamma_{APB}$ ), the P-N Barrier Energy ( $U_{P-N}$ ), the  $\gamma_s/(U_{P-N} + \gamma_{APB})$  Ratio, and Ambient-Temperature Fracture Toughness ( $K_{IC}$ ) for NbCr<sub>2</sub> and TiCr<sub>2</sub> Laves Phases**

Material	Crystal Structure	Slip System	$a_o$ (nm)	b (nm)	d (nm)	$\ell^*$ (nm)	c (GPa)	$\psi$ Deg	$\gamma_{us}$ J/m <sup>2</sup>	$\gamma_s$ J/m <sup>2</sup>	$\gamma_{APB}$ J/m <sup>2</sup>	$U_{P-N}$ J/m <sup>2</sup>	$\gamma_s/(U_{P-N} + \gamma_{APB})$	$K_{IC}$ (MPa $\sqrt{m}$ )
NbCr <sub>2</sub>	C15 (cubic)	{111} $a_o/2 < 110 >$ on $\beta$ layer	0.699	$a_o/\sqrt{2}$	$\sqrt{3}a_o/8$	0.166	79.6	84	6.51	2	0	5.6	0.036	1 <sup>[35,41]</sup>
		{111} $a_o/2 < 110 >$ on C layer	0.699	$a_o/\sqrt{2}$	$\sqrt{3}a_o/24$	0.166	79.6	28	39.2	2	0	$2.7 \times 10^3$	$7 \times 10^{-3}$	—
		{111} $a_o/6[211]^*$ on $\beta$ layer	0.699	$a_o/\sqrt{6}$	$\sqrt{3}a_o/8$	0.288	79.6	145	4.36	2	0.036 <sup>[68,69]</sup>	4.42	0.45	—
		{111} $a_o/6[211]^*$ on C layer	0.699	$a_o/\sqrt{6}$	$\sqrt{3}a_o/24$	0.288	79.6	47	13.1	2	0.036	$4.0 \times 10^2$	$5 \times 10^{-2}$	—
TiCr <sub>2</sub>	C14 (hexagonal)	{0001} $a_o/3 < 10\bar{1}0 >^{**}$ on $\beta$ layer	$a_o = 0.497$ $c_o = 0.81$	$a_o/\sqrt{6}$	$\sqrt{3}a_o/8$	0.411	79.6	192	2.24	2	0.036	0.43	4.8	—
		{0001} $a_o/3 < 10\bar{1}0 >^{**}$ on C layer	$a_o = 0.417$ $c_o = 0.81$	$a_o/\sqrt{6}$	$\sqrt{3}a_o/24$	0.288	79.6	77	2.84	2	0.036	15.1	0.13	—
		{111} $a_o/2 < 110 >^{**}$ on $\beta$ layer	0.695 $a_o = 0.497$	$a_o/\sqrt{2}$	$\sqrt{3}a_o/8$	0.167	79.0	134	4.29	2	0.036	6.21	0.32	1 to 1.5 <sup>[41]</sup>
		{0001} $a_o/3 < 10\bar{1}0 >^{**}$ on $\beta$ layer	$a_o = 0.81$	$a_o/\sqrt{6}$	$\sqrt{3}a_o/8$	0.405	79.0	190	2.17	2	0.036	0.46	4.05	—
(Nb,Ti)Cr <sub>2</sub>	C15 (hexagonal)	{111} $a_o/2 < 110 >^{**}$ on $\beta$ layer	0.697 $a_o = 0.497$	$a_o/\sqrt{2}$	$\sqrt{3}a_o/8$	0.167	81.7	136	4.44	2	0.036	6.01	0.33	1 <sup>[41]</sup>
		{0001} $a_o/3 < 10\bar{1}0 >^{**}$ on $\beta$ layer	$a_o = 0.81$	$a_o/\sqrt{6}$	$\sqrt{3}a_o/8$	0.405	81.7	192	2.24	2	0.036	0.43	4.27	—

\*\*Synchrohear

**Table III. Summaries of Crystal Structure, Slip Systems, the Lattice Parameters ( $a_0$ ,  $c_0$ ), Burgers Vector ( $b$ ), Slip Plane Spacing ( $d$ ), Elastic Constant ( $c$ ), Lattice Phase Angle ( $\psi$ ), Unstable Stacking Energy ( $\gamma_{us}$ ), Surface Energy ( $\gamma_s$ ), Antiphase Boundary Energy ( $\gamma_{APB}$ ), the P-N Barrier Energy ( $U_{P-N}$ ), the  $\gamma_s/(U_{P-N} + \gamma_{APB})$  Ratio, and Ambient-Temperature Fracture Toughness ( $K_C$ ) for Silicides**

Material	Crystal Structure	Slip System	$a_o$ (nm)	$c_o$ (nm)	b (nm)	$d$ (nm)	$\ell^*$ (nm)	$c$ (GPa)	$\psi_i$ Deg	$\gamma_{us}$ J/m <sup>2</sup>	$\gamma_s$ J/m <sup>2</sup>	$\gamma_{APB}$ J/m <sup>2</sup>	$U_{P-N}$ J/m <sup>2</sup>	$\gamma_s/(U_{P-N} + \gamma_{APB})$	$K_C$ (MPa√m)	
Nb <sub>5</sub> Si <sub>3</sub>	D8 <sub>ℓ</sub> (tetragonal)	(010)[001]	0.657	1.1884	$c_o$	$a_o$	0.0692	79.7	142	8.88	2	0	9.8	0.20	3 <sup>[36]</sup>	
		{110}[001]	0.657	1.1884	$c_o$	$a_o/\sqrt{2}$	0.0692 0.2768	79.7	105	12.56	2	0	50.7	0.04		
Nb <sub>5</sub> Si	Ti <sub>3</sub> P (tetragonal)	[001] partials on (010)	0.657	1.884	$c_o/4$ , $c_o/2$ , and $c_o/4$	$a_o$	0.1384 0.2768	79.7	560,280	3.25	2	0.49	0.02	3.92		
		(010)[001]	0.6593	1.2652	$c_o$	$a_o$	0.0650	81.5	140	10	2	0	12.0	0.17	—	
Mo <sub>5</sub> SiB <sub>2</sub>	D8 <sub>ℓ</sub> (tetragonal)	(010)[001]	0.5995	1.102	$c_o$	$a_o$	0.0746 0.2988	144	140	13.72	2	0	16.4	0.12	2 <sup>[70]</sup>	
		[001] partials on (010)	0.5995	1.102	$c_o/4$ , $c_o/2$ , and $c_o/4$	$a_o$	0.1493 0.2985	144	560,280	5.14	2	0.89 <sup>[62]</sup>				
Mo <sub>5</sub> Si <sub>3</sub>	D8 <sub>m</sub> (tetragonal)	{110}[001]	0.5995	1.102	$c_o$	$a_o/\sqrt{2}$	0.0746	144	103	21.38	2	0	91.64	0.02	—	

The  $\gamma_s/(U_{P-N} + \gamma_{APB})$  ratios for Laves phase and silicides are less than 0.5, compared to 2 to 25 for aluminides. To establish possible relations between fracture toughness and the P-N barrier energy, the fracture toughness values,  $K_C$ , of the intermetallics<sup>[35-42]</sup> at ambient temperature are also summarized in Tables I through III.

## V. FRACTURE TOUGHNESS/SLIP RELATIONSHIPS

The fracture toughness,  $K_C$ , of the intermetallics at ambient temperature is correlated with the  $\gamma_s/(U_{P-N} + \gamma_{APB})$  ratio in Figure 2(a). Fitting Eqs [26] and [27] to the experimental data yield  $A^*/kT = 20$  and  $J_0 = 3 \times 10^5$  J/m<sup>2</sup>. Since  $A^* = \ell x^* = \ell b$ , the value of  $\ell$  was computed for individual intermetallics and the results are presented in Tables I through III. In almost all cases,  $\ell \approx b$  and  $x^* = b$  for the slip system activated. Thus, it is concluded that  $x^* = b$ ,  $A^* = b^2$ , and  $v^* = b^3$ .

The value of  $J_0 = 3 \times 10^5$  J/m<sup>2</sup> was highly influenced by the  $K_C$  data for B2 Nb-Ti-Al<sup>[32]</sup> and Ni<sub>3</sub>Al.<sup>[38]</sup> The  $K_C$  data

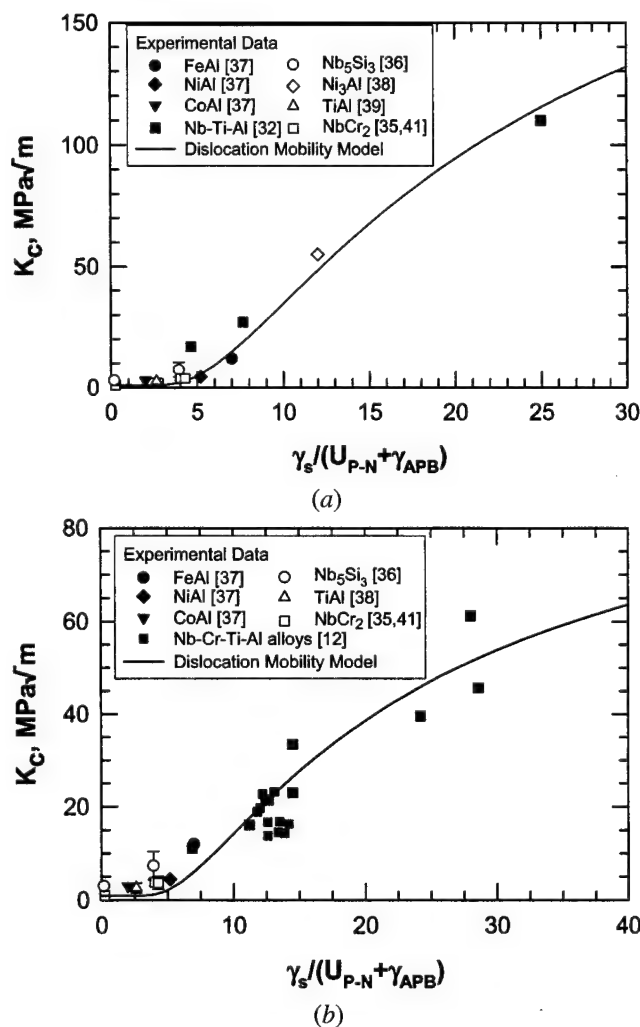


**Fig. 2—Correlation of the fracture toughness model against experimental data:** <sup>[32,35-39,41]</sup> (a) all intermetallics including  $K_C$  data of B2 Nb-Ti-Al and Ni<sub>3</sub>Al that violated the plane-strain fracture criteria, and (b) plane-strain  $K_C$  data of intermetallics and bcc Nb-Ti-Al alloys.

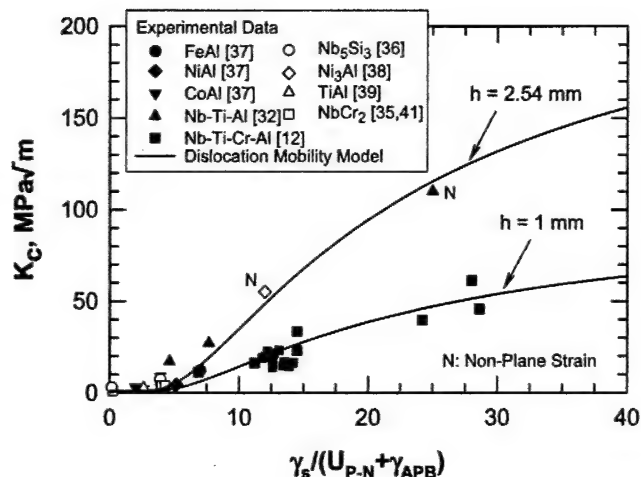


Fig. 3—A comparison of the fracture toughness data of intermetallic<sup>[32,35–39,41]</sup> and metallic alloys<sup>[12]</sup> under plane-strain and nonplane strain fracture conditions against model calculations.

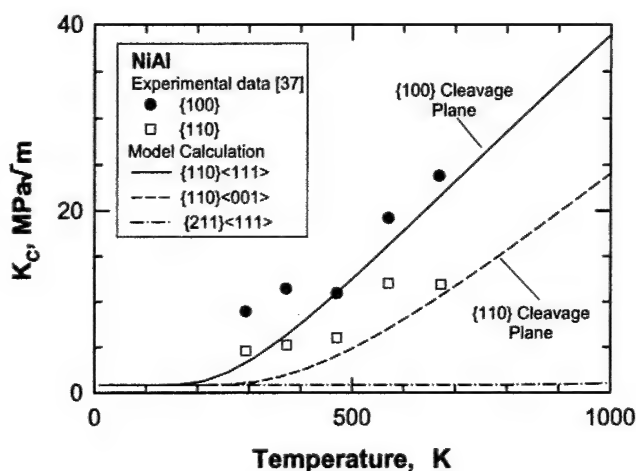


Fig. 4—Predicted  $K_{IC}$  compared against experimental data of NiAl<sup>[37]</sup> for {100}<111>, {110}<001>, and {211}<111> slip. Experimental data for {211}<111> slip are not available. Model predictions are independent of experimental data.

of these two materials were obtained under nonplane strain conditions since the specimen thickness did not meet the ASTM plane-strain criterion.<sup>[43]</sup> The B2 Nb-Ti-Al and Ni<sub>3</sub>Al data were, thus, removed and replaced with the plane strain  $K_{IC}$  data of bcc Nb-Ti Cr-Al solid solution alloys from a previous study<sup>[12]</sup> (Figure 2(b)). The revised  $K_{IC}$  data set was refitted to the fracture model. The same value of  $b^2/kT = 20$  was obtained, but the  $J_0$  value obtained was reduced to  $5 \times 10^4 \text{ J/m}^2$ , which was 1/6 of the previous value. The values of  $\rho$  and  $h$  that contributed to the  $J_0$  values for the computation shown in Figures 3 and 4 are presented in Table IV. A comparison of the two sets of  $K_{IC}$  data is shown in Figure 3. At low  $\gamma_s/(U_{P-N} + \gamma_s)$ , the computed  $K_{IC}$  values are not sensitive to the  $J_0$  value. In contrast, the computed  $K_{IC}$  is sensitive to the  $J_0$  at high  $\gamma_s/(U_{P-N} + \gamma_{APB})$  ratio because of its dependence on the density of activated dislocations and the process zone size,  $h$ . Thus, the high value of  $J_0$  from the dataset containing B2 Nb-Ti-Al and Ni<sub>3</sub>Al can be explained

Table IV. Material Constants Used in the Fracture Model to Correlate with Fracture Toughness Data of Intermetallics and Metallic Alloys

Parameter	Plane-Strain Fracture	Nonplane-Strain Fracture
$J_0 (\text{J/m}^2)$	$5 \times 10^4$	$3 \times 10^5$
$\rho$ (number of dislocation/ $\text{m}^2$ )	$3 \times 10^{11}$	$3 \times 10^{11}$
$h$ (mm)	1	2.5

on the basis of a larger process zone size,  $h$ . Based on these considerations, we concluded that  $J_0 = 5 \times 10^4 \text{ J/m}^2$  for plane-strain fracture of the materials investigated.

## VI. TEMPERATURE DEPENDENCE OF FRACTURE TOUGHNESS

To examine the validity of the fracture model, Eq. [26] was used to estimate the temperature dependence of fracture toughness of a number of intermetallics keeping the value of  $J_0$  constant ( $J_0 = 5 \times 10^4 \text{ J/m}^2$ ), while varying only the temperature and using the corresponding  $U_{P-N}$  and  $\gamma_{APB}$  values. Both  $U_{P-N}$  and  $\gamma_{APB}$  were taken to be independent of temperature and their values are shown in Tables I through III. Results for individual intermetallics are discussed in Sections A, B, C, and D.

### A. Stoichiometric NiAl

In a previous study, Chang *et al.*<sup>[37]</sup> measured the fracture toughness of NiAl single crystals as a function of temperature and crystallographic orientation. Their results, shown in Figure 5, indicated that {100} oriented crystals are tougher than {110} oriented crystals. In addition, the fracture toughness values of both orientations increase with increasing temperature. The experimental results of Chang *et al.*<sup>[37]</sup> are compared against model predictions for {110}<111>, {110}<001>, and {211}<111>, using the corresponding  $U_{P-N}$  and  $\gamma_{APB}$  values shown in Table I. Figure 4 indicates that the predicted fracture toughness values for {100} are higher than those for {110} and {211}, in accordance with experimental data. The temperature dependence of fracture toughness for both slip systems agrees reasonably with experimental results. Experimental evidence indicated that <111> slip caused cleavage fracture on {100} while <001> slip caused {110} cleavage.<sup>[37,44]</sup> Thus, the correct cleavage fracture planes are also predicted. Detailed examination of the exponential function revealed that this fracture behavior was caused mainly by the variation of the P-N barrier energy with the slip system since the antiphase boundary energy was approximately equal. The P-N energy is smallest ( $0.042 \text{ J/m}^2$ ) for {110}<111> slip; it is  $0.202 \text{ J/m}^2$  for {110}<001> slip; and it is highest ( $1.364 \text{ J/m}^2$ ) for {211}<111> slip.

Figure 5 illustrates the effects of the various energy terms on the fracture toughness of NiAl for {110}<110>. These calculations were done systematically to elucidate the relative importance of individual barrier energy terms. In general, the fracture toughness increases with decreasing heights of



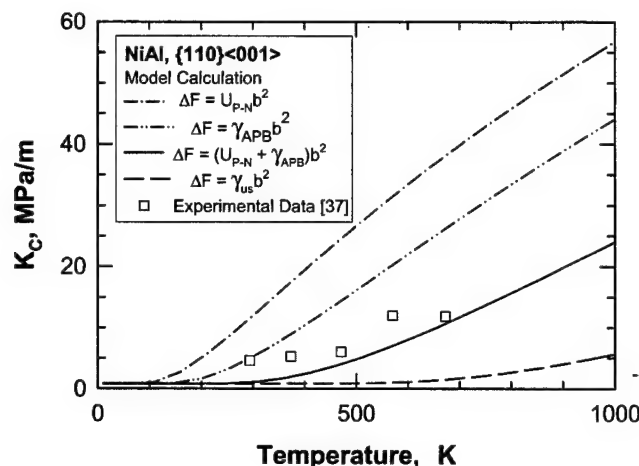


Fig. 5—Dependence of computed  $K_C$  on individual dislocation barriers for  $\{110\}\langle 001 \rangle$  slip in NiAl. The  $K_C$  increases with decreasing barrier energy since  $U_{P-N} < \gamma_{APB} < \gamma_{us}$ .

the energy barrier. The highest fracture toughness is observed when the activation barrier is the P–N barrier only. The inclusion of the antiphase boundary energy decreases the dislocation mobility and the computed fracture toughness. The lowest fracture toughness occurs when the unstable stacking fault is the activation barrier for  $\{110\}\langle 110 \rangle$ . The observed fracture toughness results are in better agreement with the model calculation based on the sum of  $U_{P-N}$  and  $\gamma_{APB}$  as the activation barrier. The implications from this result are that (1) dislocation mobility controls the fracture toughness and (2) a relatively high antiphase boundary energy is responsible for low dislocation mobility and inferior fracture resistance in NiAl.

### B. Binary TiAl

Booth and Roberts<sup>[40]</sup> determined the fracture toughness of binary TiAl (Ti-54.7Al) single crystals as a function of temperature. Two crystallographic orientations were investigated to interrogate the relative contributions of ordinary and superlattice dislocations to the fracture toughness of TiAl. The possible slip directions in TiAl are  $\langle 110 \rangle$ ,  $\langle 101 \rangle$ , and  $\langle 112 \rangle$ ; the corresponding Burgers vectors are  $1/2\langle 110 \rangle$ ,  $\langle 101 \rangle$ , and  $1/2\langle 112 \rangle$ .<sup>[45]</sup> The shortest of the Burgers vectors is  $1/2\langle 110 \rangle$  and it corresponds to the ordinary dislocations commonly observed in fcc crystals. The  $1/2\langle 112 \rangle$  dislocations are perfect dislocations with the second shortest Burgers vectors on the  $\{111\}$ . The  $\langle 101 \rangle$  dislocations are superlattice dislocations that can be dissociated into two  $1/2\langle 101 \rangle$  superlattice partials separated by an antiphase boundary. Figure 6 shows the fracture toughness data of Booth and Roberts<sup>[40]</sup> for orientations A and B. In orientation A, the ordinary and superlattice dislocations were stressed with equivalent critical resolved shear stresses. In contrast, the superlattice slip systems in orientation B experienced higher resolved shear stresses than the ordinary slip systems.

The unstable stacking and P–N barrier energies were computed for  $\{111\}$  slip by ordinary and superlattice dislocations, and the results are presented in Table I. The unstable stacking energies can be high while the P–N barrier energies for  $\{111\}$  slip by  $\langle 112 \rangle$  and  $\langle 110 \rangle$  ordinary dislocations are

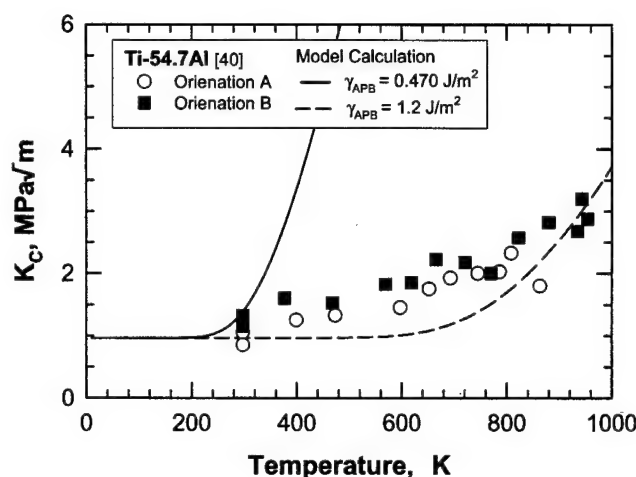


Fig. 6—Computed  $K_C$  compared against experimental data of binary TiAl (Ti-54.7Al)<sup>[40]</sup> as a function of temperature. The fracture model overpredicted the fracture toughness when the experimental  $\gamma_{APB}$  value ( $0.47 \text{ J/m}^2$ )<sup>[46]</sup> was used. The  $\gamma_{APB}$  required to fit the model to the data was  $1.2 \text{ J/m}^2$ . The high apparent  $\gamma_{APB}$  value suggests that dislocation nucleation at the crack tip might be the controlling slip mechanism.

quite low. Based on the  $U_{P-N}$  and  $\gamma_{APB}$  values, the ordinary dislocations are expected to exhibit high mobility and should lead to a high fracture resistance. The predicted high fracture resistance, however, was not observed experimentally, as shown in Figure 7. The lack of agreement prompted additional computation of the P–N barrier energy and  $K_C$  for superlattice dislocations. The mobility of the superlattice dislocations was found to be lower than those of the ordinary dislocations because of a relatively high antiphase boundary. However, the computed fracture toughness remained too high when the experimental value for the  $\gamma_{APB}$  ( $0.47 \text{ J/m}^2$ )<sup>[46]</sup> for Ti-54.7Al was used (Figure 6). The value of  $\gamma_{APB}$  required to match the experimental data of Ti-54.7Al was  $1.2 \text{ J/m}^2$ . This value of  $\gamma_{APB}$  is considerably higher than those computed by first principle methods or measured experimentally,<sup>[46–51]</sup> which are summarized in Table V. This high  $\gamma_{APB}$ , however, agrees with the unstable stacking fault energy (Table I). Thus, the anomalously high  $\gamma_{APB}$  suggests that dislocation nucleation might be the controlling fracture process in Ti-54.7Al at temperatures above the ambient temperatures.

The fracture toughness of binary TiAl alloys is known to depend on the Al content,<sup>[52–55]</sup> as shown in Figure 7. It is plausible that the observed dependence of fracture toughness on Al content might be a manifestation of the influence of Al content on the antiphase boundary energy of the superlattice dislocations. The experimental and computed values of the antiphase boundary energy in TiAl, shown in Table V, range from  $0.1$  to  $0.470 \text{ J/m}^2$ .<sup>[46–51]</sup> The fracture toughness computed based on these  $\gamma_{APB}$  values are in agreement with the experimental results, as shown in Figure 7. The result is encouraging, but it is still uncertain whether the antiphase boundary is indeed the controlling parameter since its relation with Al content has not been established. In addition, the apparent agreement in Figure 7 could be fortuitous since it is well established that ligament toughening and grain boundary toughening contribute to the fracture resistance in binary TiAl.<sup>[39,56,57]</sup>



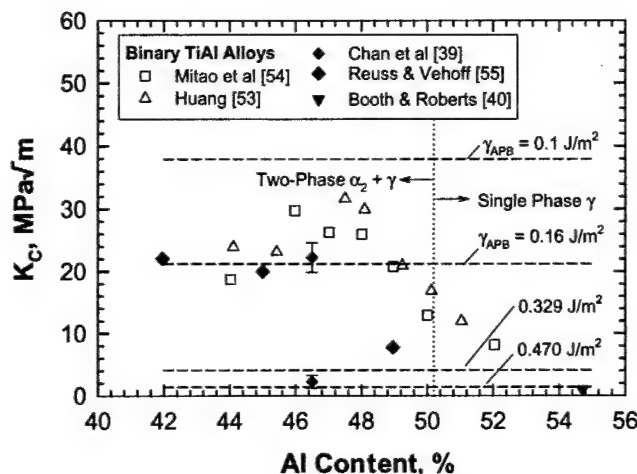


Fig. 7—Measured and computed  $K_{IC}$  values of binary TiAl<sup>[39,40,53-55]</sup> as a function of Al content. The dependence of  $K_{IC}$  on Al content might be a manifestation of the dependence of  $\gamma_{APB}$  on Al content.

Table V. Antiphase Boundary Energy Values ( $\gamma_{APB}$ ) Reported for a Fault on {111} in Binary TiAl

Composition	Measured $\gamma_{APB}$ (mJ/m <sup>2</sup> )	Computed $\gamma_{APB}$ (mJ/m <sup>2</sup> )
Ti-54.7Al	145, <sup>[47]</sup> 470 <sup>[46]</sup>	—
Stoichiometric TiAl	—	306, <sup>[50]</sup> 329, <sup>[34]</sup> 510, <sup>[51]</sup> 520, <sup>[48]</sup> 670 <sup>[49]</sup>

A systematic comparison of  $K_{IC}$ , antiphase boundary energy,  $U_{P-N}$ , and  $\gamma_{us}$  as functions of Al content is required to resolve this issue.

### C. Laves Phases

NbCr<sub>2</sub> and TiCr<sub>2</sub> are Laves phases that exhibit the C15 (cubic) structure at ambient temperatures. Both are very brittle at ambient temperatures, but have attractive creep properties at elevated temperatures. Thoma *et al.*<sup>[41]</sup> investigated the effects of nonstoichiometry on the fracture toughness of NbCr<sub>2</sub> and TiCr<sub>2</sub>. The experimental  $K_{IC}$  results are compared against model calculations in Figures 8 and 9 for Nb-xTi-67Cr and Nb-xTi-(67-2x)Cr, respectively. Figures 8 and 9 also present the corresponding results for  $U_{P-N}$ ,  $\gamma_{us}$ , and the ratio of  $\gamma_{us}/(U_{P-N} + \gamma_{APB})$ . The model computations were based on synchroshear of a pair of  $1/2\langle 110 \rangle$  Shockley partial dislocations on either the {111} layer with the  $\alpha\beta$  atom arrangement ( $\beta$  layer) or the {111} layer with the  $\alpha\gamma$ C atom arrangement (C layer).<sup>[58,59,60]</sup> The  $\beta$  layer is comprised of only small (Cr) atoms and exhibits a smaller slip plane spacing, while the C layer is comprised of both large (Nb or Ti) and small (Cr) atoms with a slip plane spacing that is 3 times that of the  $\beta$  layer.<sup>[58,59]</sup> There are three hard C layers and one soft  $\beta$  layer in a unit cell of C14 or C15. In addition, slip by synchroshear must occur simultaneously on all {111} layers in the unit cell.<sup>[58,59]</sup> The unstable stacking and the P-N barrier energies for both C15 Laves are large and the predicted fracture toughness values are about 1 MPa√m

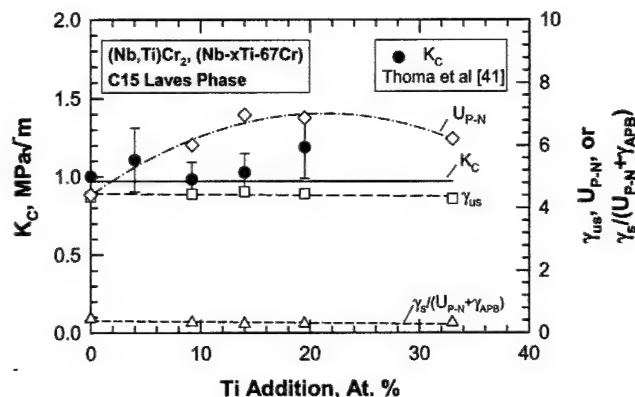


Fig. 8—A comparison of computed and measured  $K_{IC}$  values<sup>[41]</sup> of C15 (Nb,Ti)Cr<sub>2</sub> Laves phases (Nb-xTi-67Cr) as a function of Ti addition. The Ti addition results in little changes in  $U_{P-N}$ ,  $\gamma_{us}$ , and the corresponding fracture toughness.

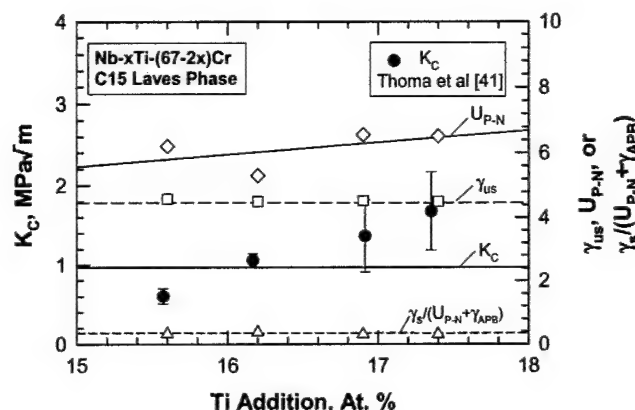


Fig. 9—Predicted and measured  $K_{IC}$ <sup>[41]</sup> of C15 Laves phase with the composition Nb-xTi-(67-2x)Cr as a function of Ti addition. The Ti addition exerts no effect on  $\gamma_{us}$  and only small effects on  $U_{P-N}$  and  $K_{IC}$ .

for NbCr<sub>2</sub>, TiCr<sub>2</sub>, and (Nb,Ti)Cr<sub>2</sub>, which are in good agreement with experimental data<sup>[41]</sup> (Figures 8 and 9).

The fracture model was used to predict the fracture toughness of (Nb,Ti)Cr<sub>2</sub> as a function of temperature. Figure 10 shows the computed fracture toughness results for synchroshear on the  $\beta$  layer ( $\alpha\beta$ ), and the results are contrasted against that on the C layer ( $\alpha\gamma$ C) in either the C15 (cubic) or the C14 (hexagonal) structure. For C15, the predicted fracture toughness values are low (1 MPa√m) for slip on the  $\beta$  and C layers. For C14, the Shockley partial dislocations are more mobile and they are predicted to produce a higher fracture toughness at higher temperatures. Unfortunately, the dislocations mobility on the C layer remains very low even for C14. Since slip by synchroshear must be operative on successive {111} layers, the fracture toughness values of C14 and C15 are likely to be controlled by the  $U_{P-N}$  of the C layer. Thus, the observed fracture toughness values for both C14 and C15<sup>[41,42]</sup> are in agreement with the model prediction for slip on the C layer, as shown in Figure 10.

NbCr<sub>2</sub> has a C15 (cubic) crystal structure and a fracture toughness of about 1 MPa√m at ambient temperature.<sup>[35,41]</sup> A small (>2 at. pct) addition of Si + Ge changes C15 NbCr<sub>2</sub>

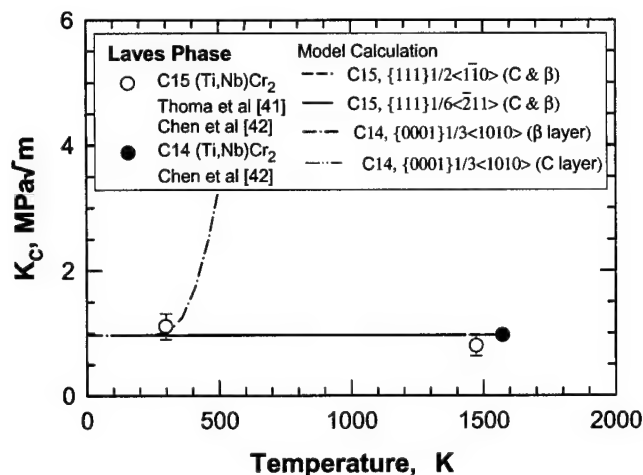


Fig. 10—Model predictions of  $K_{IC}$  in C15 and C14 Laves phase compared against experimental data<sup>[41,42]</sup> as a function of temperature. The fracture toughness in the Laves phases appears to be controlled by the slip system on the C layer that exhibits the lowest dislocation mobility.

to C14 (hexagonal), which is normally stable only at elevated temperatures. In addition, Si and Ge addition improves the fracture toughness of  $NbCr_2$  from 1  $MPa\sqrt{m}$ <sup>[35,41]</sup> to about 2 to 5  $MPa\sqrt{m}$ .<sup>[61]</sup> Computations of unstable stacking energy and P–N barrier energy performed for synchroshear<sup>[59]</sup> by a pair of  $1/6[211]$  partial dislocations on (111) layer indicated that  $\gamma_{us} = 4.36 \text{ J/m}^2$  and  $U_{P-N} = 4.42$  for synchroshear in C15. In contrast,  $\gamma_{us} = 2.24 \text{ J/m}^2$  and  $U_{P-N} = 0.43 \text{ J/m}^2$  for synchroshear in C14 because of a more favorable ratio of slip plane spacing to Burgers vector ( $d/b$ ). The lower values of  $\gamma_{us}$  and  $U_{P-N}$  suggest that dislocation nucleation and motion is easier in the C14 than in the C15 Laves phase. Consequently, Si or Ge addition to  $NbCr_2$  may improve the fracture resistance when the C14 phase is stabilized, which was observed experimentally and is shown in Figure 11. The exact mechanism responsible for the toughness improvement is not understood since synchroshear slip on the C layer should remain difficult and limit the fracture resistance. On the other hand, the toughness improvement is very modest and may indeed involve synchroshear on the  $\beta$  layer. Again, high-resolution transmission electron microscopy (TEM) work is required to resolve this issue.

#### D. $Nb_5Si_3$

$Nb_5Si_3$  can exist in either the  $D8_m$  or  $D8_l$  crystal structures; both are body-centered tetragonal phases whose deformation mechanisms are still unknown. Recently, Ito *et al.*<sup>[62]</sup> identified  $\langle 100 \rangle \{012\}$ ,  $\langle 100 \rangle \{001\}$ ,  $1/2 \langle 111 \rangle \{110\}$ , and  $\langle 110 \rangle \{001\}$  as possible slip systems in  $Mo_5SiB_2$  (T2 phase,  $D8_l$  structure). Experimental evidence, however, indicates that  $[001](010)$  is the operative slip system in the T2 phase at 1500 °C.<sup>[62]</sup> Because of the complex  $D8_l$  structure, slip in T2 appears to occur through the actions of three fractional  $[001]$  partial dislocations separated by two complex stacking faults (CSFs) according to the dissociation reaction given by<sup>[62]</sup>

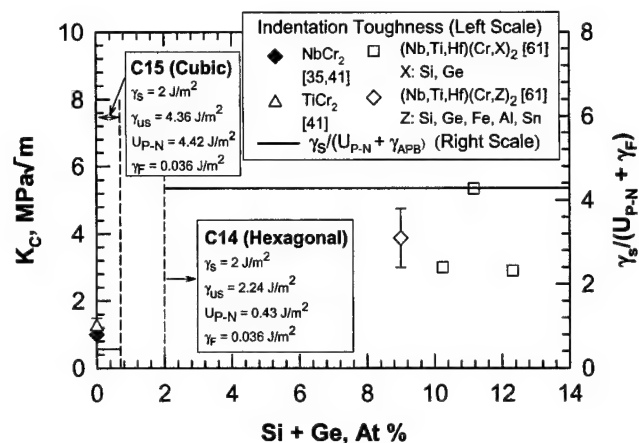
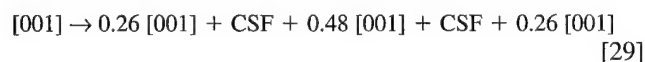


Fig. 11—Effects of Si and Ge additions on the crystal structure, unstable stacking energy, P–N barrier energy, and the fracture toughness<sup>[35,41,61]</sup> of C15 and C14  $(Nb,Ti)(Cr,Si,Ge)_2$  Laves phases.

which was suggested by Ito *et al.*,<sup>[62]</sup> through a consideration of the overlapping volume encountered by atoms on the slip plane and TEM observations. The P–N barrier energy calculation indicates that the dislocation dissociation reaction, as described in Eq. [29], is energetically favorable and significantly reduces both the unstable stacking and P–N barrier energies in  $Nb_5Si_3$  with the  $D8_l$  crystal structure. As shown in Table III, the  $\gamma_{us}$  and  $U_{P-N}$  for  $[001](010)$  slip in  $Nb_5Si_3$  are 8.88 and 9.81  $J/m^2$ , respectively. In contrast, the  $\gamma_{us}$  and  $U_{P-N}$  are reduced to 3.25 and 0.01  $J/m^2$ , respectively, if slip on (010) is accomplished by three fractional  $[001]$  partial dislocations. The CSF energy for  $Nb_5Si_3$  has not been measured, but the CSF energy for  $Mo_5SiB_2$  was found to be 0.89  $J/m^2$ .<sup>[62]</sup> An estimate of the CSF for  $Nb_5Si_3$  based on the elastic moduli and the CSF energy of  $Mo_5SiB_2$  gives  $\gamma_{CSF} = 0.49 \text{ J/m}^2$ . This CSF energy leads to a value of 3.92 for the  $\gamma_s/(U_{P-N} + \gamma_{APB})$  ratio and a computed  $K_{IC}$  of 1  $MPa\sqrt{m}$  for  $Nb_5Si_3$ , compared to 3  $MPa\sqrt{m}$ <sup>[36]</sup> observed experimentally.

An alloying addition that promotes slip by the fractional  $[001]$  partial dislocations should improve the fracture resistance of  $Nb_5Si_3$ . A recent study<sup>[61]</sup> showed that the fracture toughness of  $Nb_5Si_3$  was improved by the additions of Ti, as shown in Figure 12. In particular, the fracture toughness of alloyed  $(Nb,Ti,Hf)_5(Si,Cr,Ge)_3$  silicides increases with increasing Ti addition but decreases with the bond order.<sup>[61]</sup> Bond order is a measure of the strength of the covalent bond between atoms and is computed on the basis of the overlapping electron population.<sup>[63]</sup> This enhancement of fracture resistance by Ti addition and its relation to bond order is not well understood. One possible explanation is that Ti addition promotes the slip process by the partial dislocation mechanism, as described in Eq. [29]. According to Ito *et al.*,<sup>[62]</sup> the driving force for the dislocation dissociation process is the need to minimize the overlapping volume of atoms on the slip plane. Ito *et al.*<sup>[62]</sup> demonstrated this point in terms of contours of overlapping volume derived on the basis of a hard ball model that was used to represent the atomic interference on the slip plane. Since Ti addition reduces the bond order of  $Nb_5Si_3$ , this means that the overlapping electron population and possibly the overlapping volume, the unstable stacking energy, the CSF

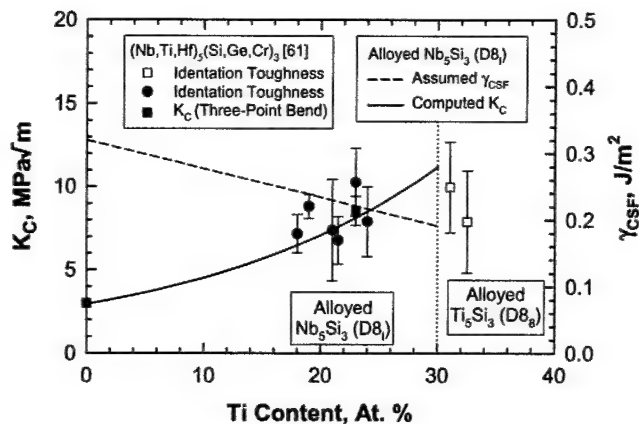


Fig. 12—Computed and measured  $K_C$  and the complex stacking energy,  $\gamma_{CSF}$ , required to fit the fracture model to the experimental data of alloyed  $Nb_3Si_3$  with the  $D8_1$  crystal structure.

energy, or the P-N barrier energy may be reduced by Ti additions.

The beneficial effect of a reduced CSF energy on the fracture toughness is illustrated in Figure 12. In this calculation, the CSF energy was assumed to decrease with increasing Ti contents in the manner depicted by the dashed line. Using the assumed CSF energy and the fracture model, the  $K_C$  of the alloyed silicides was computed as a function of Ti contents and the results are presented as the solid line in Figure 12. The computation indicated that the CSF energies required to give the observed fracture toughness are in the range of 0.2 to 0.3 J/m<sup>2</sup>, which are substantially lower than the 0.89 J/m<sup>2</sup> for the CSFs observed in  $Mo_5SiB_2$ .<sup>[62]</sup> Such a reduction of the CSF energy, if proven to occur, would promote the slip process by partial dislocations and explain the increase of fracture resistance exhibited by  $Nb_3Si_3$  alloyed with Ti additions. Obviously, high-resolution TEM studies of the dislocation structure in alloyed  $Nb_3Si_3$  are required to verify this hypothesis. In addition, a computational method is required to compute the CSF energy.

## VII. DISCUSSION

An important contribution of this study is the development of a fracture model that incorporates thermally activated slip and dislocation mobility, as well as the description of the dislocation mobility in terms of the P-N barrier energy and a generalized stacking fault energy,  $\gamma_F$ . The  $\gamma_F$  parameter is used to represent the energy of a stacking fault, an antiphase boundary, or a complex stacking fault. Expressed in terms of the J integral, the fracture model has the form given by

$$J_C = J_s + J_0 \exp \left[ -\frac{b^2}{kT} (U_{P-N} + \gamma_F) \right] \quad [30]$$

where  $\gamma_F$  represents  $\gamma_{APB}$ ,  $\gamma_{CSF}$ , or any other relevant superlattice stacking fault, while  $J_0$  is given by Eq. [27]. In this formulation,  $\rho$  and  $h$  are the dislocation density and process zone size attained at the state of full activation that occurs when the exponent term becomes unity. The term  $\pi\rho h^2$  represents the total number of dislocations activated, while  $kT/b^2$  represents the thermal energy per activated area.

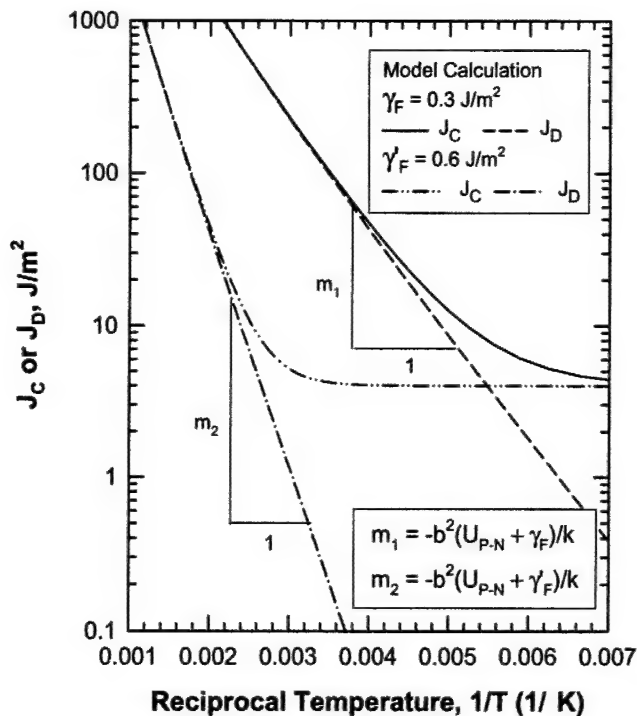


Fig. 13—A semilog plot of  $J_C$  and  $J_D$  vs  $1/T$ , which illustrates that the slope can be used to deduce the operative controlling dislocation mechanisms. Fracture is controlled by dislocation mobility when the slope is given by  $-b^2(U_{P-N} + \gamma_F)/k$ . The manifestation of a higher apparent stacking fault energy ( $\gamma'_F$ ) than the actual stacking fault energy ( $\gamma_F$ ) suggests that the fracture process might be controlled by dislocation nucleation rather than dislocation mobility.

For the P-N barriers, the activated distance, area, and volume were deduced to be  $b$ ,  $b^2$ , and  $b^3$ , respectively. The implication is that a dislocation in an ordered intermetallic moves by an atom (or Burgers vector), one at a time. When this process occurs by a pair of partial dislocations, the order structure and stoichiometry is broken down locally and a stacking fault is created between the dissociated dislocations. The presence of the stacking fault reduces the dislocation mobility since additional energy is needed to recombine the partial dislocations or move the partial dislocations with a faulted core. This process is more energetically favorable than dislocation nucleation as long as the inequality given by

$$U_{P-N} + \gamma_F < \gamma_{us} \quad [31]$$

is satisfied. This criterion appears to be met by most of the intermetallics listed in Table I. In contrast, Eq. [31] is often violated by slip systems in the Laves phases and in the silicides shown in Tables II and III. For these materials, brittle fracture is favored because both  $\gamma_{us}$  and  $U_{P-N}$  are high, such that dislocation nucleation and motion are both difficult.

The important feature of Eq. [30] is depicted in Figure 13, which shows that a plot of  $J_C$  and  $J_D$  vs  $1/T$  in a semilog plot gives a negative slope of  $-b^2(U_{P-N} + \gamma_F)/kT$  when slip is controlled entirely by dislocation mobility. On the other hand, the apparent fault energy would be greater than those of the pertinent stacking fault energy, antiphase boundary energy, or the CSF energy when fracture is controlled by dislocation nucleation from the crack tip. This is the case because the

unstable stacking energy,  $\gamma_{us}$ , is considerably larger than those of the stacking fault, antiphase boundary, and CSF. Inclusion of even a fraction of  $\gamma_{us}$  in the  $\gamma_F$  term in Eq. [30] would decrease the fracture toughness substantially. Thus, it may be feasible to distinguish the dislocation mechanism controlling brittle-to-ductile fracture transition by comparing the deduced value of the generalized stacking fault energy against the experimental values of various stacking fault energies.<sup>[64]</sup>

Since the stacking fault and the antiphase boundary energies can generally be expressed in terms of the ordering energy,<sup>[64,65,66]</sup> the importance of atomic order and bonding on dislocation mobility and fracture resistance is evident and must be emphasized. According to Eq. [30], atomic ordering tends to depress dislocation mobility, increase the brittle-to-ductile temperature, and reduce fracture toughness. In contrast, disordered materials are expected to exhibit higher dislocation mobility and fracture resistance compared to ordered materials at the same temperature and the P-N barrier energy. To improve the fracture resistance of ordered intermetallics by alloying, an alloy addition must reduce both the P-N barrier and the ordering energy. Thus, an alloy addition must be selected judiciously, preferably through a fundamental understanding of the relationships between bonding, dislocation mobility, and fracture resistance.

The question of whether fracture in intermetallics is controlled by dislocation nucleation or mobility remains an open one. Experimental data indicated the presence of pre-existing dislocations in B2 Nb-Ti-Al.<sup>[33]</sup> Thus, dislocation nucleation is not necessary and fracture toughness in this material should be controlled by dislocation mobility. There is also no consensus with regard to the importance of crack-tip dislocation nucleation compared to dislocation nucleation at nontip sites. Recent discrete dislocation modeling<sup>[67]</sup> demonstrated that dislocation nucleation at nontip sites and their subsequent movements away from the crack tip leads to a rising  $K_R$  curve. Thus, crack-tip dislocation nucleation is not necessary for the occurrence of a resistance-curve behavior. When dislocation nucleation is required, it may occur at nontip sites rather than at the crack tip.

Comparisons of the computed and observed fracture toughness values for various slip systems at different temperatures or alloying additions produced several interesting findings regarding the controlling dislocation mechanisms. For NiAl, the  $K_{IC}$ - $T$  relation varies greatly with changes in slip vector and the P-N barrier energy, suggesting dislocation mobility might be the controlling mechanism. On the other hand, the high apparent  $\gamma_{APB}$  value observed in Ti-54.7Al<sup>[40]</sup> suggests that fracture might be controlled by crack-tip dislocation nucleation or that the antiphase boundary energy is considerably higher than those reported in the literature. The P-N barrier energy and  $\gamma_{us}$  for Laves phases and silicides are extremely large and both are responsible for the low fracture toughness. Thus, the controlling dislocation mechanism appears to vary in individual intermetallics and must be determined on an individual basis.

## VIII. CONCLUSIONS

An analytical model has been developed for computing the unstable stacking and P-N barrier energies associated with slip in intermetallics. These energy parameters are

incorporated into a fracture toughness model that is formulated on the basis of thermally activated slip by either a perfect dislocation or a pair of partial dislocations separated by a generalized stacking fault. The fracture model has been applied to elucidating the relationships of fracture toughness, dislocation mobility, temperature, and alloy addition for a wide range of intermetallics. The conclusions reached in this investigation are as follows.

1. The fracture toughness of intermetallics can be related to dislocation mobility and described in terms of a thermally activated slip formulation.
2. The activated distance, area, and volume associated with a dislocation overcoming the P-N barrier in intermetallics are  $b$ ,  $b^2$ , and  $b^3$ , respectively.
3. Fracture toughness of intermetallics increases with decreasing values of the P-N barrier energy and the generalized stacking fault (stacking, antiphase boundary, and CSF) energies.
4. Fracture in intermetallics that are controlled by dislocation mobility can be identified by the P-N energy and the generalized stacking fault energy. A high apparent generalized stacking fault energy indicates that fracture may be controlled by dislocation nucleation at the crack tip.
5. The fracture toughness of intermetallics can be correlated in terms of the ratio of  $\gamma_s/(U_{P-N} + \gamma_{APB})$ .
6. The effects of alloying addition on fracture toughness can be predicted on the basis of its effects on the P-N barrier energy, stacking fault energy, or antiphase boundary energy.
7. The fracture model predicts the effects of slip vector on the fracture toughness in NiAl correctly and describes the dependence of fracture toughness of temperature reasonably well.
8. Fracture toughness of Ti-54.7Al appears to be controlled by dislocation nucleation.

## ACKNOWLEDGMENTS

This work was supported by the Air Force Office of Scientific Research through Contract No. F4962001-C-0016, Dr. Craig S. Hartley, Program Manager. Discussion of this article with Dr. David L. Davidson, SwRI (retired), is acknowledged. The clerical assistance by Ms. L. Salas, SwRI, in the preparation of the manuscript is appreciated.

## REFERENCES

1. *Structural Intermetallics*, R. Darolia, J.J. Lewandowski, C.T. Liu, P.L. Martin, D.B. Miracle, and M.V. Nathal, eds., TMS, Warrendale, PA, 1993.
2. *Structural Intermetallics*, M.V. Nathal, R. Darolia, C.T. Liu, P.L. Martin, D.B. Miracle, R. Wagner, and M. Yamaguchi, eds., TMS, Warrendale, PA, 1997.
3. *Structural Intermetallics*, K.J. Henker, D.M. Dimiduk, H. Clemens, R. Darolia, H. Inui, J.M. Larsen, V.K. Sikka, M. Thomas, and J.D. Whittenberger, eds., TMS, Warrendale, PA, 2001.
4. *Structural and Functional Intermetallics*, C.T. Liu, S.H. Whang, D.P. Pope, M. Yamaguchi, and H. Vehoff, eds., TMS, Warrendale, PA, 2000; *Mater. Sci. Eng. A*, 2002, vols. A329-A331.
5. *Gamma Titanium Aluminides*, Y.-W. Kim, R. Wanger, and M. Yamaguchi, eds., TMS, Warrendale, PA, 1995.
6. *High-Temperature Ordered Intermetallic Alloys IV*, MRS Symposium Proceedings, L.J. Johnson, D.P. Pope, and J.O. Stiegler, eds., MRS, Pittsburgh, PA, 1991, vol. 213.

7. *High-Temperature Ordered Intermetallic Alloys V*, MRS Symposium Proceedings, I. Baker, R. Darolia, J.D. Whittenberger, and M.H. Yoo, eds., MRS, Pittsburgh, PA, 1992, vol. 288.
8. *High-Temperature Ordered Intermetallic Alloys VI*, MRS Symposium Proceedings, Part I & II, J.A. Horton, I. Baker, S. Hanada, R.D. Noebe, and D.S. Schwartz, eds., MRS, Pittsburgh, PA, 1994, vol. 364.
9. *High-Temperature Ordered Intermetallic Alloys VIII*, MRS Symposium Proceedings, E.P. George, M.J. Mills, and M. Yamaguchi, eds., MRS, Pittsburgh, PA, 1998, vol. 552.
10. *Intermetallic Compounds—Principles and Practice*, J.J. Westbrook and R.L. Fleischer, eds., John Wiley & Sons, New York, NY, 2002, vol. 3.
11. *Intermetallic Compounds—Principles and Practice*, J.H. Westbrook and R.L. Fleischer, eds., John Wiley & Sons, New York, NY, 2002, vol. 3.
12. K.S. Chan: *Metall. Mater. Trans. A*, 2001, vol. 32A, pp. 2475-87.
13. K.S. Chan: in *Mechanisms and Mechanics of Fracture: The John F. Knott Symp.*, W.O. Soboyejo, J.J. Lewandowski, and R.O. Ritchie, eds., TMS, Warrendale, PA, 2002, pp. 143-48.
14. D. Farkas: *Mater. Sci. Eng.*, 1998, vol. A249, pp. 249-58.
15. U.V. Waghmare, E. Kaxiras, V.V. Bulatov, and M.S. Duesberry: *Modelling Simul. Mater. Sci. Eng.*, 1998, vol. 6, pp. 493-506.
16. G. Ghosh: *J. Phase Equilibrium*, 2002, vol. 34, pp. 310-28.
17. G.B. Olson: *Science*, 1997, vol. 277.
18. J.R. Rice: *J. Mech. Phys. Solids*, 1992, vol. 40, pp. 239-71.
19. P.B. Hirsch and S.G. Roberts: *Phil. Mag. A*, 1991, vol. 64, pp. 55-80.
20. S.G. Roberts and A.S. Booth: *Acta Mater.*, 1997, vol. 45, pp. 1045-53.
21. R.E. Peierls: *Proc. Phys. Soc.*, 1940, vol. 52, pp. 34-37.
22. F.R.N. Nabarro: *Proc. Phys. Soc.*, 1947, vol. 59, pp. 236-394.
23. K.S. Chan: *Mater. Sci. Eng.*, 2002, vols. A329-A331, pp. 513-22.
24. A.H.W. Ngan: *J. Mech. Phys. Solids*, 1997, vol. 45, pp. 903-21.
25. J.N. Wang: *Mater. Sci. Eng. A*, 1996, vol. A206, pp. 259-69.
26. J.N. Wang: *Acta Mater.*, 1996, vol. 44, pp. 1541-46.
27. A.J.E. Foreman: *Acta Metall.*, 1955, vol. 3, pp. 322-30.
28. G.R. Irwin: *Fracture Dynamics*, ASM, Cleveland, OH, 1948, pp. 147-66.
29. J.R. Rice: *J. Appl. Mech.*, 1968, pp. 379-86.
30. G.B. Gibbs: *Physica Status Solidi*, 1965, vol. 10, pp. 507-12.
31. K.S. Chan and D.L. Davidson: *Metall. Mater. Trans. A*, 1999, vol. 30A, pp. 925-39.
32. F. Ye, C. Mercer, and W.O. Soboyejo: *Metall. Mater. Trans. A*, 1998, vol. 29A, pp. 2361-74.
33. D.-H. Hou, J. Shyue, S.S. Yang, and H.L. Fraser: *Alloy Modelling and Design*, G.M. Stocks and P.E.A. Turchi, eds., TMS, Warrendale, PA, 1994, pp. 291-302.
34. D. Farkas, S.J. Zhou, C. Vacilhe, B. Mutasa, and J. Panova: *Mater. Res.*, 1997, vol. 12, pp. 93-99.
35. D.L. Davidson, K.S. Chan, and D.L. Anton: *Metall. Mater. Trans. A*, 1996, vol. 27A, pp. 3007-18.
36. R.M. Nekkanti and D.M. Dimiduk: *Materials Research Society Symposium Proceedings*, MRS, Pittsburgh, PA, 1990, vol. 194, pp. 175-82.
37. K. Chang, R. Darolia, and H. Lipsitt: *Acta Metall. Mater.*, 1992, vol. 1, pp. 2727-37.
38. G.P. Zhang, Z.G. Wang, and G.Y. Li: *Acta Mater.*, 1997, vol. 45, pp. 1705-14.
39. K.S. Chan, J. Onstott, and K.S. Kumar: *Metall. Mater. Trans. A*, 2000, vol. 31A, pp. 71-80.
40. A.S. Booth and S.G. Roberts: *Acta Mater.*, 1997, vol. 45, pp. 1045-53.
41. D.J. Thomas, K.A. Nibur, K.C. Chen, J.C. Cooley, L.B. Dauelsberg, W.L. Hulst, and P.G. Kotula: *Mater. Sci. Eng.*, 2002, vols. A329-A331, pp. 408-15.
42. K.C. Chen, S.M. Allen, and J.D. Livingston: *Mater. Sci. Eng.*, 1998, vol. A242, pp. 163-73.
43. ASTM E399-90, *Annual Book of ASTM Standards*, ASTM, Philadelphia, PA, 1995, vol. 03.01, pp. 412-42.
44. W.A. Rachinger and A.H. Cottrell: *Acta Metall.*, 1956, vol. 4, pp. 109-13.
45. M. Yamaguchi and Y. Umakoshi: *Prog. Mater. Sci.*, 1990, vol. 34, pp. 1-148.
46. P. Shechtman, M.J. Blackburn, and H.A. Lipsitt: *Metall. Trans.*, 1974, vol. 5, pp. 1373-81.
47. G. Hug, J. Douin, and P. Veyssiere: in *High Temperature Ordered Intermetallic Alloys III*, Materials Research Society Symposium Proceedings, C.T. Liu, A.I. Taub, N.S. Stoloff, and C.C. Koch, eds., MRS, Pittsburgh, PA, 1989, vol. 133, p. 125.
48. M. Yamaguchi, D.P. Pope, V. Vitek, and Y. Umakoshi: *Phil. Mag.*, 1981, vol. 43, p. 1265.
49. C. Woodward, J.M. MacLaren, and S. Rao: in *High Temperature Ordered Intermetallic Alloys IV*, Materials Research Society, Symposia Proceedings, MRS, Pittsburgh, PA, L.A. Johnson, D.P. Pope, and J.O. Stiegler, eds., 1991, vol. 213, p. 715.
50. S.I. Rao, C. Woodward, and T.A. Partharathy: in *High Temperature Ordered Intermetallic Alloys IV*, Materials Research Society, Symposia Proceedings, MRS, Pittsburgh, PA, L.A. Johnson, D.P. Pope, and J.O. Stiegler, eds., Mater. Res. Soc. Proceedings, 1991, vol. 213, p. 125.
51. C.L. Fu and M.H. Yoo: *Phil. Mag. Lett.*, 1990, vol. 62, pp. 159-65.
52. S.C. Huang and J.C. Chesnutt: in *Intermetallic Compounds—Principles and Practices*, J.H. Westbrook and R.L. Fleischer, eds., John Wiley & Sons, New York, NY, 1995, vol. 1, pp. 495-517.
53. S.C. Huang: *Metall. Trans. A*, 1992, vol. 23A, pp. 375; S. Mitao, S. Tsuyama, and K. Minakawa: *Mater. Sci. Eng. A*, 1992, vol. 143, p. 51.
54. S. Mitao, S. Tsuyama, and K. Minakawa: *Mater. Sci. Eng. A*, 1991, vol. 143, pp. 51-62.
55. S. Reuss and H. Vehoff: *Scripta Metall. Mater.*, 1990, vol. 24, pp. 1021-26.
56. K.S. Kumar, P. Wang, K. Chan, J. Arata, N. Bhates, J. Onstott, W. Curtin, and A. Needleman: in *Structural Intermetallics 2001*, K.J. Henker, D.M. Dimiduk, H. Clemens, R. Darolia, H. Inui, J.M. Larsen, V.K. Sikka, M. Thomas, and J.O. Whittenberger, eds., TMS, Warrendale, PA, 2001, pp. 249-58.
57. P. Wang, N. Bhate, K.S. Chan, and K.S. Kumar: *Acta Mater.*, 2003, vol. 51, pp. 1573-91.
58. P.M. Hazzledine and P. Pirouz: *Scripta Metall. Mater.*, 1993, vol. 28, pp. 1277-82.
59. P.M. Hazzledine, K.S. Kumar, D.B. Miracle, and A.G. Jackson: *Mater. Res. Soc. Symp. Proc.*, 1993, vol. 288, pp. 591-96.
60. F. Chu and D.P. Pope: *Materials Research Society Symposium Proceedings*, MRS, Pittsburgh, PA, 1995, vol. 365, pp. 1197-1208.
61. K.S. Chan and D.L. Davidson: *Metall. Mater. Trans. A*, 2003, vol. 34A, pp. 1833-49.
62. K. Ito, K. Ihara, K. Tanaka, M. Fujikura, and M. Yamaguchi: *Intermetallics*, 2001, vol. 9, pp. 591-602.
63. Y. Harada, M. Morinaga, J.I. Saito, and Y. Takagi: *J. Phys.: Condens. Matter*, 1997, vol. 9, pp. 8011-30.
64. Y.-Q. Sun: in *Intermetallic Compounds—Principles and Practice*, J.H. Westbrook and R.L. Fleischer, eds., John Wiley & Sons, New York, NY, 1995, vol. 1, pp. 495-517.
65. P.S. Flinn: *Trans. AIME*, 1966, vol. 239, pp. 145-54.
66. M.J. Marcinkowski: in *Treatise on Materials Science and Technology*, H. Herman, ed., Academic Press, New York, NY, 1974, vol. 5, pp. 181-287.
67. Q. Chen, V.S. Deshpande, E. Van der Giessen, and A. Needleman: *Scripta Mater.*, 2003, vol. 48, pp. 755-59.
68. P.G. Kotula, C.B. Carter, K.C. Chen, D.J. Thoma, F. Chu, and T.E. Mitchell: *Scripta Mater.*, 1998, vol. 29, pp. 619-23.
69. F. Chu, A.H. Ormeci, T.E. Mitchell, J.M. Wills, D.J. Thoma, R.C. Albers, and S.P. Chen: *Phil. Mag. Lett.*, 1995, vol. 72, pp. 147-53.
70. K. Ihara, K. Ito, K. Tanaka, and M. Yamaguchi: *Mater. Sci. Eng.*, 2002, vols. A329-A331, pp. 222-27.



**APPENDIX 3**

**"Computer-Assisted Design of Nb-Based In-Situ Composites and Superalloys"**

**Kwai S. Chan**

**Proceedings of THERMEC' 2003  
Materials Science Forum, Trans Tech Publications  
Volumes 426-432, (2003) pp. 2059-2064**

**2003**

Reprinted with permission from  
*Trans Tech Publications*, Zurich, Switzerland

## Computer-Assisted Design of Nb-Based *In-Situ* Composites and Superalloys

Kwai S. Chan

Southwest Research Institute, 6220 Culebra Road, San Antonio, TX 78238, USA

**Keywords:** computational alloy design, alloying effects, fracture toughness, Nb-based alloys, silicides, Laves phases, in-situ composites, Peierls-Nabarro barrier energy.

**Abstract:** This paper highlights a computer-assisted alloying approach for designing ductile Nb solid solution alloys. An extension of this approach to improve the fracture resistance of Nb-based silicides, Laves phases, and *in-situ* composites is described and its utility is evaluated against experimental data. Possible application of this approach to designing Nb-based superalloys containing a microstructure of Nb (bcc) solid solution with ordered B2 or L1<sub>2</sub> intermetallics is elucidated to identify potential obstacles.

### Introduction

Nb-based *in-situ* composites are multi-phase alloys that contain an Nb (bcc) solid solution phase and brittle intermetallic phases such as silicides and Laves phases. Depending on the alloy composition, as many as four silicides (Nb<sub>5</sub>Si<sub>3</sub>, Nb<sub>3</sub>Si, Ti<sub>5</sub>Si<sub>3</sub>, Ti<sub>3</sub>Si) and two Laves phases (C14 and C15) in alloyed forms can exist in the microstructure [1, 2]. The silicides and Laves phases are intended for providing high-temperature creep and oxidation resistance, while the Nb solid solution is intended to improve the ambient-temperature fracture resistance. Extensive research [1-5] has demonstrated that alloy addition can impart fracture resistance in the Nb solid solution, silicides, and Laves phases. The large number of potential alloying elements, however, makes the discovery of beneficial alloy additions a daunting task if undertaken by an empirical means alone.

There are considerable current interests in developing computational tools for designing materials with desired composition, microstructure, and performance [4, 6-10]. For designing against brittle fracture, recent computation work have focused on understanding the effects of alloying additions on (1) the unstable stacking energy [11] and the crack-tip dislocation emission process [3-6, 8-11], and (2) the Peierls-Nabarro (P-N) barrier energy and the mobility of dislocations moving away from the crack tip [3-6].

In this paper, a computer-assisted alloying approach for designing ductile Nb solid solution in *in-situ* composites is highlighted. Recent progress in extending this approach to designing alloy addition to improve the fracture resistance of silicides, Laves phases, and *in-situ* composites is then presented and compared against experimental data. Finally, potential application of this approach to designing Nb-based superalloys containing a microstructure of Nb (bcc) solid solution with ordered B2 or L1<sub>2</sub> intermetallics is examined to explore its feasibility.

### The Computational Approach

The transition of brittle-to-ductile fracture is generally viewed as a competition between the nucleation and the propagation of dislocations from the crack tip. The propensity to crack-tip nucleation is characterized in terms of the unstable stacking energy,  $\gamma_{us}$ , while the Peierls-Nabarro barrier energy,  $U_{P-N}$ , is used as a measure of the dislocation mobility. These two dislocation parameters are related through the relation given by [4]

$$U_{P-N} = \frac{8\pi^2 \gamma_{us}}{\sinh 2\psi}; \text{ with } \gamma_{us} = \frac{\kappa b^2}{2\pi^2 d} \text{ and } \psi = \frac{\pi \kappa d}{cb} \quad (1)$$

where  $b$  is Burgers vector;  $d$  is the slip plane spacing;  $\kappa$  is the dislocation line energy;  $\psi$  is a lattice phase angle which incorporates characteristics of the slip plane spacing ( $d$ ), slip direction ( $b$ ), dislocation character (edge, screw or mixed), and the elastic constant ( $c$ ) in the slip direction.

The fracture toughness and tensile ductility of metallic materials can be expressed in terms of the ratio of  $\gamma_s/U_{P-N}$ , where the surface energy,  $\gamma_s$ , is used as a measure of the material's propensity to cleavage fracture. Both  $U_{P-N}$  and  $\gamma_s/U_{P-N}$  can be altered by alloy additions [4, 6]. In particular, alloy addition can cause a small change in the lattice phase angle,  $\psi$ , that can result in a large increase or decrease in the  $U_{P-N}$ , leading to substantial changes in the dislocation mobility and fracture behavior. The strong dependence of  $U_{P-N}$  on alloy addition and a correlation developed between fracture resistance and the ratio of  $\gamma_s/U_{P-N}$  forms the foundation of the computational model for designing tough solid solution alloys [4]. The essential features of the computational model are: (1) the P-N barrier energy model, (2) the surface energy model, and (3) a ductility index in terms of the surface energy, P-N barrier energy, and the stacking fault energy if the materials have ordered crystal structures [6]. Detailed descriptions of the methods for computing the P-N barrier energy and the other energy parameters have been published [4, 6] and they will not repeated here. Instead, a summary of the application of this approach to designing fracture-resistant material is presented here with specific examples.

**Solid Solution Alloys.** Application of the computational methodology to designing ductile solid solution alloys based on the Nb-Ti-Cr system [4] is illustrated here. The solid solution phase boundary at ambient temperature was first estimated from the phase diagram. The P-N barrier energy, surface energy, and the corresponding  $\gamma_s/U_{P-N}$  energy ratio were then computed for the various solid solution alloys along the phase boundary. Once the values of  $\gamma_s/U_{P-N}$  were obtained, the corresponding tensile ductility and fracture toughness ( $K_{IC}$ ) were predicted through previously established relations of  $K_{IC}$  and tensile ductility expressed in terms of the  $\gamma_s/U_{P-N}$  parameter. The desired fracture properties and the corresponding alloy composition were then obtained by judicious alloy additions. For example, Figure 1(a) shows the design of tough Nb-Ti-Cr solid solution alloys through Ti addition [4]. To achieve a ductile alloy, Nb-Ti-Cr must contain at least 24% Ti in order to exhibit a fracture toughness of 25 MPa $\sqrt{m}$ . High fracture toughness ( $> 60$  MPa $\sqrt{m}$ ) are observed in alloys containing more than 40% Ti [3-4]. Though not shown explicitly in Figure 1(a), design of alloy composition is achieved by computing the effects of Ti and Cr additions on the P-N barrier energy, the  $\gamma_s/U_{P-N}$  ratio, and subsequently, the corresponding tensile ductility and fracture toughness. A comparison of the computed and measured fracture toughness of Nb-Ti-Cr solid solution alloys is shown in Figure 1(b) [4]. Since some of the experimental data were used to establish the  $K_{IC}$  and  $\gamma_s/U_{P-N}$  relation, Figure 1(b) is not an independent comparison of model prediction and experimental data. Nonetheless, the good agreement gives credence to the approach as an alloy design tool.

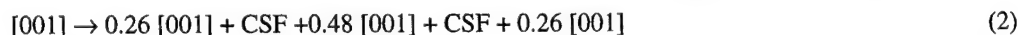
**Intermetallics.** The P-N barrier energies for several aluminides, silicides, and Laves phases were computed using Eq. (1) [6]. The unstable stacking energies for FeAl, NiAl, CoAl, Ni<sub>3</sub>Al, and TiAl were calculated by Farkas using an embedded atom method [8, 9]. These  $\gamma_{us}$  values were used in conjunction with Eq. (1) to obtain the P-N barrier energy. In addition,  $\gamma_s$  and  $\gamma_{APB}$  were also reported by Farkas [8, 9] and they were used to compute the energy ratios. For Nb<sub>5</sub>Si<sub>3</sub> and NbCr<sub>2</sub>,  $\gamma_{us}$  and  $\gamma_s$  by first principal calculations are not available. For these materials,  $\gamma_{us}$  values were estimated based on the Rice equation [11], while  $\gamma_s$  was assumed to be 2 J/m<sup>2</sup>, which is the typical value for most materials. The  $\gamma_s/(U_{P-N} + \gamma_{APB})$  ratios for NbCr<sub>2</sub> and Nb<sub>5</sub>Si<sub>3</sub> are less than 0.5, while the others range from 2 to 25. The  $\gamma_{APB}$  term is important in Ni<sub>3</sub>Al and TiAl since the  $\gamma_{APB}$  is considerably larger than the  $U_{P-N}$  [6]. Because  $\gamma_{APB}$  can be larger than  $U_{P-N}$ , the fracture toughness of the intermetallics correlates better with the  $\gamma_s/(U_{P-N} + \gamma_{APB})$  than with  $\gamma_s/U_{P-N}$ , as illustrated in Figure 2. The strong dependence of  $K_{IC}$  on the ratio  $\gamma_s/(U_{P-N} + \gamma_{APB})$ , which can be represented in



terms of a dislocation mobility-based model [12] provides an avenue for designing alloying addition to improve the fracture toughness of intermetallics by lowering  $\gamma_{us}$ ,  $U_{P-N}$ , and  $\gamma_{APB}$ .

The computation of unstable stacking and P-N barrier energies allows one to select alloy additions for improving the fracture resistance of intermetallics. This point is illustrated using examples of alloy additions in Nb-based Laves phases and silicides. Both NbCr<sub>2</sub> and TiCr<sub>2</sub> have a C15 (cubic) crystal structure and a fracture toughness of about 1 MPa√m at ambient temperature [3, 13]. A small (> 2 at %) addition of Si + Ge changes the C15 phase to the C14 phase (hexagonal), which is normally stable only at elevated temperatures. Energy calculations performed for synchroshear by a pair of  $1/6\langle\bar{2}11\rangle$  partial dislocations on a {111} layer [14] indicated that  $\gamma_{us} = 4.36 \text{ J/m}^2$  and  $U_{P-N} = 4.42$  for synchroshear in C15, Table 1. In contrast,  $\gamma_{us} = 2.24 \text{ J/m}^2$  and  $U_{P-N} = 0.43$  for  $\{0001\}1/3\langle\bar{1}0\bar{1}0\rangle$  synchroshear in C14 because of a more favorable d/b ratio. The lower values of  $\gamma_{us}$  and  $U_{P-N}$  suggest that synchroshear is easier in the C14 than in the C15 Laves phase. A Si or Ge addition to NbCr<sub>2</sub> should, therefore, improve the fracture resistance when the C14 phase is stabilized. Figure 3 shows that Si and Ge additions stabilize the C15 phase and improve the fracture toughness of NbCr<sub>2</sub> Laves phase from 1 MPa√m to about 2 to 5 MPa√m.

Nb<sub>5</sub>Si<sub>3</sub> can exist in the D8<sub>m</sub> or D8<sub>l</sub> crystal structure; both are body-centered tetragonal phases whose deformation mechanisms are still unknown. On the other hand, Ito et al. [14], have identified  $\langle 100 \rangle\{012\}$ ,  $\langle 100 \rangle\{001\}$ ,  $1/2\langle 111 \rangle\{110\}$  and  $\langle 110 \rangle\{001\}$  as possible slip systems in Mo<sub>5</sub>SiB<sub>2</sub> (T2 phase, D8<sub>l</sub> structure). Experimental evidence, however, indicates that  $[001](010)$  is the operative slip system in the T2 phase at 1500°C. Because of the complex D8<sub>l</sub> structure, slip in T2 appears to occur through the actions of three fractional  $[001]$  partial dislocations separated by two complex stacking faults (CSF) according to the dissociation reaction given by [15]



which was suggested by Ito et al. [15], through a consideration of the overlapping volume encountered by atoms on the slip plane. The overlapping volumes were computed by treating the atoms as hard balls [15]. The selection of slip systems in Nb<sub>5</sub>Si<sub>3</sub> and T2 are still poorly understood.

Theoretical calculation indicates that the dislocation dissociation reaction represented in Eq. (2) is energetically favorable and it leads to a significant reduction in both the unstable stacking and P-N barrier energies in Nb<sub>5</sub>Si<sub>3</sub> with the D8<sub>l</sub> crystal structure. As summarized in Table 1, the  $\gamma_{us}$  and  $U_{P-N}$  for  $[001](010)$  slip in Nb<sub>5</sub>Si<sub>3</sub> are 8.8 J/m<sup>2</sup> and 9.81 J/m<sup>2</sup>, respectively. In contrast, the  $\gamma_{us}$  and  $U_{P-N}$  are reduced to 3.25 J/m<sup>2</sup> and 0.01 J/m<sup>2</sup>, respectively, if slip occurs by the partial dislocation slip process described in Eq. (2). For comparison purposes, Table 1 presents the  $\gamma_{us}$  and  $U_{P-N}$  results for  $[001](010)$  slip in Mo<sub>5</sub>SiB<sub>2</sub> together with its fracture toughness (2 MPa√m) [16]. As in the case of Nb<sub>5</sub>Si<sub>3</sub>, both the  $\gamma_{us}$  and  $U_{P-N}$  results of Mo<sub>5</sub>SiB<sub>2</sub> are reduced when slip occurs by the passage of three fractional  $[001]$  partial dislocations separated by two CSF, rather than by a perfect  $[001]$  dislocation. Because of the low  $U_{P-N}$  value, dislocation mobility of the  $[001]$  partial dislocations is controlled by the energy of the complex stacking fault.

The fracture toughness of Nb<sub>5</sub>Si<sub>3</sub> has been found to improve with the additions of Ti and Hf. In particular, the fracture toughness of alloyed (Nb,Ti,Hf)<sub>5</sub>(Si,Cr,Ge)<sub>3</sub> silicide increases with increasing Ti addition but decreasing bond order, Figure 4 [12]. Bond order is a measure of the strength of the covalent bond between atoms and is computed on the basis of the overlapping electron population [17]. This enhancement of fracture resistance by Ti addition and its relation to bond order is not well understood. One possible mechanism is that Ti addition promotes the slip by the dissociated dislocation mechanism as described in Eq. (2). Previously, Ito et al. [15], suggested that the driving force for dislocation dissociation is the need to minimize the overlapping volume of atoms on the slip plane. Since Ti addition reduces the bond order of Nb<sub>5</sub>Si<sub>3</sub>, the overlapping volume may also be reduced by Ti additions. Such a reduction of the overlapping volume, if proven to occur, would promote the partial slip process and help explain the increase of fracture resistance in Nb<sub>5</sub>Si<sub>3</sub> alloyed with Ti addition.

**Nb-Based In-Situ Composites.** The preceding sections illustrate the importance of compositional design on the fracture resistance of individual phases in the in-situ composites. In addition to composition, the size, shape, and morphology of individual phases and processing condition are also important in determining the fracture resistance of Nb-based in-situ composites. Figure 5 shows a comparison of the  $K_{IC}$  of conventionally cast (CC) [12], directionally cast (DS), and extruded (EX) [2] Nb-based in-situ composites, which shows that the DS and EX materials exhibit a higher fracture toughness than the CC materials. In-situ fracture toughness testing revealed that the lower fracture toughness exhibited by the CC materials was the consequence of a relatively continuous silicide matrix phase, which exerted a high plastic constraint on the Nb solid solution such that the ductile-phase was ineffective and the resulting crack path resided almost entirely in the silicide and Laves phases [12]. The observed fracture behavior is consistent with the fracture toughness values computed for composites with a high plastic constraint using a fracture toughness model formulated on the basis of crack trapping and bridging mechanisms [18].

The fracture toughness of Ni-based superalloys with the  $\gamma/\gamma'$  microstructure is on the order of 70-100 MPa $\sqrt{m}$  at ambient temperature. The high fracture resistance originates from the high toughness of individual  $\gamma$  and  $\gamma'$  ( $Ni_3Al$ , Figure 2) phases, as well as a microstructure of  $\gamma'$  particles embedded in a continuous  $\gamma$  matrix separated by a coherent interface. In contrast, the intermetallic phases in Nb-based in-situ composites exhibit considerably lower fracture toughness and a higher degree of contiguity. Both the properties of individual phases and the microstructure contribute to the low fracture resistance observed in Nb-based in-situ composites. To achieve a less constrained microstructure, Nb-based superalloys may be developed on the basis of a microstructure of B2 and bcc Nb solid solution. Unfortunately, the B2 alloys have been shown to exhibit high tensile ductility and fracture resistance at ambient temperature, but lack creep and oxidation resistance at elevated temperatures [19]. Alternately, Nb-based superalloys may be developed to exhibit a microstructure that comprised of  $L1_2$  phases embedded in a Nb solid solution; this approach is currently being pursued by researchers at Northwestern University [20].

### Summary

This paper presents a brief overview on the use of a computational approach to design alloy composition with desired fracture performance. The approach has been applied successfully to design ductile Nb-based solution alloys. Improved fracture resistance of Nb-based silicides and Laves phases has been obtained via this approach. On the other hand, only small improvements in the fracture resistance of conventionally cast Nb-based in-situ composites have been realized because of a high plastic constraint and the contiguity of the intermetallic phases prevent the occurrence of ductile phase toughening of Nb solid solution in the in-situ composites.

### Acknowledgements

This work was supported by the Air Force Office of Scientific Research through Contract No. F4962001-C-0016, Dr. Craig S. Hartley, Program Manager. Discussion of this work with Dr. David L. Davidson (SwRI<sup>®</sup>, retired) is acknowledged. Clerical assistance by Ms. L. Salas, SwRI, in preparing this manuscript is appreciated.

### References

- [1] B.P. Bewlay, M.R. Jackson, and H.A. Lipsitt: *Metall. Mater. Trans. A*, Vol. 27A (1996), pp. 3801-3808.
- [2] P.R. Subramanian, M. G. Mendiratta, D.M. Dimiduk, and M.A. Stucke: *Mat. Sci. Eng.*, Vol. A239-340 (1997), pp. 1-13.
- [3] D.L. Davidson, K.S. Chan, and D.L. Anton: *Metall. Mat. Trans. A*, Vol. 27A (1996), pp. 3007-3018.

- [4] K.S. Chan: *Metall. Mater. Trans. A*, Vol. 32A (2001), pp. 2475-2487.
- [5] K.S. Chan: *Mater. Sci. Eng.*, Vol. A329-331 (2002), pp. 513-522.
- [6] K.S. Chan: *Mechanisms and Mechanics of Fracture: The John F. Knott Symposium*, edited by W.O. Soboyejo, J.J. Lewandowski, and R.O. Ritchie, TMS, Warrendale, PA (2002), pp. 143-148.
- [7] G.B. Olson: *Science*, Vol. 277, 29 August (1997), pp. 1237-1242.
- [8] U.V. Waghmare, E. Kaxiras, V.V. Bulatov, and M.S. Duesberry: *Modelling Simul. Mater. Sci. Eng.*, Vol. 6 (1998), pp. 493-506.
- [9] D. Farkas, S.J. Zhou, C. Vacilhé, B. Mutasa, and J. Panova: *Mater. Res.*, Vol. 12 (1977), pp. 93-99.
- [10] D. Farkas: *Mater. Sci. Eng.*, Vol. A249 (1998), pp. 249-258.
- [11] J. R. Rice: *J. Mech. Phys. Solids*, Vol. 40 (1992), pp. 239-271.
- [12] K.S. Chan: Southwest Research Institute, Unpublished Research (2002).
- [13] D.J. Thomas, K.A. Nibur, K.C. Chen, J.C. Cooley, L.B. Dauelsberg, W.L. Hults, and P.G. Kotula: *Mat. Sci. Eng.*, Vol. A329-331 (2002), pp. 408-415.
- [14] P.M. Hazzledine, K.S. Kumar, D.B. Miracle, and A.G. Jackson: *Mat. Res. Soc. Symp. Proc.*, Vol. 288 (1993), pp. 591-596.
- [15] K. Ito, K. Ihara, K. Tanaka, M. Fujikura, and M. Yamaguchi: *Intermetallics*, Vol. 9 (2001), pp. 591-602.
- [16] K. Ihara, K. Ito, K. Tanaka, and M. Yamaguchi: *Mat. Sci. Eng.*, Vol. A329-331 (2002), pp. 222-227.
- [17] Y. Harada, M. Morinaga, J.I. Saito, and Y. Takagi: *J. Phys: Condens. Matter.*, Vol. 9 (1997), pp. 8011-8030.
- [18] K.S. Chan and D.L. Davidson: *Metall. Mater. Trans. A*, Vol. 32A (2001), pp. 2717-2727.
- [19] F. Ye, C. Mercer, and W.O. Soboyejo: *Metall. Mater. Trans. A*, Vol. 29A (1998), pp. 2361-2374.
- [20] G.B. Olson: Department of Mat. Sci. and Eng., Northwestern University, Evanston, IL.

Material	Crystal Structure	Slip System	$\gamma_{us}$ , J/m <sup>2</sup>	$\gamma_s$ , J/m <sup>2</sup>	$U_{P-N}$ , J/m <sup>2</sup>	$\gamma_{APB}$ , J/m <sup>2</sup>	$\gamma_s/(U_{P-N} + \gamma_{APB})$	$K_C$ , MPa $\sqrt{m}$
NbCr <sub>2</sub>	C15	{111}1/6<211> synchroshear	4.36	2	4.42	.038	0.45	1
(Nb,Ti,Hf)(Cr,Si,Ge) <sub>2</sub>	C14	{0001}1/3<1010> synchroshear	2.24	2	0.43	.038	4.27	2-5
Nb <sub>5</sub> Si <sub>3</sub>	D8 <sub>1</sub>	[001](010)	8.88	2	9.81	0	0.21	3
(Nb,Ti,Hf) <sub>5</sub> (Si,Ge, Cr) <sub>3</sub>	D8 <sub>1</sub>	[001] partials on (010)	3.25	2	0.01	.048	3.92	6-10
Mo <sub>5</sub> SiB <sub>2</sub>	D8 <sub>1</sub>	[001](010)	15.1	2	18.1	0	0.11	2 [16]
	D8 <sub>1</sub>	[001] partials on (010)	4.2	2	2E-6	0.89 [16]	2.25	2 [16]

Table 1. A Summary of  $\gamma_{us}$ ,  $\gamma_s$ ,  $U_{P-N}$ ,  $\gamma_{APB}$ ,  $\gamma_s/(U_{P-N} + \gamma_{APB})$ , and  $K_C$  of NbCr<sub>2</sub>, Nb<sub>5</sub>Si<sub>3</sub>, and Mo<sub>5</sub>SiB<sub>2</sub> Intermetallics. The Value of Surface Energy,  $\gamma_s$ , was assumed to be 2 J/m<sup>2</sup>.

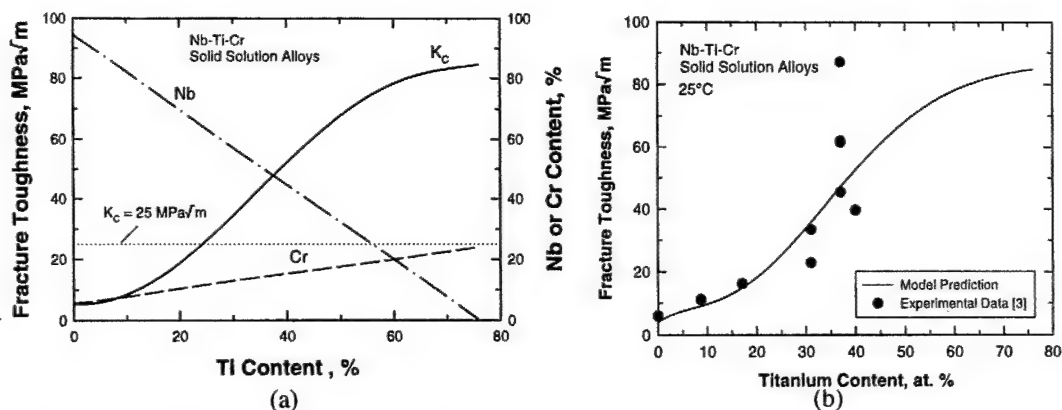


Figure 1. Computational design of a ductile Nb-Ti-Cr solid solution alloy: (a) computational results, and (b) comparison of computed and measured fracture toughness ( $K_C$ ) values [4].

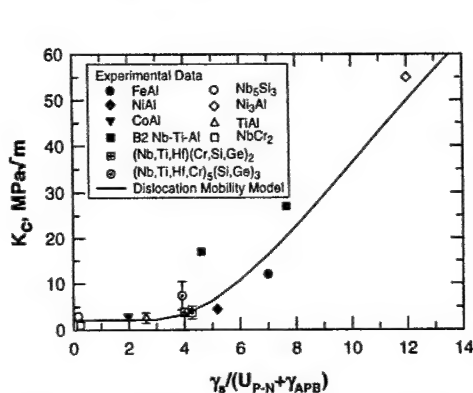


Figure 2. Dependence of fracture toughness,  $K_C$ , on the  $\gamma_s/(U_{P-N} + \gamma_{APB})$  ratio of various intermetallics. Source of data are given in [6].

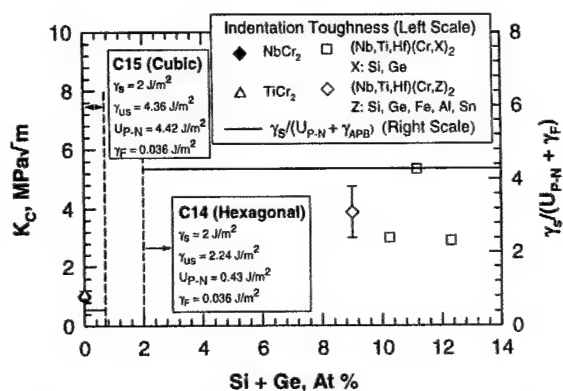


Figure 3. Additions of Si and Ge in NbCr<sub>2</sub> stabilize C14 and lower the  $\gamma_{us}$  and  $U_{P-N}$  values, leading to an increase in the  $\gamma_s/(U_{P-N} + \gamma_F)$  ratio and fracture toughness. Data are from [3, 12, 13].

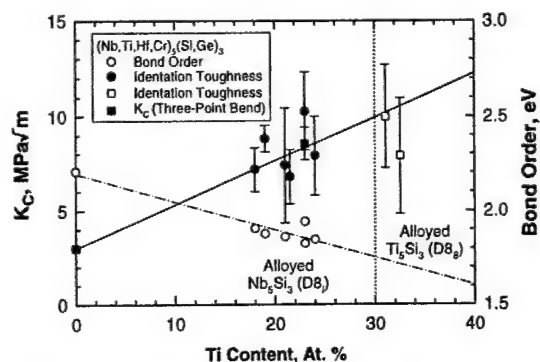


Figure 4. Dependence of fracture toughness and bond order on titanium content in alloyed Nb<sub>5</sub>Si<sub>3</sub> silicide [12].

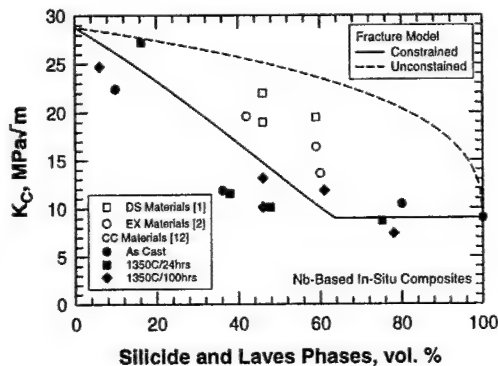


Figure 5. Fracture toughness of Nb-based in-situ composites as a function of volume % of silicide and Laves phases [12].

## **APPENDIX 4**

### **"Brittle-To-Ductile Fracture Transition in Nb-Based Alloys and Intermetallics"**

**Kwai S. Chan**

**Proceedings of the John Knott Symposium  
Edited by W. O. Soboyejo, J. T. Lewandowski, and R. O. Ritchie  
TMS, Warrendale, PA, (2002) pp. 143-148**

**December 2002**

Reprinted with permission from  
*The Minerals, Metals, and Materials Society, Warrendale, PA*

# BRITTLE-TO-DUCTILE FRACTURE TRANSITION IN Nb-BASED ALLOYS AND INTERMETALLICS

Kwai S. Chan

Southwest Research Institute  
6220 Culebra Road  
San Antonio, Texas 78238

## Abstract

The transition of brittle-to-ductile fracture in Nb-based alloys and intermetallics is assessed on the basis of the emission or propagation of dislocations from a crack tip. Analytical models have been developed and used to compute the surface energy ( $\gamma_s$ ), unstable stacking energy ( $\gamma_{us}$ ), and Peierls-Nabarro barrier energy ( $U_{P-N}$ ). The use of energy ratios based on these parameters for predicting brittle-to-ductile fracture transition is evaluated for Nb-based solid solution alloys and B2 intermetallics. These analytical models are then applied to predict alloying additions that would result in solid solution toughening in Nb-based alloys and B2 intermetallics. Possible application of this approach to toughen silicides and Laves phases are discussed.

## Introduction

Nb-based in-situ composites generally contain a multiphase microstructure of silicides, Laves phases, and a Nb solid-solution phase. The intermetallic phases are intended to provide high-temperature strength and oxidation resistance, while the Nb solid solution is intended to provide low-temperature tensile ductility and fracture resistance [1, 2].

The fracture resistance of Nb-based in-situ composites is provided by the Nb solid solution through several ductile-phase toughening mechanisms such as crack-tip blunting, crack trapping and ligament bridging [3]. Because of this, the tensile ductility and fracture toughness of the Nb solid solution phase are important factors affecting the fracture properties of the in-situ composites. On the other hand, many alloying elements (e.g., Cr and Al) that enhance oxidation resistance can embrittle Nb solid solution or vice versa. Consequently, alloying additions to improve the oxidation, fracture, and creep resistance of Nb-based in-situ composites must be optimized and controlled judiciously.

To aid the development of new Nb-based in-situ composites, the present author has developed a computational method for designing ductile Nb solid solutions that contain Ti, Al, and Cr additions [4]. The method is based on the computations of the surface energy ( $\gamma_s$ ) and the Peierls-Nabarro (P-N) [5, 6] barrier energy ( $U_{P-N}$ ) as a function of alloy contents. The surface energy is taken as a measure of the propensity to cleavage fracture, while the P-N barrier energy is taken as a measure of dislocation mobility. For many bcc Nb-Ti-Cr-Al alloys, brittle-to-ductile fracture occurs when the ratio of  $\gamma_s/U_{P-N}$  exceeds a critical value.

Design of ductile Nb solid solutions based on the critical  $\gamma_s/U_{P-N}$  criterion has been demonstrated for bcc Nb-Ti-Cr-Al [4].

In this article, the computational method is broadened to treat (1) alloy additions such as Hf, Zr, V, Ta, Mo, W, and Re, (2) B2 Nb-Ti-Al-X ordered intermetallic alloys, and (3) silicides and Laves phases. In particular, the effects of alloying addition on the ductile-to-brittle fracture transitions in binary Nb-X solid solution alloys and in B2 Nb-Ti-Al-X are examined first; the approach is then extended to consider fracture in silicides, Laves phases, and aluminides. Computational results will be presented and compared against available experimental data in the literature. All compositions are in atom percent unless specified otherwise.

## The Alloy Design Methodology

The essential features of the computational model for designing ductile Nb alloys are: (1) the Peierls-Nabarro barrier energy model, (2) the surface energy model, and (3) a ductility index in terms of the surface energy, P-N barrier energy, and the stacking fault energy.

### (1) The Peierls-Nabarro Barrier Energy Model

In the absence of thermal activation, the minimum energy required to move a dislocation rigidly and irreversibly through a discrete, periodic lattice is the Peierls-Nabarro barrier energy [5, 6]. This energy parameter can be viewed as the maximum resistance of the discrete lattice to dislocation motion and used as a measure of dislocation mobility. Calculation of the lattice resistance was first made by Peierls [5] and Nabarro [6], with subsequent modifications [7-9]. The P-N barrier energy for an anisotropic solid is given by [4, 7]

$$U_{P-N} = 4\pi^2 \gamma_{us} \left[ \frac{1}{\cosh \psi \sinh \psi} \right] \quad (1)$$

with

$$\gamma_{us} = \frac{\kappa b^2}{2\pi^2 d} \quad (2)$$

$$\psi = \frac{\pi \kappa d}{cb} \quad (3)$$

$$c = \frac{1}{3}(c_{11} - c_{12} + c_{44}) \quad (4)$$

Mechanisms and Mechanics of Fracture:

The John Knott Symposium

Edited by W.O. Soboyejo, J.J. Lewandowski and R.O. Ritchie  
TMS (The Minerals, Metals & Materials Society), 2002

where  $b$  is Burgers vector;  $d$  is the slip plane spacing;  $\gamma_{US}$  is the unstable stacking energy;  $\kappa$  is the dislocation line energy;  $\psi$  is a lattice phase angle which incorporates characteristics of the slip plane spacing ( $d$ ), slip direction ( $b$ ), dislocation character (edge, screw or mixed), and elastic constants ( $c_{ij}$ ) in the slip direction.

Calculation of the P-N barrier energy requires knowledge of the lattice parameter and the elastic properties of the alloy system. For Nb-X systems, the lattice parameter,  $a_0$ , is expressed in terms of alloy composition according to

$$a_0 (\text{\AA}) = 3.32X_{Nb} + 2.88X_{Ti} + 3.33X_{Cr} + 3.05X_{Al} + \dots + a_n X_n \quad (5)$$

where  $X_{Nb}$ ,  $X_{Ti}$ ,  $X_{Cr}$ ,  $X_{Al}$ , and  $X_n$  are the atomic fractions of Nb, Ti, Cr, Al, and element  $X_n$  in the Nb-Ti-Cr-Al- $X_n$  solid solution alloy, respectively;  $a_n$  is the lattice parameter of  $X_n$  in the bcc structure;  $X_n$  represents one of the transition elements from a group that includes Zr, Hf, V, Ta, Mo, W, and Re. Eq. (5) has been developed based on the rule of mixtures and the experimental data of lattice parameter of individual alloying elements in the bcc crystal structure. The lattice parameter of bcc Al, which is nominally fcc, was estimated based on the value reported by Diplas et al. [10]. This expression has been validated for several Nb-Ti-Cr, Nb-Ti-Cr, and Nb-Ti-Cr-Al solid solution alloys by comparing calculated elastic moduli against experimental data from the literature. Values of  $a_n$  are summarized in Table I.

Table I. Summary of  $a_n$  and  $t_n$  for Various Nb-X Solid Solution Alloys

X	Hf	Zr	V	Ta	Mo	W	Re
$a_n (\text{\AA})$	3.33	3.62	3.039	3.303	3.147	3.165	3.61
$t_n (K)$	-730	-1560	-1340	550	78	200	0

The elastic constants,  $c_{ij}$ , are expressed in terms of the  $d + s$  electrons in the alloy through a set of 7<sup>th</sup> order polynomials that were established based on experimental data of elastic constants for a number of bcc metals [4]. The expressions for the elastic constants are as follows:

$$c_{ij} = \sum_{n=0}^{n=7} p_n q^n \quad (6)$$

where  $q$  is the number of  $d + s$  electrons per atom in the alloy and  $p_n$  are the correlation coefficients obtained by regression analyses. The values for the number of  $d + s$  electrons per atom are 4, 5, 6, 7 for IVB (Ti, Zr, and Hf), VB (Cr, Mo, and W), VIB (Cr, Mo, and W), and VIIB (Re) elements, respectively. An apparent  $d + s$  value of 6 is used for Al because of contribution of  $p$  electrons to bonding in the  $d + s$  orbitals [10]. The regression analyses have been performed for  $c_{11}$ ,  $c_{12}$ , and  $c_{44}$  only because of the cubic symmetry in the bcc crystal structure.

## (2) Surface Energy Model

An empirical relation between surface energy, melting point, and the nearest atom spacing was established by Reynolds et al. [11]. This relation is given by [11]

$$\gamma_s (J/m^2) = 0.76 + 6.3604 \times 10^{-3} \left[ \frac{T_m}{a_0} \right] \quad (7)$$

where  $\gamma_s$  is surface energy in  $J/m^2$ ,  $T_m$  is melting point in  $^{\circ}K$ , and  $a_0$  is the lattice parameter in  $\text{\AA}$ . Eq. (7) was obtained by equating the nearest atom spacing to the Burgers vector and substituted the result into the empirical expression of Reynolds et al. [11]. This relation allows prediction of the surface energy of a metal or alloy once the melting point and lattice parameter are known. The melting points of the Nb-based solid solutions containing Ti, Cr, Al, and  $X_n$  additions are given by

$$T_m (^{\circ}K) = 2.742 \times 10^3 - 4.57 \times 10^2 X_{Ti} - 3.04 \times 10^3 X_{Cr} - (3 \times 10^3 X_{Ti} + 1000) X_{Al} + \dots + t_n X_n \quad (8)$$

where  $t_n$  is the change of melting point per atom fraction of  $X_n$ . Values of  $t_n$  are tabulated in Table I. Eq. (8) has been developed based on the binary phase diagrams of the Nb-Ti, Nb-Cr, Nb-Al, Nb-X, and ternary Nb-Ti-Cr alloys. The incorporation of Eq. (8) into the Reynolds correlation, Eq. (7), allows one to compute the surface energy as function of alloy compositions. Since the Reynolds correlation was derived using pure elements, not alloys, there is likely to be error in the value of the surface energy computed for alloys using this method but no other method was found to make this estimate. The application of the Reynolds correlation to alloys is valid as long as changes in the surface energy due to alloying is reflected as changes in the melting point of the alloys.

## (3) Ductility Index

According to the theory proposed by Ritchie, Knott, and Rice, [12] cleavage fracture occurs when the stress at a characteristic distance ahead of the crack tip reaches the cleavage fracture stress. A brittle-to-ductile fracture transition results when crack-tip plastic deformation limits the near-tip stress and prevent it from exceeding the cleavage fracture stress. Several energy ratios have been proposed as possible indices for indicating crack-tip ductile behavior. Rice suggested that the ratio of the surface energy to the unstable stacking energy ( $\gamma_s/\gamma_{US}$ ) can be used as a measure of the propensity for brittle fracture and also as a criterion for brittle-to-ductile transition [13]. The  $\gamma_s/\gamma_{US}$  ratio has been used by Farkas [14, 15] and Waghmare et al. [16] as the basis for selecting ternary alloying additions to improve the ductility of several intermetallics by first principle calculations of  $\gamma_s$  and  $\gamma_{US}$ .

When the nucleation of dislocations at the crack tip is relatively easy or preexisting dislocations are present, the mobility of dislocations moving away from the crack tip dictates the mode of fracture. Under this circumstance, brittle-to-ductile fracture transition is described by the energy ratio of  $\gamma_s/U_{P-N}$ . Work on Nb-Ti-Cr has shown that the energy ratio of  $\gamma_s/U_{P-N}$  is a better indicator than  $\gamma_s/\gamma_{US}$  for predicting the brittle-to ductile fracture transition in Nb solid solution alloys [17].

To encompass both approaches, a ductility index,  $\beta$ , may be defined as

$$\beta = \frac{\gamma_s}{\gamma_n + U_{P-N} + \gamma_{SF}} \quad (9)$$

where  $\gamma_n$  is the energy for dislocation nucleation and  $\gamma_{SF}$  is the stacking fault energy. In general,  $\gamma_n = \gamma_{US}$ . For many metals,



dislocation nucleation is not necessary due to the presence of preexisting dislocations, then  $\gamma_n$  may be taken as zero. The  $\gamma_{SF}$  term is included in Eq. (9) to account for a reduction in the dislocation mobility by a stacking fault or by an anti-phase boundary in an ordered lattice [8].

### Model Applications

The model was applied to compute the ratio of surface energy to the Peierls-Nabarro barrier energy for a number of Nb-based solid solution alloys, which include binary Nb-X and the B2 phase of Nb-Ti-Al-X. The input to these calculations was the alloy composition. Based on the number of  $d + s$  electrons/atom for the specified alloy composition, the analytical model computed the elastic moduli, the P-N barrier energy, the surface energy, and then the energy ratio. In all cases, P-N calculations were performed for  $(110)[\bar{1}\bar{1}1]$  slip by edge dislocations. Preexisting dislocations were assumed to be present so that dislocation nucleation was unnecessary and  $\gamma_n$  was taken to be zero. For Nb-X solid solution alloys,  $\gamma_{SF} = 0$  because only edge dislocations were considered. Experimental values of the anti-phase boundary energy, which are in the range of 0.015 - 0.18 J/m<sup>2</sup> [18], were used in the calculations for B2 Nb-Ti-Al alloys. Finally, the P-N barrier energy and ductility index for several aluminides, Nb<sub>5</sub>Si<sub>3</sub>, and NbCr<sub>2</sub> were computed using  $\gamma_{US}$  and  $\gamma_{APB}$  information in the literature.

### Binary Nb-X Alloys

The calculated values of  $\gamma_s$  and  $\gamma_{US}$  are relatively constant and do not vary with alloying addition. In constant, the P-N barrier energy vary significantly with alloying addition. Consequently, the ductility index, which is the ratio of  $\gamma_s/U_{P-N}$ , is a strong function of alloying addition, Figure 1. The results in Figure 1 indicate that alloying additions of Ti, Zr, and Hf up to the amount indicated in the parenthesis increases the ductility index of Nb-X solid solution. Two-phase alloys form when the alloy content exceeds 5 at.% Zr or 10 at.% Hf. V and Ta have small effects on the ductility index of Nb-V and Nb-Ta alloys. In contrast, Cr, Al, Mo, W, and Re all decrease the ductility index.

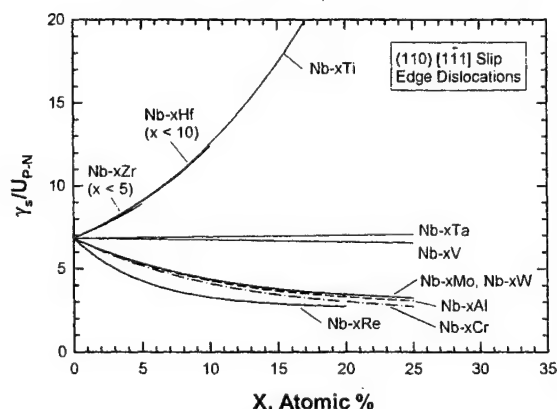


Figure 1. Computed values of  $\gamma_s/U_{P-N}$  as a function of alloying addition for various Nb-X solid solution alloys.

An increasing ductility index means the ductility is improved, while the opposite is true when the ductility index is reduced. The implications of these results are: (1) Zr, Hf, and Ti improve the tensile ductility, (2) V and Ta have small effects,

and (3) Cr, Al, Mo, W, and Re decrease the tensile ductility of Nb-X alloys. These predictions are qualitatively in agreement with experimental data shown in Figure 2 [19]. Re, Cr, Al, W, and Mo all increase the brittle-to-ductile fracture transition (BTDT) temperature. Zr increases the BTDT temperature, but it needs to be excluded because the Zr content exceeds the solid solution limit. Ti and Hf have no effects on the BTDT as long as the alloy content is within the solubility limit (< 10% for Hf; no limit for Ti). The model also predicted the increase in the BTDT temperature by alloying additions in the correct order.

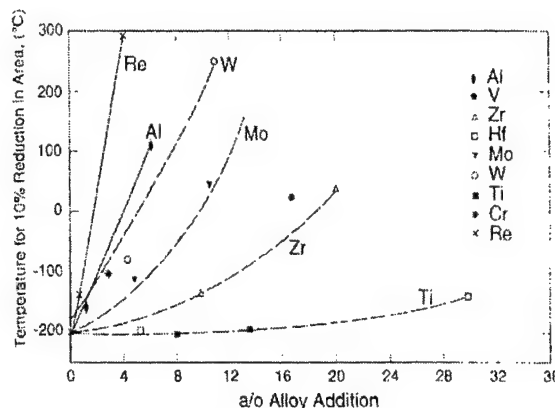


Figure 2. Effect of binary alloy additions on the brittle-to-ductile fracture transition temperature of Nb (from R. T. Begley [19]).

### B2 Nb-Ti-Al-X Alloys

The ductility index was computed for  $(110)[\bar{1}\bar{1}1]$  slip by edge dislocations in Nb-xTi-15Al. Calculations were made for four different values of the antiphase boundary energy ( $\gamma_{APB}$ ), ranging from 0 to 0.18 J/m<sup>2</sup>, as  $\gamma_{APB}$  varies with Ti content. In particular,  $\gamma_{APB}$  is 0.015 J/m<sup>2</sup> for Nb-40Ti-15Al, but it is 0.18 J/m<sup>2</sup> for Nb-10Ti-15Al [18]. As shown in Figure 3, the ductility index is computed for  $\gamma_{APB} = 0, 0.015$ , and 0.18 J/m<sup>2</sup>. In the fourth case,  $\gamma_{APB}$  is assumed to vary with Ti content as follows:

$$\begin{aligned} \gamma_{APB} &= 0.18 \text{ J/m}^2 \text{ for } X_n \leq 10 \text{ at.}\%; \\ \gamma_{APB} &= 0.235 - 5.5E-3X_n \text{ J/m}^2 \text{ for } 10 \text{ at.}\% < X_n < 40 \text{ at.}\%; \\ \gamma_{APB} &= 0.015 \text{ J/m}^2 \text{ for } X_n \geq 40 \text{ at.}\%. \end{aligned} \quad (10)$$

Figure 3 indicates that the ductility index of B2 Nb-xTi-15Al increases with increasing Ti contents. A higher ductility index is obtained when  $\gamma_{APB}$  is zero or very small. A  $\gamma_{APB}$  value as small as 0.18 J/m<sup>2</sup> reduces the ductility index significantly because its magnitude is comparable to  $U_{P-N}$ .

A fair number of Nb-Ti-Al-X alloys are known to exhibit the B2 structure and they are listed in Table II. The computed values of  $\gamma_s$ ,  $U_{P-N}$ , and the ductility index for  $(110)[\bar{1}\bar{1}1]$  slip in these alloys by edge dislocations are presented in Table II, which also shows the tensile elongation data [18, 20-23]. The values of  $\gamma_{APB}$  for these alloys are mostly unknown and they have been estimated based on Eq. (10). Table II indicates that the  $\gamma_s/U_{P-N}$  ratio of these B2 alloys ranges from 6 to 86 when  $\gamma_{APB}$  is ignored. In contrast, the  $\gamma_s/(U_{P-N} + \gamma_{APB})$  ratio ranges from 3.6 to 43.6 when  $\gamma_{APB}$  is included. In general, Al and Mo additions decrease

the ductility index, while Ti additions increase it. Both  $\gamma_S/U_{P-N}$  and  $\gamma_S/(U_{P-N} + \gamma_{APB})$  correlate well with the tensile elongation data reported for the B2 alloys, but the available data are limited.

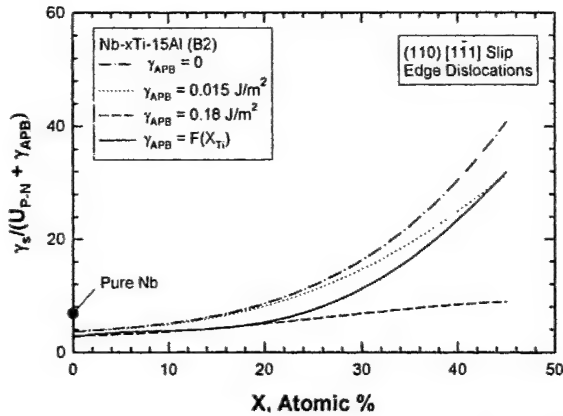


Figure 3. Computed values of  $\gamma_S/(U_{P-N} + \gamma_{APB})$  for Nb-xTi-15Al solid solution alloys with the B2 structure.  $\gamma_{APB} = F(X_{Ti})$  indicates  $\gamma_{APB}$  is a function of  $X_{Ti}$  as given in Eq. (10).

The ductility index has been used to correlate with tensile elongation and fracture toughness of disordered Nb-Ti-Cr-Al alloys as well as ordered B2 Nb-Ti-Al alloys. Least-square fits with 4<sup>th</sup> order polynomial function was used as shown in Figure 4. The correlation for the tensile elongation indicates that the tensile elongation increase with the ductility index.

Furthermore, the ductility index must exceed 14 in order to obtain at least 4% tensile elongation. The tensile elongation is nil when the ductility index is less than 10. Thus,  $\beta \geq 10$  may be used as a BTDT criterion for Nb-Ti-Cr-Al solid solution alloys.

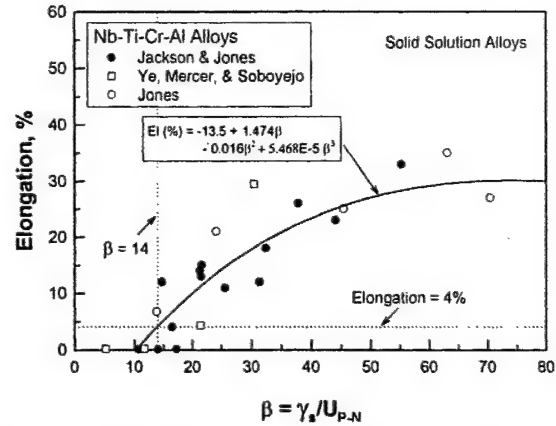


Figure 4. Correlation of tensile elongation, El, against  $\gamma_S/U_{P-N}$  for Nb-Ti-Al and Nb-Ti-Cr-Al alloys. A tensile elongation of 4 pct. requires  $\gamma_S/U_{P-N} \geq .14$ . Experimental data are from Jackson and Jones [21], Jones [20], and from Ye et al. [22] (from Chan [4]).

Table II. Computed Values of  $U_{P-N}$ ,  $\gamma_S$ ,  $\gamma_{APB}$ ,  $\gamma_S/U_{P-N}$ , and  $\gamma_S/(U_{P-N} + \gamma_{APB})$  Compared Against Tensile Elongation for Various B2 Nb-Ti-Al-X Alloys

B2 Alloy	$U_{P-N}$ , J/m <sup>2</sup>	$\gamma_S$ , J/m <sup>2</sup>	$\gamma_{APB}$ , J/m <sup>2</sup>	Ductility Index		Tensile Elongation, %
				$\gamma_S/U_{P-N}$	$\gamma_S/(U_{P-N} + \gamma_{APB})$	
Nb-10Ti-15Al [18, 22]	0.441	2.251	0.18	5.1	3.6	0-0.17 [18, 22]
Nb-25Ti-15Al [22]	0.185	2.166	0.098*	11.7	7.7	0.19 [22]
Nb-30Ti-15Al [24]	0.132	2.138	0.07*	16.2	10.6	—
Nb-40Ti-15Al [18, 22]	0.068	2.082	0.015	30.6	25.1	20-30 [18, 22]
Nb-50Ti-25Al [24]	0.068	1.896	0.015*	27.9	22.8	—
Nb-50Ti-38Al [24]	0.154	1.726	0.015*	11.2	10.2	—
Nb-62Ti-20Al [24]	0.028	1.879	0.015*	86.2	43.6	—
Nb-34Ti-17Al-17Mo [24]	0.340	2.041	0.048*	6.0	5.3	—
Nb-40Ti-12Al-1.5Mo [23]	0.062	2.110	0.015*	33.9	27.4	11.4 [23]
Nb-31Ti-13Al-5Cr [20]	0.150	2.078	0.07*	13.8	9.4	11.8 [20]

\* Computed based on Eq. (10).

#### Aluminides, Silicides, and Laves Phases

The P-N barrier energy for several aluminides, silicides, and Laves phases were estimated using Eq. (1). Isotropic elastic materials were assumed so that  $\kappa = 1$  in Eq. (2) and  $\kappa = 1/(1-\nu)$  in Eq. (3), where  $\nu$  is the Poisson's ratio and the elastic-constant  $c$  was computed based on Young's and shear moduli. Farkas previously computed the unstable stacking fault energies for FeAl, NiAl, CoAl, Ni<sub>3</sub>Al, and TiAl using an embedded atom method (EAM) [14, 15]. These  $\gamma_{US}$  values were used in conjunction with Eq. (1) to obtain the P-N barrier energy.  $\gamma_S$  and  $\gamma_{APB}$  were also reported by Farkas [14, 15] and they were used to compute the energy ratios. For Nb<sub>3</sub>Si<sub>3</sub> and NbCr<sub>2</sub>,  $\gamma_{US}$

and  $\gamma_S$  by first principal calculations are not available. For these materials,  $\gamma_{US}$  values were estimated based on the Rice equation, Eq. (2) with  $\kappa = 1$ , while  $\gamma_S$  was assumed to be 2 J/m<sup>2</sup>. Results of the  $\gamma_{US}$ ,  $c$ ,  $b$ ,  $d$ ,  $\psi$ ,  $U_{P-N}$ ,  $\gamma_S$ , and  $\gamma_S/U_{P-N}$  are summarized in Table III, which also lists the fracture toughness,  $K_{IC}$ , of the intermetallics. The  $\gamma_S/(U_{P-N} + \gamma_{APB})$  ratios for NbCr<sub>2</sub> and Nb<sub>3</sub>Si<sub>3</sub> are less than 0.5, while the others range from 2 to 25. The  $\gamma_{APB}$  term is important in Ni<sub>3</sub>Al and TiAl since the  $\gamma_{APB}$  is considerably larger than the  $U_{P-N}$ . The fracture toughness correlates better with the  $\gamma_S/(U_{P-N} + \gamma_{APB})$  than with  $\gamma_S/U_{P-N}$ . It is illustrated in Figure 5, which shows a plot of  $K_{IC}$  as a function of  $\gamma_S/(U_{P-N} + \gamma_{APB})$ .

Table III. Summary of Crystal Structure, Slip System, Lattice Parameter ( $a_0$ ), Burgers Vector ( $b$ ), Slip Plane Spacing, ( $d$ ),  $c$ ,  $\psi$ ,  $\gamma_{US}$ ,  $\gamma_{APB}$ ,  $U_{P-N}$ , Ductility Index, and Fracture Toughness ( $K_{IC}$ ) of Various Aluminides, Niobium Silicides, and Laves Phase.

Material	Structure	Slip System	$a_0$ (nm)	$b$ (nm)	$d$ (nm)	$c$ (GPa)	$\psi$ , deg.	$\gamma_{US}$ (J/m <sup>2</sup> )	$\gamma_S$ (J/m <sup>2</sup> )	$\gamma_{APB}$ (J/m <sup>2</sup> )	$U_{P-N}$ (J/m <sup>2</sup> )	Ductility Index		$K_{IC}$ , MPa $\sqrt{m}$
												$\gamma_S/U_{P-N}$	$\gamma_S/(U_{P-N}+\gamma_{APB})$	
NbCr <sub>2</sub>	C15	(111)R <sup>#</sup>	0.699	0.285	0.050	79.6	47	13.1	2	.038	4.2	0.48	0.47	1 [28]
Nb <sub>5</sub> Si <sub>3</sub>	D8 <sub>r</sub>	(010)[001]	0.657	1.188	0.657	81.5	142	8.9	2	—	9.8	0.20	0.20	3[25]
FeAl [14]	B2	(110)[1 1 1]	0.291	0.252	0.206	62.9	219	0.377	1.282	0.115	0.0281	45.6	7	12 [14]
NiAl [14]	B2	(110)[1 1 1]	0.288	0.249	0.204	61.9	219	0.364	1.688	0.286	0.0421	40.4	5.2	4.5 [14]
CoAl [14]	B2	(110)[1 1 1]	0.286	0.248	0.202	65.1	219	0.888	1.546	0.715	0.0663	23.3	2.0	3 [14]
Ni <sub>3</sub> Al [14]	L1 <sub>2</sub>	(111)1/6[2 1 1]	0.357	0.146	0.206	70.3	380	0.279	1.684	0.140	7 $\times 10^{-3}$	2.4 $\times 10^4$	12	55 [26]
TiAl [14]	L1 <sub>0</sub>	(111)1/6[2 1 1]	0.403	0.164	0.232	78.7	376	0.182	1.146	0.329	6 $\times 10^{-3}$	1.9 $\times 10^4$	3.5	2-4 [27]
Nb-10Ti-15Al	B2	(110)[1 1 1]	0.327	0.283	0.231	49.1	210	0.861	2.251	0.180	0.441	5.1	3.6	17 [22]
Nb-25Ti-15Al	B2	(110)[1 1 1]	0.327	0.283	0.231	47.1	210	0.827	2.166	0.098	.185	11.7	7.7	18 [22]
Nb-40Ti-15Al	B2	(110)[1 1 1]	0.327	0.284	0.232	41.2	210	0.725	2 of 2	0.015	.132	30.6	25.1	110 [22]

+ Interlamellar fracture

#  $R = 1/6 [11\bar{2}] + 1/12 [111]$  synchroshear

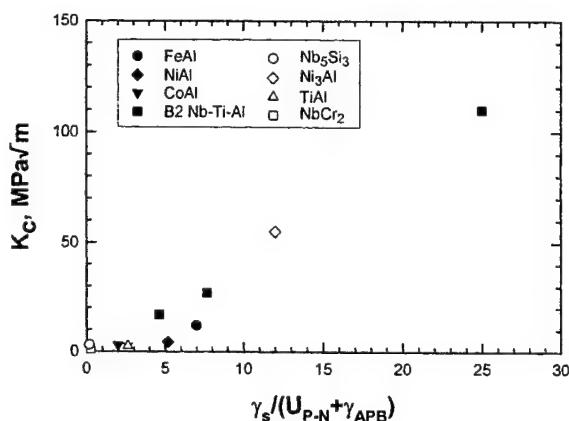


Figure 5. Increasing fracture toughness ( $K_{IC}$ ) with increasing values of the ductility index defined in terms of the  $\gamma_S/(U_{P-N}+\gamma_{APB})$  ratio for various intermetallics.

### Discussion

The results of this investigation indicate that a ductility index may be used to assess the effects of alloying addition on the tensile elongation of Nb-based bcc and B2 solid solution alloys, including the brittle-to-ductile fracture transition. In addition, the ductility index is also applicable to intermetallics with more complex ordered crystal structures and slip systems. Ordering is likely to reduce the tensile ductility and fracture toughness, as ordering reduces dislocation mobility. Even a small value of the stacking fault or antiphase boundary energy can have a large effect on the ductility index when the magnitude of  $\gamma_{SF}$  or  $\gamma_{APB}$  is comparable to the Peierls-Nabarro barrier energy.

A detailed examination of the various term that contribute to the P-N barrier energy has revealed that alloying addition affects mostly the lattice phase angle,  $\psi$ , which depends on the Burgers vector, the slip plane spacing, and the elastic constants. The ratio of  $d/b$ , on the other hand, depends on the crystal structure and the operative slip system. Alloying alters the Burgers vector, the slip band spacing, and the elastic constants only slightly and has little effects on the surface energy and the unstable stacking energy. Alloying, however, has a significant effect on the P-N energy because small changes in  $\psi$  is magnified by the  $\sinh(2\psi)$  term in the expression for  $U_{P-N}$ , Eq. (1). Figure 6 shows a plot of the

change,  $\Delta\psi$ , of the lattice phase angle as a function of alloying addition, where  $\Delta\psi = \psi(Nb-X) - \psi(Nb)$ . Ductilizing elements such as Ti, Zr, and Hf increase the lattice phase angle, while embrittling elements such as Cr, Al, Mo, W, and Re decrease the lattice phase angle. The P-N barrier energy approaches zero when  $\psi$  is large. Thus, a large lattice phase angle is desirable from tensile ductility and fracture resistance points of view.

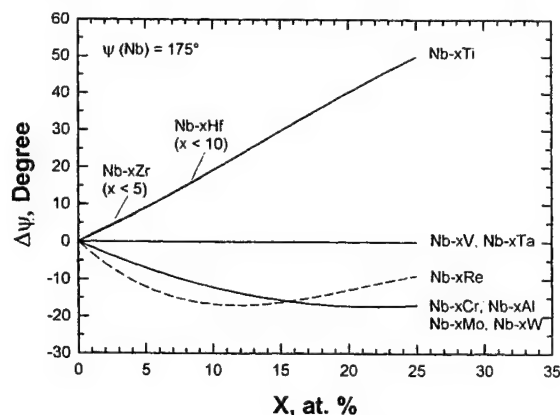


Figure 6. Change of the lattice phase angle  $\Delta\psi = \psi(Nb-X) - \psi(Nb)$ , as a function of alloying addition for various Nb-X binary alloys. Ductilizing elements (Ti, Hf, and Zr) increases the lattice phase angle ( $\Delta\psi > 0$ ), while embrittling elements (Cr, Al, Mo, W, and Re) decreases the lattice phase angle ( $\Delta\psi < 0$ ).

Physically, the  $\psi$  parameter can be considered as a measure of the distortion in the periodic lattice created by a dislocation. For a perfect lattice, an arbitrary Burgers circuit is closed, yielding  $\psi = 2\pi$ . In contrast, the same Burgers circuit enclosing a dislocated lattice would be open and give  $\psi < 2\pi$ . Since  $\psi$  depends on  $d/b$ , which in turn, the ratio depends on the crystal structure and the slip system, alloying addition would exert a significant impact on  $\psi$  and the P-N barrier energy structure. The significant impact that crystal structure exerts on  $\psi$  and  $U_{P-N}$  are evident in Table III. In the absence of a structural change, alloying additions can alter the  $\psi$  parameter by affecting the elastic constants,  $c_{ij}$ , which in turn changes the line energy of the

dislocation through the  $\kappa/c$  ratio in Eq. (3). As the line energy of the dislocation is changed, so is the P-N barrier energy and, consequently, the dislocation mobility and the ductility index.

Although only the results for similar Nb<sub>5</sub>Si<sub>3</sub> and NbCr<sub>2</sub> are presented in Table III, similar results for Nb<sub>3</sub>Al (A15) and Nb<sub>3</sub>Si (A15, L1<sub>2</sub>, Ti<sub>3</sub>P, and Perovskite cubic) were also obtained. For most Nb-based silicides and Laves phases, the  $U_{P-N}$  value is usually high and the ductility index is low. On the other hand, the results on B2 Nb-Ti-Al indicates that a high ductility index can be achieved in an Intermetallic when the lattice phase angle,  $\psi$ , is high, and  $\gamma_{APB}$  is small. A high  $\psi$  angle requires a high d/b ratio, which is generally observed on close-packed slip planes and close-packed slip directions. To enhance the ductility and fracture resistance of silicides and Laves phases, alloying additions must be directed toward promoting a change of the crystal structure and the operative slip systems from low d/b ratios to those with high d/b values.

### Conclusions

The conclusions reached in this study are as follows:

1. Alloying has a significant effect on the Peierls-Nabarro barrier energy and the brittle-to-ductile fracture transition by virtue of its influence on the lattice phase angle.
2. Alloying reduces the Peierls-Nabarro barrier and enhances tensile elongation and fracture resistance when it increases the lattice phase angle. The opposite is true when alloying reduces the lattice phase angle.
3. Even a small stacking fault or antiphase boundary energy can exert a significant effect on the ductility index when the fault energy is on the order of the Peierls-Nabarro barrier energy.
4. The tensile elongation and fracture resistance of several solid solution alloys and intermetallics increases with increasing values of the ductility index.

### Acknowledgments

This work was supported by the Air Force Office of Scientific Research through Contract No. F49620-01-C-0016, Dr. Craig S. Hartley, Program Manager. The clerical assistance of Ms. L. Salas, SwRI®, in preparation of this manuscript is appreciated.

### References

1. P. R. Subramanian et al., *Mat. Sci. Eng.*, A239-340 (1997), 1-13.
2. B. P. Bewlay, M. R. Jackson, and H. A. Lipsitt, *Metall. Mater. Trans. A*, 27A (1996), 3801-3808.
3. K. S. Chan and D. L. Davidson, *JOM*, 48 (9) (1966), 62-68.
4. K. S. Chan, *Metall. Mater. Trans. A*, 32A (2001), 2475-2487.
5. R. E. Peierls, *Proc. Phys. Soc.*, 52 (1940), 34-37.
6. F. R. N. Nabarro, *Proc. Phys. Soc.*, 52 (1940), 2236-394.

7. J. N. Wang, *Acta Mater.*, 44 (1996), 1541-1546.
8. J. N. Wang, *Mat. Sci. & Eng., A*, A206 (1996), 1541-1546.
9. A. H. W. Ngan, *J. Mech. Phys. Solids*, 45 (1997), 903-921.
10. S. Diplas et al., *Intermetallics*, 7 (1999), 937-946.
11. C. L. Reynolds, P. R. Couchman, and F. E. Karasz, *Phil. Mag.*, 34 (1976), 659-661.
12. R. O. Ritchie, J. F. Knott, and J. R. Rice, *J. Mech. Phys. Solids*, 21 (1973), 395-410.
13. J. R. Rice, *J. Mech. Phys. Solids*, 40 (1992), 239-271.
14. D. Farkas et al., *Mater. Res.*, 12 (1997), 93-99.
15. D. Farkas, *Mat. Sci. Eng.* A249 (1998), 249-258.
16. U. V. Waghmare et al., *Modelling Simul. Mater. Sci. Eng.*, 6 (1998), 493-506.
17. K. S. Chan and D. L. Davidson, *Met. And Mat. Trans. A*, 30A (1999), 925-939.
18. D.-H. Hou et al., *Alloy Modeling and Design*, ed. G. M. Stocks and P. E. A. Turchi, (Warrendale, PA: TMS, 1994), 291-302.
19. R. T. Begley, *Evolution of Refractory Metals and Alloys*, ed. E. N. C. Dalder, T. Grobstein, and C. S. Olsen (Warrendale, PA: TMS, 1994), 29-48.
20. K. D. Jones, "Microstructural and Tensile Property Study of Experimental Niobium-Titanium Base Alloys" (M.S. thesis, Rensselaer Polytechnic Institute, 1990).
21. M. R. Jackson and K. D. Jones, *Refractory Metals: Extraction, Processing and Applications* ed. K. Nona, C. Kiddell, D. R. Sadoway, and R. G. Bautista (Warrendale, PA: TMS, 1990), 311-319.
22. F. Ye, C. Mercer, And W. O. Soboyejo, *Metall. Mat. Trans. A*, 29A (1998), 2361-2374.
23. W. O. Soboyejo, J. Dipasquale, F. Ye, C. Mercer, T. S. Serivatsan, and D. G. Konitzer, *Metall. Mater. Trans. A*, 30A (1999), 1025-1038.
24. S. Naka, M. Thomas, M. Martry, G. Lapasset, and T. Khan, *Structural Intermetallics* ed R. Darolia, et al., (Warrendale, PA: TMS, 1993), 647-656.
25. R. M. Nekkanti and D. M. Dimiduk, *Mat. Res. Soc. Symp. Proc.*, vol. 194 (Pittsburgh, PA: 1990), 175-182.
26. G. P. Zhang, Z. G. Wang, and G. Y. Li, *Acta Mater.*, 45 (1997), 1705-1714.
27. K. S. Chan, J. Onstott, and K. S. Kumar, *Metall. Mater. Trans. A*, 31A (2000), 71-80.
28. D. L. Davidson, K. S. Chan, and D. L. Anton, *Metall. Mter. Trans. A*, 27A (1996), 3007-3018.

**APPENDIX 5**

**“Cyclic Oxidation Response of Multiphase Niobium-Based Alloys”**

**Kwai S. Chan**

**Metallurgical and Materials Transactions A  
Volume 35A, (2004) pp. 589-597**

**February 2004**

Reprinted with permission from  
*Metallurgical and Materials Transactions A*, Pittsburgh, PA

# Cyclic Oxidation Response of Multiphase Niobium-Based Alloys

KWAI S. CHAN

Cyclic oxidation tests were performed on multiphase Nb-based alloys containing silicide, Laves, and Nb solid solution phases. In particular, the oxidation resistance of six alloys with various compositions (Nb, Ti, Hf, Cr, Ge, and Si) and microstructures was characterized by thermal cycling from ambient temperature to a peak temperature that ranges from 900 °C to 1400 °C. Weight change data were obtained and the corresponding spalled oxides were collected and identified by X-ray diffraction. The results indicated that Nb-based alloys formed a mixture of  $\text{CrNbO}_4$ ,  $\text{Nb}_2\text{O}_5$ , and  $\text{Nb}_2\text{O}_5 \cdot \text{TiO}_2$ , with possibly small amounts of  $\text{SiO}_2$  or  $\text{GeO}_2$ . The oxidation resistance was improved when  $\text{CrNbO}_4$  formed instead of  $\text{Nb}_2\text{O}_5$  and  $\text{Nb}_2\text{O}_5 \cdot \text{TiO}_2$ . These results were used to assess the influence of microstructure and composition on the oxidation resistance of multiphase Nb-based alloys.

## I. INTRODUCTION

EXTENSIVE work has been undertaken to develop niobium-based structural alloys for high-temperature applications. The early studies (*e.g.*, References 1 through 9) focused mostly on the use of alloying addition to reduce the oxidation kinetics of Nb alloys by modifying the oxidation products. The early efforts, which were reviewed extensively by Stringer<sup>[10]</sup> and others,<sup>[11,12,13]</sup> were largely unsuccessful because of the formation of  $\text{Nb}_2\text{O}_5$ , a nonprotective oxide, which was too dominant to be altered by alloying addition. Subsequent studies<sup>[14-19]</sup> were concentrated on an aluminide-based system and the use of Al addition to improve oxidation resistance of Nb-based alloys through the formation of a protective alumina layer. While the formation of a protective alumina was feasible, the resulting alloys had low melting points and were too brittle to be used as structural materials.<sup>[16]</sup>

Recent efforts have focused mostly on materials that contain substantial amounts of niobium silicides and Laves phases.<sup>[20-32]</sup> These new systems include Nb-Si, Nb-Ti-Si, Nb-Ti-Al-Si, Nb-Ti-Cr-Si, and, among others, Nb-Ti-Hf-Cr-Al-Si. In these Nb-based alloys, Ti and Hf additions are intended for improvement in fracture<sup>[24,33,34]</sup> and oxidation resistance.<sup>[32,35]</sup> The Cr, Al, and Ge additions<sup>[32,35]</sup> are intended to enhance oxidation resistance, while Si is intended to provide oxidation and creep resistance<sup>[35]</sup> through the formation of various refractory-metal silicides (*e.g.*, alloyed  $\text{Nb}_5\text{Si}_3$ ,  $\text{Nb}_3\text{Si}$ ,  $\text{Ti}_5\text{Si}_3$ , and  $\text{Ti}_3\text{Si}$ ) and Laves phases (*e.g.*, alloyed  $\text{NbCr}_2$ ). Often referred to as refractory metal intermetallic composites (IMCs),<sup>[28,29]</sup> the salient characteristics of these Nb-based alloys are multiphase microstructures comprised of silicides, Laves phases, and Nb solid solution. Hereafter, these Nb-based materials will be referred to either as multiphase alloys or *in-situ* composites in this article. The silicides and Laves phases are intended to provide high-temperature strength and oxidation resistance, while the "ductile" Nb solid solution is intended to provide tensile ductility and fracture resistance at ambient temperature. The oxidation resistance of these multiphase Nb-based alloys,

which is substantially better than that of conventional Nb alloys,<sup>[22,25,26,28,32]</sup> is comparable to that of Ni-based superalloys at 1000 °C. Unfortunately, the oxidation resistance of the multiphase Nb-based alloys is still inadequate for structural materials in the 1200 °C to 1400 °C range, as the oxides that formed on these materials are nonprotective.<sup>[22,25,26,28,32]</sup> To improve the oxidation resistance, it is necessary to promote the formation of a protective oxide layer on the Nb-based alloys.

Wang *et al.*<sup>[36,37]</sup> and Gesmundo *et al.*<sup>[38,39]</sup> recently analyzed the critical conditions for the formation of nonprotective and protective oxide scales on a generic two-phase binary alloy. These results indicated that for two-phase alloys, the critical value of the average concentration of the active element required for the exclusive growth of a protective oxide layer is higher than that for single-phase alloys. The critical values depend also on the solubility of the active element in the solid solution,<sup>[37]</sup> as well as the volume fraction, the size, and the shape of the second phase.<sup>[36]</sup> Current understanding on the formation of protective  $\text{Cr}_2\text{O}_3$ ,  $\text{Al}_2\text{O}_3$ , and  $\text{SiO}_2$  scales on iron-, nickel-, and cobalt-based alloys is summarized in a recent review article.<sup>[40]</sup> Very little information, however, is available on the conditions required for the formation of a protective oxide scale on Nb-based materials. Thus, it is unknown whether any of these theoretical oxidation models can be applied to improve the oxidation resistance of multiphase Nb-based alloys.

This article presents the results of an investigation whose objectives were (1) to characterize the cyclic oxidation behavior of several multiphase Nb-based alloys and (2) to develop an oxidation model and approach for enhancing the oxidation resistance of Nb-based multiphase alloys or *in-situ* composites. Experimental characterization of the oxidation resistance of the six Nb-based alloys is presented in this article, while the results of the modeling effort are described elsewhere.<sup>[41]</sup> In particular, cyclic oxidation tests were performed on six alloys with various compositions and microstructures at temperatures ranging from 900 °C to 1400 °C. Weight change data were obtained and the corresponding spalled oxides were collected and identified by X-ray diffraction. These results were used to assess the influence of microstructure and alloy composition on the oxidation resistance in Nb-based multiphase alloys.

KWAI S. CHAN, Institute Scientist, is with the Department of Materials Engineering, Southwest Research Institute, San Antonio, TX 78238. Contact e-mail: kchan@swri.edu

Manuscript submitted February 24, 2003.



## II. EXPERIMENTAL PROCEDURE

The oxidation resistance of six experimental Nb-based multiphase alloys was studied in this investigation. Four of the alloys (Nbx, AX, M1, and M2) were fabricated at Pittsburgh Materials Technology (Pittsburgh, PA), while two alloys (UES-AX and CNG-1B) were cast at the Air Force Research Laboratory (Dayton, OH). The compositions and interstitial contents of the *in-situ* composites, shown in Table I, were determined by a commercial vender (Chicago Spectro Service Laboratory, Chicago, IL) using ASTM standard methods.<sup>[42]</sup>

Rectangular strip specimens (40 × 6 × 3 mm) were cut from the cast buttons and heat-treated in a flowing Ar gas atmosphere. The heat-treatment conditions included (1) 1350 °C/100 h/furnace cool and (2) 1350 °C/24 h/furnace cool. The microstructures of the heat-treated materials (1350 °C for 100 hours) are shown in Figure 1. The microstructures of the as-cast materials were similar to those shown in Figure 1, but the volume percents of individual phases were different. Individual phases in the microstructure were identified by dispersive energy spectroscopy, while their volume fractions were measured by performing quantitative metallographic analyses on micrographs of the microstructure taken in the backscattered scanning electron mode (BSE). Details of the experimental procedure were described earlier.<sup>[43]</sup> In the BSE images shown in Figures 1(a) through (f), the dark phase is the Laves phase, the gray phase is the silicide, and the light phase is the Nb-solid solution, Nbss. In Figure 1(d), the light phase along the grain boundary is a Ge-rich intermetallic, while the gray phase is the Nb-solid solution. The white phase in Figure 1(e) is a Ti-rich silicide. The composition of individual phases and their volume fractions in the *in-situ* composites are summarized in Table II and III, respectively.

As shown in Table I, Nbx contained low Cr and Si. It was intended to be a solid solution alloy. The presence of 3 pct Ge, however, led to the formation of Ge-rich intermetallics (light phase) along the grain boundaries (Figure 1(d)). Compared to Nbx, M1 contained higher Cr and Si contents and exhibited higher volume fractions of Laves phase (dark or black phase) and silicides (gray phase). Among all of these alloys, M2 contained the highest Cr and Si and exhibited the largest volume fractions of Laves and silicide phases. Alloys AX and UES-AX are essentially the same alloy, but were processed at two different laboratories. Their Si contents laid between those of M1 and M2, while the Cr contents were almost the same as M1. Alloy CNG-1B contained Fe and Sn additions, which were intended to improve low-temperature oxidation resistance. Heat treatment varied the volume

percents of the silicides in individual alloys, but the volume percents of the Laves phase remained essentially unchanged before and after heat treatment.

The cyclic oxidation specimens, 12.7 × 6 × 3 mm in size, were cut from rectangular strips in the as-cast as well as heat-treated conditions. Cyclic oxidation tests were performed by heating coupon specimens to the maximum temperature, which ranged from 900 °C to 1400 °C. The specimens were held at the peak temperature for 22 hours and then furnace cooled to ambient temperature in 2 hours. The specimens were weighed before and after each thermal cycle. This process was repeated for a total oxidation time of up to ≈500 hours, depending on the oxidation temperature. Weight change data were obtained as a function of time of oxidation. The oxide spalls were collected in a ceramic dish for individual alloys. After cyclic oxidation tests, the types of oxides formed were determined by X-ray diffraction. Metal recessions were measured on sectioned specimens using metallographic techniques.

## III. RESULTS

The weight change data of M2 and M1 for cyclic oxidation at various peak temperatures are presented in Figures 2(a) and (b), respectively. At 1100 °C, M2 exhibited small weight gain, but began to show small weight loss after 500 hours. The weight change increased for thermal cycling at 900 °C, 1200 °C, 1315 °C, and 1400 °C (Figure 2(a)). In contrast, M1 exhibited large weight loss at all temperatures, as shown in Figure 2(b). Figures 3(a) and (b) present the weight change curves of AX and UES-AX, respectively. Alloy AX showed similar weight change curves for 1100 °C, 1200 °C, and 1315 °C, but large weight loss at 900 °C (Figure 3(a)). For UES-AX, the weight change curves were similar for 1000 °C and 1200 °C. Weight loss increased when the maximum cycling temperature was either increased to 1315 °C or decreased to 900 °C.

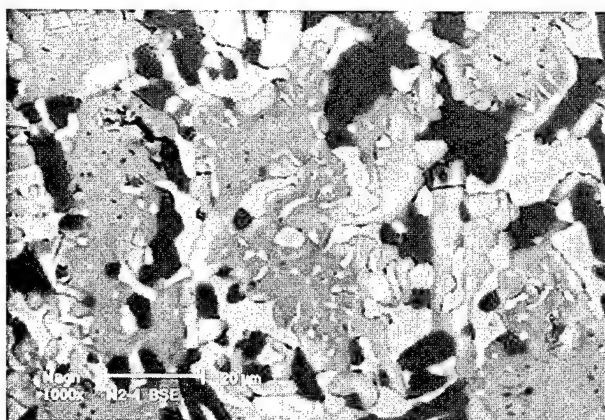
The weight change curves of various alloys are compared in Figure 4(a) and (b) for 900 °C and 1100 °C and in Figures 5(a) and (b) for 1200 °C and 1315 °C, respectively. Nbx exhibited large weight loss at all four temperatures; the results for 900 °C and 1000 °C are presented in Figure 4, while those for 1200 °C and 1315 °C are not shown. M1 and CNG-1B exhibited less oxide spallation than the other alloys at 900 °C, but both spalled more at higher temperatures (1100 °C or higher). M2 was more resistant to weight loss than other alloys at 1100 °C, 1200 °C, and 1315 °C, but showed somewhat larger weight

Table I. The Actual Chemical Composition and Interstitial Contents of Nb-Base Multiphase Alloys Investigated in This Study

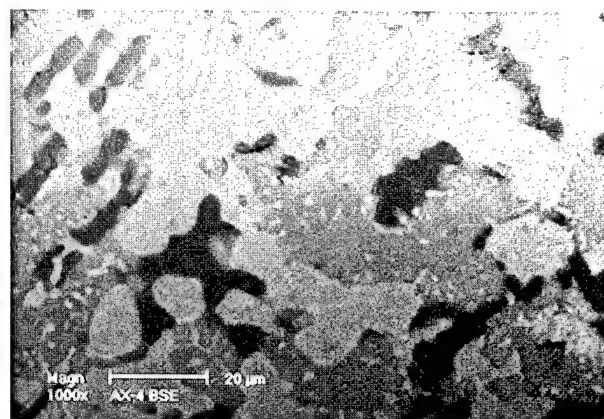
Alloy	Compositions (At. Pct)						Interstitial Contents (Wt Ppm)		
	Nb	Ti	Hf	Cr	Si	Ge	C	N	O
Nbx	62.7	26.6	4.2	2.5	1.0	3.0	<100	62	210
M1	46.3	22.2	4.4	12.3	9.7	5.1	<100	34	320
M2	35.8	22.5	4.0	15.6	17.3	4.8	100	26	220
AX	41.3	22.4	3.9	12.5	14.8	5.1	100	60	220
UES-AX	41.2	23.0	4.7	11.2	15.2	4.7	100	36	280
CNG-1B*	48.7	21.5	2.0	6.7	9.0	4.7	200	44	320

\*Also contained 3.5 pct Fe, 2.6 pct Al, and 1.3 pct Sn.

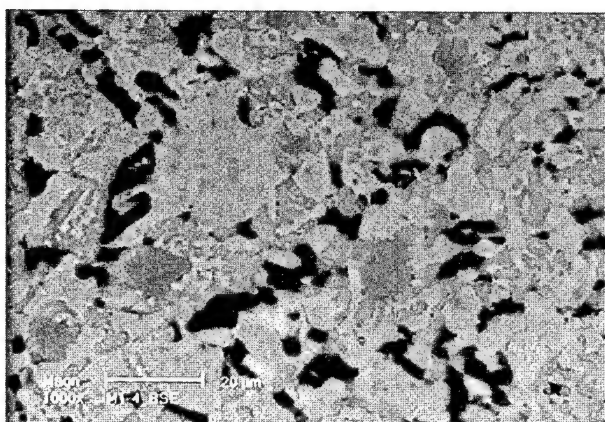




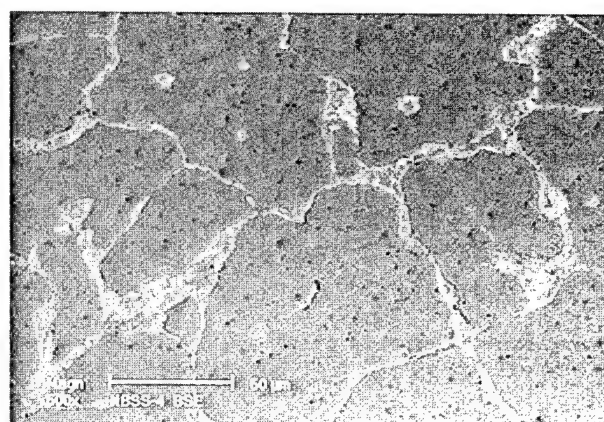
(a)



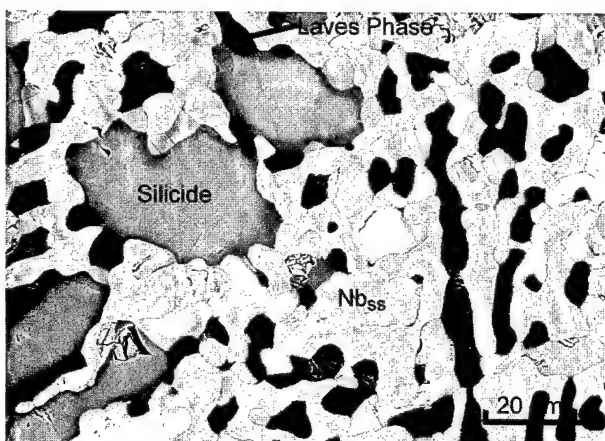
(b)



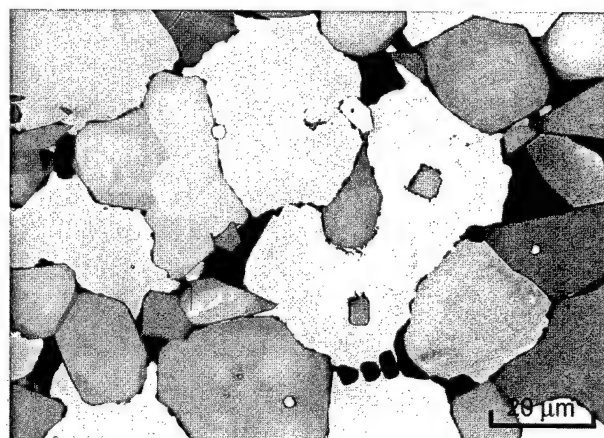
(c)



(d)



(e)



(f)

Fig. 1—Microstructures of Nb-based multiphase alloys in the as-cast and heat-treated (1350 °C for 100 h) conditions: (a) as-cast M2, (b) as-cast AX, (c) as-cast M1, (d) as-cast NbX, (e) heat-treated UES-AX, and (f) heat-treated CNG-1B.

loss at 900 °C (Figure 4(a)). Alloys AX and UES-AX were more prone to weight loss than M2 at all four temperatures. At 1200 °C, both AX and UES-AX exhibited repeated sequential weight gain and loss behaviors (Figure 5(a)). All alloys showed substantial weight loss at 1315 °C after 100 hours of thermal cycling. Weight change data of AX (GE-AX) reported by Bewlay and Jackson<sup>[44]</sup> are compared against current data in Figure 5. The two sets of data were

consistent even though they were generated under different thermal cycling rates.

The oxide spalls of individual alloys were identified by X-ray diffraction peaks and comparing the characteristic diffractions peaks against the JCPDF standards.<sup>[45]</sup> Figures 6(a) through (d) present the results of M2 for 900 °C, 1100 °C, 1315 °C, and 1400 °C, respectively. A mixture of oxides formed on M2, including  $\text{CrNbO}_4$ ,  $\text{Nb}_2\text{O}_5$ ,  $\text{Ti}_2\text{Nb}_{10}\text{O}_{29}$ , and  $\text{Nb}_2\text{O}_5 \cdot \text{TiO}_2$ .

**Table II. The Chemical Compositions and Crystal Structures of Constituent Phases in Various Nb-Based Multiphase Alloys in the As-Cast and Heat-Treated Conditions**

Alloy	Heat Treatment	Nb <sub>ss</sub> Phase (Bcc)	Silicide Phase* (D8 <sub>1</sub> )	Laves Phase (C14)	Ge-Rich Phase (Unknown)
M2-1	as-cast	—	Nb-23Ti-3Hf-4Cr-6Ge-28Si	Nb-12Ti-4Hf-52Cr-2Ge-9Si	—
M1-1	as-cast	Nb-20Ti-3Hf-12Cr-4Ge-4Si	Nb-20Ti-4Hf-3Cr-10Ge-25Si	Nb-10Ti-4Hf-49Cr-2Ge-9Si	—
AX-1	as-cast	Nb-24Ti-3Hf-14Cr-2Ge-1Si	Nb-21Ti-3Hf-3Cr-8Ge-27Si	Nb-15Ti-6Hf-49Cr-2Ge-8Si	—
Nbx-1	as-cast	Nb-29Ti-4Hf-3Cr-3Ge-3Si	—	—	Nb-39Ti-6Hf-3Cr-9Ge-6Si
UES-AX	1350 °C/100 h	Nb-26Ti-3Hf-14Cr-3Ge-1Si	Nb-24Ti-4Hf-1Cr-6Ge-29Si	Nb-12Ti-3Hf-54Cr-1Ge-8Si	—
M2-3	1350 °C/100 h	Nb-23Ti-1Hf-10Cr-3Ge-3Si	Nb-19Ti-5Hf-2Cr-7Ge-28Si	Nb-12Ti-4Hf-50Cr-2Ge-8Si	—
M1-3	1350 °C/100 h	Nb-18Ti-1Hf-10Cr-2Ge-3Si	Nb-17Ti-5Hf-3Cr-12Ge-23Si	Nb-10Ti-4Hf-49Cr-2Ge-9Si	—
AX-3	1350 °C/100 h	Nb-20Ti-1Hf-10Cr-3Ge-3Si	Nb-18Ti-5Hf-1Cr-8Ge-28Si	Nb-11Ti-4Hf-48Cr-2Ge-9Si	not determined
Nbx-3	1350 °C/100 h	Nb-24Ti-3Hf-3Cr-4Ge-3Si	—	—	Nb-28Ti-19Hf-0.3Cr-27Ge-10Si
CNG-1B**	1350 °C/100 h	Nb-21Ti-1Hf-8Cr-0.8Ge-0.8Si-2.6Fe-2Sn-2Al	Nb-19Ti-2.3Hf-1.7Cr-9.5Ge-20Si-2Al-1.8Fe-1Sn	Nb-15Ti-2.8Hf-31Cr-1Ge-8Si-2Al-15Fe-0.1 Sn	—

\*\*Hot-isostatically pressed at 1420 °C under 207 MPa pressure for 6 h.

\*Also contained small amounts of (Ti, Nb)<sub>5</sub>Si<sub>3</sub> (D<sub>8</sub> structure) and possibly Nb<sub>3</sub>Si (Ti<sub>3</sub>P structure).

**Table III. A Summary of the Volume Percents of Intermetallics and Nb Solid Solution Phase (Nb<sub>ss</sub>) in Nb-Based Multiphase Alloys**

Alloy	HT	Vol Pct Nb <sub>ss</sub>	Vol Pct Silicides	Vol Pct Laves Phase	Vol Pct Ge-Rich Phase
M2-1	as-cast	0	73	27	0
M1-1	as-cast	64	28	8	0
AX-1	as-cast	20	66	14	—
Nbx-1	as-cast	91	—	—	9
UES-AX	1350 °C/100 h	54	32	14	—
M2-3	1350 °C/100 h	22	53	25	—
M1-3	1350 °C/100 h	54	35	11	—
Nbx-3	1350 °C/100 h	94	—	—	6
AX-3	1350 °C/100 h	39	40	15	6
CNG-1B*	1350 °C/100 h	43.6	50.7	5.7	—
M2-4	1350 °C/24 h	24.0	48.7	26.5	—
M1-4	1350 °C/24 h	60.2	27.9	10	—
AX-4	1350 °C/24 h	50.6	33.7	14	—
Nbx-4	1350 °C/24 h	83.7	—	—	16.3

\*Hot-isostatically pressed at 1420 °C under 207 MPa pressure for 6 h.

The characteristic peaks of the latter two oxides overlap extensively and could not be delineated with a degree of confidence. The small peak at  $2\theta = 21.8$  deg was identified as possibly that of GeO<sub>2</sub> or cristoballite SiO<sub>2</sub>. The JCPDF identification card numbers of these oxides are indicated in Figure 6. While the types of oxides formed were similar, the relative amounts formed were different for various temperatures. At 1100 °C, CrNbO<sub>4</sub> appeared to be the predominant oxide formed on M2 by virtue of the relative peak heights of this oxide compared to those for other oxides (Figure 6(b)). In contrast, Nb<sub>2</sub>O<sub>5</sub>, Ti<sub>2</sub>Nb<sub>10</sub>O<sub>29</sub>, and Nb<sub>2</sub>O<sub>5</sub> · TiO<sub>2</sub> were the predominant oxides and little CrNbO<sub>4</sub> oxides were observed at 1400 °C, as shown in Figure 6(d). The peak heights for Nb<sub>2</sub>O<sub>5</sub>, Ti<sub>2</sub>Nb<sub>10</sub>O<sub>29</sub>, and

Nb<sub>2</sub>O<sub>5</sub> · TiO<sub>2</sub> in M2 at 900 °C and 1315 °C laid in between those for 1100 °C and 1400 °C, as shown in Figures 6(a) and (c).

The oxides formed in M1, AX, UES-AX, and CNG-1B at 1100 °C are compared in Figure 7. The comparison indicated that all four alloys formed a mixture of CrNbO<sub>4</sub>, Nb<sub>2</sub>O<sub>5</sub>, Ti<sub>2</sub>Nb<sub>10</sub>O<sub>29</sub>, and Nb<sub>2</sub>O<sub>5</sub> · TiO<sub>2</sub>. The X-ray diffraction patterns of the oxides formed in these alloys are similar to those observed in M2 at 1100 °C, but with lower CrNbO<sub>4</sub> peak heights and higher Nb<sub>2</sub>O<sub>5</sub> peak heights. For Nbx, the oxide spalls were primarily Nb<sub>2</sub>O<sub>5</sub> · TiO<sub>2</sub> with little or no CrNbO<sub>4</sub>, but small amounts of GeO<sub>2</sub> could be present. The oxidation products observed in all six alloys are consistent with those reported for Nb alloys and NbCr<sub>2</sub> in the literature.<sup>[1,3,10,14]</sup>

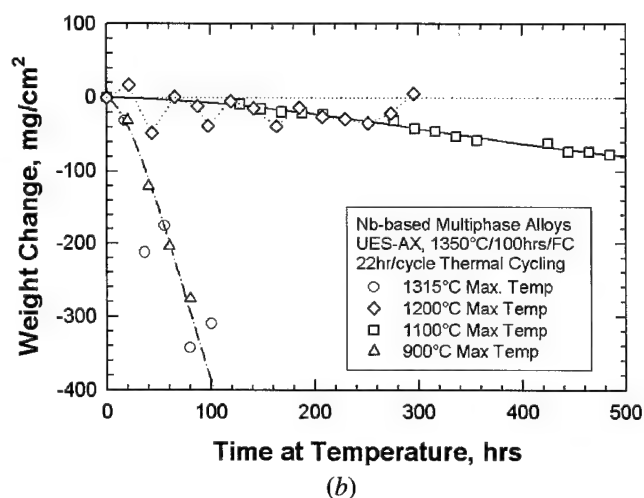
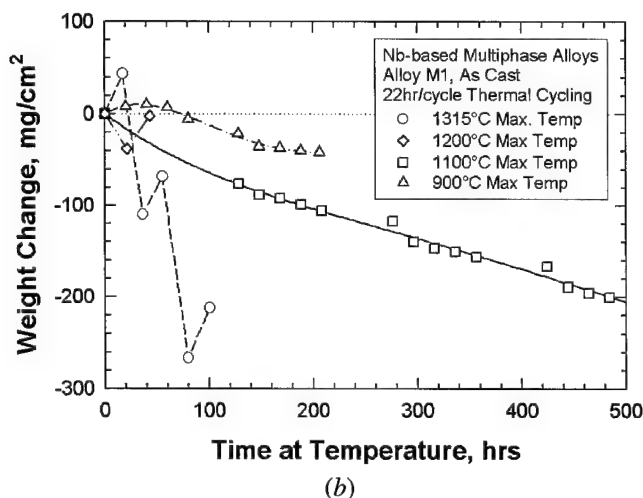
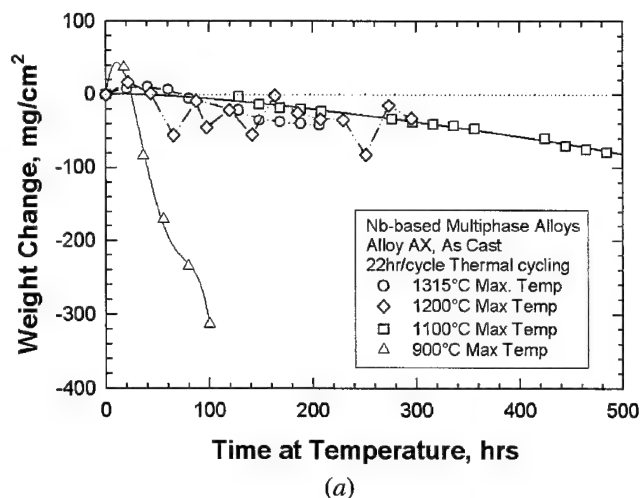
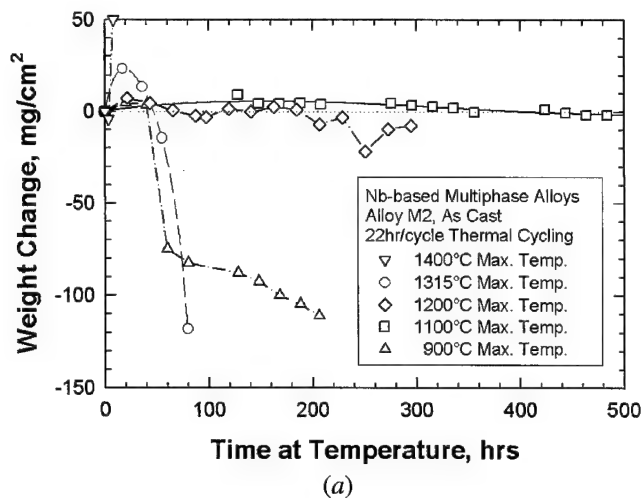


Fig. 2—Weight change data of as-cast M2 and M1 at various peak temperatures: (a) M2 and (b) M1.

Fig. 3—Weight change data of AX and UES-AX: (a) as-cast AX and (b) heat-treated UES-AX (1350 °C/100 h/furnace cooled).

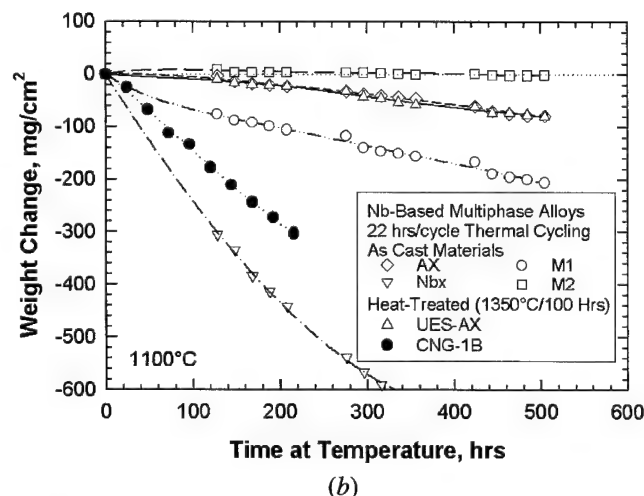
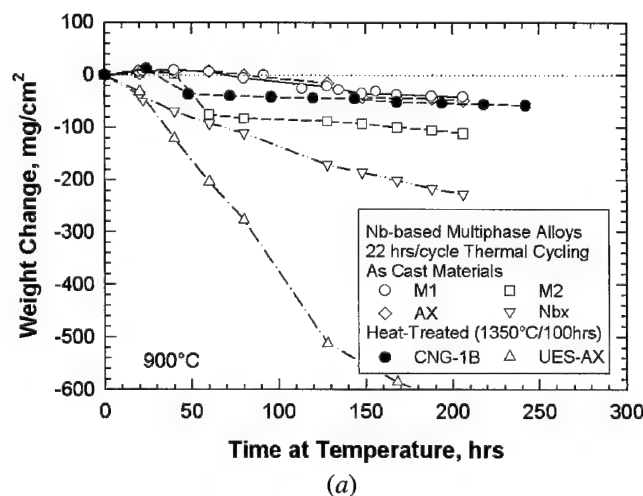


Fig. 4—Comparison of weight change data of various alloys at 900 °C and 1100 °C: (a) 900 °C and (b) 1100 °C.

#### IV. DISCUSSION

In a recent article,<sup>[46]</sup> Menon *et al.*, reported the static oxidation behavior of a number of Nb-silicides containing mul-

ticomponent alloys for the temperature range of 600 °C to 1300 °C. The oxidation products observed in these alloys, which include  $\text{TiNb}_2\text{O}_7$ ,  $\text{CrNbO}_4$ , cristoballite  $\text{SiO}_2$ ,  $3\text{Nb}_2\text{O}_5 \cdot \text{TiO}_2$ ,

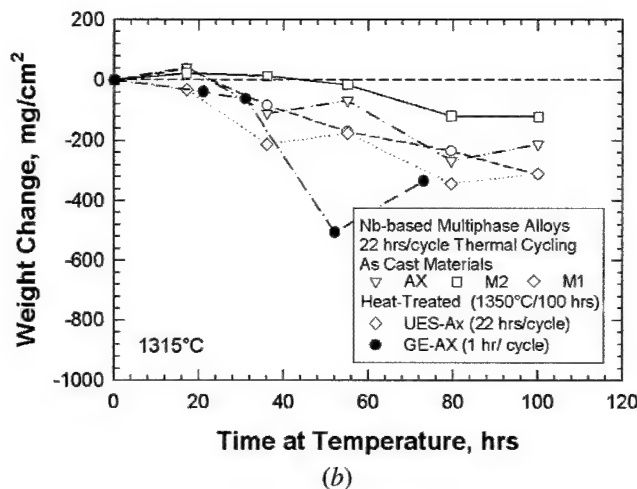
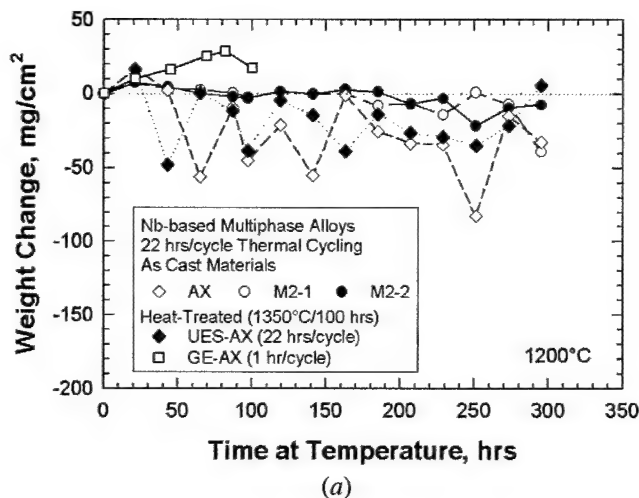


Fig. 5—Summary of weight change data of various alloys at 1200 °C and 1315 °C: (a) 1200 °C and (b) 1315 °C. Data of GE-AX are from Bewlay and Jackson.<sup>[44]</sup>

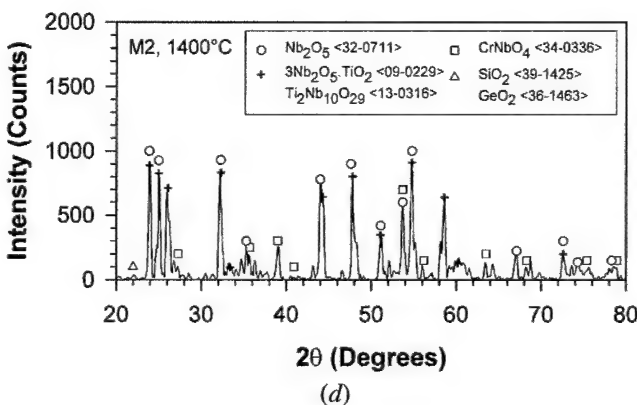
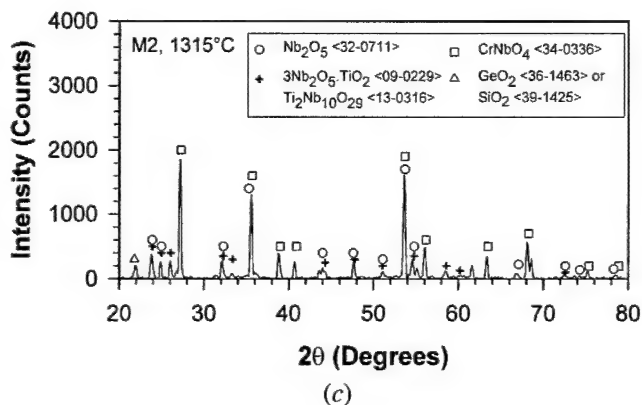
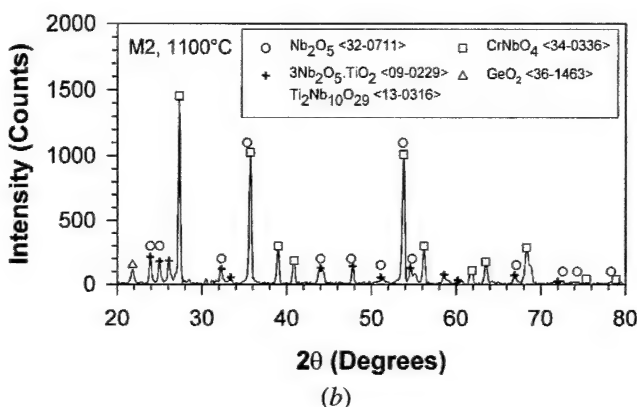
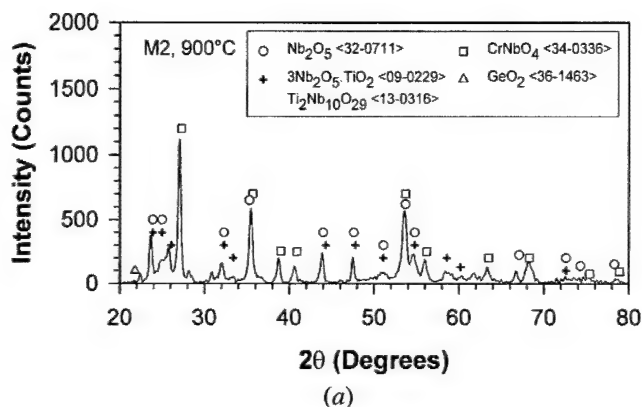


Fig. 6—Characteristic XRD peaks of oxide spalls of alloy M2 for various peak cyclic oxidation temperatures: (a) 900 °C, (b) 1100 °C, (c) 1315 °C, and (d) 1400 °C.

and  $\text{Nb}_2\text{O}_5$ , are consistent with those observed in this study for cyclic oxidation. Their results also indicated that the Nb solid solution phase oxidized selectively, while the silicide phase in the microstructure did not oxidize. At temperatures below 900 °C, internal oxidation caused numerous microcracks that laid parallel to the surfaces just below the oxide layer. These microcracks resulted in spallation of the oxide scales and breakaway oxidation at low temperature. The lower cyclic oxidation resistance observed in the current alloys at

900 °C compared to 1100 °C probably originated from this type of internal oxidation.

Among all the alloys studied, M2 contained the highest Cr and Si contents and this alloy exhibited the best oxidation resistance at 1100 °C (Figure 6(b)). At this temperature, the oxidation products were mostly  $\text{CrNbO}_4$  with small amounts of  $\text{Nb}_2\text{O}_5$  and  $\text{Nb}_2\text{O}_5 \cdot \text{TiO}_2$ . At other temperatures as well as in other alloys, the oxidation resistance decreased with increasing amounts of  $\text{Nb}_2\text{O}_5$  and  $\text{Nb}_2\text{O}_5 \cdot \text{TiO}_2$  in the oxide

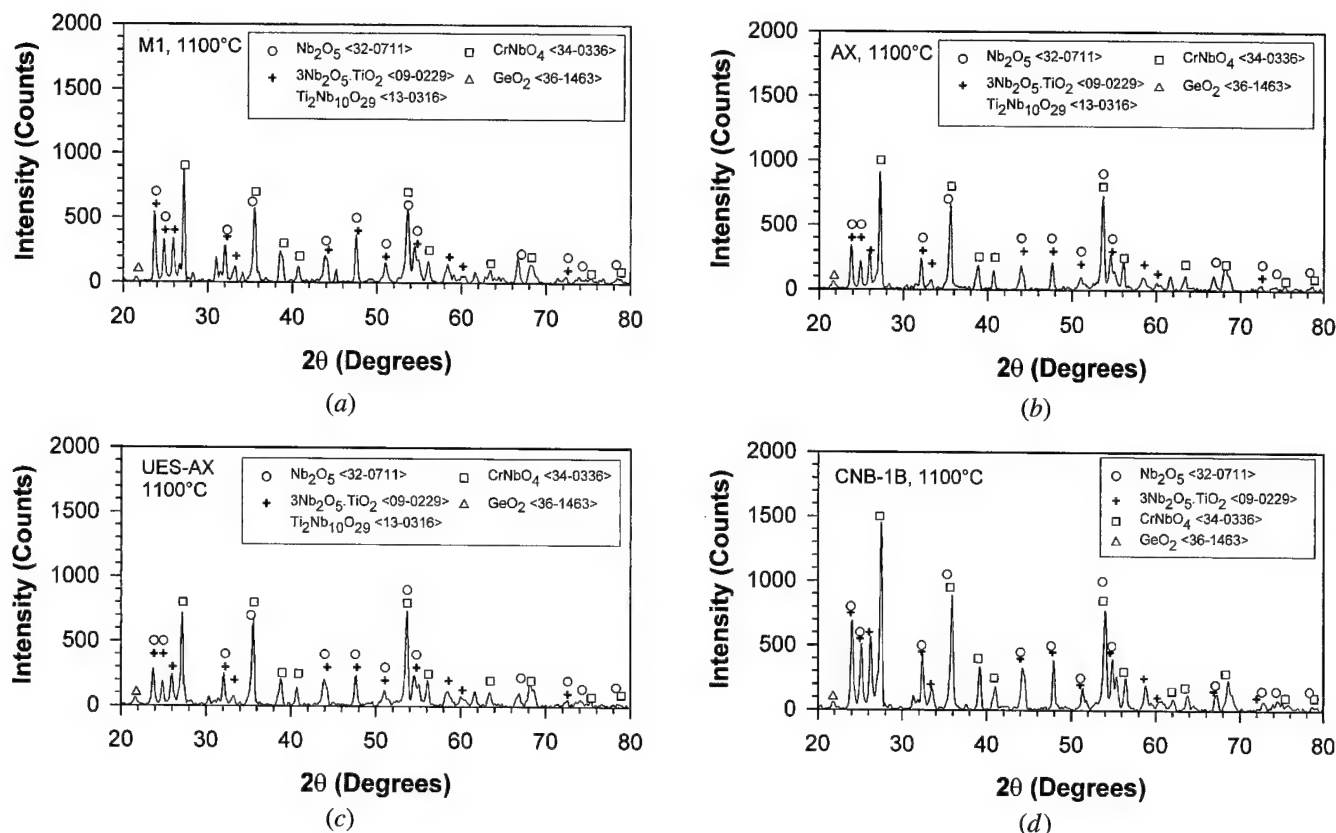


Fig. 7—Characteristic XRD peaks of oxide spalls of four Nb-based multiphase alloys ((a) M1, (b) AX, (c) UES-AX, and (d) CNG1-B) tested at a peak oxidation temperature of 1100 °C.

mixtures. For these alloys, the worst oxidation resistance occurred at 1400 °C and the oxide product mixture contained mostly  $\text{Nb}_2\text{O}_5$  and  $\text{Nb}_2\text{O}_5 \cdot \text{TiO}_2$  with little  $\text{CrNbO}_4$ . The intensity of the XRD pattern for  $\text{CrNbO}_4$  occurs at  $2\theta = 27.3$  deg, while those for  $\text{Nb}_2\text{O}_5$  and  $\text{Nb}_2\text{O}_5 \cdot \text{TiO}_2$  occur at  $2\theta = 23.9$  deg. The ratio of the intensity,  $I_{\text{CrNbO}_4}$ , of the  $\text{CrNbO}_4$  peak at  $2\theta = 27.3$  deg to the intensity,  $I_{\text{Nb}_2\text{O}_5 \cdot \text{TiO}_2}$ , at  $2\theta = 23.9$  deg can be used as a measure of the relative amounts of  $\text{CrNbO}_4$ ,  $\text{Nb}_2\text{O}_5$ , and  $\text{Nb}_2\text{O}_5 \cdot \text{TiO}_2$  in the oxidation product. The values of this relative intensity ratio were obtained for all six alloys tested at various temperatures. The results are plotted as a function of volume percents of Nb solid solution phase in the alloy in Figure 8. The relative intensity ratio is seen to decrease with increasing volume percent of Nb solid phase in the alloy. A high  $I_{\text{CrNbO}_4}/I_{\text{Nb}_2\text{O}_5 \cdot \text{TiO}_2}$  ratio was observed only in M2 at 1100 °C and 1315 °C.

A clear picture of the relationship between the microstructure and oxidation resistance emerged when the relative intensity ratio and metal recession were plotted as a function of vol pct Nb solid phase. For example, Figure 9 shows the results of the relative intensity ratio and material recession of the various alloys after 500 hours of cyclic oxidation at a peak temperature of 1100 °C. Three general trends can be deduced from Figure 9: (1) high material recession is associated with the formation and spallation of  $\text{Nb}_2\text{O}_5$  and  $\text{Nb}_2\text{O}_5 \cdot \text{TiO}_2$ , (2) low material recession is associated with the formation and spallation of  $\text{CrNbO}_4$ , and (3) the formation and spallation of  $\text{Nb}_2\text{O}_5$  and  $\text{Nb}_2\text{O}_5 \cdot \text{TiO}_2$  is favored in alloys containing high volume percents of Nb solid solu-

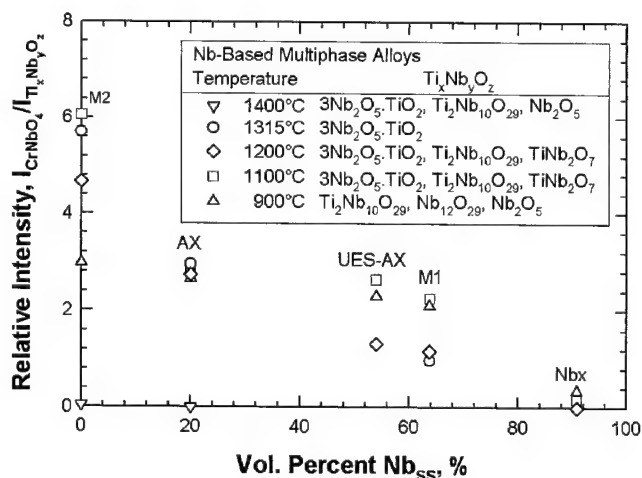


Fig. 8—XRD intensity ratio,  $I_{\text{CrNbO}_4}/I_{\text{Nb}_2\text{O}_5 \cdot \text{TiO}_2}$ , plotted as a function of volume percents of Nb solid solution in Nb-based multiphase alloys for various peak oxidation temperatures.

tion phase, while  $\text{CrNbO}_4$  formation and spallation is favored in alloys with high volume percents of silicide and Laves phase. The lowest oxidation resistance was observed in NbX, which contained the lowest Cr content, while M2, which contained the highest Cr content, exhibited the highest oxidation resistance. Unfortunately,  $\text{CrNbO}_4$  does not offer long-term protection and the oxidation resistance of M2,



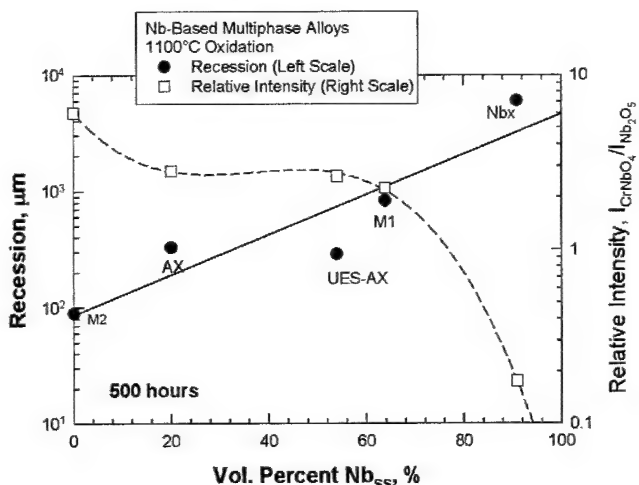


Fig. 9—Metal recession and relative intensity ratio plotted as a function of Nb solid solution in Nb-based multiphase alloys for cyclic oxidation at 1100 °C peak temperature.

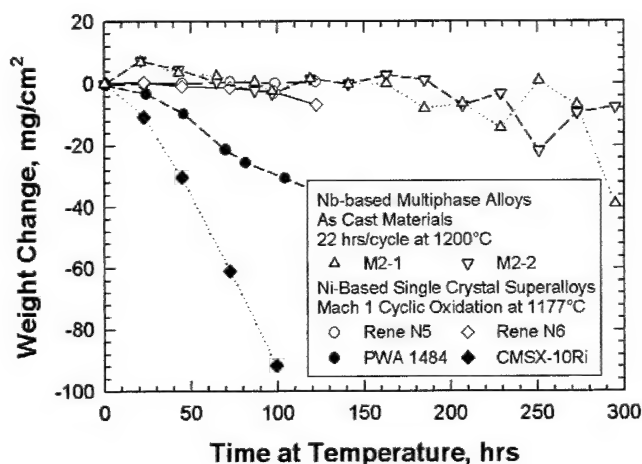


Fig. 10—A comparison of the weight change curves of the Nb-based multiphase alloy M2 (M2-1 and M2-2 are duplicate specimens) from this study against those of four Ni-based single-crystal superalloys, which are RENE N5, RENE N6, PWA 1484, and CMSX-10Ri, from Walston *et al.*<sup>[47]</sup>

which varies widely with temperatures, is limited to 500 hours at 1100 °C and is less at other temperatures.

The formation of mixed oxides of Nb<sub>2</sub>O<sub>5</sub> and TiO<sub>2</sub> leads to poor oxidation resistance in Nb-based multiphase alloys tested at other temperatures (*e.g.*, 900 °C and 1315 °C). Break-away oxidation (weight loss > 50 mg/cm<sup>2</sup>) was common in NbX and M1 because these alloys contained large volume percents (>60 pct) of Nb<sub>ss</sub> in the microstructure. All alloys were susceptible to excessive oxidation at temperatures above 1315 °C because of mixed oxide formation involving Nb<sub>2</sub>O<sub>5</sub> and TiO<sub>2</sub>. Only small amounts of SiO<sub>2</sub> and some Ge oxides were observed in the Nb-based alloys. Thus, the role of Si and Ge in the oxidation resistance appears to be limited. Heat treatment alters oxidation resistance by changing the Cr content and the volume percents of the Nb solid solution phase in the microstructure. A higher Cr content in the Nb<sub>ss</sub> enhances oxidation resistance, but a larger volume percent of Nb<sub>ss</sub> in the microstructure produces the opposite effect.

Because Nb-based multiphase alloys are intended for high-temperature structural applications, it is of interest to compare the oxidation resistance of M2 against those of Ni-based single-crystal superalloys. Such a comparison is presented in Figure 10, which shows that the oxidation resistance of M2 at 1200 °C is as good as, if not better, than those of RENE\* N5 and N6<sup>[47]</sup> for oxidation times up to 150 hours.

\*RENE is a trademark of General Electric Aircraft Engines, Cincinnati, OH.

Furthermore, M2 exhibits better oxidation resistance than those of PWA 1484 and CMSX-10Ri at 1177 °C.<sup>[47]</sup> The weight change data of the Ni-based single-crystal superalloys have been computed by dividing the weight loss results reported in Walston *et al.*,<sup>[47]</sup> by the surface area (7.6 cm<sup>2</sup><sup>[48]</sup>). This observation is consistent with recent reviews that show state-of-the-art Nb-based multiphase alloys exhibit higher oxidation resistance than cast Ni-based alloys at temperatures above ≈1100 °C.<sup>[32,35]</sup>

## V. CONCLUSIONS

The cyclic oxidation resistance of six Nb-based multiphase alloys containing silicides, Laves phase, and Nb-solid solution phases in the Nb-Ti-Hf-Cr-Ge-Si system has been investigated. The conclusions reached in this investigation are as follows.

1. The oxidation products associated with thermal cycling of Nb-based multiphase alloys at a peak temperature of 900 °C to 1400 °C are a mixture of CrNbO<sub>4</sub>, Nb<sub>2</sub>O<sub>5</sub>, Ti<sub>2</sub>Nb<sub>10</sub>O<sub>29</sub>, and Nb<sub>2</sub>O<sub>5</sub> · TiO<sub>2</sub>, with possibly small amounts of SiO<sub>2</sub> or GeO<sub>2</sub>.
2. The oxidation resistance of Nb-based multiphase alloys were enhanced by the formation of CrNbO<sub>4</sub> instead of Nb<sub>2</sub>O<sub>5</sub>, Ti<sub>2</sub>Nb<sub>10</sub>O<sub>29</sub>, and Nb<sub>2</sub>O<sub>5</sub> · TiO<sub>2</sub>.
3. The oxidation resistance of Nb-based alloys increased with increasing Cr content in the Nb solid solution and decreasing volume fractions of the Nb solution phase in the microstructure.
4. Among the materials investigated, the best oxidation resistance was observed in as-cast M2 whose microstructure contained Nb-based silicides and Laves phase, with little or no Nb solid solution phase.

## ACKNOWLEDGMENTS

This work was supported by the Air Force Office of Scientific Research through Contract No. F49620-01-C-0016, Dr. Craig S. Hartley, Program Manager. The author is grateful to Dr. Young-Won Kim, UES, Inc., for supplying alloys UES-AX and CNG-1B, and to Dr. Melvin R. Jackson, General Electric Global Research Laboratories (Schenectady, NY), for providing the compositions and oxidation data of GE alloys. Technical assistance by Messrs. F. Campbell, B. Chapa, and James Spencer, Southwest Research Institute (SwRI), in conducting the oxidation experiments, microstructural characterization, and X-ray diffraction analyses are acknowledged. The clerical assistance of Ms. L. Salas, SwRI, in the preparation of this manuscript is appreciated.

## REFERENCES

1. J.W. Semmel, Jr.: *Refractory Metals and Alloys*, AIME Metallurgical Society Conf., M. Semchyshen and J.J. Hardwood, eds., Interscience Publishers, New York, NY, 1960, vol. 11, pp. 119-68.
2. A.B. Michael: *Reactive Metals*, AIME Metallurgical Society Conf., W.R. Clough, ed., Interscience Publishers, New York, NY, 1958, vol. 2, pp. 487-507.
3. G.T.J. Mayo, W.H. Shepherd, and A.G. Thomas: *J. Less-Common Met.*, 1960, vol. 2, pp. 223-32.
4. H. Inouye: *Columbium Metallurgy*, AIME Metallurgical Society Conf., D.L. Douglas and F.W. Kunz, eds., Interscience Publishers, New York, NY, 1960, pp. 649-65.
5. S.T. Wlodek: *Columbium Metallurgy*, AIME Metallurgical Society Conf., D.L. Douglas and F.W. Kunz, eds., Interscience Publishers, New York, NY, 1960, vol. 10, pp. 553-83.
6. S.T. Wlodek: *Columbium Metallurgy*, AIME Metallurgical Society Conf., D.L. Douglas and F.W. Kunz, eds., Interscience Publishers, New York, NY, 1960, vol. 10, pp. 175-203.
7. R.E. Pawel, J.V. Cathcart, and J.J. Campbell: *Columbian Metallurgy*, AIME Metallurgical Society Conf., D.L. Douglas and F.W. Kunz, eds., Interscience Publishers, New York, NY, 1960, vol. 10, pp. 667-84.
8. P. Lublin, W.J. Sutkowski, E. Rittershaus, and J. Brett: *Refractory Metals and Alloys IV Research and Development—Vol. II*, AIME Metallurgical Society Conf., R.I. Jaffee, G.M. Ault, J. Maltz, and M. Semchyshen, eds., Gordon and Breach Science Publishers, New York, NY 1965, vol. 41, pp. 1083-105.
9. J.D. Cox and J.R. Kerr: *Refractory Metals and Alloys IV Research and Development—Vol. II*, AIME Metallurgical Society Conf., R.I. Jaffee, G.M. Ault, J. Maltz, and M. Semchyshen, eds., Gordon and Breach Science Publishers, New York, NY, 1965, vol. 41, pp. 901-17.
10. J.F. Stringer: *High Temperature Corrosion of Aerospace Alloys*, AGARD-AG-200, Advisory Group for Aerospace Research and Development, NATO, Neuilly-sur-Seine, France, Aug. 1975.
11. H. Inoue: *Proc. Int. Symp. on Niobium*, H. Stuart, ed., TMS, Warrendale, PA, 1984, pp. 615-36.
12. R.T. Begley: in *Evolution of Refractory Metals and Alloys*, E.N.C. Dalder, T. Grobstein, and C.S. Olsen, eds., TMS, Warrendale, PA, 1994, pp. 29-48.
13. R.A. Perkins and G.H. Meier: *JOM*, 1990, vol. 42, pp. 17-21.
14. R.C. Svedberg: *Proc. Symp. on Properties of High Temperature Alloys*, Z.A. Foroulis and F.S. Pettit, eds., The Electrochemical Society, Princeton, NJ, 1976, pp. 331-62.
15. R.A. Perkins, K.T. Chiang, and G.H. Meier: *Scripta Metall.*, 1988, vol. 22, pp. 419-24.
16. R.A. Perkins, K.T. Chiang, G.H. Meier, and R. Miller: in *Oxidation of High Temperature Intermetallics*, T. Grobstein and J. Doychak, eds., TMS, Warrendale, PA, 1988, pp. 157-69.
17. J.S. Lee, J.J. Stephens, and T.G. Nieh: in *High Temperature Niobium Alloys*, J.J. Stephens and I. Amad, eds., TMS, Warrendale, PA, 1991, pp. 143-55.
18. R.A. Perkins and G.H. Meier: *Microscopy of Oxidation*, Institute of Metals, London, 1991, pp. 183-92.
19. G.H. Meier: *Mater. Corr.*, 1996, vol. 47, pp. 595-618.
20. R.L. Fleischer and R.J. Zabala: *Metall. Trans. A*, 1990, vol. 21A, pp. 2149-54.
21. D.L. Anton and D.M. Shah: *MRS Symp. Proc.*, 1990, vol. 194, pp. 175-82.
22. M.R. Jackson, K.D. Jones, S.C. Huang, and L.A. Peluso: in *Refractory Metals: Extrusion, Processing and Applications*, K.C. Liddell, D.R. Sadoway, and R.G. Bustista, eds., TMS, Warrendale, PA, 1990, pp. 335-46.
23. D.M. Dimiduk, M.G. Mendiratta, and P.R. Subramanian: in *Structural Intermetallics*, R. Darolia, J.J. Lewendowski, C.T. Liu, P.L. Martin, D.B. Miracle, and M.V. Nathal, eds., TMS, Warrendale, PA, 1993, pp. 619-30.
24. B.P. Bewlay, H.A. Lipsitt, W.J. Reeder, M.R. Jackson, and J.A. Sutliff: in *Processing and Fabrication of Advanced Materials IV*, V.A. Ravi, T.S. Srivatsan, and J.J. Moore, eds., TMS, Warrendale, PA, 1994, pp. 547-65.
25. M.R. Jackson, R.G. Rowe, and D.W. Skelly: *Mater. Res. Soc. Symp. Proc.*, 1995, vol. 364, pp. 1339-44.
26. P.R. Subramanian, M.G. Mendiratta, and D.M. Dimiduk: *JOM*, 1996, vol. 48, pp. 33-38.
27. P.R. Subramanian, M.G. Mendiratta, D.M. Dimiduk, and M.A. Stucke: *Mater. Sci. Eng.*, 1997, vols. A239-A340, pp. 1-13.
28. M.R. Jackson, B.P. Bewlay, R.G. Rowe, D.W. Skelly, and H.A. Lipsitt: *JOM*, 1996, vol. 48, pp. 39-44.
29. B.P. Bewlay, M.R. Jackson, and H.A. Lipsitt: *Metall. Mater. Trans. A*, 1996, vol. 27A, pp. 3801-08.
30. P.R. Subramanian, M.G. Mendiratta, and D.M. Dimiduk: *Mater. Res. Soc. Symp. Proc.*, 1994, vol. 322, pp. 491-502.
31. B.P. Bewlay, M.R. Jackson, W.J. Reeder, and H.A. Lipsitt: *Mater. Res. Soc. Symp. Proc.*, 1995, vol. 364, pp. 943-48.
32. H.A. Lipsitt, M.J. Blackburn, and D.M. Dimiduk: in *Intermetallic Compounds—Principles and Practices*, vol. 2, J.H. Westbrook and R.L. Fleischer, eds., John Wiley & Sons, New York, NY, 2002, pp. 471-99.
33. D.L. Davidson, K.S. Chan, and D.L. Anton: *Metall. Mater. Trans. A*, 1996, vol. 27A, pp. 3007-18.
34. K.S. Chan and D.L. Davidson: *Metall. Mater. Trans. A*, 1999, vol. 30A, pp. 471-39.
35. S.J. Balsone, B.P. Bewlay, M.R. Jackson, P.R. Subramanian, J.-C. Zhao, A. Chatterjee, and T.M. Heffernan: in *Structural Intermetallics 2001*, K.J. Hemker, D.M. Dimiduk, H. Clemens, R. Darolia, H. Inui, J.M. Larsen, V.K. Sikka, M. Thomas, and J.D. Whittenberger, eds., TMS, Warrendale, PA, 2001, pp. 99-108.
36. G. Wang, B. Gleeson, and D.L. Douglass: *Oxid. Met.*, 1991, vol. 35, pp. 333-48.
37. G. Wang, B. Gleeson, and D.L. Douglass: *Oxid. Met.*, 1991, vol. 35, pp. 317-22.
38. F. Gesmundo, F. Viani, Y. Niu, and D.L. Douglass: *Oxid. Met.*, 1993, vol. 39, pp. 197-209.
39. F. Gesmundo, F. Viani, Y. Niu, and D.L. Douglass: *Oxid. Met.*, 1993, vol. 40, pp. 373-93.
40. F.H. Stott, G.C. Wood, and J. Stringer: *Oxid. Met.*, 1995, vol. 44, pp. 113-45.
41. K.S. Chan: Southwest Research Institute, San Antonio, TX, unpublished research, 2003.
42. *Annual Book of ASTM Standards*, ASTM E1085-87, ASTM Philadelphia, PA, 1995, vol. 03.06.
43. K.S. Chan: *Metall. Mater. Trans. A*, 2003, vol. 34A, pp. 1833-49.
44. B.P. Bewlay and M.R. Jackson: in *Comprehensive Composite Materials*, A. Kelly and C. Zweben, eds., vol. 3, *Metal Matrix Composites*, T.W. Clyne, ed., Elsevier, New York, NY, 2000, vol. 3, pp. 579-613.
45. Joint Committee on Powder Diffraction Files, International Center for Diffraction Data, Swarthmore, PA, 1992.
46. E.S.K. Menon, M.G. Mendiratta, and D.M. Dimiduk: in *Structural Intermetallics 2001*, J.J. Hemker, D.M. Dimiduk, H. Clemens, R. Darolia, H. Inui, J.M. Larsen, V.K. Sikka, M. Thomas, and J.D. Whittenberger, eds., TMS, Warrendale, PA, 2001, pp. 591-600.
47. W.S. Walston, K.S. O'Hara, E.W. Ross, T.M. Pollock, and W.H. Murphy: in *Superalloy 1996*, R.D. Kissinger, D.J. Deye, D.L. Anton, A.D. Cetel, M.V. Nathal, T.M. Pollock, and D.A. Woodford, eds., TMS, Warrendale, PA, 1996, pp. 27-34.
48. W.S. Walston: General Electric Aircraft Engines, Cincinnati, OH, private communication, July 25, 2003.



## **APPENDIX 6**

### **"Cyclic Oxidation Resistance of Niobium-Based In-Situ Composites: Modeling and Experimentation"**

**Kwai S. Chan**

**Oxidation of Metals  
Volume 61, Nos. 3/4, (2004) pp. 165-194**

**April 2004**

Reprinted with permission from  
*Springer*, New York, NY

## Cyclic-Oxidation Resistance of Niobium-Base *in situ* Composites: Modeling and Experimentation

K. S. Chan\*†

Received March 6, 2003; Revised December 31, 2003

Despite significant improvements in recent years, the oxidation resistance of niobium-base *in situ* composites is still inadequate for high-temperature applications because of their fast oxidation and the difficulty to form a coherent, protective-oxide layer on the Nb solid solution. Recently, several oxidation models have been proposed in the literature for treating the oxidation behavior of two-phase materials, which show features that are applicable to niobium-base *in situ* composites. In this article, the theoretical oxidation model proposed by Gesmundo et al. [Oxidation of Metals 39, 197–209 (1993)] for treating independent isothermal oxidation of two-phase binary alloys has been extended to cyclic oxidation and applied to analyze existing oxidation data of niobium-base *in situ* composites. The critical conditions required to form a protective-oxide layer on Nb-base *in situ* composites is predicted via existing models proposed by Wang et al. [Oxidation of Metals 35, 317–322, 333–348 (1991)]. The analytical results are then used to identify possible means for improving the oxidation properties of the Nb-base *in situ* composites. Key conditions required for achieving a continuous protective oxide are predicted and compared against critical experiments performed on Nb-base *in situ* composites.

**KEY WORDS:** cyclic oxidation; Nb-base *in situ* composites; oxidation modeling; protective oxide formation.

### INTRODUCTION

Extensive work has been undertaken to develop niobium-base structural alloys for high-temperature applications. The early studies,<sup>1–9</sup> which were

\*Southwest Research Institute®, 6220 Culebra Road, San Antonio, TX 78238, USA.  
†e-mail: kchan@swri.org

reviewed extensively by Stringer,<sup>10</sup> and others,<sup>11-13</sup> focused mostly on the use of alloying addition to reduce the oxidation kinetics of Nb alloys by modifying the oxidation products. These studies indicated that the formation of Nb<sub>2</sub>O<sub>5</sub>, a non-protective oxide, was too dominant to be altered by alloying additions. Subsequent studies<sup>14-19</sup> were concentrated on an aluminide-base system and the use of Al additions to improve the oxidation resistance of Nb-base alloys through the formation of a protective alumina layer. While the formation of protective alumina scales was shown to be feasible, the resulting alloys had low melting points and were too brittle to be used as structural materials.<sup>16</sup>

Recent efforts have focused mostly on materials that are based on niobium silicides and Laves phases.<sup>20-35</sup> These new systems include Nb-Si, Nb-Ti-Si, Nb-Ti-Al-Si, Nb-Ti-Cr-Si, and among others, Nb-Ti-Hf-Cr-Al-Si. Often referred to as refractory-metal intermetallic composites (IMCs),<sup>26,27</sup> the salient characteristics of these Nb-base *in situ* composites are multiphase microstructures comprised of silicides, Laves phases and Nb solid solution. The silicides and Laves phases are intended to provide high-temperature strength and oxidation resistance, while the "ductile" Nb solid solution is intended to provide tensile ductility and fracture resistance at ambient temperature. The oxidation resistance of these Nb-base *in situ* composites, which is substantially better than that of conventional Nb alloys,<sup>23,25,26,28,32</sup> is comparable to that of Ni-base superalloys at 1000°C. Unfortunately, the oxidation resistance of Nb-base *in situ* composites are still inadequate as structural materials in the 1200-1400°C range, as the oxides that form on these materials are non-protective.<sup>22,25,26,28,32</sup> For both static and cyclic oxidation, the oxidation products of Nb-base *in situ* composites are a mixture of oxides that include Nb<sub>2</sub>O<sub>5</sub>, CrNbO<sub>4</sub>, Ti<sub>2</sub>Nb<sub>10</sub>O<sub>29</sub> and Nb<sub>2</sub>O<sub>5</sub>·TiO<sub>2</sub> plus small amounts of cristoballite SiO<sub>2</sub> and GeO<sub>2</sub>.<sup>34,35</sup> To improve the oxidation resistance of the Nb-base *in situ* composites, it is necessary to promote the formation of a more protective-oxide layer.

The current understanding of the formation of protective Cr<sub>2</sub>O<sub>3</sub>, Al<sub>2</sub>O<sub>3</sub>, and SiO<sub>2</sub> scales on iron-, nickel-, and cobalt-base alloys has been discussed in a recent review article.<sup>36</sup> Very little information, however, is available on the conditions required for the formation of protective oxide scales on Nb-base materials. Wang *et al.*,<sup>37,38</sup> and Gesmundo *et al.*<sup>39-45</sup> recently analyzed the conditions leading to the formation of non-protective and protective oxide scales on generic two-phase binary alloys. These results indicated that for two-phase alloys, the critical value of the average concentration of the active element required for the exclusive growth of a protective-oxide layer is higher than that for single-phase alloys. In addition, the critical values depend also on the solubility of the active

element in the solid solution,<sup>37</sup> as well as the volume fraction, the size, and the shape of the second phase.<sup>38</sup> The exclusive formation of a protective-oxide layer is predicted not to occur when the ratio between the parabolic rate constant of oxidation and the alloy interdiffusion coefficient becomes large or the solubility of the most reactive compound in the most noble metal is too small, regardless of the concentration of the active element.

The objective of this paper is to extend the oxidation models of Gesmundo *et al.*,<sup>39,40</sup> Wang *et al.*,<sup>37,38</sup> and Gesmundo and Gleeson<sup>43</sup> to analyze the cyclic-oxidation behavior of Nb-base *in situ* composites. In particular, the independent oxidation model of Gesmundo *et al.*,<sup>39</sup> for isothermal temperature, is extended to treat independent cyclic oxidation of individual phases in Nb-base *in situ* composites. The analyses by Wang *et al.*,<sup>37,38</sup> Gesmundo *et al.*,<sup>40</sup> and Gesmundo and Gleeson<sup>43</sup> are then applied to identify: (1) the conditions that lead to the formation of mixed oxides, and (2) possible means for instigating the development of a protective-oxide layer on Nb-base *in situ* composites. The accuracy of the model predictions is assessed by comparison against critical cyclic-oxidation experiments performed on a series of Nb-base *in situ* composites.<sup>35</sup> This paper is organized into three main parts. In the first part, current models for treating oxidation of multiphase microstructures are presented. In the second section, relevant models are applied to analyze oxidation data of Nb-base *in situ* composites and to predict means for improving the oxidation resistance of the composites. In the third section, cyclic-oxidation experiments performed on five Nb-base *in situ* compositions are reported, and the results are used to assess the accuracy of the oxidation models.

### OXIDATION OF MULTIPHASE MATERIALS

The oxidation process of multiphase materials can take place in several forms without a common mechanism for their scaling behavior. At least three different oxidation behaviors have been identified by experimental observations,<sup>43</sup> which include: (1) independent oxidation of individual phases, (2) cooperative oxidation of two or more phases, and (3) exclusive oxidation of a single phase to form a slow-growing, protective-oxide layer that drastically reduces the oxidation kinetics of the multiphase alloy.<sup>43</sup> Each of these three oxidation mechanisms is analyzed and the analysis is applied to treat the cyclic-oxidation behavior of Nb-base *in situ* composites. Particular attention will be focused on developing a mean for predicting the transitions from an independent oxidation or a cooperative oxidation of individual phases to the exclusive oxidation of a single phase with formation of a slow-growing, protective-oxide layer.

### Independent Oxidation

The oxidation of two-phase binary  $A$ - $B$  alloys was previously analyzed by Gesmundo *et al.*,<sup>39</sup> for isothermal conditions. Several restrictive assumptions were adopted in this oxidation analysis,<sup>39</sup> including: (1) the two-phase microstructure is comprised of a  $B$ -rich phase,  $\beta$ , dispersed as isolated particles in the  $A$ -rich matrix,  $\alpha$ , (2) only one oxide each is formed by  $A$  and  $B$  and no ternary oxides form, (3) the oxide of  $A$  is less stable and grows more rapidly than that of  $B$ , (4) the two oxides grow according to the parabolic rate law, and (5) the oxygen activity prevailing at the alloy/scale interface corresponds to the equilibrium value of the formation of the less stable oxide so that both oxides can form at the site. An obvious and necessary consequence of these assumptions is that the overall weight change,  $\Delta W$ , measured after some time of isothermal oxidation is the sum of the contributions from the individual phases. Using this mass-balance relation as the starting point, Gesmundo *et al.*,<sup>39</sup> derived the general relation between the parabolic rate constant of a two-phase alloy in terms of the volume fractions and the parabolic rate constants of the constituent elements. In addition, Gesmundo *et al.*, elucidated the effects of the size and distribution of the second-phase particles on the overall oxidation kinetics, and identified the critical conditions that would lead to the formation of a continuous layer of the protective oxide.

In this paper, we extend the approach of Gesmundo *et al.*, to treat the cyclic-oxidation behavior of multiphase alloys containing multiple elements. Such an extension is considered valid since the fundamental relation is basically a mass balance. Specifically, the overall weight change,  $\Delta W$ , measured after some time of cyclic oxidation is assumed to be the sum of contribution from individual phases. Therefore,

$$\Delta W = \sum_{i=1}^{i=n} \Delta W_i \quad (1)$$

where  $\Delta W_i$  is the weight change and  $n$  is the number of individual phases. In addition, the cyclic-oxidation response of each individual phase is assumed to proceed according to the parabolic rate law and to involve spallation according to the power law proposed by Chan.<sup>46</sup> Substituting the appropriate expressions gives

$$\frac{\Delta W_i}{S_i} = \sqrt{k_{p(i)}t} - q_i \Delta T^2 \left[ \frac{W_i}{W_o} \right]^{m_i} \quad (2)$$

where  $S_i$  is the surface area,  $k_{p(i)}$  is the parabolic oxidation rate constant,  $q_i$  is the spallation constant, and  $m_i$  is the spallation exponent of the  $i$ th

phase. Moreover,  $W_i$  is the weight of the oxide formed by the  $i$ th phase;  $W_o$  is the reference weight taken to be  $1 \text{ mg/cm}^2$ ; and  $\Delta T$  is the temperature change during cyclic oxidation. The formulation of Eq. (2) has been described in detail by Chan in an earlier publication.<sup>46</sup> The first term on the right-hand side of Eq. (2) corresponds to weight gain due to oxidation of individual elements while the second term is the weight loss due to spallation of individual oxides. As will be shown in a later section (Model Applications), the assumption of the parabolic rate relation for describing the oxidation kinetics of the constituent phases (Nb solid-solution, silicides, and Laves phase) in Nb-base *in situ* composites is valid for certain, though not all, compositions. It is also noted that Eq. (2) reduces to that for isothermal-oxidation conditions when oxide spallation due to thermal cycling (second term in Eq. (2)) is negligible ( $q_i = 0$ ). The overall weight change per unit area can be obtained by substituting Eq. (2) into Eq. (1), leading to

$$\frac{\Delta W}{S} = \sum_{i=1}^{i=n} \frac{S_i}{S} \left[ \sqrt{k_{p(i)} t} - q_i \Delta T^2 \left( \frac{W_i}{W_o} \right)^{m_i} \right] \quad (3)$$

where  $S$  is the overall area. Eq. (3) may be rewritten as

$$\frac{\Delta W}{S} = \sum_{i=1}^{i=n} f_i \sqrt{k_{p(i)} t} - \sum_{i=1}^{i=n} f_i q_i \Delta T^2 \left( \frac{W_i}{W_o} \right)^{m_i} \quad (4)$$

since the ratio  $S_i/S$  is the area fraction,  $f_i$ , of the  $i$ th phase. The general expression for the overall weight change is given by

$$\frac{\Delta W}{S} = \sqrt{k_p t} - q \Delta T^2 \left( \frac{W}{W_o} \right)^m \quad (5)$$

where  $W$  is the weight of oxide,  $k_p$  is the parabolic constant defined in terms of weight gain,  $q$  is the spallation constant, and  $m$  is the spallation exponent of the overall microstructure. Eq. (5) can be equated to Eq. (4) to give

$$k_p^{1/2} = \sum_{i=1}^{i=n} f_i k_{p(i)}^{1/2} \quad (6)$$

and

$$q = \sum_{i=1}^{i=n} f_i q_i (f_i d_i)^{m_i} \left( \frac{W}{W_o} \right)^{m_i - m} \quad (7)$$

with

$$m = \sum_{i=1}^{i=n} f_i m_i \quad (8)$$

where  $d_i$  is the density of the individual oxides. Equations (6) and (7) indicate that for independent oxidation, the parabolic rate constant and the spallation constant of a multiphase microstructure can be computed on the basis of the area fraction ( $f_i$ ), weight fraction ( $f_i d_i$ ), the parabolic rate constant ( $k_{p(i)}$ ), and the spallation constant ( $q_i$ ) of individual phases. For isothermal oxidation, the spallation term in Eq. (5) vanishes ( $q_i = 0$ ) and Eq. (6) recovers the expression reported by Gesmundo *et al.*<sup>43</sup> for independent isothermal oxidation of a two-phase microstructure.

#### Exclusive Formation of a Protective-Oxide Layer

Wagner's classical analysis<sup>47</sup> identified critical conditions for the exclusive formation of a slow-growing, protective-oxide scale on the surface of a solid-solution alloy containing  $A$  and  $B$  by selective oxidation of the more reactive element,  $B$ . According to Wagner's analysis,<sup>47</sup> the minimum concentration,  $N_{B(W)}^*$ , of the more reactive component  $B$  required for its exclusive oxidation on the surface of a binary alloy containing elements  $A$  and  $B$  is given by<sup>40</sup>

$$N_{B(W)}^* \geq \sqrt{\pi u} \quad (9)$$

with

$$u = \frac{1}{2} \sqrt{\frac{k_r}{D}} \quad (10)$$

where  $k_r$  is the parabolic rate constant defined in terms of thickness of metal recession ( $X_r = (k_r t)^{1/2}$ , where  $X_r$  is thickness of metal recession) and  $D$  is the interdiffusion coefficient in the alloy. The analysis by Wagner,<sup>47</sup> which is based on a fixed alloy/scale interface with a zero solute concentration, has been extended by Wang *et al.*,<sup>37</sup> and by Gesmundo *et al.*,<sup>40</sup> to allow for movement of the alloy/scale interface with a non-zero solute concentration. The extended analysis by Wang *et al.*,<sup>37</sup> gives the critical concentration as

$$N_B^* \geq N_B^e + [1 - N_B^e] F(u) \quad (11)$$

with

$$F(u) \equiv \sqrt{\pi u} \exp(u^2) \operatorname{erfc}(u) \quad (12)$$



where  $N_B^e$  is the minimum solute composition for preferential oxidation of  $B$  required by thermodynamics and  $\text{erfc}(u)$  represents the complementary error function of  $u$ . The right-hand side of the criterion given by Eq. (11) represents the combination of the thermodynamic and kinetics requirements for the exclusive oxidation of  $B$  in the alloy. In many analyses,<sup>40,47</sup>  $N_B^e$  is taken to be negligible, and selection oxidation of  $B$  is then dictated solely by the kinetics requirement as represented by the auxiliary function  $F(u)$ . As shown earlier by Wang *et al.*,<sup>37</sup>  $N_B^* \leq N_{B(W)}^*$  and Eq. (11) gives a more realistic value for the critical concentration than Eq. (9).

For two-phase alloys, the critical concentration of solute necessary for its exclusive oxidation was analyzed by Wahl.<sup>48</sup> This analysis was approximate because of two assumptions: (1) there was a steady-state flux of solute atoms to the alloy/solute-metal-oxide interface, and (2) the solubility of  $B$  in the matrix was nil. Recently, Gesmundo and Gleeson<sup>43</sup> extended Wahl's treatment to account for the presence of the solute in the matrix. According to this analysis, the exclusive oxidation of the solute,  $B$ , for a two-phase ( $\alpha + \beta$ ) alloy occurs at the condition given by<sup>43</sup>

$$\{N_{B(\alpha)} [N_{B(\alpha)} + 2f_\beta (N_{B(\beta)} - N_{B(\alpha)})]\}^{1/2} \geq N_{B(W)}^* = \sqrt{\pi}u \quad (13)$$

where  $N_{B(\alpha)}$  and  $N_{B(\beta)}$  are the mole fractions of  $B$  in the  $\alpha$  phase (Nb solid solution) and the  $\beta$  (intermetallic particles) phase, respectively, while  $f_\beta$  is the volume fraction of the  $\beta$  phase. From Eq. (13), the critical volume fraction,  $f_\beta^*$ , of the  $\beta$  phase (intermetallic particles) for the exclusive oxidation of  $B$  is

$$f_\beta^* \geq \frac{\pi u^2 - N_{B(\alpha)}^2}{2N_{B(\alpha)}(N_{B(\beta)} - N_{B(\alpha)})} \quad (14)$$

and the corresponding critical concentration is

$$N_B^* \geq \frac{1}{2} \left[ \frac{\pi u^2}{N_{B(\alpha)}} + N_{B(\alpha)} \right]. \quad (15)$$

Both Eqs. (14) and (15) are approximate because steady-state condition and a planar interface between phase fields are assumed in the flux balance.

In addition to volume fraction, the size and distribution of the  $\beta$  phase are also important variables affecting the oxidation kinetics. According to an analysis by Wang *et al.*,<sup>38</sup> the ratio of precipitate volume fraction,  $f_\beta$ , to precipitate radius,  $r$ , must exceed a critical value in order to ensure exclusive formation of the solute-metal oxide on the surface of a two-phase alloy. The critical  $f_\beta/2r$  ratio is related to the interdiffusion

coefficient,  $D$ , according to the expression given by<sup>38</sup>

$$\frac{f_\beta}{2r} \geq \frac{1}{3\sqrt{Dt}} \Phi \left( \frac{N_{B(\alpha)}}{N_{B(W)}^*} \right) \quad (16)$$

where  $t$  is the time of oxidation and the function  $\Phi$  can be approximated as

$$\Phi = A \left( \frac{N_{B(W)}^*}{N_{B(\alpha)}} \right)^{-3/2} \quad (17)$$

where  $A$  is a constant and  $N_{B(W)}^*$  is given by Eq. (9). The value of  $A (= 0.0479)$  was obtained by fitting Eq. (17) to the numerical results reported by Wang *et al.*<sup>38</sup> Substituting Eq. (17) into Eq. (16) leads to

$$\frac{f_\beta}{2r} \geq \frac{0.0479}{3\sqrt{Dt}} \left( \frac{\sqrt{\pi u}}{N_{B(\alpha)}} \right)^{3/2} \quad (18)$$

as the criterion for the onset of the formation of a continuous, slow-growing oxide scale on the surface of a binary alloy with a two-phase microstructure.

#### MODEL APPLICATIONS TO Nb-BASE *IN SITU* COMPOSITES

The various oxidation models are compared against the oxidation data of Nb-base *in situ* composites in this section. The comparison requires an evaluation of the parabolic rate constants for oxidation of the constituent phases of the *in situ* composites. To obtain the parabolic constants, experimental data of weight gain from the literature were plotted against  $t^{1/2}$ , where  $t$  is time of oxidation. Figure 1a illustrates the parabolic oxidation behaviors observed in Nb-25Ti<sup>49</sup> and Nb-38Ti-12Hf-12Al<sup>24</sup> during isothermal oxidation at 800–1200°C. Parabolic oxidation behavior has also been reported for isothermal oxidation of pure Nb, as well as for four of nine multicomponent Nb-base alloys at 800–1200°C.<sup>34</sup> These Nb-base alloys contained Ti, Hf, Cr, Si, and Ge contents that are similar to those investigated in this study. When the oxidation behavior deviated from the parabolic rate law, the time exponent was in the range of 0.1–0.6<sup>34</sup> for the multicomponent Nb-alloys. On the other hand, some Nb-base alloys containing high-Al contents were reported to exhibit linear oxidation kinetics.<sup>16,34</sup> Thus, the time exponent for isothermal oxidation of Nb-base alloys can range from 0.1 to 1, depending on alloy composition. For simplicity, parabolic oxidation behavior was assumed for all Nb-base alloys considered in this study. The parabolic rate constant in terms

of weight gain,  $k_p$ , was obtained by least-square, linear-regression analysis of the weight-gain data. The corresponding parabolic rate constant in terms of metal recession,  $k_r$ , was then computed based on  $k_p$ , the composition of the oxides, and the molar volume of the alloy. A summary of the  $k_p$  and  $k_r$  rate constants for Nb-25Ti<sup>49</sup> and Nb-38Ti-12Hf-12Al<sup>22</sup> and NbCr<sub>2</sub><sup>14</sup> is presented in Table I.

The parabolic rate constants were plotted against reciprocal temperature, Figs. 1b and c, to obtain the activation energy, according to the general expressions.

$$k_p = k_{p0} \exp\left(-\frac{Q_{ox}}{RT}\right) \quad (19)$$

and

$$k_r = k_{r0} \exp\left(-\frac{Q_{ox}}{RT}\right) \quad (20)$$

where  $k_{p0}$  and  $k_{r0}$  are appropriate pre-exponential coefficients for weight gain and material recession, respectively. The values of the activation energy,  $Q_{ox}$ , and of  $k_{p0}$  and  $k_{r0}$  are presented in Table II. Parabolic rate constants for NbCr<sub>2</sub>, Cr<sub>2</sub>O<sub>3</sub>, Al<sub>2</sub>O<sub>3</sub>, and SiO<sub>2</sub> are from the literature.<sup>50-52</sup> The parabolic rate constants shown in Table II were used to perform model calculations for comparison against experimental data, as well as for parametric evaluation of the oxidation models.

Material recession was computed as a function of temperature for Nb-25Ti, Nb-Ti-Hf-Al, and NbCr<sub>2</sub>. The resulting oxide scale was assumed to be a mixture of TiO<sub>2</sub>, Nb<sub>2</sub>O<sub>5</sub>, CrNbO<sub>4</sub>, and Cr<sub>2</sub>O<sub>3</sub>, based on the experimental data used to establish the  $k_r$  constants.<sup>1,14,49</sup> The results are compared against those for the formation of a continuous layer of

Table I. Parabolic Oxidation Rate Constants  $k_p$  and  $k_r$  for Nb Alloys and NbCr<sub>2</sub>

Material	$T, ^\circ\text{C}$	$k_{p,m}, \text{mg}^2/\text{cm}^4/\text{hr}$	$k_r, \mu\text{m}^2/\text{hr}$
Nb-25Ti <sup>49</sup>	1200	526.7	8064.8
	1000	55.2	845.0
NbCr <sub>2</sub> <sup>14</sup>	1200	10.68	151.9
	1038	2.9	41.4
	927	1.7	24.9
	500	$2.2 \times 10^{-3}$	$3.2 \times 10^{-2}$
	1200	248.7	989.0
Nb-38Ti-12Hf-12Al <sup>22</sup>	1000	11.2	44.4
	800	3.3	13.0

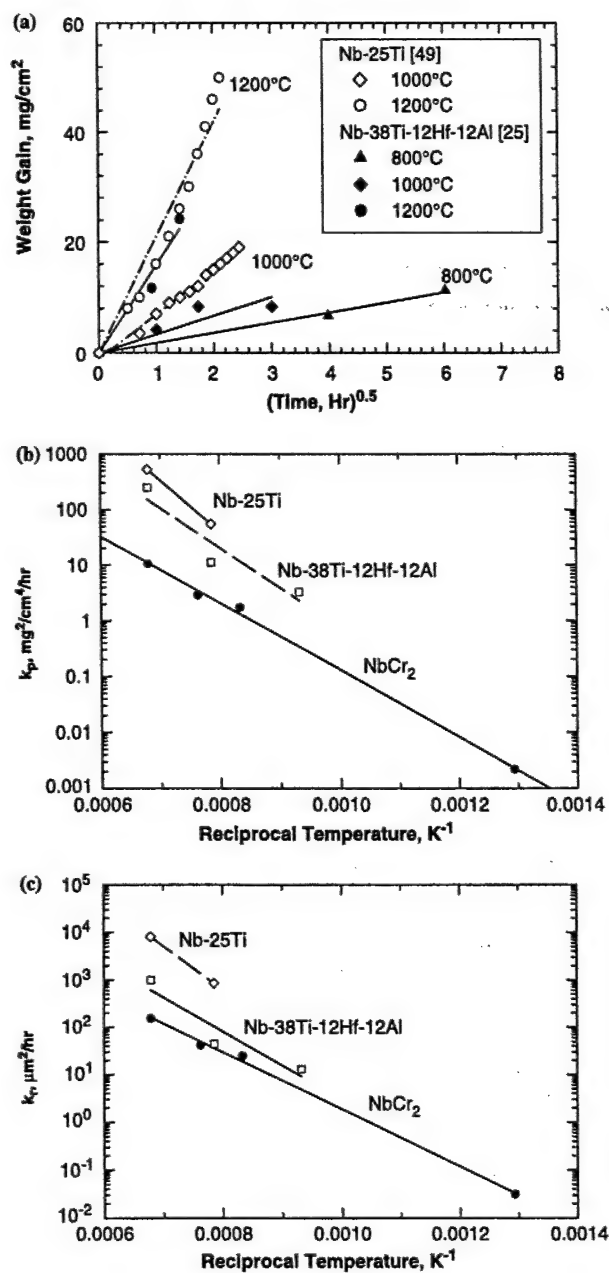


Fig. 1. Parabolic oxidation rate constants for selected Nb-base alloys: (a) plot of weight gain vs.  $t^{1/2}$ , (b)  $k_p$ , and (c)  $k_r$ .

Table II. Pre-exponent Coefficients ( $k_{po}$  and  $k_{ro}$ ) and Activation Energy ( $Q_{ox}$ ) of the Parabolic Oxidation Rate Constants for Nb-base Alloys, NbCr<sub>2</sub>, Al<sub>2</sub>O<sub>3</sub> Former, SiO<sub>2</sub> Former, and Cr<sub>2</sub>O<sub>3</sub> Former. The Activation Energy,  $Q_{ox}$ , is Normalized by the Universal Gas Constant,  $R$

Material	$k_{po}$ , mg <sup>2</sup> /cm <sup>4</sup> /hr	$k_{ro}$ , μm <sup>2</sup> /hr	$Q_{ox}/R$ , °K
Nb-25Ti	$9.065 \times 10^8$	$1.388 \times 10^{10}$	$2.115 \times 10^4$
Nb-Ti-Hf-Al	$4.686 \times 10^7$	$1.864 \times 10^8$	$1.658 \times 10^4$
NbCr <sub>2</sub>	$1.2871 \times 10^5$	$1.849 \times 10^6$	$1.379 \times 10^4$
Al <sub>2</sub> O <sub>3</sub>	$5.946 \times 10^{10}$	$1.694 \times 10^{12}$	$4.342 \times 10^4$
SiO <sub>2</sub>	15.0	$1.093 \times 10^3$	$1.316 \times 10^4$
Cr <sub>2</sub> O <sub>3</sub>	$3.2125 \times 10^7$	$1.1914 \times 10^9$	$2.777 \times 10^4$

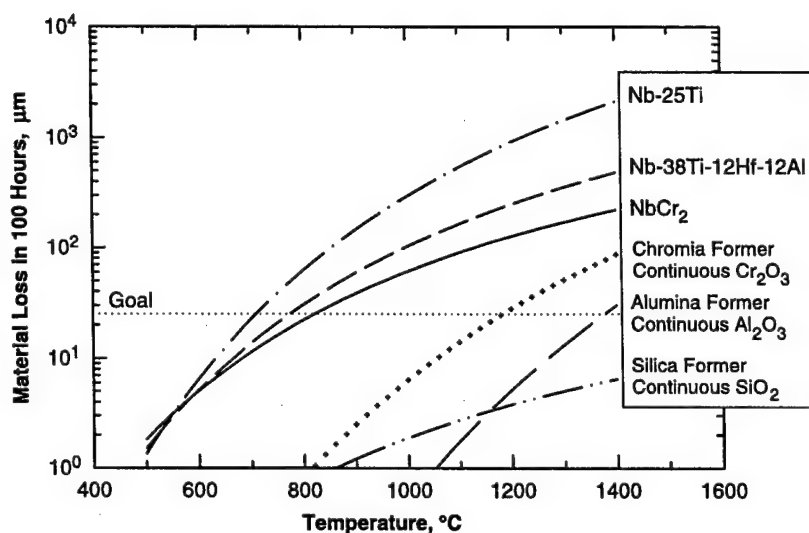


Fig. 2. Model calculations of material loss in 100 hr at various temperatures for Nb-25Ti, Nb-38Ti-12Hf-12Al, NbCr<sub>2</sub>, and those that form a continuous layer of Cr<sub>2</sub>O<sub>3</sub>, Al<sub>2</sub>O<sub>3</sub>, or SiO<sub>2</sub>.

Cr<sub>2</sub>O<sub>3</sub>,<sup>19,50,51</sup> Al<sub>2</sub>O<sub>3</sub>,<sup>52</sup> and SiO<sub>2</sub>,<sup>52</sup> in Fig. 2, together with the oxidation goal, which is less than 25 μm after 100 hr of exposure for the Nb-base *in situ* composites in a high-temperature structural application. The comparison indicates that the oxidation resistance of Nbss/NbCr<sub>2</sub> *in situ* composites would not be sufficient to meet the oxidation goal without the formation of a continuous Cr<sub>2</sub>O<sub>3</sub> layer. Similarly, Nb-Ti-Hf-Cr-Al/silicides *in situ* composites require a continuous layer of SiO<sub>2</sub> or Al<sub>2</sub>O<sub>3</sub>.

The recession in Nbss/silicide *in situ* composites was calculated using the  $k_p$  values for Nb-Ti-Hf-Al-Cr as the matrix<sup>22</sup> and  $\text{SiO}_2$ <sup>52</sup> for the silicides, assuming that  $\text{SiO}_2$  forms by oxidation of the silicide phase. The computation was performed for 100 hr of oxidation at 1200°C, for which experimental data are reported in the literature.<sup>22,24-32</sup> Figure 3 shows a comparison of the calculated material recession after 100 hr against experimental data. The calculations for the *in situ* composite are generally poor, but are in agreement with some of the experimental data of silicide IMCs and Laves IMCs. The recession data observed in Nb-Ti-Si and Nb-Ti-Al-Si exceeded the model calculation. Review of the experimental data<sup>22,23,25-32</sup> indicated that these materials did not oxidize according to a parabolic rate law, but according to a linear rate law. IMCs containing silicide, Laves, or a combination of silicide and Laves phases appear

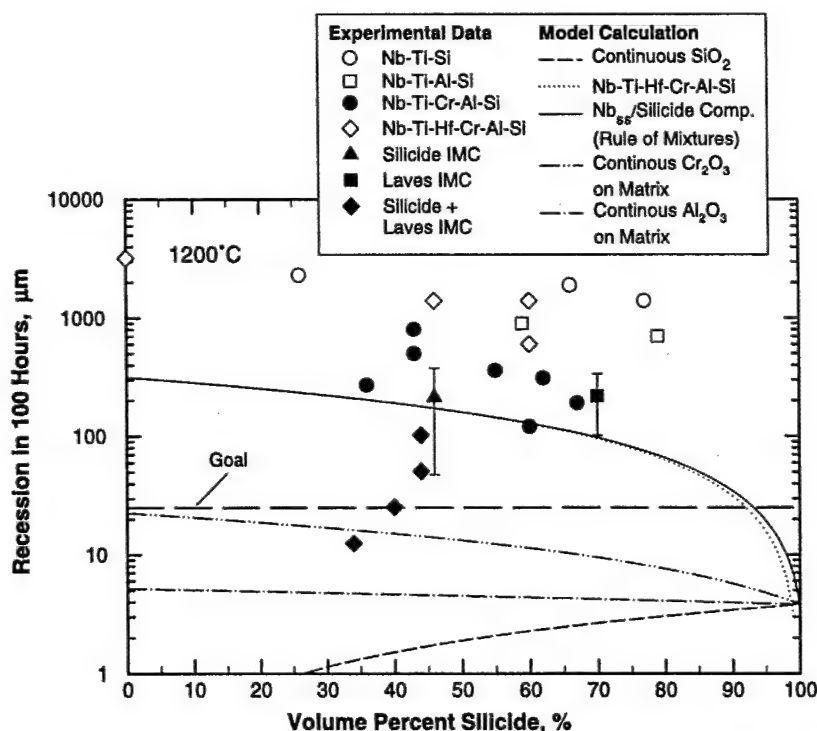


Fig. 3. Comparison of calculated and measured material recession after 100 hr of oxidation for Nb-base *in situ* composites at 1200°C. Materials that exhibit higher material recession than the model calculations did not obey parabolic oxidation kinetics. Experimental data are from the literature.<sup>22,23,25-32</sup>

to exhibit parabolic scale growths whose kinetics are largely described by the rule-of-mixtures, suggesting that oxidation of individual phase occurs primarily independently. Figure 3 also indicates that a continuous layer of  $\text{Cr}_2\text{O}_3$ ,  $\text{Al}_2\text{O}_3$ , or  $\text{SiO}_2$  is required in order to meet the oxidation goal. Only one composite met the oxidation goal of  $25\text{ }\mu\text{m}$  recession<sup>27-29</sup> after 100 hr of exposure and another one was close to meeting the goal. The source of oxidation resistance in these two materials has yet to be established.

The critical conditions for the transition from independent oxidation to exclusive formation of  $\text{SiO}_2$  and  $\text{Cr}_2\text{O}_3$  were calculated using the formulation of Gesmundo and Gleeson.<sup>43</sup> The volume percents of silicide and Laves phase required were calculated via Eq. (14). Figure 4 shows a plot of critical values of volume percents silicide or Laves phase required for the onset of exclusive oxidation vs. the normalized parameter  $u$ . The model calculation indicates that the value of  $u$  must be less than 0.03 to 0.15 in order for the exclusive formation of  $\text{SiO}_2$  and  $\text{Cr}_2\text{O}_3$  to occur, respectively. Experimental data for the niobium-base *in situ* composites all

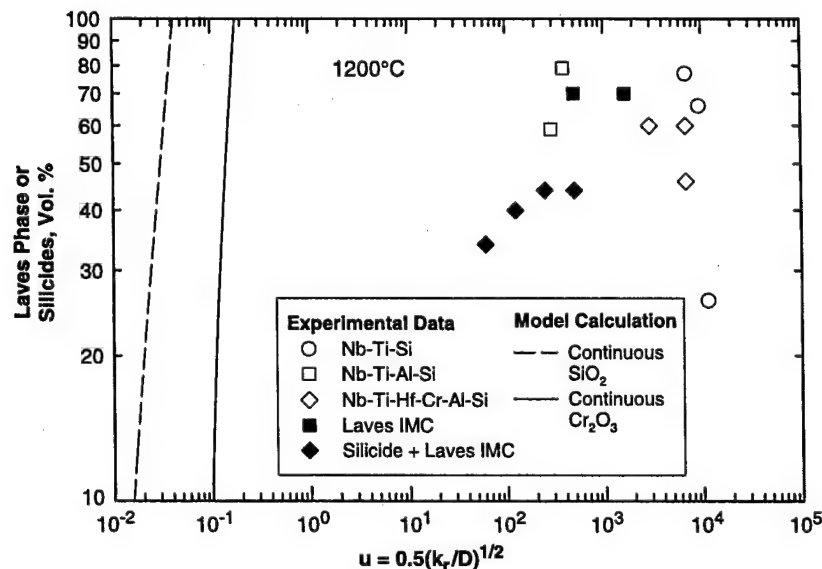


Fig. 4. Experimental data of Nb-base *in situ* composites compared against model predictions of the critical volume percent of Laves phase of silicides required to form a continuous protective  $\text{Cr}_2\text{O}_3$  or  $\text{SiO}_2$  layer for various values of the normalized parameter  $u$ . The  $u$  values for Nb-base *in situ* are several orders of magnitude larger than the critical values predicted by the model.



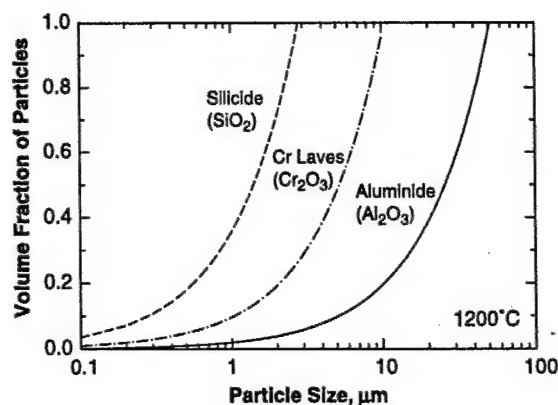


Fig. 5. Model calculations of the critical volume fraction of particles as a function of particle size (diameter) for forming a protective-oxide layer of  $\text{SiO}_2$ ,  $\text{Cr}_2\text{O}_3$ , and  $\text{Al}_2\text{O}_3$  for silicide, Cr Laves phase, and aluminide particles, respectively, after 2 hr exposure at  $1200^\circ\text{C}$ .

exceed this range of  $u$  values by several orders of magnitude. For all experimental data points shown in Fig. 4, the parameter  $u$  was computed based on experimental values of parabolic rate constant,  $k_p$ , and interdiffusion coefficient,  $D$ ,<sup>10,53-55</sup> reported in the literature. The interdiffusion coefficients used corresponded to those for diffusion of  $\text{Si}^{54}$  and  $\text{Cr}^{10}$  in Nb. The implication of the results in Fig. 4 is that exclusive formation of a continuous layer of  $\text{SiO}_2$  or  $\text{Cr}_2\text{O}_3$  on Nb-base *in situ* composites is difficult, if not impossible, unless the value of the  $u$  parameter can be significantly reduced below the current values.

The possibility of controlling the particle size as a means for improving the oxidation resistance of Nb-base *in situ* composites was examined using the criterion, Eq. (18), proposed by Wang *et al.*<sup>38</sup> Figure 5 shows the critical volume fraction of particles as a function of particle size (diameter) required for onset of the formation of a continuous oxide layer of  $\text{SiO}_2$ ,  $\text{Cr}_2\text{O}_3$ , and  $\text{Al}_2\text{O}_3$  for silicides, Laves, and aluminide particles, respectively. The computations were performed for 2 hr exposure at  $1200^\circ\text{C}$ . The size requirements are most severe for silicides, followed by Laves particles and aluminide particles. This ranking is the consequence of a low Si solubility ( $\approx 0.015$ ) in Nb<sup>27</sup> and a high Al diffusivity in Nb.<sup>53</sup>

The stringent conditions required for the exclusive formation of a  $\text{SiO}_2$  or  $\text{Cr}_2\text{O}_3$  layer suggests that mixed oxides are likely to form on Nb-base *in situ* composites. Figure 6 shows a comparison of calculated results

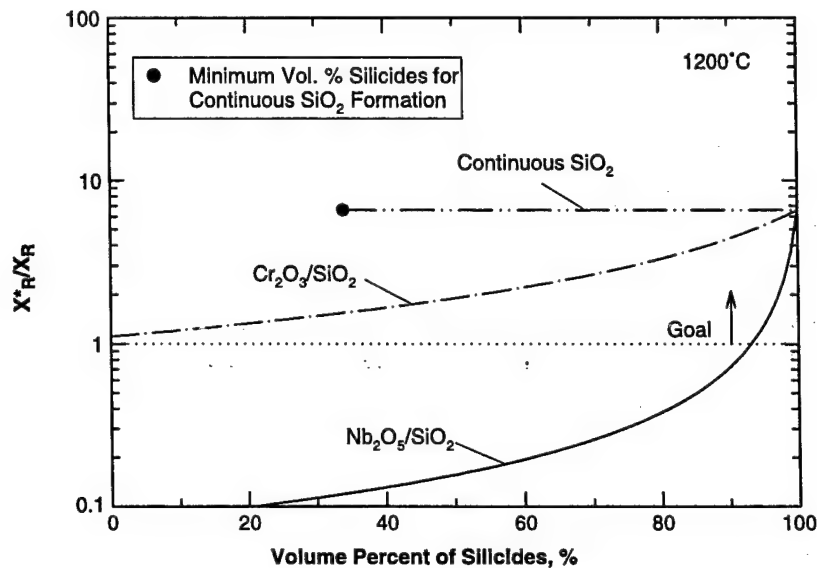


Fig. 6. Material recession goal normalized by calculated material recession for various combinations of mixed oxides compared against that for a continuous  $\text{SiO}_2$  layer for 100 hr isothermal oxidation at  $1200^\circ\text{C}$ .

of metal recession,  $X_R$ , after 100 hr isothermal oxidation at  $1200^\circ\text{C}$  associated with three cases: (1) mixed  $\text{Nb}_2\text{O}_5$  and  $\text{SiO}_2$ , (2) mixed  $\text{Cr}_2\text{O}_3$  and  $\text{SiO}_2$ , and (3) continuous  $\text{SiO}_2$ . These computations were performed using Eqs. (5)–Eq. (7) and assuming no spallation ( $q_i = 0$ ). In addition,  $\text{Nb}_2\text{O}_5$  or  $\text{Cr}_2\text{O}_3$  was assumed to form on the Nb solid-solution phase while  $\text{SiO}_2$  was assumed to form on the silicide phase. In Fig. 6, the results are shown as  $X_R^*/X_R$ , where  $X_R^* = 25\ \mu\text{m}$  after 100 hr of oxidation is the maximum metal recession targeted for the Nb-base *in situ* composites. Figure 6 indicates that the oxidation-resistance goal may be attained with a mixture of  $\text{Cr}_2\text{O}_3$  and  $\text{SiO}_2$ , while the formation of  $\text{Nb}_2\text{O}_5$  must be suppressed. To achieve a continuous  $\text{SiO}_2$ , the volume percent of silicides in the *in situ* composites must exceed 34%.

### MODEL VERIFICATION

The model calculations were evaluated against cyclic-oxidation data for several Nb-base *in situ* composites, which were fabricated as cast buttons by arc melting. Four of the alloys ( $\text{Nb}_x$ , AX, M1, and M2) were

Table III. Chemical Composition of Nb-base *In Situ* Composites in Weight Percent

	Nb <sub>x</sub>	AX	UES-AX	M1	M2
Ti	15.46	15.24	15.45	14.29	15.94
Cr	1.57	9.25	8.15	8.63	11.94
Hf	9.11	9.91	11.82	10.61	10.67
Ge	2.61	5.28	4.76	4.99	5.10
Si	.34	5.89	5.98	3.65	7.19
Nb	Balance	Balance	Balance	Balance	Balance

fabricated at Pittsburgh Materials Technology (Pittsburgh, PA), and one alloy (UES-AX) was cast at the Air Force Research Laboratory, (Dayton, OH). The compositions of these *in situ* composites, shown in Table III, were determined by Chicago Spectro Service Laboratory (Chicago, IL) using an ASTM standard procedure.<sup>56</sup> The microstructures of Nbss, AX, M1, and M2 in the as-cast condition are presented in Fig. 7, together, with the microstructure of UES-AX in the heat-treated condition (1350°C for 100 hr, HIP'ed at 207 MPa/1350°C/6 hr, followed by furnace-cool). Individual phases in the microstructure were identified by energy-dispersive spectroscopy, while their volume fractions were measured by performing quantitative-metallographic analyses on scanning-electron micrographs of the microstructure taken in the back-scattered mode. The microstructure, the size, and the volume fraction of the phases present in these alloys are summarized in Table IV. As indicated in Table IV, Nbss contained 91 vol.% Nb solid solution with about 9 vol.% of Ge-rich particles along the grain boundaries. Alloys M1, AX, and UES-AX contained Nb solid solution, C14 Laves phase, and silicides (mostly (Nb, Ti)<sub>5</sub>Si<sub>3</sub>). In comparison, M2 contained Laves phase and silicides, but no Nb solid solution. Detailed descriptions of the compositions of individual phases in these Nb-base *in situ* composites are presented in Table V.<sup>35,57</sup>

Cyclic-oxidation tests were performed by heating coupon specimens to 1100°C, which were then held at temperature for 22 hr and subsequently furnace-cooled to ambient temperature in 2 hr. The specimens were weighed before and after each thermal cycle. This process was repeated for a total oxidation time of ≈500 hr. Weight-change data were obtained as a function of time of oxidation. The oxide spalls were collected in a ceramic dish for individual alloys. After-cyclic oxidation tests, the oxides formed were determined by X-ray diffraction. Metal recessions were measured on sectioned specimens using metallographic techniques. Details of the experimental procedure are presented in a recent publication.<sup>35</sup>

Table IV. Summary of Nominal Composition, Heat-treatment, Microstructure, Volume Fractions of Individual Phases, Recession, Relative Intensity, and Oxidation Products in Nb-base *In Situ* Composites

Material	Nominal composition (atomic pct.)	Heat-treatment	Micro-structure	Nb solid solution (Vol.%)	Silicides (Vol.%)	Laves (Vol.%)	Recession (after 500 hr) $\mu\text{m}$	Relative intensity $I_{\text{CrNbO}_4}/I_{\text{Nb}_2\text{O}_5 \cdot \text{TiO}_2}$	Oxides*
Nbx	Nb-28Ti-4Hf-3Cr-3Ge-1Si	As-cast	Beta Laves	+ 90.8	0	9.2	6025	0.18	Nb <sub>2</sub> O <sub>5</sub> ·TiO <sub>2</sub> , CrNbO <sub>4</sub> , HfGeO <sub>4</sub> (minor)
AX	Nb-22.5Ti-4Hf-13Cr-5Ge-15Si	As-cast	Beta silicides Laves	+ 20	66	14	330	2.28	3Nb <sub>2</sub> O <sub>5</sub> ·TiO <sub>2</sub> , CrNbO <sub>4</sub> , Ti <sub>2</sub> Nb <sub>10</sub> O <sub>29</sub> , GeO <sub>2</sub> (minor)
M1	Nb-22.5Ti-4Hf-13Cr-5Ge-10Si	As-cast	Beta silicides Laves	+ 63.8	38.3	7.9	838	2.26	3Nb <sub>2</sub> O <sub>5</sub> ·TiO <sub>2</sub> , Cr <sub>2</sub> NbO <sub>4</sub> , Ti <sub>2</sub> Nb <sub>10</sub> O <sub>29</sub> , GeO <sub>2</sub> (minor)
M2	Nb-22.5Ti-4Hf-16Cr-5Ge-18Si	As-cast	Silicides Laves	+ 0	73.5	26.5	90	6.07	CrNbO <sub>4</sub> , 3Nb <sub>2</sub> O <sub>5</sub> ·TiO <sub>2</sub> , Ti <sub>2</sub> Nb <sub>10</sub> O <sub>29</sub> , GeO <sub>2</sub> (minor)
UES-AX	Nb-22.5Ti-4Hf-13Cr-5Ge-15Si	1350°C/100 hr HIP'ed@207 MPa 1350°C/6 hr	Beta silicides Laves	+ 54	34	12	292	2.64	Nb <sub>2</sub> O <sub>5</sub> , CrNbO <sub>4</sub> , GeO <sub>2</sub> (minor), 3Nb <sub>2</sub> O <sub>5</sub> ·TiO <sub>2</sub> , Ti <sub>2</sub> Nb <sub>10</sub> O <sub>29</sub>

\*CrNbO<sub>4</sub> <34-03338>; 3Nb<sub>2</sub>O<sub>5</sub>·TiO<sub>2</sub> <09-0229>; GeO<sub>2</sub> <36-1463>; Nb<sub>2</sub>O<sub>5</sub> <32-0711>; TiNb<sub>10</sub>O<sub>29</sub> <13-0316>; HfGeO<sub>4</sub> <34-0409>; TiNb<sub>2</sub>O<sub>7</sub> <09-1407>; Cristoballite SiO<sub>2</sub> <39-1425>.

Table V. The Chemical Compositions and Crystal Structures of Constituent Phases in Various Nb-base *In Situ* Composites

Alloy	Heat-treatment	Nbss phase (bcc)	Silicide phase* (D8 <sub>1</sub> )	Laves phase (C14)	Ge-Rich phase (unknown)
M2-1	As-cast	—	Nb-23Ti-3Hf-4Cr-6Ge-28Si	Nb-12Ti-4Hf-52Cr-2Ge-9Si	—
M1-1	As-cast	Nb-20Ti-3Hf-12Cr-4Ge-4Si	Nb-20Ti-4Hf-3Cr-10Ge-25Si	Nb-10Ti-4Hf-49Cr-2Ge-9Si	—
AX-1	As-cast	Nb-24Ti-3Hf-14Cr-2Ge-1Si	Nb-21Ti-3Hf-3Cr-8Ge-27Si	Nb-15Ti-6Hf-49Cr-2Ge-8Si	—
Nbx-1	As-cast	Nb-29Ti-4Hf-3Cr-3Ge-3Si	—	—	Nb-39Ti-6Hf-3Cr-9Ge-6Si
UES-	1350°C/	Nb-26Ti-3Hf-14Cr-3Ge-1Si	Nb-24Ti-4Hf-1Cr-6Ge-29Si	Nb-12Ti-3Hf-54Cr-1Ge-8Si	—
AX	10 hr	—	—	—	—

\*Also contained small amounts of (Ti, Nb)<sub>3</sub>Si<sub>2</sub>(D8 Structure) and possibly Nb<sub>3</sub>Si (Ti<sub>3</sub>P structure).

The oxides spalled from the surfaces of individual alloys were identified by X-ray diffraction, comparing the observed diffraction peaks against the JCPDF standards.<sup>58</sup> These oxides are reported in Table IV together with the JCPDF card number. For Nb<sub>x</sub>, the oxide spalls were primarily Nb<sub>2</sub>O<sub>5</sub>·TiO<sub>2</sub> with small amounts of CrNbO<sub>4</sub> and HfGeO<sub>4</sub>. In AX, UES-AX, and M1, the oxide spalls contained various amounts of CrNbO<sub>4</sub> and Nb<sub>2</sub>O<sub>5</sub>·TiO<sub>2</sub>, with evidence of small amounts of possibly GeO<sub>2</sub> or cristoballite SiO<sub>2</sub>. In M2, the oxide spalls were primarily CrNbO<sub>4</sub>, but the presence of Nb<sub>2</sub>O<sub>5</sub> and GeO<sub>2</sub> could not be ruled out. The GeO<sub>2</sub> peak could possibly be that of cristoballite SiO<sub>2</sub>. The observed oxidation products are consistent with those reported for Nb alloys and NbCr<sub>2</sub> in the literature.<sup>1,3,10,14</sup> The dominant peak of CrNbO<sub>4</sub> occurs at  $2\theta = 27.3^\circ$ , while those for Nb<sub>2</sub>O<sub>5</sub>, Nb<sub>2</sub>O<sub>5</sub>·TiO<sub>2</sub>, 3Nb<sub>2</sub>O<sub>5</sub>·TiO<sub>2</sub>, and TiNb<sub>2</sub>O<sub>7</sub> all occur at  $2\theta = 23.9^\circ$ . Since Nb<sub>2</sub>O<sub>5</sub>, Nb<sub>2</sub>O<sub>5</sub>·TiO<sub>2</sub>, 3Nb<sub>2</sub>O<sub>5</sub>·TiO<sub>2</sub>, and TiNb<sub>2</sub>O<sub>7</sub> could not be distinguished based on the XRD data, they will be referred to collectively as Nb<sub>2</sub>O<sub>5</sub>·TiO<sub>2</sub> in the remainder of this paper. The intensity,  $I_{\text{CrNbO}_4}$ , at  $2\theta = 27.3^\circ$  of the CrNbO<sub>4</sub> peak was normalized by the intensity,  $I_{\text{Nb}_2\text{O}_5\cdot\text{TiO}_2}$ , at  $2\theta = 23.9^\circ$  of the Nb<sub>2</sub>O<sub>5</sub>·TiO<sub>2</sub> peak and the result was plotted as a function of volume percents of Nb solid-solution phase in Fig. 8. Figure 8 also shows the result of material recession after 500 hr of cyclic oxidation at a peak temperature of 1100°C. Three general trends can be deduced from Fig. 8: (1) high material recession is associated with the formation and spallation of Nb<sub>2</sub>O<sub>5</sub>·TiO<sub>2</sub>, (2) low material recession is associated with the formation and spallation of CrNbO<sub>4</sub>, and (3) the formation and spallation of Nb<sub>2</sub>O<sub>5</sub>·TiO<sub>2</sub> is favored in alloys containing high volume percents of Nb solid-solution phase, while CrNbO<sub>4</sub> formation and spallation is favored in alloys with high volume percents of silicide and Laves phase.

The weight-change data of the Nb-base *in situ* composites are presented in Fig. 9. The alloys exhibited a wide range of cyclic-oxidation behaviors, which were deduced based on the weight damage of the test specimens and the weight of the spalled oxides collected as a function of thermal cycles. Nb<sub>x</sub> spalled readily and showed material loss after 120 hr. of oxidation. In contrast, M2 showed very little spallation or material loss after 500 hr. Both the weight change of the test specimens and the weight of spalled oxides were very small for thermal exposure up to 500 hr. Alloys M1, AX, and UES-AX exhibited cyclic-oxidation data that lay between those of Nb<sub>x</sub> and M2. The weight-change curves of AX and UES-AX were essentially identical; these two materials had similar compositions but exhibited different microstructures because UES-AX was heat-treated, while AX was in the as-cast condition.

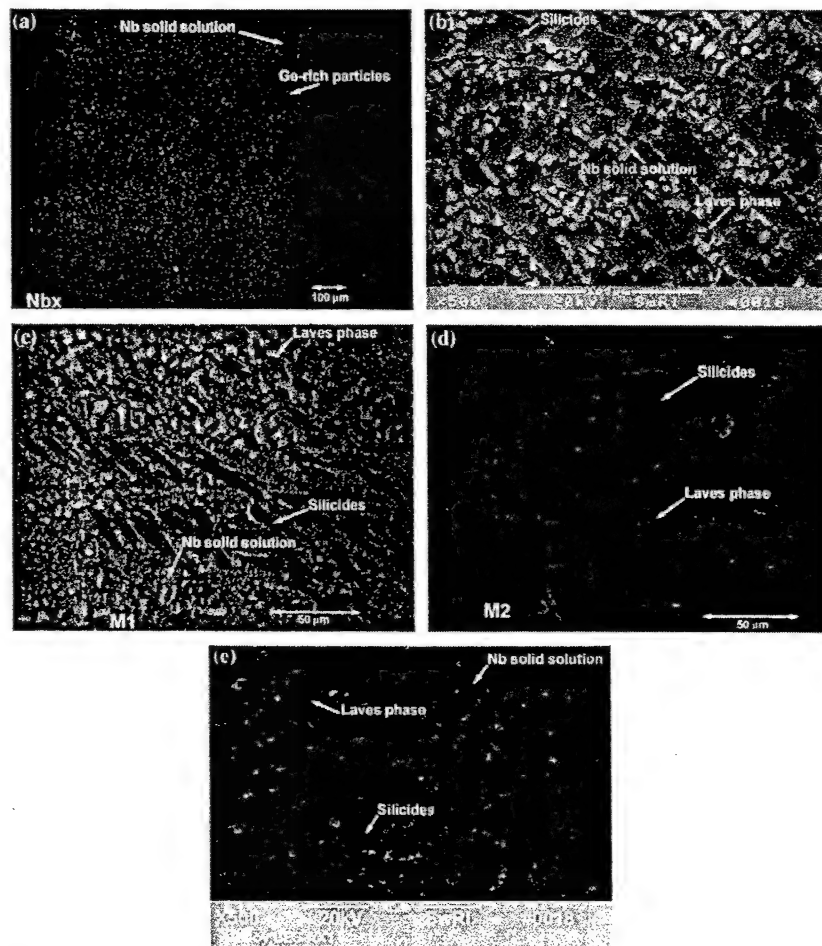


Fig. 7. Microstructures of Nb-base *in situ* composites: (a) as-cast  $Nb_x$ , (b) as-cast AX, (c) as-cast M1, (d) as-cast M2, (e) heat-treated UES-AX.

The experimental weight-change results are compared against theoretical calculations using Eq. (4) for independent oxidation. In applying the model for independent oxidation, the *in situ* composites were treated as two-phase materials containing an Nb solid-solution phase and intermetallics of both silicide and Laves phases.  $Nb_x$  weight-change data were used to obtain the parabolic rate and the spallation constants for the formation of  $Nb_2O_5 \cdot TiO_2$  on the Nb solid-solution phase. Similarly, the weight-change data for M2 were used to determine the parabolic rate and spallation constants for the formation of  $CrNbO_4$  on the silicide and



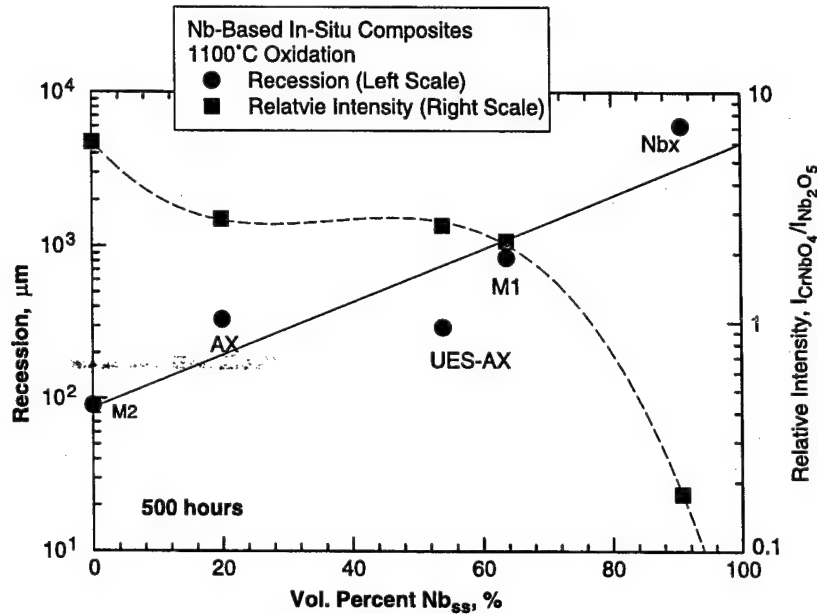


Fig. 8. Intensity of the  $\text{CrNbO}_4$  peak normalized by the intensity of the  $\text{Nb}_2\text{O}_5 \cdot \text{TiO}_2$  and material recession as a function of volume percent of Nb solid-solution phase.

Laves phases. A computer code described in previous publications<sup>46,59</sup> was utilized to obtain the material constants and to perform the cyclic oxidation computation. For determining the model constants for M2, the initial portion ( $t \leq 300$  hr) of the weight-change curve was used to obtain the value of  $k_p$  by setting  $q = 0$  so that the computed weight gain response was parabolic. The values of  $q$  and  $m$  were then chosen by fitting the computed weight-change curve to the experimental data. For  $\text{Nb}_x$ , the value of  $k_p$  for  $\text{Nb-38Ti-12Hf-12Al}$  was used since the experimental data showed only weight loss. Using the assumed  $k_p$  value, the values of  $q$  and  $m$  for  $\text{Nb}_x$  were determined by fitting the computed weight-change curve to the experimental data. A summary of the model constants is presented in Table VI. Using this set of model constants, the weight changes for the five alloys were then computed using Eq. (4) and experimentally determined values of the volume fraction of Nb solid-solution phase. The calculated curves are in perfect agreement with experimental data for  $\text{Nb}_x$  and M2, as shown in Fig. 9, because the model was fitted to these experimental data. The calculated curves for AX, UES-AX, and M1 are model predictions. As indicated in Fig. 9, the model over-predicted the weight changes for M1, AX, and UES-AX, when the actual values of the

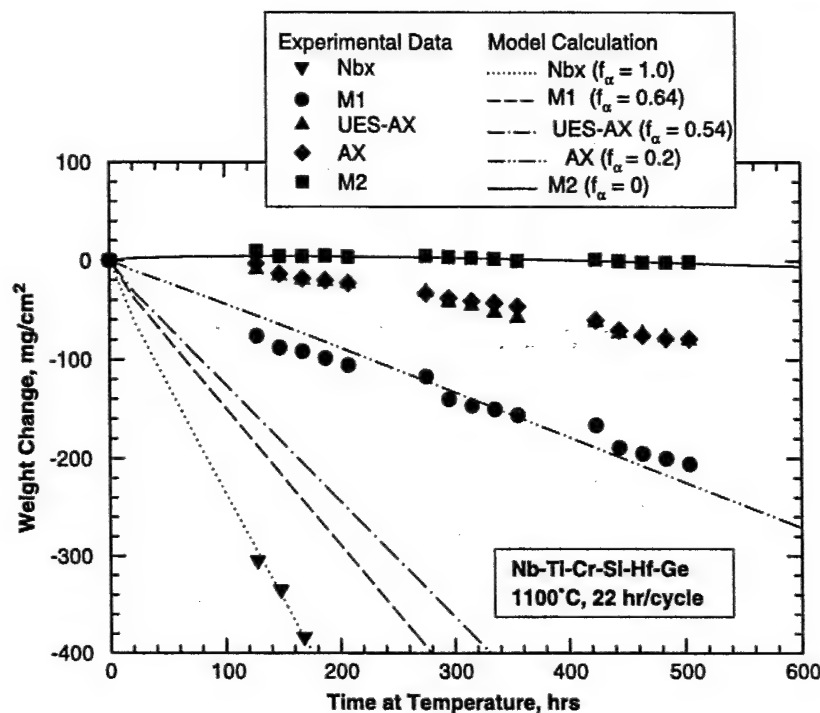


Fig. 9. Experimental weight-change data compared against calculated weight-change curves for Nb-base *in situ* composites. Model calculations were performed via Eq. (4) and the assumption of independent oxidation of individual phases. The area fractions of surfaces covered by  $\text{Nb}_2\text{O}_5 \cdot \text{TiO}_2$  and  $\text{CrNbO}_4$  were taken to correspond to the volume fractions of Nb solid solution ( $f_\alpha$ ) and intermetallic (silicide + Laves) phases, respectively.

volume fraction of Nb solid-solution phase in the alloys was used. The discrepancy suggested that the area fractions covered by  $\text{Nb}_2\text{O}_5 \cdot \text{TiO}_2$  in these alloys were smaller than those of Nb solid-solution phase in the microstructure. Conversely, the area fractions covered by  $\text{CrNbO}_4$  could be larger than those of silicide and Laves phase. A possible implication is that oxidation of the constituent phases in the microstructure might not be totally independent. More importantly, this result also suggests that there might be a tendency for  $\text{CrNbO}_4$  to displace  $\text{Nb}_2\text{O}_5$  or  $\text{Nb}_2\text{O}_5 \cdot \text{TiO}_2$ , which might ultimately result in a continuous layer of  $\text{CrNbO}_4$ . The area fractions that were covered by  $\text{Nb}_2\text{O}_5 \cdot \text{TiO}_2$  were deduced by fitting the model to the weight-change data. As shown in Fig. 10, the area fractions covered by  $\text{CrNbO}_4$  were 0.06, 0.06, and 0.2 for AX, UES-AX, and M1, respectively. In comparison, the volume fractions of Nb solid-solution phase in these alloys were 0.2, 0.54 and 0.64 for AX, UES-AX, and M1,

Table VI. A Summary of Material Constants for the Cyclic-Oxidation Model of Nb-base *In Situ* Composites at 1100°C

Model constant	Nb <sub>x</sub>	M2
$k_p$ (mg <sup>2</sup> /cm <sup>4</sup> /hr)	1.82	0.25
$q$	$4.0 \times 10^{-8}$	$1 \times 10^{-9}$
$m$	1.40	1.05

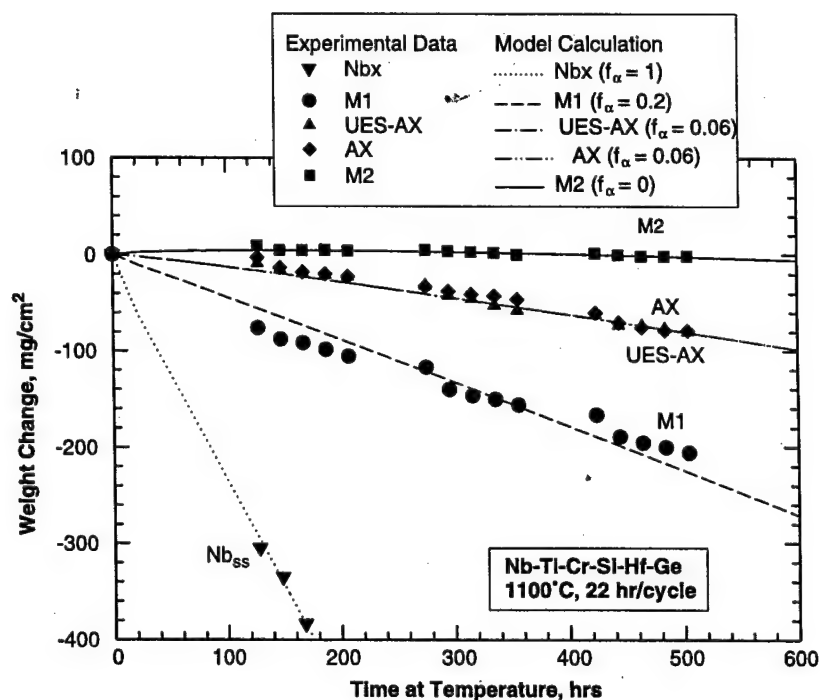


Fig. 10. Comparison of measured and computed weight-change curves for Nb-base *in situ* composites. The model was fitted to the experimental weight change data to deduce the area fractions ( $f_a$ ) of Nb solid-solution phases covered by  $\text{Nb}_2\text{O}_5 \cdot \text{TiO}_2$  for M1, UES-AX and AX. The deduced values  $f_a$  for these alloys are significantly lower than the volume fraction of the Nb solid-solution phase, which suggests that there is a tendency to form  $\text{CrNbO}_4$  at the expense of  $\text{Nb}_2\text{O}_5 \cdot \text{TiO}_2$ .

respectively. Thus, the oxide layer on AX and UES-AX could be close to being continuous and could possibly be comprised mostly of  $\text{CrNbO}_4$ . Nonetheless, the small amounts of  $\text{Nb}_2\text{O}_5 \cdot \text{TiO}_2$  that formed on AX and UES-AX exerted significant influence on the spallation behavior.

The critical condition for the exclusive formation of  $\text{CrNbO}_4$  was computed using Eq. (20) and published data of the interdiffusion coefficient of Cr in Nb<sup>10</sup> at 1100°C since the corresponding value for ternary or multicomponent alloys could not be found in the literature. In particular,  $D$  was set equal to  $8.3 \times 10^{-6} \mu\text{m}^2/\text{hr}$  at 1100°C. This value of  $D$  was also used for M2 since no diffusion data could be found for either the silicide or the Laves phase. The calculated curves for oxidation times of 10, 100, and 500 hr are shown in Fig. 11, together with the experimental data for the four Nb-base *in situ* composites. At a given volume fraction, the calculated critical particle sizes required for the exclusive formation of  $\text{CrNbO}_4$  are significantly smaller than those observed experimentally in M2. The model failed to predict the exclusive formation of  $\text{CrNbO}_4$  in M2. An analysis of the model calculation indicated that the interdiffusion coefficient ( $D = 8.3 \times 10^{-6} \mu\text{m}^2/\text{hr}$ ) might not be appropriate since it was for diffusion of Cr in Nb, but no Nb solid solution existed in M2. By fitting the model to the data for M2, the  $D$  value for Cr diffusion in silicide and Laves phase was  $2.2 \times 10^{-5} \mu\text{m}^2/\text{hr}$ . Using this

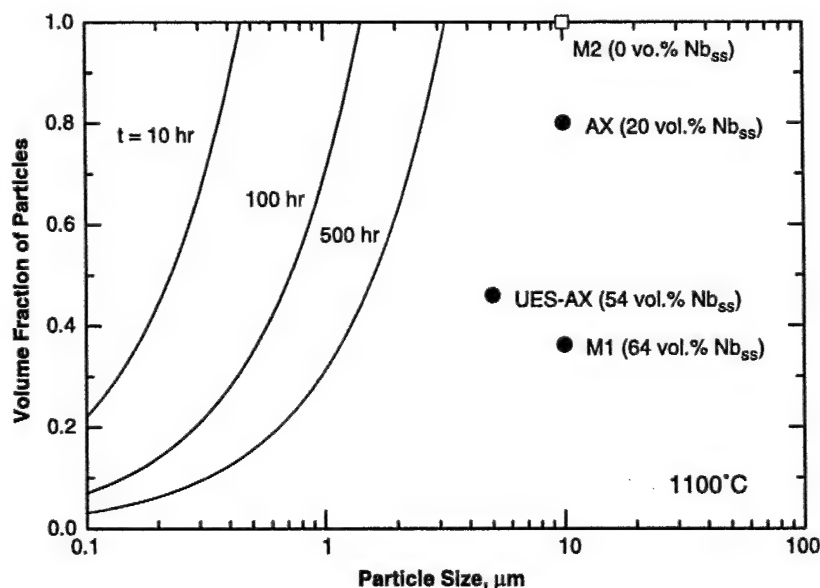


Fig. 11. Computed critical volume fractions and particle sizes of intermetallics (silicide and Laves phases) required for the exclusive formation of a continuous  $\text{CrNbO}_4$  scale at 1100°C compared against experimental data, using  $D = 8.3 \times 10^{-6} \mu\text{m}^2/\text{hr}$  for Cr in Nb. The model failed to predict the formation of a continuous  $\text{CrNbO}_4$  on M2 using this value for the interdiffusion coefficient.

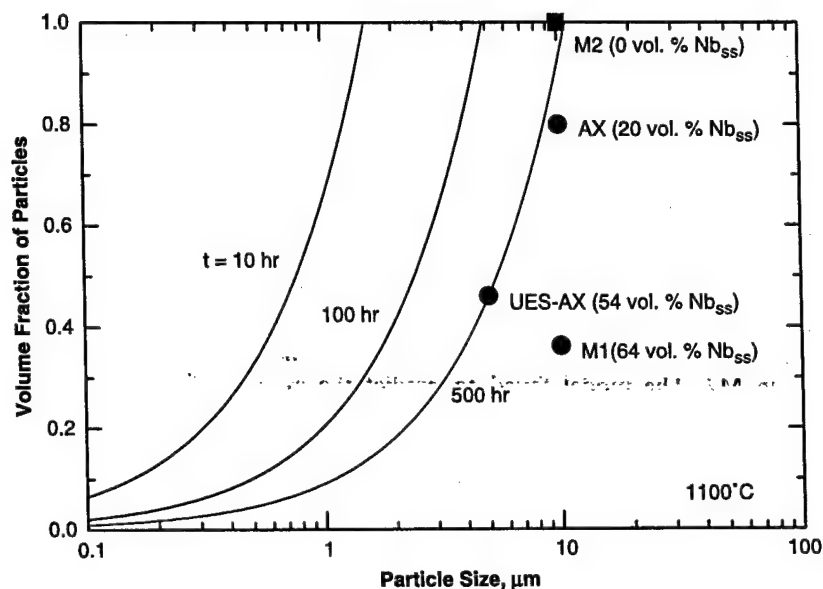


Fig. 12. Comparison of computed and measured volume fractions and particle sizes for the formation of a continuous  $\text{CrNbO}_4$  scale at  $1100^\circ\text{C}$ . The  $D$  value required to fit the experimental data is  $2.2 \times 10^{-5} \mu\text{m}^2/\text{hr}$ , compared to  $D = 8.3 \times 10^{-6} \mu\text{m}^2/\text{hr}$  for Cr in Nb. With  $D = 2.2 \times 10^{-5} \mu\text{m}^2/\text{hr}$ , the model predicts the occurrences of a continuous  $\text{CrNbO}_4$  on M2, a nearly continuous  $\text{Cr}_2\text{NbO}_4$  on AX and UES-AX, and a mixture of  $\text{Nb}_2\text{O}_5 \cdot \text{TiO}_2$  and  $\text{CrNbO}_4$  oxides on M1.

$D$  value, the predicted critical particle sizes are in better agreement with the experimental data. As shown in Fig. 12, the model predicted the exclusive formation of  $\text{CrNbO}_4$  in M2 and the occurrence of nearly continuous layers of  $\text{CrNbO}_4$  in AX and UES-AX, as well as the absence of a continuous  $\text{CrNbO}_4$  layer in M1. In addition, the identical cyclic-oxidation behaviors observed in AX and UES-AX can be explained on the basis of the smaller particle size in UES-AX.

### DISCUSSION

Oxidation models<sup>37-43</sup> exist in the literature for treating independent oxidation and the exclusive formation of an oxide layer on two-phase binary alloys. These models have been used to provide bounds of cyclic-oxidation behaviors and to identify the critical conditions for the formation of a continuous, protective-oxide layer on Nb-base *in situ*

composites, which are multiphase, multicomponent alloys. Since there is no corresponding theoretical treatment for multiphase, multicomponent alloys, the use of the simpler theoretical models for two-phase binary alloys appears to be justified since they are formulated essentially on the basis of a mass balance. The discrepancy between the model predictions and experimental results in Figs. 9 and 11 can be attributed to uncertainties in the area functions of the individual phases (Fig. 10) and the coefficient of interdiffusion (Fig. 12). Though not an absolute proof, the deduced values of area fractions of individual phases and the interdiffusion coefficient are reasonable and provide a basis for further model improvement and experimental verification. Nonetheless, the limitations of the two-phase models for applications to multiphase, multicomponent alloys are acknowledged. Other possible sources of the observed discrepancy include the inadequacy of the two-phase model (e.g., the linear dependence on the volume fractions, etc.) for complex multiphase, multicomponent systems and the various assumptions made to extend the two-phase models to multiphase systems.

Although the cyclic oxidation models are not in quantitative agreement with the experimental data, insight can be gained from applying the two-phase models to multiphase systems. The theoretical calculations indicated that for independent oxidation of Nb-base *in situ* composites, the cyclic-oxidation behavior of the Nb solid-solution phase is likely to dominate. Independent oxidation is likely to give the lowest oxidation resistance, while the exclusive formation of a protective-oxide layer should provide better oxidation resistance. Moreover, the critical conditions for the exclusive formation of a continuous layer of  $\text{Al}_2\text{O}_3$ ,  $\text{Cr}_2\text{O}_3$ , or  $\text{SiO}_2$  are quite stringent and are difficult to achieve. The formation of a continuous  $\text{SiO}_2$  on Nb-base solid solution alloys and *in situ* composites is most difficult because of the low solubility of Si in Nb.

Comparison of computed and measured weight change curves for several Nb-base *in situ* composites containing various volume fractions of Nb solid solution, Laves phase, and silicides suggested that cyclic oxidation of the various phases in the microstructure did not proceed independently. Instead, it appeared that  $\text{Nb}_2\text{O}_5 \cdot \text{TiO}_2$  interacted with  $\text{Cr}_2\text{O}_3$  to form  $\text{CrNbO}_4$ . The interaction led to the formation of a continuous  $\text{CrNbO}_4$  layer in M2 and nearly continuous layers of  $\text{CrNbO}_4$  plus  $\text{TiO}_2$  in AX and UES-AX. The lower oxidation resistance in AX and UES-AX may be attributed to the presence of  $\text{TiO}_2$  formation and the lack of a continuous  $\text{CrNbO}_4$  layer. The cooperative oxidation behavior cannot be described by current models, but could be bounded by current models for independent oxidation and for the exclusive formation of a continuous oxide layer. The theoretical model of Wang *et al.*,<sup>38</sup> indicates that an

increase in the volume fractions and a decrease in the sizes of the Laves phase can enhance the formation of a continuous  $\text{CrNbO}_4$  oxide layer.

Although the formation of a continuous protective  $\text{SiO}_2$ ,  $\text{Cr}_2\text{O}_3$ , or  $\text{Al}_2\text{O}_3$  layer is difficult to achieve on Nb-base *in situ* composites, the cyclic-oxidation resistance of certain Nb-base *in situ* composites meets the desired oxidation goal for the temperature investigated. The oxidation resistance of these alloys appears to arise from the formation of mixed or double oxides such as  $\text{CrNbO}_4$ . According to Eqs. (4), (16) and (18), the key material parameters required to achieve exclusive formation of a continuous oxide layer include: (1) a low parabolic rate constant ( $k_r$ ), (2) a high interdiffusion coefficient,  $D$ , (3) a small particle size, and (4) a low spallation constant,  $q$ . Material attributes that lead to a low spallation constant ( $q$ ) are low defect density and thermally-induced stresses ( $\Delta E \Delta \alpha$ ) in the oxides,<sup>46</sup> but a high fracture toughness for the oxides.<sup>46</sup> A detailed analysis of the weight-change curve of M2, shown in Fig. 10, indicated a combination of low  $k_r$  and  $q$  values; both could be attributed to the interaction of  $\text{Nb}_2\text{O}_5$  and  $\text{Cr}_2\text{O}_3$  to form  $\text{CrNbO}_4$ . The apparent absence of weight change observed at oxidation times exceeding 200 hr was the result of a balance between oxidation and spallation. These experimental observations confirmed three theoretical predictions by the oxidation models: (1) a continuous layer of  $\text{SiO}_2$  or  $\text{Cr}_2\text{O}_3$  is unlikely to form on current Nb-base *in situ* composites, (2) the formation of mixed oxides may provide sufficient oxidation resistance to meet the oxidation goal, and (3) the exclusive formation of a continuous  $\text{CrNbO}_4$  oxide layer can be achieved by reducing the size of the particles preferentially oxidized in the microstructure.

The critical conditions for the formation of a continuous  $\text{CrNbO}_4$  layer are likely to vary with temperature since  $k_r$ ,  $D$ ,  $q$ , and the microstructure are all temperature-dependent. More recent data<sup>35</sup> indicated that a continuous  $\text{CrNbO}_4$  layer could not form when the test temperature was increased from 1100 to 1400°C or decreased from 1100 to 900°C. In all cases, the cyclic-oxidation resistance of Nb-base *in situ* composites decreases when the formation of  $\text{Nb}_2\text{O}_5 \cdot \text{TiO}_2$  is favored over that of  $\text{CrNbO}_4$ . Among the materials examined, M2 exhibited the best cyclic-oxidation behavior with an oxidation life of  $\approx 500$  hr at 1100°C, but less than 200 hr at 900, 1200, and 1315°C.

## CONCLUSIONS

Computational models were utilized to identify possible means for improving the oxidation resistance of Nb-base *in situ* composites. The conclusions reached in this investigation are as follows:



1. The cyclic-oxidation behaviors of Nb-base *in situ* composites are bounded by those of independent oxidation and the selective oxidation of the most reactive element to form an exclusive continuous layer.
2. The oxidation behavior of the Nb solid-solution phase and the formation of  $\text{Nb}_2\text{O}_5 \cdot \text{TiO}_2$  dominates the cyclic-oxidation behavior of Nb-base *in situ* composites.
3. The exclusive formation of a continuous layer of  $\text{Cr}_2\text{O}_3$  or  $\text{SiO}_2$  on Nb-base *in situ* composites is more difficult than the formation of a layer of mixed oxides with  $\text{Nb}_2\text{O}_5$ ,  $\text{Cr}_2\text{O}_3$ , and  $\text{SiO}_2$ .
4. The formation of a continuous layer of  $\text{CrNbO}_4$  by interaction of  $\text{Nb}_2\text{O}_5$  and  $\text{Cr}_2\text{O}_3$  may provide oxidation resistance in Nb-base *in situ* composites for up to 500 hr at  $1100^\circ\text{C}$ .
5. For Nb-base *in situ* composites, a high volume fraction of small (5–10  $\mu\text{m}$ ) Laves and silicide phases is required for the formation of a continuous  $\text{CrNbO}_4$  oxide layer.

#### ACKNOWLEDGEMENTS

This work was supported by the Air Force Office of Scientific Research through Contract No. F49620-01-C-0016, Dr. Craig S. Hartley, Program Manager. The author is grateful to Dr. Young-Won Kim at UES, Inc. for supplying a cast bar of alloy UES-AX and to Dr. Melvin R. Jackson at General Electric (GE) for providing the compositions and oxidation data of GE alloys. Technical assistance by Messrs. F. Campbell, B. Chapa, and James Spencer, all of Southwest Research Institute® (SwRI®), in conducting the oxidation experiments, microstructural characterization and X-ray diffraction analyses are acknowledged. The clerical assistance of Ms. L. Salas, SwRI, in the preparation of this manuscript is appreciated.

#### REFERENCES

1. J. W. Semmel, Jr., in *Refractory Metals and Alloys*, AIME Metallurgical Society Conferences, M. Semchyshen, and J. J. Hardwood, eds. (Interscience Publishers, New York, 1960), Vol-11, pp. 119–168.
2. A. B. Michael, in *Reactive Metals*, AIME Metallurgical Society Conferences, W. R. Clough, ed. (Interscience Publishers, New York, 1958), Vol 2, pp. 487–507.
3. G. T. J. Mayo, W. H. Shepherd, and A. G. Thomas, *Journal of the Less-Common Metals* 2, 223–232 (1960).
4. H. Inouye, in *Columbian Metallurgy*, AIME Metallurgical Society Conferences, D. L. Douglass and F. W. Kunz, eds. (Interscience Publishers, New York, 1960), pp. 649–665.
5. S. T. Wlodek, in *Columbian Metallurgy*, AIME Metallurgical Society Conferences, D. L. Douglass and F. W. Kunz, eds. (Interscience Publishers, New York, 1960), Vol. 10, pp. 553–583.

6. S. T. Wlodek, in *Columbian Metallurgy, AIME Metallurgical Society Conferences*, D. L. Douglass and F. W. Kunz, eds. (Interscience Publishers, New York, 1960), Vol. 10, pp. 175-203.
7. R. E. Pawel, J. V. Cathcart, and J. J. Campbell, in *Columbian Metallurgy, AIME Metallurgical Society Conferences*, D. L. Douglass and F. W. Kunz, eds. (Interscience Publishers, New York, 1960), Vol. 10, pp. 667-684.
8. P. Lublin, W. J. Sutkowski, E. Rittershaus, and J. Brett, in *Refractory Metals and Alloys IV Research and Development—Vol. II, AIME Metallurgical Society Conferences*, R. I. Jaffee, G. M. Ault, J. Maltz, and M. Semchyshen, eds. (Gordon and Breach Science Publishers, New York, 1965), Vol. 41, pp. 1083-1105.
9. J. D. Cox, and J. R. Kerr, in *Refractory Metals and Alloys IV Research and Development—Vol. II, AIME Metallurgical Society Conferences*, R. I. Jaffee, G. M. Ault, J. Maltz, and M. Semchyshen, eds. (Gordon and Breach Science Publishers, New York, 1965), Vol. 41, pp. 901-917.
10. J. F. Stringer, *High-Temperature Corrosion of Aerospace Alloys*, (AGARD-AG-200, Advisory Group for Aerospace Research and Development, NATO, August 1975).
11. H. Inoye, in *Proceedings of the International Symposium on Niobium*, H. Stuart, ed. (TMS, Warrendale, 1984), pp. 615-636.
12. R. T. Begley, in *Evolution of Refractory Metals and Alloys*, E. N. C. Dalder, T. Grobstein, and C. S. Olsen, eds. (TMS, Warrendale, 1994), pp. 29-48.
13. R. A. Perkins and G. H. Meier, *Journal of Metals* **42**, 17-21 (1990).
14. R. C. Svedberg, in *Proceedings of the Symposium on Properties of High Temperature Alloys*, Z. A. Foroulis and F. S. Pettit, eds. (The Electrochemical Society, Princeton, 1976), pp. 331-362.
15. R. A. Perkins, K. T. Chiang, and G. H. Meier, *Scripta Metallurgica et Materialia* **22**, 419-424 (1988).
16. R. A. Perkins, K. T. Chiang, G. H. Meier, and R. Miller, in *Oxidation of High Temperature Intermetallics*, T. Grobstein and J. Doychak, eds. (TMS, Warrendale, 1988), pp. 157-169.
17. J. S. Lee, J. J. Stephens, and T. G. Nieh, in *High-Temperature Niobium Alloys*, J. J. Stephens and I. Amad, eds. (TMS, Warrendale, 1991), pp. 143-155.
18. R. A. Perkins and G. H. Meier, *Microscopy of Oxidation* (Institute of Metals, London, 1991), pp. 183-192.
19. G. H. Meier, *Materials and Corrosion* **47**, 595-618 (1996).
20. R. L. Fleischer and R. J. Zabala, *Metallurgical Transactions A* **21A**, 2149-2154 (1990).
21. D. L. Anton and D. M. Shah, *MRS Symposium Proceedings* **194**, 175-182 (1990).
22. M. R. Jackson, K. D. Jones, S. C. Huang, and L. A. Peluso, in *Refractory Metals: Extrusion, Processing and Applications*, K. C. Liddell, D. R. Sadoway, and R. G. Bustista, eds. (TMS, Warrendale, 1990), pp. 335-346.
23. D. M. Dimiduk, M. G. Mendiratta, and P. R. Subramanian, in *Structural Intermetallics*, R. Darolia, J. J. Lewndowski, C. T. Liu, P. L. Martin, D. B. Mieracle, and M. V. Nathal, eds. (TMS, Warrendale, 1993), pp. 619-630.
24. B. P. Bewlay, H. A. Lipsitt, W. J. Reeder, M. R. Jackson, and J. A. Sutliff, in *Processing and Fabrication of Advanced Materials IV*, V. A. Ravi, T. S. Srivatsan, and J. J. Moore, eds. (TMS, Warrendale, 1994), pp. 547-565.
25. M. R. Jackson, R. G. Rowe, and D. W. Skelly, *Materials Research Society of Symposium Proceedings* **364**, 1339-1344 (1995).
26. P. R. Subramanian, M. G. Mendiratta, and D. M. Dimiduk, *Journal of Metals* **48**, 33-38 (1996).
27. P. R. Subramanian, M. G. Mendiratta, D. M. Dimiduk, and M. A. Stucke, *Materials Science Engineering* **239-340**, 1-13 (1997).
28. M. R. Jackson, B. P. Bewlay, R. G. Rowe, D. W. Skelly, and H. A. Lipsitt, *Journal of Metals* **48**, 39-44 (1996).
29. B. P. Bewlay, M. R. Jackson, and H. A. Lipsitt, *Metallurgical Materials Transactions A*, **27A**, 3801-3808 (1996).

30. P. R. Subramanian, M. G. Mendiratta, and D. M. Dimiduk, *Materials Research Society of Symposium Proceedings* **322**, 491–502 (1994).
31. B. P. Bewlay, M. R. Jackson, W. J. Reeder, and H. A. Lipsitt, *Materials Research Society of Symposium Proceedings* **364**, 943–948 (1995).
32. H. A. Lipsitt, M. J. Blackburn, and D. M. Dimiduk, in *Intermetallic Compounds—Principles and Practice*, J. H. Westbrook and R. L. Fleischer, eds. John Wiley & Sons, New York, 2002), Vol. 3(23) pp. 471–499.
33. B. P. Bewlay and M. R. Jackson, in *Comprehensive Composite Materials*, A. Kelly and C. Zweben, eds. Vol. 3, Metal Matrix Composites, T. W. Clune, ed. (Elsevier, 2000), Vol. 3(22), pp. 579–613.
34. E. S. K. Menon, M. G. Mediratta, and D. M. Dimiduk, in *Structural Intermetallics 2001*, K. J. Hemker, D. M. Dimiduk, H. Clemens, R. Darolia, H. Inui, J. M. Larsen, V. K. Sikka, M. Thomas, and J. D. Whittenberger, eds. (TMS, Warrendale, 2001), pp. 591–600.
35. K. S. Chan, *Metallurgical and Materials Transactions. A*, **35A**, 589–597 (2004).
36. F. H. Stott, G. C. Wood, and J. Stringer, *Oxidation of Metals* **44**, 113–145 (1995).
37. G. Wang, B. Gleeson, and D. L. Douglass, *Oxidation of Metals* **35**, 317–322 (1991).
38. G. Wang, B. Gleeson, and D. L. Douglass, *Oxidation of Metals* **35**, 333–348 (1991).
39. F. Gesmundo, F. Viani, Y. Niu, and D. L. Douglass, *Oxidation of Metals* **39**, 197–209 (1993).
40. F. Gesmundo, F. Viani, Y. Niu, and D. L. Douglass, *Oxidation of Metals* **40**, 373–393 (1993).
41. F. Gesmundo, F. Viani, and Y. Niu, *Oxidation of Metals* **42**, 285–301 (1994).
42. F. Gesmundo, F. Viani, Y. Niu, and D. L. Douglass, *Oxidation of Metals* **42**, 465–483 (1994).
43. F. Gesmundo, and B. Gleeson, *Oxidation of Metals* **44**, 211–237 (1995).
44. F. Gesmundo, F. Viani, and Y. Niu, *Oxidation of Metals* **42**, 409–429 (1994).
45. F. Gesmundo, P. Castello, and F. Viani, *Oxidation of Metals* **46**, 383–398 (1996).
46. K. S. Chan, *Metallurgical and Materials Transactions A*, **28A**, 422 (1997).
47. C. Wagner, *Zeitschrift Fur Elektrochemie* **63**, 772 (1959).
48. G. Wahl, *Thin Solid Films* **107**, 417–426 (1983).
49. W. D. Kloop, D. J. Waykuth, C. T. Sims, and R. I. Jaffee, *Oxidation and Contamination Reactions of Niobium and Niobium Alloys*, Battelle Memorial Institute Report No. 1317, (1959).
50. S. K. Rhee and A. R. Spencer, *Metallurgical Transactions A*, **1**, 2021–2022 (1970).
51. B. Gleeson and M. A. Harper, *Oxidation of Metals* **49**, 373–399 (1998).
52. C. E. Remsberg, P. Beatrice, K. Kurokawa, and W. L. Worrell, *Materials Research Society of Symposium Proceedings* **322**, 243–253 (1994).
53. J. G. L. Ruiz-Aparicio and F. Ebrahimi, *Journal of Alloys and Compounds*, **202**(12), 117–123 (1993).
54. M. Zhang, W. Yu, W. H. Wang, and W. K. Wang, *Thin Solid Films* **287**, 293–296 (1996).
55. Z. Bochníček and I. Vávra, *Materials Letter* **45**, 120–124 (2000).
56. ASTM E1085-87 *Annual Book of ASTM Standards* (ASTM Philadelphia, 1995) Vol. 3(6).
57. K. S. Chan and D. L. Davidson, *Metallurgical and Materials Transactions. A* **34A**, 1833–1849 (2003).
58. Joint Committee on Powder Diffraction Files, International Center for Diffraction Data, Swarthmore, PA, (1992).
59. K. S. Chan, N. S. Cheruvu, and G. R. Leverant, *Journal of Engineering for Gas Turbines and Power* **121**, 484–488 (1999).

**APPENDIX 7**

**"Modeling Creep Behavior of Niobium Silicide In-Situ Composites"**

**Kwai S. Chan**

**Materials Science and Engineering  
Volume A337, (2002) pp. 59-66**

**February 2003**

Reprinted with permission from  
the Copyright Clearance Center, Inc.

# Modeling creep behavior of niobium silicide in-situ composites

Kwai S. Chan \*

Southwest Research Institute, PO Drawer 28510, 6220 Culebra Road, San Antonio, TX 78228-0510, USA

Received 28 August 2001; received in revised form 5 December 2001

## Abstract

A creep model for metal-matrix composites has been extended to treat creep in Nb-based in-situ composites containing silicides in a creeping matrix. Model calculations revealed that the creep exponent of the in-situ composites is significantly influenced by the creep behavior of the stronger reinforcement (silicide or Laves) phase. The wide range of creep exponent (1–11) observed in Nb–Ti–Hf–Si in-situ composites can be explained on the basis of the rigid or creeping behavior of the silicide (or Laves) phase during creep in the in-situ composites. The application of the creep model to designing creep-resistant microstructure for Nb-based in-situ composites is discussed in conjunction with the roles of alloy addition and Peierls–Nabarro stress in influencing the creep resistance of the in-situ composites. © 2002 Elsevier Science B.V. All rights reserved.

**Keywords:** Creep modeling; Creep-resistant microstructure; Niobium silicides; In-situ composites; Nb–Ti–Hf–Si alloys

## 1. Introduction

Niobium silicide in-situ composites are characterized by a microstructure containing niobium silicides toughened with a niobium solid solution. This class of in-situ composites is attractive as high temperature structural materials because it exhibits high tensile strength and creep resistance at elevated temperatures, as well as adequate tensile ductility and fracture toughness at ambient temperatures [1–4]. Significant progress has been made to improve the oxidation resistance of these composites, even though they might still require a coating for very high temperature applications [5].

There have been several recent studies on the creep resistance of niobium silicide in-situ composites [6–12]. In a series of papers [9–12], Henshall and coworkers investigated the primary and steady state creep response of ductile-phase toughened Nb<sub>5</sub>Si<sub>3</sub>/Nb in-situ composites through a combination of analytical modeling and numerical simulation, using experimental data generated by Subramanian et al. [6,7]. These studies, which treated the Nb<sub>5</sub>Si<sub>3</sub> as the continuous phase, demonstrated that the creep behavior of the in-situ composites is dominated by the silicide phase, which is stronger and

bears a higher load than the weaker Nb solid solution. At a given stress, the steady state creep rate of the niobium silicide in-situ composites [7,8] is significantly lower than that of the Nb<sub>ss</sub> phase, even though it is higher than that exhibited by monolithic silicides [6]. The creep exponent of the in-situ composite is about 2 [7,8], compared with  $\approx 1$  for Nb<sub>5</sub>Si<sub>3</sub> [6] and 5.8 for Nb [9,10] or Nb(Si) solid solution [12]. Despite several attempts, Henshall et al. [9–12], were not successful in simulating the correct creep exponent observed in the in-situ composites using continuum methods. These authors attributed the discrepancy to a possible change in the creep mechanisms in the in-situ composites and in monolithic Nb<sub>5</sub>Si<sub>3</sub>.

Bewlay et al. [8], reported the steady state creep rates of a number of niobium-silicide based in-situ composites that contained Ti, Hf, and Mo alloy additions. Fig. 1 compares the results of Bewlay et al. [8], for Nb–Ti–Hf–Si materials against those for Nb–Si [8–10], Nb [9], and monolithic Nb<sub>5</sub>Si<sub>3</sub> [6]. The creep behavior of the Nb–Ti–Hf–Si material exhibited a wider variation compared with those of the binary Nb–Si materials. For example, the creep exponent of the Nb–Ti–Hf–Si materials varies from 1.08 to 11. In contrast, the creep exponent is on the order of 2–3 for Nb–Si and about 1 for Nb<sub>5</sub>Si<sub>3</sub>. The various creep behaviors observed in these niobium silicide in-situ composites are undoubt-

\* Tel.: +1-210-522-2053; fax: +1-210-522-6965

E-mail address: kchan@swri.edu (K.S. Chan).

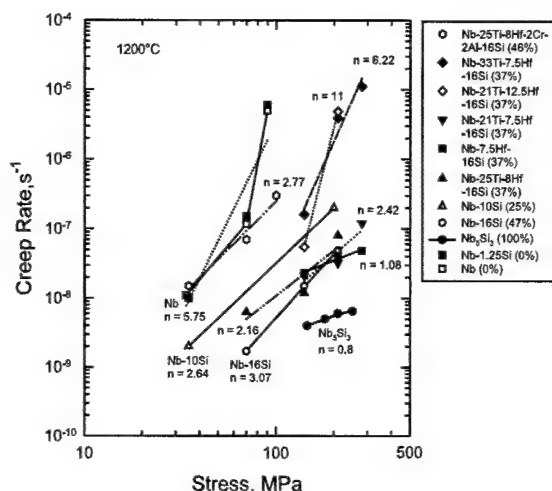


Fig. 1. Steady state creep rates of Nb [9,10], Nb<sub>5</sub>Si<sub>3</sub> [6], Nb–10Si [3], Nb–16Si [8], and Nb–Ti–Hf–Si in-situ composites [8].

edly related to composition, microstructure, or both. Unfortunately, the source and cause of this wide range of creep response are not well understood.

The microstructure of niobium silicide-based in-situ composites depends on the alloy composition. In binary Nb/Nb<sub>5</sub>Si<sub>3</sub> materials, such as Nb–10Si and Nb–16Si, the microstructure is comprised of large primary Nb particles embedded within a matrix of continuous niobium solid solution and Nb<sub>5</sub>Si<sub>3</sub> eutectic [3]. The microstructures of the recently developed Nb–Ti–Cr–Al–Si in-situ composites either with or without Hf, however, are entirely different from those in the binary Nb–Si system [3]. The typical microstructure in Nb–Ti–Hf–Cr–Al–Si alloys consists of a continuous or near continuous bcc ( $\beta$ ) Nb-matrix with dispersed refractory metal silicides, Laves phases or both, depending on alloy composition [3]. This is illustrated in Fig. 2, which shows

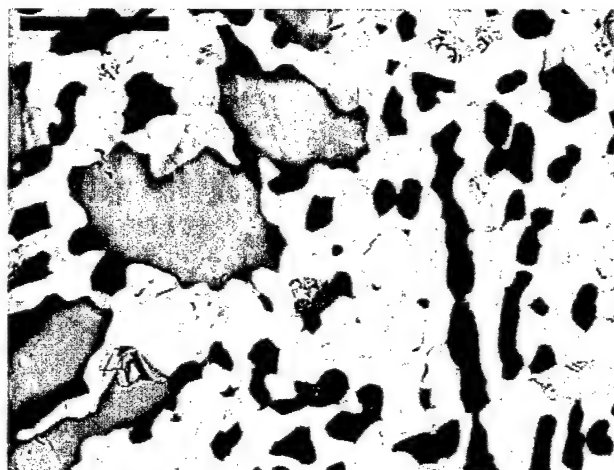


Fig. 2. Microstructure of an Nb–Ti–Hf–Cr–Si–Ge in-situ composite shows a continuous bcc ( $\beta$ ) Nb matrix (light phase) with equiaxed Laves grains (dark phase) and elongated or fibrous silicide grains (gray phase).

the microstructure of an Nb–Ti–Hf–Cr–Si–Ge in-situ composite heat-treated at 1350 °C for 100 h. The microstructure of this alloy is comprised of a Nb solid solution matrix (light phase) with dispersed silicides (gray phase) and Laves phases (dark phase). The volume percents of the Nb solid solution, silicides, and Laves phases are 54, 34, and 12%, respectively. The morphology of the silicide and Laves phase ranges from equiaxed to rod-like with an aspect ratio as high as 5. The alloyed silicides can be M<sub>3</sub>Si or M<sub>5</sub>Si<sub>3</sub>, where M represents Nb, Ti, or Hf, and the Laves phases can be of the C14 or C15 structure, depending on composition. In Nb–Ti–Al in-situ composites, the matrix can have the ordered B2 structure similar to that in NiAl, while the intermetallic phase in the microstructure is Nb<sub>3</sub>Al. The creep behavior of Nb–Nb<sub>5</sub>Si<sub>3</sub> in-situ composites with a continuous silicide matrix has been modeled by Henshall et al. [9–12]. In contrast, the creep behavior of Nb-based in-situ composites with a continuous bcc Nb-matrix or an ordered B2-matrix has not been modeled.

The objective of this article is to present the results of an investigation whose goal was to model the creep response of niobium silicide in-situ composites on the basis of the microstructure and the creep properties of individual constituent phases. A description of the creep model for a two-phase microstructure is presented first. The model is then applied to analyze the creep response of Nb–Ti–Hf–Cr–Si and Nb–Si in-situ composites. The wide range of creep exponents observed in these materials will be explained on the basis of the proposed creep model. In addition, the application of the creep model to improving the creep resistance of niobium silicide in-situ composites is illustrated with a discussion of the importance of alloy addition and the Peierls–Nabarro stress in influencing the creep behavior of the in-situ composites. Possible application of the creep model to B2 based composites, such as NiAl containing short fibers is also discussed.

## 2. Creep model

Several creep models [13–21] have been proposed for treating the steady state creep behavior of metal-matrix composites containing long fibers, short whiskers, or particles. In these models, the metal matrix is considered to exhibit power law creep while the reinforcement phase is usually treated as rigid solids [13–15,17–21]. A few models treat creep in composites containing creeping fibers in a creeping matrix [13,14,16]. Most of the current creep models [9–12] for in-situ composites consider creep to occur in the constituent phases.

In this article, we will apply the approach of Kelly and Street [14] to consider creep in in-situ composites containing: (1) a rigid phase in a creeping matrix and (2) a creeping phase in a creeping matrix. The morphol-

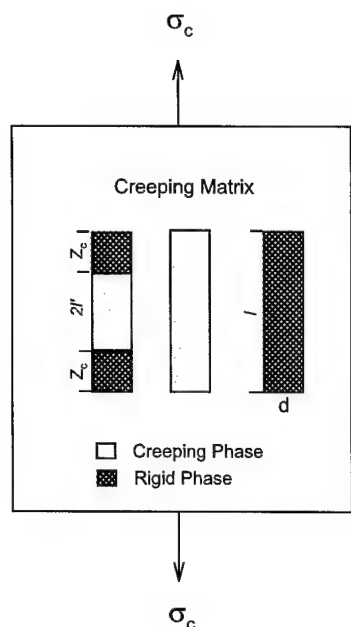


Fig. 3. Schematics of an in-situ composite containing rigid and creeping reinforcement phases in a creeping Nb solid solution matrix subjected to an applied stress,  $\sigma_c$ .

ogy of the silicides and Laves phases dictate that both equiaxed and fibrous grains must be considered. Fig. 3 shows schematically the microstructure of an in-situ composite containing a metallic phase, M, and a fibrous phase, f, which can be a silicide or a Laves intermetallic. The aspect ratio,  $l/d$ , will be varied so that both equiaxed and fibrous grains can be modeled. The volume fraction of the fibrous phase is  $V_f$  and the matrix phase exhibits power law creep as given by:

$$\sigma_m = \sigma_{mo} \left( \frac{\dot{\epsilon}_m}{\dot{\epsilon}_{mo}} \right)^{1/m} \quad (1)$$

where  $\sigma_m$ ,  $\dot{\epsilon}_m$ , and  $m$  are the stress, creep rate, and creep exponent of the metallic phase and the corresponding reference stress and creep rate are signified as  $\sigma_{mo}$ , and  $\dot{\epsilon}_{mo}$ , respectively. For phase compatibility, equal strain rates are assumed in individual constituent phases. Thus:

$$\dot{\epsilon}_c = \dot{\epsilon}_m = \dot{\epsilon}_f \quad (2)$$

where,  $\dot{\epsilon}_c$ ,  $\dot{\epsilon}_m$  and  $\dot{\epsilon}_f$  are creep rates in the composite, matrix, and the fibrous phase. The assumption of equal strain rates and the rule-of-mixtures leads to a composite stress,  $\sigma_c$ , given by [14]:

$$\sigma_c = \sigma_f V_f + \sigma_m (1 - V_f) \quad (3)$$

where  $\sigma_f$  is the average stress in the fibrous phase.

### 2.1. Rigid reinforcement phase in a creeping matrix

During creep of composites containing a rigid phase, strain compatibility at the phase boundary is maintained

by shear along the interface of the matrix and the rigid phase. Using a shear lag model, Kelly and Street [14] calculated the stress transfer between the matrix and the rigid phase, yielding:

$$\sigma_f = \phi \left( \frac{l}{d} \right)^{(m+1)/m} \sigma_m \quad (4)$$

where  $l$  and  $d$  are the length and diameter of the fibrous phase, respectively. The stress transfer function,  $\phi$ , is given by<sup>1</sup> [14]:

$$\phi = \left( \frac{2}{3} \right)^{1/m} \left( \frac{m}{2m+1} \right) \left( \frac{m}{m+1} \right) \times \left[ \left( \frac{2\sqrt{3}}{\pi} V_f \right)^{-1/2} - 1 \right]^{-1/m} \quad (5)$$

which can be combined with Eq. (3) and Eq. (4) to give:

$$\sigma_c = \sigma_{mo} \left( \frac{\dot{\epsilon}_m}{\dot{\epsilon}_{mo}} \right)^{1/m} \left[ 1 + \left[ \phi \left( \frac{l}{d} \right)^{(m+1)/m} - 1 \right] V_f \right] \quad (6)$$

and the creep rate of the composite is:

$$\dot{\epsilon}_c = \left( \frac{\dot{\epsilon}_{mo}}{\sigma_{mo}^m} \right) \left[ \frac{\sigma_c}{\phi(l/d)^{(m+1)/m} V_f + 1 - V_f} \right]^m \quad (7)$$

since  $\dot{\epsilon}_c = \dot{\epsilon}_m$ . Eq. (7) indicates that the creep exponent of the composite is identical to that of the matrix, but the creep rate in the composite is decreased because of a reduced stress level in the matrix.

### 2.2. Creeping reinforcement phase in a creep matrix

Creep in the fibrous phase is assumed to exhibit power-law creep according to:

$$\sigma_f = \sigma_{fo} \left( \frac{\dot{\epsilon}_f}{\dot{\epsilon}_{fo}} \right)^{1/n} \quad (8)$$

where  $\sigma_f$ ,  $\dot{\epsilon}_f$ , and  $n$  are the stress, creep rate, and creep exponent of the fibrous phase;  $\sigma_{fo}$  and  $\dot{\epsilon}_{fo}$  are the corresponding reference stress and reference creep rates, respectively. Creep in the fibrous phase is considered to commence at the mid-length and spread towards the two ends, forming a creep zone of length  $2l'$  and two stress transfer zones of length  $Z_c$  at both ends. The average stress in the fibrous phase derived by Kelly and Street [14] is:

<sup>1</sup> The  $(m/m+1)$  term is missing from Eq. (12a) of Kelly and Street [14].



$$\sigma_f = \sigma_{mo} \left( \frac{\dot{\epsilon}_m}{\dot{\epsilon}_{mo}} \right)^{1/m} \left( \frac{2d}{l} \right) \times \left[ 2^{(m+1)/m} \phi \left( \frac{l'}{d} \right)^{(2m+1)/m} + 4\beta' \left( \frac{m}{m+1} \right) \times \left( \frac{l'}{d} \right)^{(m+1)/m} \left( \frac{Z_c}{d} \right) \right] \quad (9)$$

with

$$\beta' = \frac{1}{2} \left( \frac{4}{3} \right)^{1/m} \left[ \left( \frac{2\sqrt{3}V_f}{\pi} \right)^{-1/2} - 1 \right]^{-1/m} \quad (10)$$

and the ratio  $l'/d$  is given by Eq. (21) of Kelly and Street [14]. It is noted that a negative sign is missing from the exponent in Eq. (21) of Kelly and Street [14]. After combining Eqs. (7)–(9) via a lengthy mathematical manipulation, Eq. (7) is simplified to:

$$\sigma_f = \alpha \sigma_{fo} \left( \frac{\dot{\epsilon}_f}{\dot{\epsilon}_{fo}} \right)^{1/n} \quad (11)$$

with

$$\alpha = \left[ 1 - \left( \frac{1+m}{2m+1} \right) \left( \frac{2l'}{l} \right) \right] \quad (12)$$

which can be combined with Eq. (3) to obtain:

$$\sigma_c = \alpha V_f \sigma_{fo} \left( \frac{\dot{\epsilon}_f}{\dot{\epsilon}_{fo}} \right)^{1/n} + (1 - V_f) \sigma_{mo} \left( \frac{\dot{\epsilon}_m}{\dot{\epsilon}_{mo}} \right)^{1/m} \quad (13)$$

for creep in an in-situ composite with interaction between the creeping matrix and the creeping silicide phase. Interaction between the fibrous phase and the matrix includes the initiation of a creep zone at the center of the fibrous phase, the expansion of the creep zone toward the fiber ends, and the transfer of stresses from the fibrous phase to the creeping matrix. Eq. (13) reduces to Eq. (25) of Kelly and Street [14] when creep occurs fully along the entire length ( $2l' = l$ ) of the fibrous phase.

### 3. Model application

The creep model is applied to compute the steady-state creep response of niobium silicide in-situ composites. Since the creep responses of the five alloyed silicides and Laves phases in the in-situ composites are not known, their creep behaviors are assumed to be rigid in one extreme and creeping like  $\text{Nb}_5\text{Si}_3$  in the other extreme. The two extremes with pertinent creep exponents should encompass all possible creep behaviors of the alloyed silicides and Laves phases. Material input to the creep model is the creep properties of  $\text{Nb}_5\text{Si}_3$  and Nb, which are summarized in Table 1. It is noted that the maximum solubility of Si in Nb is between 1 and

Table 1

Material constants in the creep model for steady state creep

Phase	$\dot{\epsilon}_{mo}$ or $\dot{\epsilon}_{fo}$ ( $\text{s}^{-1}$ )	$\sigma_{mo}$ or $\sigma_{fo}$ (MPa)	$m$ or $n$	Reference
Nb	1	68.24	5.76	[10]
$\text{Nb}_5\text{Si}_3$	1	$3.666 \times 10^{10}$	1	[10]
$\text{Nb}_5\text{Si}_3$	1	$2.236 \times 10^6$	2	Assumed

1.5% depending on alloy compositions. The creep responses of Nb and Nb–1.25Si are identical, as shown in Fig. 1. Thus, the use of creep properties of Nb (or Nb–1.25Si) as the creep properties of the Nb solid solution matrix of the in-situ composites is justified. For creep calculations involving rigid phase, the aspect ratio ( $l/d$ ) is taken to be 5 unless specified otherwise. Creep calculations involving creeping silicides are independent of the  $l/d$  ratio. The creep exponent for Nb is 5.76 while it is 1 for  $\text{Nb}_5\text{Si}_3$ , as shown in Fig. 4. The steady state creep curves of composites with rigid and creeping silicide phases are compared against those of Nb and  $\text{Nb}_5\text{Si}_3$  in Fig. 4. The volume percent silicides used in these calculations was 37% because it was typical of the experimental data shown in Fig. 1. As will be reported later in this paper, creep calculations were also performed for various volume percents of silicides and Laves phases ranging from 25 to 50%. The volume fraction of silicides in the in-situ composites were

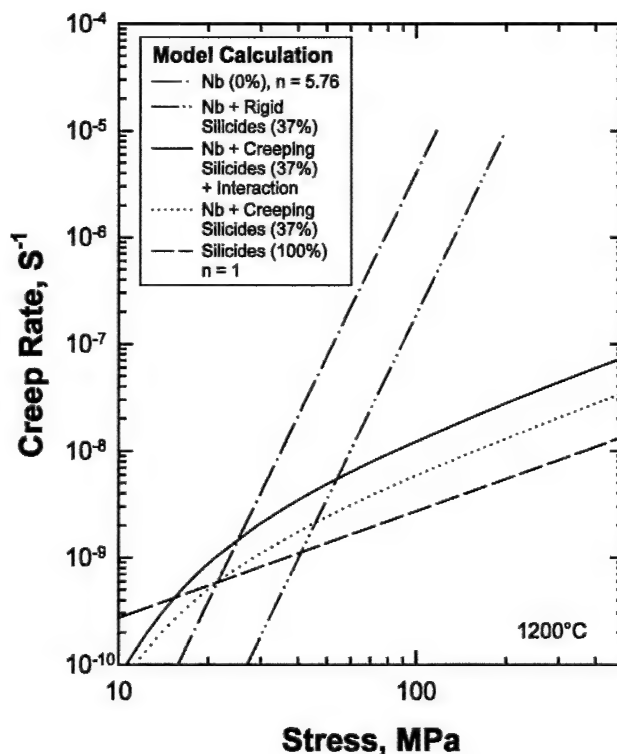


Fig. 4. Calculated steady-state creep rates of Nb,  $\text{Nb}_5\text{Si}_3$ , and Nb in-situ composites with rigid silicides, creeping silicides, and creeping silicides with matrix interactions. The creep exponent of an in-situ composite depends on the creep response of the silicide phase.

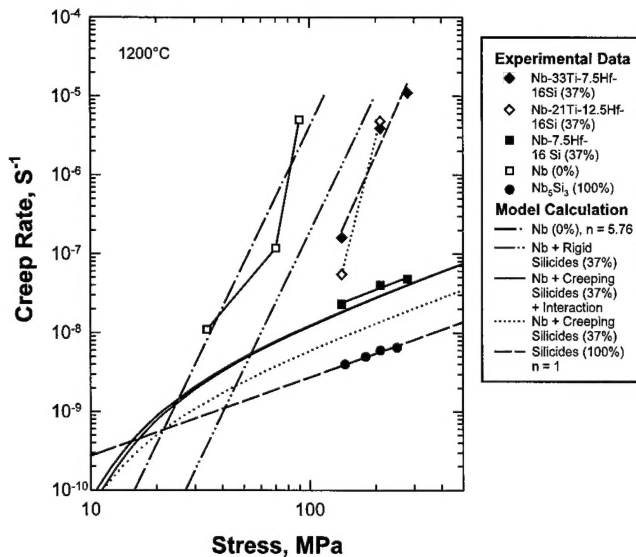


Fig. 5. Comparison of experimental and calculated steady-state creep rates for Nb, Nb<sub>5</sub>Si<sub>3</sub>, and three Nb–Ti–Hf–Si in-situ composites. Experimental data are from the literature [6–10]. A high creep exponent can be correlated to composites with rigid silicides, while a low creep exponent can be attributed to the presence of creeping silicides in the microstructure.

computed using the lever rule and pseudo-ternary phase diagrams [3]. For a Nb-composite with rigid silicides, the creep curve resembles that of the Nb phase and it exhibits an identical slope ( $n = 5.76$ ) as that of Nb but the creep rate is lower at a given stress. The result is that the creep curve of the composite can be obtained by a translation of the creep curve of the metal matrix to a higher stress while keeping the slope constant. In contrast, the creep curve of a composite containing 37% creeping silicides resembles that of the silicide phase at high stresses but exhibits an apparent threshold at lower stresses. Both the creep exponent and the creep rate are higher in the composite containing creeping silicides with matrix interaction than those observed in the monolithic silicide phase. Thus, the creep behavior of the reinforcement phase exerts a major influence on the creep response of the in-situ composite.

Fig. 5 shows a comparison of the calculated creep curves against those of Nb–Ti–Hf–Si in-situ composites. Since the experimental data of Nb and Nb<sub>5</sub>Si<sub>3</sub> were used as input to the creep model, the good agreement between model and experiment is expected. As can be seen in Fig. 5, Nb<sub>5</sub>Si<sub>3</sub> exhibits a higher creep resistance than Nb. For Nb–33Ti–7.5Hf–16Si and Nb–21Ti–12.5Hf–16Si, the slopes of the creep curves resemble that for the composite with rigid silicides even though the model over-predicted the creep rate at a given stress level. A creep exponent of 11 was measured for Nb–21Ti–12.5Hf–16Si, but only two data points were available for this alloy. In contrast, the creep curve for Nb–7.5Hf–16Si, agrees with that calculated for creeping silicides with matrix interaction. Thus, the different

creep behaviors exhibited by these in-situ composites can be explained on the basis of rigid and creeping silicides.

The calculated creep curves are not in agreement with the experimental data of a few in-situ composites, which include Nb–10Si, Nb–16Si, and three other Nb–Ti–Hf–Si in-situ composites. As shown in Fig. 6, these composites exhibit a creep exponent in the range of 2 to 3 and creep rates that are bounded by the creep curves of Nb and Nb<sub>5</sub>Si<sub>3</sub>. A creep exponent of 2–3 cannot be explained on the basis of a creep exponent of 1 for the Nb<sub>5</sub>Si<sub>3</sub>. To overcome this difficulty, it was stipulated that the controlling creep mechanism in these in-situ composites is limited by the Nb<sub>ss</sub>/silicide interface and has a creep exponent of 2. It was plausible because the in-situ composites contain numerous Nb<sub>ss</sub>/silicide interfaces that do not exist in monolithic Nb<sub>5</sub>Si<sub>3</sub>. In addition, a review of creep mechanisms [21] indicates that the stress exponent for interface-controlled creep process is 2. It is also possible that the creep exponent of one of the alloyed silicide or Laves phases is 2, since several alloyed silicides and Laves phases exist in the Nb–Ti–Cr–Si materials. The assumed material properties of the interface-controlled creep in Nb<sub>5</sub>Si<sub>3</sub> are also shown in Table 1. The calculated creep curve for Nb<sub>5</sub>Si<sub>3</sub> with  $n = 2$  is shown in Fig. 7, which also presents the calculated creep curves for in-situ composites. As shown in Fig. 7, the model calculations are in better agreement with the experimental data. The creep exponents for the calculated creep curves of the in-situ composites are now in the range of 2–3 and the calculated creep rates are also in agreement with the observed values.

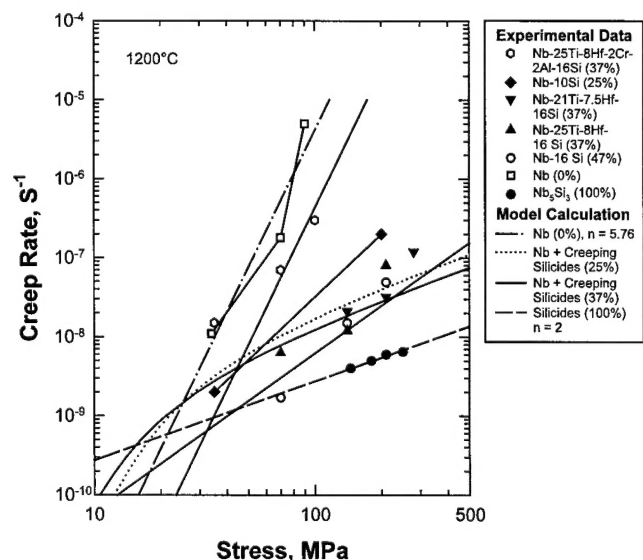


Fig. 6. Calculated steady-state creep rates are not in agreement with the experimental data for Nb–10Si [3], Nb–16Si [8], and three other Nb–Ti–Hf–Si in-situ composites [8], which exhibit a creep exponent of 2–3.

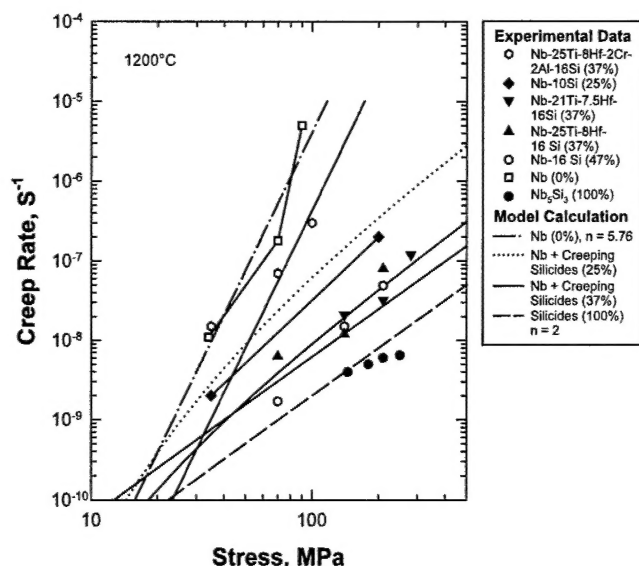


Fig. 7. Comparison of experimental creep data against model calculations using a creep exponent of 2 for the silicide phase. The change of  $n$  from 1 to 2 is assumed to be caused by the presence of Nb/silicide interfaces in the in-situ composite, which are not present in

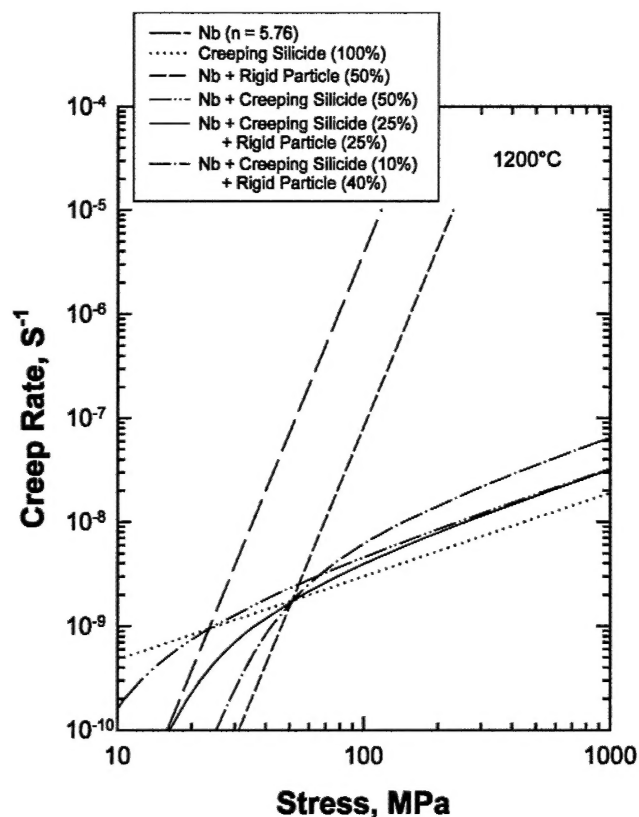


Fig. 8. Model calculations show that creep-resistant in-situ composites require creeping silicides with  $n = 1$  in the microstructure.

The creep model was used to predict the creep curves of in-situ composites containing 50% silicides, but the relative percentages of the rigid and creeping silicides were varied systematically. As shown in Fig. 8, the

composite with rigid silicides exhibits the highest creep exponent and the least desirable creep characteristic. The combination of rigid and creeping silicides resulted in creep curves with a creep exponent on the order of 1 at high stresses ( $> 100$  MPa) and an apparent creep threshold at lower stresses ( $< 30$  MPa). The exact value of the creep threshold depends on the amount of rigid particles in the composites while the creep exponent is approximately equal to that of the monolithic silicide as long as creeping silicides are present in the composites.

#### 4. Discussion

The current creep model predicts that a rigid phase in an in-situ composite would result in a creep curve that is a translation of creep curve of the metal phase to a higher stress. This model prediction is supported by limited experimental data of Nb in-situ composites. In addition, this model prediction is supported by creep data of NiAl reinforced with either alumina particles or whiskers [22], as shown in Fig. 9. A comparison with NiAl-based composites is of interest because the microstructure is similar to those of Nb–Ti–Hf–Cr–Si in-situ composites with a continuous  $\beta$  Nb-matrix and to those of the Nb–Ti–Al in-situ composites with a continuous ordered B2 matrix. As in the case of Nb in-situ composites, the creep data of alumina/NiAl composites are parallel to the creep data of NiAl but are shifted to higher stresses. Comparison of the model calculation against experimental data, shown in Fig. 8, indicates

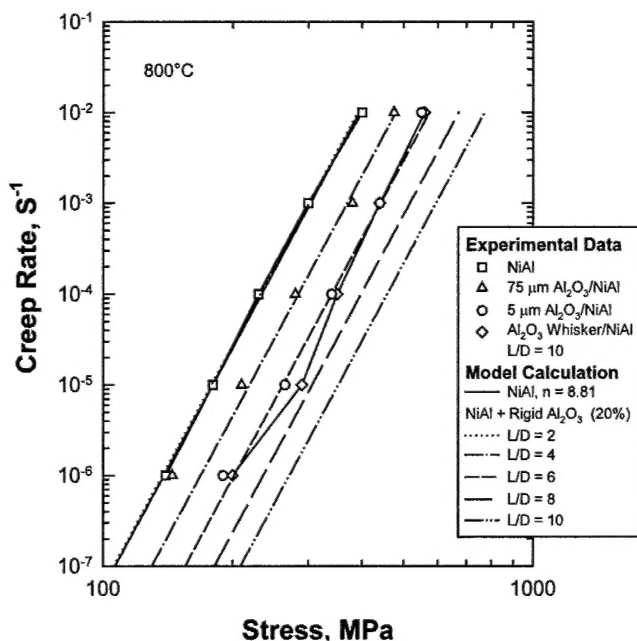


Fig. 9. Calculated and measured steady-state creep rates of NiAl reinforced with alumina particles or whiskers [21]. The creep exponents of the MMCs are comparable to that of the NiAl matrix, suggesting that the alumina particles and whiskers are rigid at 800 °C.

reasonable agreement. Further support of the creep model was provided by the work of Gonzalez–Doncel and Sherby [20], which showed the existence of a creep threshold in aluminum composites reinforced with SiC particles or whiskers. A creep threshold stress is also present in alloys containing hard dispersoids [15].

Both Fig. 5 and Fig. 9 show that the creep model overpredicted the creep rate of composites containing a rigid phase. The discrepancy observed in the Nb-based in-situ composites may be attributed to the value of  $l/d = 5$  in the creep calculations. However, the experimental value of  $l/d = 10$  was used for the creep calculation for composites with alumina whiskers. Thus, the discrepancy between the model and experimental data shown in Fig. 9 cannot be attributed to an incorrect value of  $l/d$ , but suggests a possible deficiency in the model. Finite-element creep modeling by Dragone and Nix [17] indicated that several geometric factors other than the reinforcement aspect ( $l/d$ ) ratio might also influence the creep rate of metal-matrix composites, which include the volume fraction, spacing, and overlap of the reinforcements. Neither the reinforcement spacing nor the overlap are treated in the current model, and they may be the sources of the observed discrepancy. For composites with creeping matrix and reinforcements, the major microstructural parameters are the creep exponent and the volume fraction of the reinforcement phase.

One of the important findings of this investigation is that creeping silicides are beneficial for creep resistance of the in-situ composites, as long as the creep exponent of the creep silicides is low (e.g.  $n = 1$ ). The same conclusion was reached by Henshall et al. [9–12]. Rigid particles or creeping particles with a high creep exponent ( $n > 3$ ) are both undesirable from the viewpoint of creep resistance. For optimum creep resistance in composites, the desirable characteristics are reinforcement phases that are rigid at low stresses but creep with a low stress exponent ( $n = 1$ ) at higher stresses. Thus, diffusional creep [23–25] and Harper–Dorn Creep [26] in the silicide or Laves phases are preferred over power-law creep with  $n > 1$ . The wide range of creep exponents observed in Nb–Ti–Hf–Si in-situ composites may be the consequence of the presence of rigid and creeping silicides in these composites. Alloying addition is known to alter the Peierls–Nabarro stress [27,28] of Nb solid solutions [29,30] and possibly silicide and Laves phases. Recent theoretical work has established a link between the Peierls–Nabarro (P–N) stress and the creep exponent of  $n = 1$  in Harper–Dorn creep [30,32,33]. A high P–N stress can make a silicide or Laves phase act as a rigid particle, and leads to unfavorable creep characteristics. With proper alloying addition to reduce the P–N stress, it may be possible to induce Harper–Dorn [26] or diffusional [23–25] creep in the silicide or Laves phase in

order to attain a low creep exponent, leading to more favorable creep characteristics.

## 5. Conclusions

(1) The wide ranges of the creep exponent observed in Nb in-situ composites, can be explained on the basis of the presence of rigid or creeping silicides in the composites. (2) The presence of both rigid and creeping phases in a creeping matrix can result in an apparent threshold in the creep curve. (3) Composites with rigid silicides exhibit a creep exponent that is identical to that of the creeping matrix, while composites with creeping matrix and creeping silicides exhibit the creep exponent of the silicides. (4) The creep resistance of in-situ composites can be tailored by controlling the relative volume fractions of rigid and creep intermetallics in the microstructure. (5) A creep resistant microstructure requires the stronger reinforcement phase to exhibit low creep rates with a small stress exponent (e.g.  $n = 1$ ).

## Acknowledgements

This work was supported by the Air Force Office of Scientific Research through Contract no. F49620-01-C-0016, Dr Craig S. Hartley, Program Manager. The author is grateful to Dr Young-Won Kim at UES, Inc for providing the micrograph shown in Fig. 2. The clerical assistance of L. Salas, in the preparation of this manuscript is appreciated.

## References

- [1] D.M. Dimiduk, M.G. Mendiratta, P.R. Subramanian, in: R. Darolia, J.J. Lewandowski, C.T. Liu, P.L. Martin, D.B. Miracle, M.V. Nathal (Eds.), *Structural Intermetallics*, TMS, Warrendale, 1993, pp. 619–630.
- [2] B.P. Bewlay, M.R. Jackson, H.A. Lipsitt, *Metall. Mater. Trans. A* 27A (1996) 3801–3808.
- [3] P.R. Subramanian, M.G. Mendiratta, D.M. Dimiduk, M.A. Stucke, *Mater. Sci. Eng. A* 239–340 (1997) 1–13.
- [4] H. Lipsitt, M.J. Blackburn, D.M. Dimiduk, in: R.L. Fleischer, J.H. Westbrook (Ed.), *Intermetallic Compounds*, Wiley, 2002, in press.
- [5] M. Jackson, B. Bewlay, R. Coderman, *Proceedings of the US–Japan Workshop on Very High Temperature Structural Materials*, 9–11 December 1998, Turtle Bay, Hawaii 1998 pp. 49–52.
- [6] P.R. Subramanian, T.A. Parthasarathy, M.G. Mendiratta, D.M. Dimiduk, *Scripta Metall. et Mater.* 32 (8) (1995) 1227–1232.
- [7] P.R. Subramanian, T.A. Parthasarathy, M.G. Mendiratta, D.M. Dimiduk, paper presented at the 1994 MRS Symposium on High Temperature Ordered Intermetallic Alloys—VI, 30 November 1994, Boston, MA. See also, M.G. Mendiratta et al., *Materials Development Research*, WL-TR-96-4113, WPAFB, Dayton, OH 1996.
- [8] B.P. Bewlay, P.W. Whiting, A.W. Davis, C.L. Briant, *MRS Symposium Proceedings* 552 (1999) KK6.11.1–KK6.11.5.

- [9] G.A. Henshall, M.J. Strum, MRS Symposium Proceedings 364 (1995) 937–942.
- [10] G.A. Henshall, M.J. Strum, P.R. Subramanian, M.G. Mendiratta, Scripta Metall. et Mater. 30 (7) (1994) 845–850.
- [11] G.A. Henshall, M.J. Strum, Acta Mater. 44 (8) (1996) 3249–3257.
- [12] G.A. Henshall, P.R. Subramanian, M.J. Strum, M.G. Mendiratta, Acta Mater. 45 (8) (1997) 3135–3142.
- [13] S.T. Mileiko, J. Mater. Sci. 5 (1970) 254–261.
- [14] A. Kelly, K.N. Street, Proc. R. Soc. Lond. A 328 (1972) 283–293.
- [15] J.H. Hausselt, W.D. Nix, Acta Mater. 25 (1977) 1491–1502.
- [16] E. Bullock, M. McLean, D.E. Miles, Acta Metall. 25 (1977) 333–344.
- [17] T.L. Dragone, W.D. Nix, Acta Metall. Mater. 38 (10) (1990) 1941–1953.
- [18] T.L. Dragone, J.J. Schlautmann, W.D. Nix, Metall. Trans. A 22A (1991) 1029–1036.
- [19] K. Wakashima, B.H. Choi, Mater. Sci. Eng. A127 (1990) 57–64.
- [20] G. Gonzalez-Doncel, O.D. Sherby, Acta Metall. 41 (10) (1993) 2797–2805.
- [21] K. Xu, R.J. Arsenault, Acta Mater. 47 (10) (1999) 3023–3040.
- [22] M.E. Kassner, M.-T. Pérez-Prado, Prog. Mater. Sci. 45 (1) (2000) 1–102.
- [23] F.R.N. Nabarro, Report of a Conference on the Strength of Solids (Bristol), the Physical Society, London 1948 pp. 75.
- [24] C.J. Herring, J. Appl. Phys. 21 (1950) 437.
- [25] R.L. Coble, J. Appl. Phys. 34 (1963) 1679.
- [26] J. Harper, J.E. Dorn, Acta Metall. 5 (1957) 654.
- [27] R.E. Peierls, Proc. Phys. Soc. 52 (1940) 34–37.
- [28] F.R.N. Nabarro, Proc. Phys. Soc. 59 (1947) 236–394.
- [29] K.S. Chan, D.L. Davidson, Metall. Mater. Trans. A 30A (1999) 925–939.
- [30] K.S. Chan, Metall. Mater. Trans. 32A (2001) 2475–2487.
- [31] J.N. Wang, T.G. Langdon, Acta Metall. Mater. 42 (7) (1994) 2487–2492.
- [32] J.N. Wang, Acta Mater. 44 (3) (1996) 855–862.
- [33] J.N. Wang, T.G. Nieh, Acta Metall. Mater. 43 (4) (1995) 1415–1419.